Synthesis, structures and properties of inorganic framework materials

Sarah E. Lister

Abstract

"Synthesis, Structures and Properties of Inorganic Framework Materials"

PhD Thesis Sarah E. Lister December 2008

Chapter 1 reviews the literature on the structures and properties of inorganic framework materials that are of relevance to this thesis. In particular the phenomenon of negative thermal expansion and the AM_2O_8/AM_2O_7 families of materials are discussed.

Chapter 2 describes the methods of synthesis and characterisation of the materials investigated in this thesis.

Chapter 3 discusses the dehydration reaction of $MoO_2.H_2O.PO_3OH$. The study involved the introduction of a new methodology for whole pattern powder fitting; this method was later verified by full Rietveld analysis. This investigation led to the discovery and structure solution of two new molybdenum phosphates using powder XRD. These materials have been named β-$MoOPO_4$ and β-$(MoO_2)_2P_2O_7$. A structural pathway for the dehydration reactions has been proposed which is consistent with all of these structures and other analytical data obtained.

Chapter 4 describes investigations into the structures of α-$(MoO_2)_2P_2O_7$ by powder diffraction and NMR methods. The high temperature structure was confirmed to be related to a literature model. The low temperature structure was further studied by electron diffraction, second harmonic generation and solid state NMR. The use of these complementary techniques with powder X-ray and neutron diffraction data, led to the solution of the complex superstructure.

Chapter 5 describes a study into the structures of $(MoO)_2P_4O_{13}$. The material undergoes a phase transition at 523 K. The low temperature structure contains 441 unique atoms and as such is the most crystallographically complex oxide solved to date. The high temperature structure contains 253 unique atoms and is the second most complex oxide in the ICSD.

Chapter 6 describes the *in-situ* X-ray studies on the synthesis of MoP_2O_7 from precursors $MoO_2(PO_3)_2$ and $(MoO)_2P_4O_{13}$ in an H_2 environment. $(MoO_2)_2P_2O_7$ was studied under similar conditions and found to decompose to an unidentifiable poorly crystalline phase.

Chapter 7 describes the discovery of a new high temperature synthetic route to cubic $ZrMo_2O_8$ using extremely rapid time-resolved XRD data recorded at the ESRF. The cubic material forms from its constituent oxides at 1350 K and can be isolated back at room temperature using a quench cooling method. A pure phase sample can be prepared using a ZrO_2:MoO_3 ratio of 1:3. The entire synthesis occurs within seconds and precise control of temperature and time is crucial for this synthesis.

Synthesis, Structures and Properties of Inorganic Framework Materials

Sarah E. Lister M.Chem (Dunelm)

Durham University

Supervisor: Prof. John S. O. Evans

A thesis submitted in partial fulfillment of the requirements

for the degree of Doctor of Philosophy

Department of Chemistry

Durham University

2008

Praise be to the name of God for ever and ever;
wisdom and power are his.

He changes times and seasons;
he sets up kings and deposes them.
He gives wisdom to the wise
and knowledge to the discerning.

He reveals deep and hidden things;
he knows what lies in darkness,
and light dwells with him.

I thank and praise you, O God of my fathers:
You have given me wisdom and power,
you have made known to me what we asked of you

Daniel 2 v 20-23

Acknowledgements

John: Your enthusiasm, encouragement, belief, effort, availability and patience over the last 5(+) years have been truly amazing, and your continued support and understanding when things haven't gone to plan/I haven't been up to scratch have been an inspiration. *Es nulli secundus.*

Ivana: Your status as unofficial second supervisor and friend is well-deserved. Thanks for your encouragement, help in all things single crystal, company on numerous trips to central facilities, food and gossip to name but a few.

Many thanks to those who have helped in a scientific capacity: NMR, Anne Soleilhavoup and Paul Hodgkinson. Beamline scientists Sarah Poulton/Mark Green at NIST, Tim Prior at Daresbury, Richard Ibberson at HRPD, Jon Wright and Irene Margiolaki at the ESRF. Also to Professors Ray Withers (EDPs) and P Shiv Halasyamani (SHG).

To Drs Hampsons, Howard, Stinton and Hickey who went before me, thank you for motivating me to start, at times assuring me I could finish, and for constant long-distance encouragement along the way.

Thanks to all my fellow incumbents of CG31 during my PhD: Lôc, for being lab guru, and all your enthusiasm, advice and gossip. Lars, for the huge impartation of crystallographic knowledge, understanding that phosphates are truly character-building and coffee. Graham, Topas help, source of all things cricket and being a distraction *via* the magic that is gmail. Anne, for keeping me company over the last 3 years and for being an invaluable source of all things NMR. Dave "everybody's dead Dave" Free, your banter, constant source of full spectrum help (random-microsoft-complicated crystallography) and faith have kept me going. Julia, early morning conversation, random questions and cheeriness. Sam, TEA! And a first year's enthusiasm. To the 4th year project students: Charlie, Dave, May, Tom, Alex, Francesca, Oliver, Yuandi, Erin, Victoria and Zoe, thanks for teaching me many things and reminding me that there is life outside the office.

To Lucy, Becca, Sonia, Katherine, Alex and Jayne who have stuck around since undergrad days: Thank you for long distance support and insanity, I promise to be in touch more often from now on.

To Jenny B, James+Jenny, John+Hannah, the Taylors, the Parkers, Sandra, Mrs G and Cora, who have fed me and provided me with tea, time out, listening ears and places to stay at times over the last three years: I could not have done this without you all, thanks for helping me to the finishing line.

To mum, dad, 'little' bro and gran: for your absolute and unconditional love, support and acceptance I owe you everything.

Mark, for taking on both me and my thesis when we got together, thank you. It's just me from now on...

Declaration and Statement of Copyright

The work described in this thesis is entirely my own, except where I have acknowledged help from a named person or given a reference to a published source of a thesis.

The research presented was performed in the Department of Chemistry, Durham University between October 2005 and November 2008, the results of which have not been submitted for a degree in this or any other university. This thesis conforms to the work limit set out in the Degree Regulations of the university.

Table of Contents

Abbreviations

BVS	Bond Valence Sum
CIF	Crystallographic Information File
DPT	Displacive Phase Transition
DSC	Differential Scanning Calorimetry
EDP	Electron Diffraction Pattern
ESD	Estimated Standard Deviation
ESRF	European Synchrotron Radiation Facility
FOM	Figure of Merit
GOF	Goodness of Fit
HRPD	High Resolution Powder Diffractometer at ISIS
HT	High Temperature
ICSD	Inorganic Crystal Structure Database
INADEQUATE	Incredible NAtural Abundance DoublE QUantum Transfer Experiment
IR	Infrared (spectroscopy)
LT	Low Temperature
MAS	Magic Angle Spinning
MoPO	Molybdenum phosphate material
NCNR	National Center for Neutron Research
NIST	National Institute of Science and Technology
NTE	Negative Thermal Expansion
PDF	Powder Diffraction File
PSD	Position Sensitive Detector
PTE	Positive Thermal Expansion
PV	Pseudo Voigt (peak shape)
qRUM	quasi-Rigid Unit Mode
RT	Room Temperature
RUM	Rigid Unit Mode
SHG	Second Harmonic Generation
SLR	Shift Limiting Restraint
SRM	Standard Reference Material
SU	Standard Uncertainty
TCHZ	Thompson-Cox-Hastings (peak shape)
TGA	Thermogravimetric Analysis
TOF	Time of Flight
TOPAS	TOtal Pattern Analysis System
VT	Variable Temperature
XRD	X-ray diffraction

1. Introduction and Literature Review

1.1 Overview

This thesis describes investigations into families of framework materials with interesting structure-property relationships. The framework materials described here are extended solids constructed from relatively rigid metal-centred polyhedra that are linked by more flexible bridges. Examples of the use of such materials include the use of zeolites and aluminophosphates as molecular sieves, in applications from water purification and detergents to the petroleum industry, and the use of phosphate materials as intercalation hosts for batteries. Here the focus is on negative thermal expansion (NTE), in which the material actually contracts on heating; and displacive phase transitions seen on cooling where an "idealised" structure at high temperature adopts a much larger superstructure at low temperature to balance the short- and long-range structural requirements within the system. The possibility of forming new metastable framework materials with interesting properties is also investigated. These can be synthesised by *topotactic* reactions – in which the crystal structure of a precursor phase leads to the formation of a new product phase with a particular structure.[1]

Very low or negative thermal expansion is not a new phenomenon, being first reported in the material Invar, $Fe_{0.65}Ni_{0.35}$, in the late 1800s;[2,3] however, there has been much interest in this area of chemistry due to potential application of these materials, both in industry and for day-to-day use. The ability to control the thermal expansion within composite materials leads to potential in creating materials specifically tailored to their use, *e.g.* in highly precise scientific equipment. To quote two every day examples, as low thermal expansion compounds are more resistant to thermal shock they can be transferred straight from hot ovens to cold tables without shattering or used in dental fillings that should not fall out.

Creating such products begins with the synthesis and investigation of the components of the composites. This chapter seeks to review the physical basis for NTE – using examples from the literature – to serve as an introduction to this thesis. Compound-specific discussions of the literature are given in later chapters.

1.2 Classical ideas of thermal expansion

A classical description of thermal expansion in materials often begins with discussion of the relationship between potential energy and interatomic distance in a diatomic molecule; this is illustrated in Figure 1.1. As the energy of the system rises and higher vibrational energy levels within the diatomic become occupied, the average interatomic distance increases due to the anharmonicity of the potential well. Consequently on increasing temperature the average bond length increases; NTE conflicts with these basic principles. Some very strong bonds may be viewed as having an almost constant average bond length;[4] some bonds have been found to decrease in length on increasing temperature, although this is rare.[4,5]

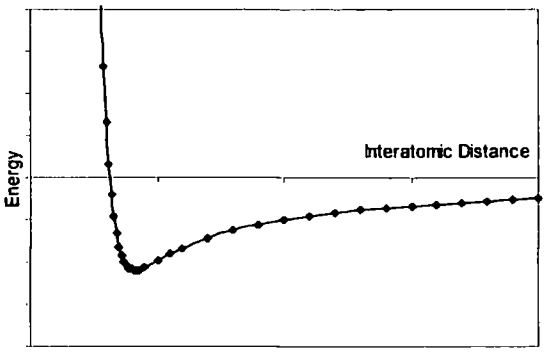

Figure 1.1 Relationship between the energy and interatomic distance of a diatomic molecule.

Figure 1.1 can be considered to represent a typical bond within an isolated molecule; however, to apply this simple picture to larger, more complicated systems, would not precisely describe all the interactions present. In larger systems, for example extended framework materials, strong interatomic forces are present: if one atom is perturbed from its equilibrium position, all closely linked atoms are affected in a wave-like motion through the solid.[6] This means that the variation in population of the whole phonon density of states with temperature must be considered.

The summation of all volume changes within a solid over a defined temperature range results in (normally reversible) changes on a macroscopic scale. If the volume change with increasing temperature is negative, the material can be classified as an NTE material, of which there are two main types, those with intrinsic NTE properties, and those with extrinsic properties.

An intrinsic NTE material is one in which decreasing cell parameter values, whether in one, two or all three dimensions, combine to give an overall decrease in cell volume with temperature. These changes are normally quantified in terms of the coefficient of linear thermal expansion (α_l), which is defined as:

$$\alpha_l = \frac{(L - L_0)}{L_0(T - T_0)} \qquad (1.1)$$

where L is the length at temperature T, and L_0 the length at temperature T_0.[7] It is necessary to state the temperature range over which the quoted coefficient applies, as α is a temperature dependent quantity. This coefficient can be used to quote changes in length along each axis in a crystal, which is useful in the case of anisotropic expansion. However, it is often easier to quote the volume coefficient of thermal expansion,[5] (α_v):

$$\alpha_v = \frac{(V - V_0)}{V_0(T - T_0)} \qquad (1.2)$$

For NTE materials these coefficients will have a negative value over a certain range of temperature. For isotropic materials it is possible to show that the relationship between equations 1.1 and 1.2[5] is:

$$\alpha_l = \frac{1}{3}\alpha_v \tag{1.3}$$

This means that the overall volume change - the quantity measured on a macroscopic scale - is directly proportional to that occurring along each axis. Structurally anisotropic materials are, as a general rule, found to exhibit anisotropy in their expansion; similarly, isotropic materials (cubic systems) undergo isotropic expansion.

NTE has also been found in some compounds exhibiting "normal" positive volume expansion at the unit cell level.[8] Such extrinsic behaviour is found in ceramic bodies containing highly anisotropic crystallites. At high temperatures – or after repeated thermal cycling - microcracks develop due to the stresses imposed on the system from the anisotropic expansion. On reheating from lower temperature the cracks close up, giving rise to negative thermal expansion. These microcracks reduce the mechanical strength - and hence the useful lifetime - of the material in question, and consequently isotropic NTE materials would be preferred for technological applications.

These extrinsic effects also prevent reproducibility between composite samples, an undesirable effect. Other required properties for manufacture include the ability to make the materials using relatively fast standard synthetic procedures from reagents that are easy to obtain, NTE over a large temperature range including ambient temperature and no phase transitions at low pressure, as processing of the material may require compression.[9]

1.3 Mechanisms of NTE

For the coefficient of thermal expansion of a material to be negative there must be a mechanism present within the structure that can outweigh the increase in volume due to bond expansion. There are examples of NTE that point to the conclusion that thermal contraction is not a function of chemical constitution alone, but of the particular crystal structure within that material. One such example is that of plutonium, as only the delta species – stable between 592 and 724 K – contracts on heating; all other allotropes expand.[10]

1.3.1 Transverse vibrations

One description of atomic motion found to explain NTE in several oxides considers the vibrations of a linear arrangement of atoms, for example M-O-M, on increasing temperature. The atoms can vibrate in one of two directions, either in a longitudinal or in a transverse sense, pictured in Figure 1.2. The longitudinal motion (left hand side of the diagram) stretches the M-O bonds, increasing the average M-M distance on increasing temperature. However, a transverse motion (right hand side of the diagram) bends the linear linkage away from 180 °. Metal-oxygen bonds of metals in high oxidation states are generally strong and hence longitudinal motion and, therefore, thermal expansion will be small.[11] Consequently, as the M-O bond length is effectively not varying, transverse bending of the linkage brings the two M atoms closer together on average – *a contraction*.

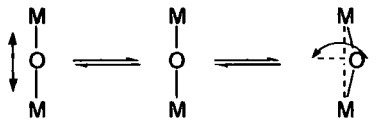

Figure 1.2 The possible vibrations of a metal-oxygen-metal bond with increasing temperature.

In order to understand the expansive behaviour of complex materials, it is necessary to know how these vibrations are affected by temperature, and in turn, how they affect the volume of the material in question. Transverse modes are lower in energy than their longitudinal counterparts; hence at lower temperatures they dominate the phonon density of states. The Grüneisen relationship connects the thermal expansion of a material with its volume:[12]

$$\alpha_v = \frac{\gamma C_v K}{V} \tag{1.4}$$

where α_v is the thermal expansion of the material in question, γ is the so-called Grüneisen parameter, C_v is the specific heat at a constant volume, V, and K is the isothermal compressibility. γ is related to the frequency, ν, of a mode such that:

$$\gamma = \frac{-d(\ln \nu)}{d(\ln V)} \tag{1.5}$$

It follows that modes that decrease in frequency with decreasing volume have negative values of γ and hence contribute a negative component to the overall thermal expansion. If, as outlined above, the overall value of γ – from the addition of each modal contribution – is negative, negative thermal expansion is seen in the material.

Although this mechanism may sound straightforward, there are some conditions necessary for it to occur.[13] The oxygen atoms within the structure must generally be in two-fold coordination, any other interactions of the oxygen will decrease the ability of the linkage to vibrate transversely. The structure must also be an open framework, with no interstitial cations or anions present in the structure, so as not to inhibit the low energy transverse modes. The structure must also have the right topology; this is discussed later in this introduction. Finally, the M-O bond length should not be found to vary significantly over the temperature range where negative thermal expansion takes place. Hazen and Prewitt undertook a compilation of expansion coefficients for metal oxygen bonds.[14] They noted that the thermal expansions of both Si-O and Al-O bonds are very low; in fact, the change in bond lengths can be considered to be zero over a large temperature range. This finding led to the assumption that other (strong) metal-oxygen bonds can be considered in the same way.

1.3.2 Rigid unit modes

For some frameworks there are phonon modes present that were described by Megaw in terms of Rigid Unit Modes (RUMs).[6] These low-energy modes propagate through the structure, causing the rigid polyhedra to rock back and forth if the framework is flexible enough,[15] and with increasing

temperature these vibrational modes are excited and can shrink the lattice, giving rise to the property of negative thermal expansion. This rotation can be viewed in Figure 1.3. If these polyhedra share corners such that the bridging oxygen atom is at the centre of an M-O-M bonding arrangement, these RUMs result in the local transverse vibrations described in Section 1.3.1; correlation of these transverse vibrations across the structure can then give rise to NTE.[16] It is the Rigid Unit Modes that bend the M-O-M inter-polyhedral bonds, enabling the transverse vibration of the oxygen atoms, and hence average M-M distances between adjacent polyhedra contract.[17]

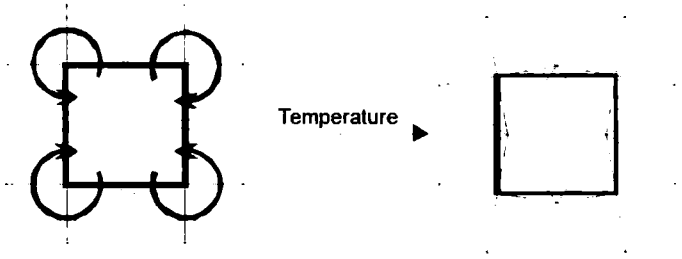

Figure 1.3 The aligned octahedra on the left-hand side of the diagram can rotate with temperature to an arrangement with the same connectivity but with slightly different spatial alignment, as indicated on the right-hand side.

This theory has since been developed computationally by Dove and co-workers.[18,19] Phonon modes that do not distort the polyhedra are described in terms of a RUM; high-frequency phonon modes are non-RUM phonons as these distort the polyhedra. This seemingly black and white situation has become obscured by the realisation that some minimal distortion of polyhedra at relatively low frequencies occurs.[17] It is possible to apply these low frequency modes to a RUM-like model.[20] These so-called quasi-RUMs (qRUMs), have been found in materials exhibiting NTE that do not possess any RUMs, such as some of the AM_2O_7 compounds to be discussed in Section 1.4.2.[21]

1.3.3 RUMs in modelling structural phase transitions

The occurrence of displacive phase transitions (DPTs) in some compounds can be described using similar ideas. DPTs have been described as being caused by the disappearance of a *soft mode*, that is, a phonon mode with a frequency that falls to zero at a certain temperature.[22] Below this temperature the restoring force acting against the deformation vanishes, and the structure can spontaneously deform, freezing the distortion into the structure. Below this transition temperature, structures often have reduced symmetry and volume,[11,23] and if NTE is present above this phase transition it often disappears below it.[8] No changes are normally seen in the chemical bonding; however, the distortion changes the bond angles of the structure, especially the M-O-M angle. These displacive phase transitions have been found to depend on the connectivity in the framework[11] and also on the effective charges[23] within the system.

Two materials found to exhibit such transitions are ZrV_2O_7[11] and the $A_2(MO_4)_3$ family[23] respectively. The former will be discussed further in Section 1.4.2. Many members of the $A_2(MO_4)_3$ family have been found to undergo a volume decreasing phase transition from orthorhombic to monoclinic symmetry, for example in $Sc_2(MoO_4)_3$ this occurs at 178 K on cooling.[23]

There have been three main forces thought to be important in driving these displacive transitions.[24] The first of these occurs due to the long-range dispersive interactions that are caused by the high polarisability of the oxygen atoms. These produce an inward pressure that seeks to reduce the volume of the structure, driving it to a denser, lower symmetry structure, within the limits of the short-range repulsive attractions. The second force is due to the attraction that a cation in a cavity exerts to the surrounding oxygen lattice. This inward pull aims to force the cavity to collapse in on itself, reducing the symmetry of the system. The third main force involves the angular preference of the atoms in the material. For example Si-O-Si bonds prefer to be in the region of 145 – 150 °,[25] and pyrovanadate and pyrophosphate systems prefer non-linear bonding arrangements.[26,27] It is possible that this final effect can either prefer or oppose distortion, depending on whether the bonding arrangements in the higher temperature phase are favourable or not. The energy of these three forces is not always large enough to distort the polyhedra in the system; therefore DPTs found in the systems will often be distortions allowed in the RUM model. RUMs can hence be described as natural soft modes for phase transitions.[22] The delicate balance between these forces within a structure makes it difficult to predict which RUM in a high temperature phase will be responsible for the DPT.

1.4 Materials exhibiting NTE

Due to the increasing interest in this field, it is not practical to review all the literature published on negative thermal expansion in inorganic framework materials. Some good reviews are available.[5,9,28] The materials that will be discussed here in most detail are the AM_2O_7 and AM_2O_8 oxide families as they form the backbone to the work undertaken and are discussed in Chapters 3 to 7 of this thesis. Some other interesting non-oxide materials will also be discussed briefly.

1.4.1 AM_2O_8 phases

The most well studied AM_2O_8 material is ZrW_2O_8 having attracted wide-scale scientific and commercial interest since it was discovered to undergo isotropic NTE from 0.3 K up to 1050 K, its decomposition temperature.[29] Despite the NTE in zirconium tungstate being observed in the 1960s,[30,31] it is only within the last twelve years that the material's structure and properties have attracted much interest, as the structure was elucidated using both x-ray and neutron diffraction studies.[29,32,33]

The structure of ZrW_2O_8 is constructed from ZrO_6 octahedra close to the origin and face-centres of the cubic unit cell, with these polyhedra connected through corner-sharing WO_4 tetrahedra, as shown in Figure 1.4. Each octahedron is connected to six tetrahedra, forming Zr-O-W linkages; however, only three corners of each tetrahedron are linked to an octahedron, leaving one free W-$O_{terminal}$ bond - formally a one-coordinate oxygen atom - found to be appreciably shorter than for those in 2-fold coordination sites.

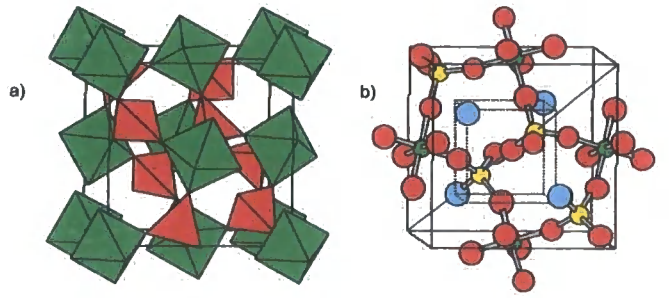

Figure 1.4 The structure of cubic ZrW_2O_8 (a) showing ZrO_6 octahedra (green) and WO_4 tetrahedra (red) (b) ball and stick representation with Zr (green), W (yellow), O (bridging, red, terminal blue) coloured.

The room temperature structure was solved in space group $P2_13$ with lattice parameter, a, equal to 9.1575 Å. The material undergoes a phase transition at 448 K, from the acentric low temperature α-form to a high temperature β-structure in centric space group $Pa\bar{3}$.[32] The material thus has cubic symmetry across the whole range of its stability.[a] In the low temperature structure the paired WO_4 tetrahedra lying on the 3-fold axis are arranged such that the W-O terminal bonds point in the same direction. Above the phase transition these groups become dynamically disordered, giving a time-averaged structure in space group $Pa\bar{3}$.[34] ^{17}O NMR has been used to show that all oxygen sites undergo exchange in the high temperature phase.[35]

The thermal behaviour of the cubic cell parameter of ZrW_2O_8 is illustrated in Figure 1.5.[5] The plot is derived from both dilatometric and neutron powder diffraction data. The discontinuity at ~450 K is clearly visible; α_l is -9.07×10^{-6} K^{-1} (0-350 K),[34] this is of a comparable magnitude to the positive thermal expansion of common ceramics, Table 1.2, page 22.

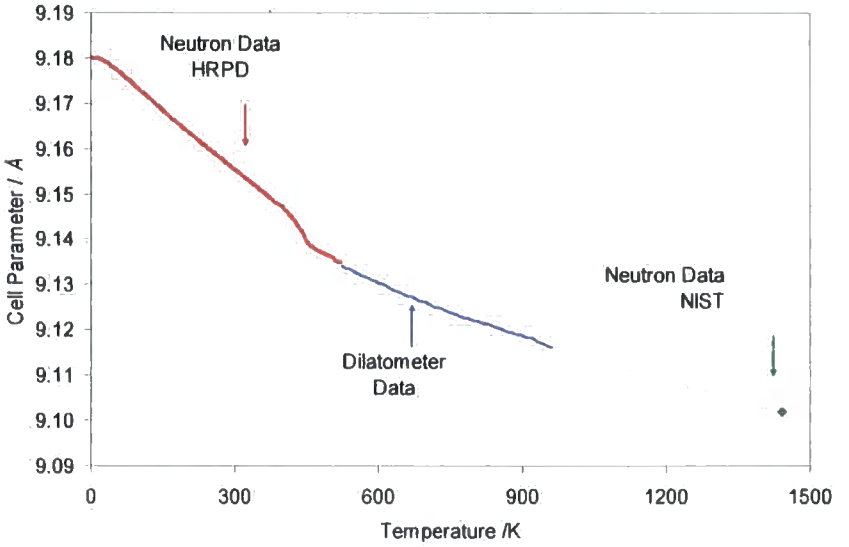

Figure 1.5 Thermal expansion data for ZrW_2O_8. Data reproduced from reference 5 with kind permission.

[a] First observations of ZrW_2O_8 discussed that it is only metastable at room temperature, being formed on quenching from high temperature; slow cooling leads to disproportionation of the compound to zirconia and tungsten oxide. The compound has been found to have high kinetic stability below 1050 °C if quench-cooled.

The origin of the NTE in ZrW_2O_8 has been studied by many groups. An investigation into the phonon modes within the structure led to a description of the structure in terms of the RUM model.[36] This enabled description of the structure in terms of collective rotation of the polyhedra to contract the framework. More recently study of the material using the total scattering technique on neutron data, has led to quantitative measurements to support the description of the motion of the rigid polyhedra within the structure.[37]

As well as the α- and β-polymorphs described above, two other forms of ZrW_2O_8 have been prepared. The γ-form is orthorhombic and is formed at 0.2 GPa.[38-40] The structure of this polymorph differs to the cubic forms by not containing a terminal W-O bond; these oxygen atoms have cross linked to other W's to form a denser structure. A further trigonal phase has been isolated using sol-gel chemistry.[41]

The isostructural compound HfW_2O_8 is found to exhibit the same properties as ZrW_2O_8 over the same temperature ranges, including the phase transition at ~430 K.[29] Syntheses of cubic $ZrW_{2-x}Mo_xO_8$ have been undertaken,[42] and found to have decreasing α-β phase transition temperatures over the range x=0 (448 K) to x=1 (270 K).[43] The related family of cubic AMo_2O_8 (A=Zr, Hf) materials, have been prepared using low temperature methods,[44] and found to have XRD patterns very similar to the analogous tungsten compounds. The cubic $ZrMo_2O_8$ material has also been studied as a potential NTE composite material. This material is the subject of Chapter 7.

1.4.2 AM_2O_7 phases

A second group of oxide framework materials, the cubic AM_2O_7 phases, have also been studied in great detail. These compounds are less flexible than the cubic AM_2O_8 phases as they have one fewer oxygen per formula unit and an additional M-O bond leading to the formation of an M_2O_7 group.[17] The structure is constructed of corner-connected octahedra and tetrahedra, with formula $A^{4+}M^{5+}{}_2O_7$, with octahedra sharing six corners with tetrahedra, these in turn share three vertices with octahedra, the final vertex being shared with another tetrahedra to form an $M_2O_7^{4-}$ group. The ideal structure for cubic ZrV_2O_7 is illustrated in Figure 1.6, in space group $Pa\bar{3}$.[11] This shows the bridging V-O-V bond (oxygen coloured blue in b)) which is constrained to be linear by the space group symmetry. Much of the structural chemistry of these compounds relates to the unfavourable nature of this arrangement.

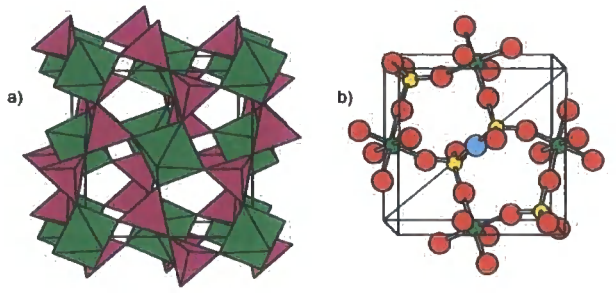

Figure 1.6 a) The ideal form of ZrV_2O_7, with ZrO_6 octahedra shown in green and V_2O_7 groups shown in pink. b) A ball and stick diagram showing the blue bridging V-O-V atom on the body diagonal constrained to 180 ° by symmetry in the high temperature structure.

The first investigation into the AM_2O_7 family of compounds was by Levi and Peyronel in 1935.[45] They reported the Si, Sn and Group 14 pyrophosphates to have cubic symmetry in space group $Pa\bar{3}$ with a cell parameter of ~8 Å. Many other AM_2O_7 type materials have since been synthesised and studied. These include those made with A^{4+} = Si, Ti, Ge, Zr, Nb, Mo, Sn, Ce, Hf, W, Re, Pb, Th, U and Pu when M = P,[45-57] with A^{4+} = Zr, Hf and Pb when M = V[58-60] and with A^{4+} = Zr and Th when M = As.[61,62]

Later studies revealed that the 8 Å cubic unit cell was only an accurate description at high temperatures in many of these compounds; phase transitions were found to occur on cooling forming a superstructure with a unit cell 27 times bigger than at low temperature.[b,58] This larger unit cell accounts for some weaker reflections in the X-ray diffraction patterns caused by relaxation of the symmetry constraints placed on the system in the larger unit cell.[63] At temperatures above the phase transition the structure can exhibit dynamic disordering, *i.e.* the unfavourable bonding constraints can be alleviated by dynamic bending of the bridging P-O-P bond, leading to the averaged structure being that of the smaller cell. However, on cooling through the phase transition these distortions freeze into the structure and the formation of a supercell allows static ordering of bent M_2O_7 groups across the tripled-volume structure.

Above this phase transition, some members of this family have been shown to undergo NTE,[5] and in other members extremely low thermal expansion is present. This has been described in terms of the qRUM model:[20] the rocking of relatively rigid polyhedra in the AM_2O_7 structure is not possible without minimal changes in their geometries, giving rise to qRUMs. These lead to a contraction of the M-M distance and gives rise to the NTE observed.

Due to space constraints it is not possible to include all of the work that has been undertaken on these compounds; the trends within this family of compounds are discussed with reference to the data in Table 1.1. As the A^{4+} radii increase, the relative size of the polyhedra changes; it is clear from these data that with increasing polyhedral size, comes greater flexibility and hence greater propensity for negative thermal expansion.[64]

Table 1.1 Trends in the AM_2O_7 family of materials.

Compound	Ionic Radius[65] of A^{4+} /Å	Cell parameter *a* /Å (RT subcell)	Expansion	Reference
TiP_2O_7	0.605	7.893 Å	Positive TE (PTE)	46
ZrP_2O_7	0.72	8.258 Å	Low PTE (> 573 K)	47
UP_2O_7	0.89	8.631 Å	NTE (> 773 K)	55,56
ThP_2O_7	0.94	8.725 Å	NTE (> 573 K)	55
ZrV_2O_7	0.72	8.777 Å	Strong NTE (> 423 K)	57

[b] Classification of the tripled structure as a (*e.g.* 3x3x3) superstructure is only possible if the compound has been found to exist as the (1x1x1) substructure at higher temperature, *i.e.* the classification is a relative description.

This is highlighted in the differences in thermal behaviour between ZrP_2O_7 and ZrV_2O_7, illustrated in Figure 1.7.[21,66] On increasing temperature both materials undergo structural transitions, with positive thermal expansion in the pyrophosphate compared to the NTE present in ZrV_2O_7 above 663 K (Figure 1.7b)).

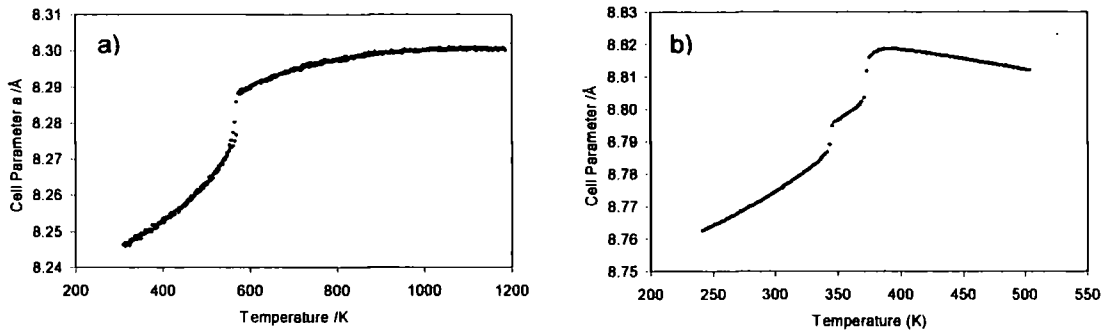

Figure 1.7 Cubic cell parameters of a) ZrP_2O_7 and b) ZrV_2O_7 with increasing temperature.

Research into the formation of superstructures continues, and reports of low temperature 8 *Å* structures require critical examination as to whether this is the true structure, or whether the superlattice reflections (indicating a lowering of symmetry) are so weak they have not been detected. Evidence for supercells has been found for many compounds in this family, *e.g.* in Si, Ti, Sn, Hf and ReP_2O_7.[46,51,54,58,63,67]

1.4.3 Molybdenum phosphates

Mo^{IV} forms a pyrophosphate with similar structure to the cubic AM_2O_7 materials. The pyrophosphate MoP_2O_7 was first prepared by Kinomura *et al.* and found to be isostructural with ZrP_2O_7 having a cubic structure, in space group $Pa\bar{3}$, with cell parameter a=7.952(4) *Å*.[50] Later work by Leclaire *et al.* elucidated the structure using single crystal methods at 294 K.[68] This work used only 55 reflections and proved to have high thermal parameters for the bridging oxygen. This may be an indication that a superstructure is formed, and later work using synchrotron radiation has shown a supercell to be present,[69] with orthorhombic symmetry, but this structure has not been published in detail to my knowledge.

Molybdenum is also known to be stable in octahedral coordination in oxidation states of +3 to +6. This, along with flexible ways of linking octahedra, leads to a wide variety of framework molybdenum phosphates. The known phases with Mo:P < 1 are shown in Figure 1.8,[68,70-74] with the oxidation state of the Mo indicated by the number of sides on the polygon for each material. Although each material is built up from MoO_6 octahedra and PO_4 tetrahedra, they differ in the connectivity of the polyhedra; the easiest distinction is the PO_4 grouping, either as a lone PO_4^{3-}, a pyrophosphate $P_2O_7^{4-}$, a tetraphosphate $P_4O_{13}^{6-}$ or chains of PO_3^- tetrahedra. The synthesis of the material MoP_2O_7 has been investigated by reducing molybdenum phosphates of higher oxidation states, Chapter 6. The structures of some of these materials are the subject of Chapters 3-5 in this thesis.

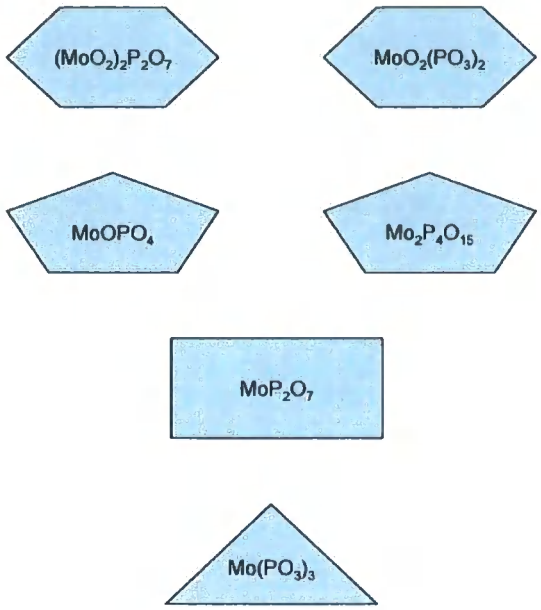

Figure 1.8 Known molybdenum phosphates with Mo ≤ P. Top row are Mo^{VI}, then Mo^{V}, Mo^{IV} with Mo^{III} at the bottom.

1.4.4 Non-oxide materials

The mechanisms of NTE described in Section 1.3 can be extended to non-oxide materials as well. The flexibility of the M-O-M linkages can be increased by adding an additional atom to the linkage, for example a CN group. The material $Zn(CN)_2$ consists of an ordered metal lattice with a disordered array of CN linkages between them.[75] The thermal expansion of this material was studied from 25-350 K using neutron diffraction by Goodwin and Kepert.[76] The coefficients of thermal expansion are given in Table 1.2 alongside other materials.[77-80] This material undergoes larger NTE than that of ZrW_2O_8, which is brought about by the increased flexibility of the CN linkage increasing the number of vibrational modes present in the system. The NTE has been attributed to transverse vibrations of the CN linkages, drawing the adjacent metal sites closer together. The related Prussian Blue analogue $Fe[Co(CN)_6]$ exhibits very small NTE.[81]

Table 1.2 The thermal expansion of some materials for reference.

Material	Space Group	α_l /10^{-6} K^{-1}	Temperature Range /K	Reference
Invar	-	0.07	278-303	7
ZrW_2O_8	$P2_13$	-9.1	0-300	33
$Zn(CN)_2$	$Pn\bar{3}m$	-16.9	25-375	76
Si	$Fd3m$	+2.45	223-373	77
NaCl	$Fm3m$	+39.6	293	78
$(Mn_{0.96}Fe_{0.04})_3(Zn_{0.5}Ge_{0.5})N$	$Pm\bar{3}m$	-25	316-386	79
$Ag_3[Co(CN)_6]$	$P\bar{3}1m$	α_a +130 – +150 α_c -120 – -130	20-300	80
$Fe[Co(CN)_6]$	$Fm\bar{3}m$	-1.47	4.2-300	81
$Yb_{2.75}C_{60}$	$Pcab$	-550	30 K (maximum value)	82
$Sm_{2.75}C_{60}$	$Pcab$	-400	4.2-32	83

To extend the complexity in the cyanide containing materials further, led to study of materials such as the highly under constrained material, $Ag_3[Co(CN)_6]$. The structure contains Ag^+ and $[Co(CN)_6]^{3-}$ building blocks which form a framework containing Co-C-N-Ag-N-C-Co linkages.[80] The material exhibits the newly termed "colossal" thermal expansion, in both positive and negative directions. Study of the material has led to the understanding that at low temperature there is a strong argentophilic interaction with $Co(CN)_6$-Ag-$Co(CN)_6$ contacts. On increasing temperature the Ag-Ag distances increase but the framework topology forces contraction in the perpendicular direction. These factors are strongly coupled in order to preserve the structural connectivity.

The above examples can all be described in terms of the flexibility of the framework linkages within the structures. In other materials a change in valence state can bring about negative thermal expansion. In the fulleride materials $Yb_{2.75}C_{60}$ and $Sm_{2.75}C_{60}$, a sudden change in the thermal expansion properties is noted on cooling, at 60 and 32 K respectively.[82,83] Below these temperatures the materials display strong negative thermal expansion. These phenomena have been rationalised using electronic structure arguments. The C_{60} t_{1u} band has a similar energy to the Yb/Sm 4f band. Above the quoted temperatures the 4f electrons are excited into the conduction band; on cooling these electrons are forced back into the 4f band, thus increasing the ionic radii of the atoms and causing the negative thermal expansion observed.

The metallic compound YbGaGe has been reported in one publication to exhibit negligible volume change (100-400 K). The material contains puckered GaGe layers perpendicular to the *c* axis, with Yb ions between the layers. Analysis of the lattice parameters over this temperature region shows that the *ab* plane area decreases on increasing temperature, while the *c* axis increases in size. These two effects balance each other to give ~zero thermal expansion over this temperature range. The phenomenon underlying these changes is a continual electronic valence transition as the Yb^{3+} gains an electron on cooling to from Yb^{2+}, causing an increase in the *ab* plane.

1.5 Summary

Many framework materials are known and have been studied in the literature. The inherent ability of the structure to be flexible gives rise to interesting structure-property relationships. These properties include negative thermal expansion, a phenomenon that at first seems counter-intuitive to simple ideas of chemical bonding. Framework solids are also of interest as many undergo phase transitions and form superstructures due to the need for a balance between the short- and long-range structural requirements within the system.

Within the study of framework materials, *in-situ* diffraction techniques enable investigation of reactions to an extent not possible using standard *ex-situ* techniques. These methods can be valuable to give new insights into synthesis temperatures, times and pressures required for *ex-situ* preparations. These methods may also provide new routes to previously unknown materials of chemical and industrial interest. One route to new materials is through a topotactic reaction, in which the crystal structure of the parent phase actually determines the product phase that is formed.[1] This introduces the possibility that new, metastable phases can be prepared. These reactions require so-called "soft" conditions to avoid the compound transforming into a more thermodynamically stable phase.[84]

This is an emerging area of importance as new materials are required to meet the needs of rapidly changing industry and more day-to-day challenges. This thesis reports the investigations into the syntheses, structures and properties of several inorganic framework materials.

1.6 References

1. F. K. Lotgering, *J. Inorg. Nucl. Chem.*, 1959, **9**, 113-123.
2. C. E. Guillaume, *C. R. Acad. Sci.*, 1897, **125**, 235-238.
3. W. F. Schlosser, G. M. Graham and P. P. M. Meincke, *J. Phys. Chem. Solids*, 1971, **32**, 927-939.
4. A. W. Sleight, *Inorg. Chem.*, 1998, **37**, 2854-2860.
5. J. S. O. Evans, *J. Chem. Soc., Dalton Trans.*, 1999, **19**, 3317-3326.
6. H. D. Megaw, *Crystal Structures: A Working Approach*, Saunders, Philadelphia, 1973.
7. R. Roy, D. K. Agrawal and H. A. McKinstry, *Ann. Rev. Mater. Sci.*, 1989, **19**, 59-81.
8. A. W. Sleight, *Curr. Opin. Solid State Mat. Sci.*, 1998, **3**, 128-131.
9. A. W. Sleight, *Ann. Rev. Mater. Sci.*, 1998, **28**, 29-43.
10. R. W. Cahn, *Nature*, 1997, **386**, 22-23.
11. V. Korthuis, N. Khosrovani, A. W. Sleight, N. Roberts, R. Dupree and W. W. Warren, *Chem. Mater.*, 1995, **7**, 412-417.
12. E. Grüneisen, *Handbuch Physik 10*, Springer-Verlag, New York, 1926.
13. J. S. O. Evans, T. A. Mary and A. W. Sleight, *Physica B*, 1998, **241-243**, 311-316.
14. R. M. Hazen and C. T. Prewitt, *Am. Mineral.*, 1977, **62**, 309-315.
15. N. Khosrovani and A. W. Sleight, *J. Solid State Chem.*, 1996, **121**, 2-11.
16. J. Z. Tao and A. W. Sleight, *J. Solid State Chem.*, 2003, **173**, 442-448.
17. K. D. Hammonds, M. T. Dove, A. P. Giddy, V. Heine and B. Winkler, *Am. Mineral.*, 1996, **81**, 1057-1079.

18. K. D. Hammonds, M. T. Dove, A. P. Giddy and V. Heine, *Am. Mineral*, 1994, **79**, 1207-1209.
19. A. P. Giddy, M. T. Dove, G. S. Pawley and V. Heine, *Acta Crystallogr., Sect. A*, 1993, **49**, 697-703.
20. H. V. Heine, P. R. L. Welche and M. T. Dove, *J. Am. Ceram. Soc.*, 1999, **82**, 1793-1802.
21. R. L. Withers, J. S. O. Evans, J. Hanson and A. W. Sleight, *J. Solid State Chem.*, 1998, **137**, 161-167.
22. M. T. Dove, *Am. Mineral.*, 1997, **82**, 213-244.
23. J. S. O. Evans and T. A. Mary, *Int. J. Inorg. Mat.*, 2000, **2**, 143-151.
24. M. T. Dove, V. Heine and K. D. Hammonds, *Mineral. Mag.*, 1995, **59**, 629-639.
25. P. J. Heaney, C. T. Prewitt and G. V. Gibbs, *Silica: Physical Behavior, Geochemistry and Materials Applications*, Mineralogical Society of America, Michigan, 1994.
26. J. S. O. Evans, J. C. Hanson and A. W. Sleight, *Acta Crystallogr., Sect. B.*, 1998, **54**, 705-713.
27. M. O'Keeffe, B. Domenges and G. V. Gibbs, *J. Phys. Chem.*, 1985, **89**, 2304-2309.
28. G. D. Barrera, J. A. O. Bruno, T. H. K. Barron and N. L. Allan, *J. Phys.: Condens. Matter*, 2005, **17**, R217-R252.
29. T. A. Mary, J. S. O. Evans, T. Vogt and A. W. Sleight, *Science*, 1996, **272**, 90-92.
30. J. Graham, A. D. Wadsley, J. H. Weymouth and L. S. Williams, *J. Am. Ceram. Soc.*, 1953, **42**, 570-570.
31. L. L. U. Chang, M. G. Scroger and B. Phillips, *J. Am. Ceram. Soc.*, 1967, **50**, 211-215.
32. M. Auray, M. Quarton and M. Leblanc, *Acta Crystallogr., Sect. C*, 1995, **51**, 2210-2213.
33. J. S. O. Evans, T. A. Mary, T. Vogt, M. A. Subramanian and A. W. Sleight, *Chem. Mater.*, 1996, **8**, 2809-2823.
34. J. S. O. Evans, W. I. F. David and A. W. Sleight, *Acta Crystallogr., Sect. B*, 1999, **55**, 333-340.
35. M. R. Hampson, J. S. O. Evans and P. Hodgkinson, *J. Am. Chem. Soc.*, 2005, **127**, 15175-15181.
36. A. K. A. Pryde, K. D. Hammonds, M. T. Dove, V. Heine, J. D. Gale and M. C. Warren, *Phase Transitions*, 1997, **61**, 141-153.
37. M. G. Tucker, A. L. Goodwin, M. T. Dove, D. A. Keen, S. A. Wells and J. S. O. Evans, *Phys. Rev. Lett.*, 2005, **95-255501**, 1-4.
38. J. S. O. Evans, Z. Hu, J. D. Jorgensen, D. N. Argyriou, S. Short and A. W. Sleight, *Science*, 1997, **275**, 61-65.
39. Z. Hu, J. D. Jorgensen, S. Teslic, S. Short, D. N. Argyriou, J. S. O. Evans and A. W. Sleight, *Physica B*, 1998, **241-243**, 370-372.
40. J. D. Jorgensen, Z. Hu, S. Teslic, D. N. Argyriou, S. Short, J. S. O. Evans and A. W. Sleight, *Phys. Rev. B*, 1999, **59**, 215-225.
41. A. P. Wilkinson, C. Lind and S. Pattanaik, *Chem. Mater.*, 1999, **11**, 101-108.
42. C. Closmann, A. W. Sleight and J. C. Haygarth, *J. Solid State Chem.*, 1998, **139**, 424-426.
43. J. S. O. Evans, P. A. Hanson, R. M. Ibberson, N. Duan, U. Kameswari and A. W. Sleight, *J. Am. Chem. Soc.*, 2000, **122**, 8694-8699.
44. C. Lind, A. P. Wilkinson, Z. Hu, S. Short and J. D. Jorgensen, *Chem. Mater.*, 1998, **10**, 2335-2337.
45. G. R. Levi and G. Peyronel, *Z. Kristallogr.*, 1935, **92**, 190-209.

46. E. Tillmanns, W. Gebert and W. H. Baur, *J. Solid State Chem.*, 1973, **7**, 69-84.
47. D. E. Harrison and F. A. Hummel, *J. Am. Ceram. Soc.*, 1959, **42**, 487-490.
48. D. E. Harrison, H. A. McKinstry and F. A. Hummel, *J. Am. Ceram. Soc.*, 1954, **37**, 277-288.
49. H. Fukuoka, H. Imoto and T. Saito, *J. Solid State Chem.*, 1995, **119**, 98-106.
50. N. Kinomura, M. Hirose, N. Kumada and F. Muto, *Mat. Res. Bull.*, 1985, **20**, 379-382.
51. C-H. Huang, O. Knop, D. A. Othen, F. W. D. Woodhams and R. A. Howie, *Can. J. Chem.*, 1975, **53**, 79-91.
52. J. C. Brantley and J. R. Huizenga, *J. Am. Chem. Soc.*, 1952, **74**, 6101-6101.
53. Z. S. Teweldemedhin, K. V. Ramanujachary and M. Greenblatt, *Mat. Res. Bull.*, 1993, **28**, 427-434.
54. E. Banks and R. Sacks, *Mat. Res. Bull.*, 1982, **17**, 1053-1055.
55. C. W. Bjorklund, *J. Am. Chem. Soc.*, 1958, **79**, 6347-6350.
56. A. Burdese and M. Lucco Borlera, *Ann. Chim. Roma*, 1963, **53**, 333-343.
57. A. Cabeza, M. G. Aranda, F. M. Cantero, D. Lozano, M. Martinez-Lara and S. Bruque, *J. Solid State Chem.*, 1996, **121**, 181-189.
58. H. Völlenke, A. Wittmann and H. Nowotny, *Monatsh. Chem.*, 1963, **94**, 956-963.
59. G. Peyronel, *Gazz. Chim. Ital.*, 1942, **72**, 77-83.
60. D. F. Craig and F. A. Hummel, *J. Am. Ceram. Soc.*, 1972, **55**, 532-532.
61. H. Onken, *Naturwissenschaften*, 1965, **52**, 344-344.
62. G. Le Flem, J. Lamic and P. Haggenmuller, *Bull. Soc. Chim. France*, 1966, **6**, 1880-1883.
63. L-O. Hagman and P. Kierkegaard, *Acta Chem. Scand.*, 1969, **23**, 327-328.
64. N. Khosrovani, A. W. Sleight and T. Vogt, *J. Solid State Chem.*, 1997, **132**, 355-360.
65. R. D. Shannon, *Acta Crystallogr., Sect. A*, 1976, **32**, 751-761.
66. R. L. Withers, Y. Tabira, J. S. O. Evans, I. J. King and A. W. Sleight, *J. Solid State Chem.*, 2001, **157**, 186.
67. J. Sanz, J. E. Iglesias, J. Solia, E. R. Losilla, M. A. G. Aranda and S. Bruque, *Chem. Mater.*, 1997, **9**, 996-1003.
68. A. Leclaire, M. M. Borel, A. Grandin and B. Raveau, *Eur. J. Solid State Inorg. Chem.*, 1988, **25**, 323-328.
69. R. C. Haushalter and L. A. Mundi, *Chem. Mater.*, 1992, **4**, 31-48.
70. P. Kierkegaard, *Ark. Kemi*, 1962, **19**, 1-14.
71. P. Kierkegaard, *Ark. Kemi*, 1962, **18**, 521-532.
72. P. Kierkegaard and M. Westerlund, *Acta Chem. Scand.*, 1964, **18**, 2217-2225.
73. S. E. Lister, I. R. Evans, J. A. K. Howard, A. Coelho and J. S. O. Evans, *Chem. Commun.*, 2004, **22**, 2540-2541.
74. I. M. Watson, M. M. Borel, J. Chardon and A. Leclaire, *J. Solid State Chem.*, 1994, **111**, 253-256.
75. D. J. Williams, D. E. Partin, F. J. Lincoln, J. Kouvetakis and M. O'Keeffe, *J. Solid State Chem.*, 1997, **134**, 164-169.
76. A. L. Goodwin and C. J. Kepert, *Phys. Rev. B*, 2005, **71**, 140301.
77. Y. Okada and Y. Tokumaru, *J. Appl. Phys.*, 1984, **56**, 314-320.
78. T. H. K. Barron, J. G. Collins and G. K. White, *Adv. Phys.*, 1980, **29**, 609-730.

79. K. Takenaka and H. Takagi, *Appl. Phys. Lett.*, 2005, **87**, 261902.

80. A. L. Goodwin, M. Calleja, M. J. Conterio, M. T. Dove, J. S. O. Evans, D. A. Keen, L. Peters and M. G. Tucker, *Science*, 2008, **319**, 794-797.

81. S. Margadonna, K. Prassides and A. N. Fitch, *J. Am. Chem. Soc.*, 2004, **126**, 15390-15391.

82. S. Margadonna, J. Arvanitidis, K. Papagelis and K. Prassides, *Chem. Mater.*, 2005, **17**, 4474-4478.

83. J. Arvanitidis, K. Papagelis, S. Margadonna, K. Prassides and A. N. Fitch, *Nature*, 2005, **425**, 599-602.

84. B. Gérand and L. Seguin, *Solid State Ionics*, 1996, **84**, 199-204.

2. Methods of Characterisation

All materials discussed within this thesis have been prepared using the detailed synthetic procedures included in the relevant chapter of this thesis, unless otherwise stated. Samples and experiments have been labelled sequentially throughout, SEL101 – SEL323. Samples prepared during a Master's project in this laboratory were labelled SEL001 – SEL062.[1] Routine powder diffraction scans of all samples have been carried out on one of the four diffractometers described in Sections 2.3.1 and 2.3.2, and have been denoted dx_nnnnn (where x defines the diffractometer used and n is a digit 0-9) respectively.

The main method of characterisation used within this thesis is that of X-ray diffraction, both single crystal and powder methods. This chapter describes these methods and some of the general theory behind them, alongside the instrumentation used to obtain the data contained in this thesis. Other methods of characterization, namely electron and neutron diffraction, solid state NMR, SHG and thermal techniques are also described.

2.1 Diffraction

Crystalline structures are constructed through translational repetition of a regularly repeating unit cell. This repetition within the crystal leads to the concept of a lattice point, where each point has an identical environment to the next. By associating a motif (*e.g.* a single atom or a molecule) with each lattice point one builds up a regular 3D periodically repeating crystal structure.

Diffraction is an interference event that occurs when scattering objects are separated by distances comparable to the wavelength of the radiation involved. X-rays, neutrons and electrons can be produced with wavelengths similar in size to the interatomic distances in a crystalline material. The regularly repeating electron density within the material can, therefore, act as a diffraction grating, re-emitting the radiation as if from a set of point sources. The radiation is scattered in all directions, such that, in most directions, the radiation combines destructively and cancels out. In some directions, the radiation combines constructively; this constructive interference can be recorded as the diffraction pattern.

The diffraction of the incident radiation can be described geometrically as reflection from lattice planes within the crystal. Although this may not be physically rigorous, it allows easy geometric interpretation of the diffraction phenomenon. These planes are labeled with Miller indices, *hkl*, intercepting the unit cell axes at positions *a/h*, *b/k* and *c/l*; this defines the Miller indices for that family of planes with interplanar spacing d_{hkl}. Prediction of these diffracted beams uses Bragg's law:

$$\lambda = 2d_{hkl} \sin \theta_{hkl} \qquad (2.1)$$

where λ is the wavelength of the radiation used, d_{hkl} is the interplanar spacing and θ_{hkl} the incident angle with respect to the planes. The Bragg condition is satisfied every time the difference in path length of the X-rays between successive Miller planes is an integer. To gain maximum structural information about a compound it is necessary to systematically record the diffraction from each plane by satisfying its diffracting condition from Bragg's law.

In X-ray and neutron diffraction the peak intensities recorded give information about the atom positions in the structure, either from the electron density (X-ray) or atomic nucleus (neutron). The methods and instrumentation used in both the powder and single crystal techniques which have been employed are described in the following sections.

2.1.1 Single crystal techniques

The first step in a single crystal experiment is to find suitable single crystals by viewing a sample under a polarizing microscope. Crystals are then attached to a fibre attached to a metal pin either in oil – for low temperature work – or in glue – for high temperature work. The metal pin is then mounted in a goniometer head and placed in the diffractometer. The crystal is centred in the X-ray beam such that when the crystal rotates during the data collection it rotates within the beam without translation. The crystal is then rotated in the diffractometer to collect initial frames of data in order to establish an orientation matrix from which the unit cell parameters can be determined. A data collection strategy, *i.e.* how many quadrants need to be collected to obtain all the necessary intensity information, can be decided following unit cell determination, depending on the symmetry of the crystal. A full data collection consists of rotating both the crystal and the diffractometer circles such that the diffracted peak positions and intensities from the crystal can be recorded. Following this collection the data are integrated to yield 3D positional information about the intensities recorded, I, and their standard uncertainties, $\sigma(I)$.

The next step in the experiment is to apply a correction to adjust for differences in absorption of the X-radiation of the data collected, due to differences in path length for each reflection. One such correction is the SADABS absorption correction,[2] a semi-empirical method, which compares the intensities of equivalent reflections and estimates the absorption anisotropy present in the dataset. A high redundancy factor is required to ensure that the correction function applied across the whole range is accurate. Comparing the intensities of the equivalent reflections gives an indication of the quality of the data collection. This is quantified by a residual factor, R_{int}, which should decrease following corrections for absorption. This stage of the experiment also includes reducing the amount of data present by merging the reflections equivalent by symmetry and reflections measured more than once, giving a "unique set of corrected and scaled data."[3]

The data are output into two files; the first of these files, an "hkl" file, contains a list of the intensity and standard uncertainty of each hkl reflection. The second, an "ins" file, contains the information about the cell parameters, space group and other general information from the data collection.

Analysis of these data is undertaken in the form of a structure solution and refinement process. A partial structure solution is usually achieved using one of two methods, namely Patterson and direct methods. This trial solution is then refined using least-squares processes, until a satisfactory agreement factor has been achieved and a chemically/physically plausible model is obtained.

2.1.2 Powder diffraction and the Rietveld method

Powder diffraction methods rely on a large number of randomly orientated crystallites being present in the sample undergoing diffraction, such that some of them will be orientated correctly to diffract at each Bragg angle. Powder diffraction patterns are recorded by recording the intensity present, y_i, at each small increment, i, at an angle $2\theta_{hkl}$ between the incident beam and detector. As it is assumed that all crystallite orientations are present within the powdered sample, no information about the individual orientations of each crystallite is known, and hence only a 1D pattern of intensity versus 2θ is recorded. The geometry of the unit cell is related to the positions of the peaks and the atomic positions to the relative intensities of those peaks.

The Rietveld method is a least-squares refinement technique that seeks to minimise the residual, S_y, between the entire observed and calculated patterns.[4,5] This residual is given by:

$$S_y = \sum_i w_i \left(Y_i(obs) - Y_i(calc)\right)^2 \qquad (2.2)$$

Where $w_i = 1/Y_i(obs)$

$Y_i(obs)$ = the observed intensity at the ith step

$Y_i(calc)$ = the calculated intensity at the ith step

This is an iterative process, and a good initial model is required so that the global minimum is found during the refinement, and not a local minimum. It is therefore necessary to know approximate information about the crystal structure(s) and the diffractometer used to record the data. Hence, this is specifically a structure refinement technique, not a method for structure solution.

Examples of refined parameters are given in Table 2.1, split into two groups, depending on whether they are phase specific or not.

Table 2.1 Parameters refined during Rietveld Analysis.

Global Parameters	Phase Specific
Zero Error/Sample Height	Scale Factor
Instrument Parameters	Lattice Parameters
Background	Atomic Coordinates
	Thermal Parameters
	Preferred Orientation
	Peak Shape

If multiple phases are present within a sample, it is possible to obtain an indication of the relative fraction of each phase within that sample, from their refined scale factor parameters and known masses.

All refinements in this report use a pseudo-Voigt peak shape function, either as parameterised by Alan Coelho (PV)[6] or by Thomson, Cox and Hastings (TCHZ).[7]

The quality of fit between the calculated and observed pattern, depends on the quality of the model used. This can be quantified in the form of residual (*R*) factors. The most commonly quoted of these is the *R*-weighted profile as given in Equation 2.3. The values $Y_i(obs)$ and $Y_i(calc)$ are the observed and calculated values of the intensity at point i. w_i is the weighting applied to that data point with a value equal to $1/\sigma Y_i(obs)$ where $\sigma Y_i(obs)$ is the error of $Y_i(obs)$.

$$R_{wp} = \left[\sqrt{\frac{\sum w_i (Y_i(obs) - Y_i(calc))^2}{\sum w_i Y_i(obs)^2}} \right]^{1/2} \tag{2.3}$$

R_{wp} gives the most useful quantity as the numerator is S_y, the residual being minimised and hence provides the best indication of the progress of the refinement. A measure of the expected value from statistical analysis is given by R_{exp}. In Equation 2.4 *M* is the number of datapoints and *P* is the total number of refined parameters. This number should always be positive, indicating an appropriate number of parameters have been refined against the recorded observations. The ratio of the R_{wp} to R_{exp} is defined as the Goodness of Fit (GOF).

$$R_{exp} = \sqrt{\frac{\sum (M - P)}{\sum w_i Y_i(obs)^2}} \tag{2.4}$$

$$GOF = \sqrt{\chi^2} = \frac{R_{wp}}{R_{exp}} = \sqrt{\frac{\sum w_i (Y_i(obs) - Y_i(calc))^2}{M - P}} \tag{2.5}$$

An alternative index is R_{Bragg} (Equation 2.6) where the I_k values are the intensities of each of the reflections within the model. This introduces a bias towards the model being refined into the calculation. However, this is the best approximation to the R_p factors quoted in single crystal refinements.

$$R_{Bragg} = \sqrt{\frac{\sum (I_k(obs) - I_k(calc))}{\sum I_k(obs)}} \tag{2.6}$$

It should also be noted that the refined model must make chemical sense, *i.e.* that the structural models contain bond lengths and angles appropriate to them, and not vastly different to anything known for those atoms/compounds. An alternative factor can also be calculated by subtracting the contribution of the background, here these R-factors are primed, *e.g.* R_{wp}', to distinguish them from their regular counterparts.

Preferred orientation occurs when a sample has a strong tendency to pack in a particular orientation, thereby giving false intensity information. This typically occurs for layered or platey crystal morphology, as the layers tend to align themselves within the sample holder they are packed into, thus reducing the randomness of crystal orientation. One way to counteract this is to prepare the samples by sprinkling them on a flat glass slide smeared with Vaseline as an adhesive. If sprinkling the sample on an XRD plate does not remove all preferred orientation effects, they can be modelled using *e.g.*

spherical harmonics. These are mathematical functions in the spherical polar coordinate system that are dependent on the angles θ and φ. When spherical harmonic functions are used to correct for preferred orientation effects they act as scaling factors dependent on the *hkl* direction of the reflection. Spherical harmonics have also been used to model *hkl* dependent peakshapes within some structures. The general equation for spherical harmonic functions is given in Equations 2.7 and 2.8.[8]

$$Y_{l,m}(\theta,\phi) = \theta_{l,m}(\theta)\phi_m(\phi) \tag{2.7}$$

$$Y_{l,m}(\theta,\phi) = \sqrt{\frac{(2l+1)}{4\pi}\frac{(l-|m|)!}{(l+|m|)!}}P_l^{(m)}\cos\theta e^{im\phi} \tag{2.8}$$

Rietveld refinements were carried out using the Academic version of the TOtal Pattern Analysis System (TOPAS Academic).[6] This analysis software has been used in input mode, where files have been written using a software specific programming language to enable refinement of parameters. Input files have been included in the E-appendix where indicated. The software will be referred to as "Topas" throughout, but it has always been the Academic version of the program that has been used.

2.1.3 Synchrotron sources

Synchrotrons can be used to produce X-rays with intensities much greater than lab-based sources and are highly useful for problems that cannot be solved using *in-house* equipment. Synchrotron radiation also has high collimation and can be tuned to specific wavelengths.

When electrons moving at approximately the speed of light are caused to move along a bent trajectory, they emit synchrotron radiation tangentially at GeV frequencies. At synchrotron radiation sources electrons are injected first into a linear accelerator and then into a booster ring where the beam of electrons are accelerated to approximately the speed of light (using an electric field) and kept within the ring using bending magnets. The beam is transferred to a storage ring where bending magnets are used to keep it in a circular orbit. The ring must be kept under very high vacuum to prevent beam and energy loss. Also within the ring are insertion devices which generate stronger radiation within the straight sections of the "ring", increasing the intensity of the beam; these devices are called wigglers or undulators as they cause the electrons to move sinusoidally within the ring. At points where the beam is bent, *i.e.* at positions in the ring where the insertion devices or the bending magnets are present, beam energy is lost as synchrotron radiation tangentially to the direction of the beam. It is at these points where openings in the ring are made onto the beamlines, which include slits, mirrors and monochromators to deliver radiation of a required wavelength and collimation to an experimental station, each designed for a specific type of investigation on samples by scientists and beamline users.

2.1.4 Neutron sources

Neutrons are uncharged spin ½ particles which can be produced with energies similar to a wide range of atomic and electronic processes; this enables a wide range of different experiments to be performed, from quantum tunnelling to electronic transitions in materials investigations. It is also possible to investigate magnetic structures in materials as neutrons possess a magnetic moment.

Both magnetic and elemental/structural effects can be analysed during the same (optimized) experiments as the scattering cross-sections are of the same magnitude. Thermal neutrons have approximately the same wavelengths as the X-ray sources used for diffraction studies. Thus thermal neutrons – from both spallation and reactor sources – can be used to provide complementary data for the investigation of materials.

An advantage of neutron diffraction over X-ray diffraction comes from the matter-radiation interaction differences. X-rays can be destructive, often probing only the surface of a sample and interacting with the electron cloud of the elements in a material. The scattering power of an element/ion is dependent on the number of electrons it has, and hence an X-ray pattern is dominated by the heavier elements, yielding little information about the lighter ones, *e.g.* hydrogen. Neutrons, however, react weakly with matter and as such are less destructive, but are also scattered by the whole sample, not just the surface, hence providing information about the bulk material structure. Neutrons are scattered by the atomic nuclei, and so the neutron scattering cross-sections are not dependent on the number of electrons; they can vary considerably between atoms in the same period of the periodic table. Neutrons are able to differentiate between *e.g.* H/D atoms, as isotopes of the same element can also have very different scattering power. However, despite the advantages of neutron over X-ray diffraction, the production and ability to ensure safe working environments at central facilities is expensive. Also, their uncharged and weakly interacting nature causes a problem in their detection as they do not cause ionisation or charge build-up themselves. Hence a neutron detector typically contains either a ^{3}He gas medium or a solid ^{6}Li containing medium which both form an ionic by-product on interaction with a neutron. For this process to be efficient the readout times of the detectors must be low.

In a reactor source the induced nuclear chain reactions are maintained in a controlled manner; research reactors are simpler and operate at lower temperatures *c.f.* power reactors. They require highly enriched uranium and need core cooling systems and neutron moderators to obtain useable neutron energies.

The production of neutrons at a spallation source is as follows. A beam of H^- ions is linearly accelerated to ~70 MeV where it enters a synchrotron ring. The beam passes through an alumina electron stripper such that the H^- ions become H^+. The proton beam is allowed to accumulate in the synchrotron until there are ~ 10^{13} protons, at which point the beam is divided into two bunches and extracted to bombard a heavy metal Ta target for spallation. This process occurs 50 times a second. The proton beam causes the Ta source to release energy by ejecting neutrons. The intense neutron pulse generated is too energetic and too fast to be useful and must be slowed down. Moderation of the pulse is achieved using H-containing moderators (water, methane and liq H_2) for collision and energy loss.

2.1.5 The TOF neutron technique

At the pulsed sources used in this thesis (Section 2.3.7), reflection intensities are obtained as a function of the time-of-flight (TOF), that is, the time it takes for the neutron to travel from the target

source along a fixed/known path length to the detector. The neutron's de Broglie wavelength is calculated as follows:

$$\lambda = \frac{ht}{md} \tag{2.9}$$

where h is Planck's constant, t is the TOF, m is the mass of a neutron and d is the known pathlength. Hence the wavelength of the neutron is directly proportional to its TOF. In the TOF technique a beam of white neutrons are used to investigate samples recording the TOF-intensity information at fixed 2θ positions. The Bragg equation can then be solved to yield information about the d-spacings of the intensities.

2.2 Methodologies

2.2.1 Variable temperature XRD measurements

The data available from standard thermal analysis techniques can provide information about phase transition temperatures (DSC) or phase changes and decomposition temperatures (TGA); however, the extra information available from variable temperature (VT) XRD experiments have made them an invaluable tool during the course of this research. VT XRD experiments have been carried out routinely on all materials prepared to check for phase transitions over the approximate range 16-800 K. Sample decomposition pathways can be probed, as can product formation from precursor phases with time or temperature or both as the variable.

However, there is a trade-off that is present when recording multi-temperature datasets. The ability to record data quickly at successive temperatures is in opposition to the requirement to use long data collection times to record good-quality data. Inevitably it is necessary to find a situation midway between these two extremes to gain maximum time advantage while limiting the amount of noise recorded in the spectrum, thus slightly reducing the amount of information that is available from the data.

2.2.2 Methods of calibration in VT XRD measurements

In order to accurately determine cell parameters and temperature from VT measurements, it is necessary to make use of standard materials as a method of calibration. The standards employed have cell parameters known over a large range of temperature to a high degree of accuracy.[9,10] A small quantity of the standard material is mixed in with the material undergoing investigation. It is necessary to choose the standard for each experiment carefully to avoid peak overlap with the sample where possible. Rietveld refinement of the lattice parameters for the standard material alongside those of the investigated material will enable temperature calibration of experiments. Details of the experimental calibration are given prior to experimental results in each appropriate section of this thesis.

A second use of standard materials is to accurately determine unit cell parameters of materials. An example of this is using the NIST Standard Reference Material (SRM) 640c Silicon. The silicon lattice

parameter is known to be 5.4311946(92) Å at 295.5 K for this material.[11] In refinements this value can be fixed to its ideal value to refine a $\Delta 2\theta$ calibration curve for the dataset.

2.2.3 Methodologies for analysis of multiple datasets

Sequential Rietveld refinements have been automated using the local Fortran 77 program run in *DOS Command Line* called *Multitopas/Multitopas_Files*[12,13] *Multitopas* enables multiple refinements to be run one after another using an input file method. This can be used to *e.g.* calculate the change in cell parameters with temperature by using the initial cell parameters obtained from the first refinement as input values for the second scan and so on. *Multitopas* can also be used to calculate the changing composition of a system over multiple scans on changing temperature, for example monitoring phase transitions and chemical processes. A summary of the information obtained from the Rietveld analysis is given in graphical form in the results chapters in this thesis; the input files and excel spreadsheets are included in the E-appendix for each investigation.

2.2.4 Peak fitting and indexing in TOPAS

Peak fitting was performed in TOPAS Academic.[6] Peaks were found using the automatic peak search function to compile a preliminary list of peak positions and intensities. This list was inspected visually and improved manually to ensure all peaks were included. These positions were then refined against data to obtain optimal values.

The peak positions were then used to try and index the peaks. This used the indexing method of Coelho.[14] The output from the indexing method was a list of unit cell parameters and space groups alongside a measure of the quality of the indexing, the Figure of Merit. In searching for the correct cell, a high figure of merit as well as a cell that indexed all the peaks was sought.

Pawley fitting of the cell parameters in the set of indexing solutions indicates the ability of that cell to fit all peaks from the unknown phase, using the space group of lowest symmetry in that crystal class. Following a successful fit between those cell parameters in that space group, it is possible to identify or limit the number of potential space groups for the material by investigation of the systematic absences. Comparing the list of predicted *hkl*s with their calculated intensities obtained from the Pawley fitting in Topas enables the identification of *hkl*s that are predicted in the lowest symmetry space group, but which are systematically absent in the indexed material. This then leads to a set of reflection conditions that can be compared with the lists given in the International Tables.[15] Structure solution within this (reduced) list of space groups should yield a good fit to the data in the correct space group.

2.2.5 Structure solution using the charge flipping method

The structure solution method of charge flipping was first introduced by Oszlányi and Sütő in 2004.[16] The method is *ab initio* requiring no initial knowledge of the phase or its chemical composition.

The algorithm uses calculations in both real and reciprocal space; it works as follows. Structure factor amplitudes are obtained from the diffraction data recorded. These are combined with randomly

generated phases, and following a Fourier Transform an electron density map is calculated. All points within the map that are above a threshold level (the δ-value)[c] are assumed to be atomic peaks and are accepted. Points below the threshold level are multiplied by -1, *i.e.* the sign is changed (flipped), to give a modified map. New phases are calculated following charge flipping and combined with the experimental structure factor amplitudes to produce a new map. The process is then iterated until convergence when the true electron density map is calculated.[17] This cycle can be repeated multiple times to find the electron density cloud with the lowest residual factor.

The results from the charge flipping process are not the xyz positions of the atoms, but instead the electron density in real space, from which the atomic positions can be calculated from the peak maxima. If the system under study is disordered, the electron density peaks will be broader, and thus the atomic position assignment will require careful study. Optimal diffraction data are recorded at low temperatures, as with the increase in temperature comes increased atomic displacement parameters. The algorithm can tolerate imperfect data; thus error free diffraction data complete to a certain resolution is not required. The algorithm works using the entire contents of the unit cell, *i.e.* not just the asymmetric unit, and does not fix the origin to increase the likelihood of solution during any given iteration sequence.

2.2.6 Structure solution from powders using simulated annealing

Although complete structure solution from powder data has almost become a routine method of structure elucidation, the sometimes lengthy process can be reduced by including known chemical information about the material in question, increasing the likelihood of finding the correct structure. To this end, the superstructures studied in this thesis have been investigated using the process of simulated annealing, or more specifically a randomisation/convergence technique. This is a direct space method of structure solution. It is possible to use this technique for these materials as, in the case of the superstructure problems, the connectivity of the atoms is known, due to the superstructure being related to known substructure models. Hence taking the approximated atom coordinates from the substructure model in the supercell (taking into account special positions), will give an approximate starting point for structure refinement. The method of simulated annealing undertakes finding the true superstructure by performing numerous cycles of refinement and user defined randomisation of those atomic positions until a global minimum is found. The model must still be chemically sensible; this can be verified by bond length, angle and bond valence sum calculations to see if the calculated model is plausible.

In this work atomic coordinates for each of the atoms in supercells were generated using ISODISPLACE.[18] The *cif* for the substructure was uploaded to the website and then the cell and its contents transformed using the appropriate transformation matrix to give the total contents of the supercell in its requested (allowed) space group. The atoms retain their original numbering with the additional indicator "_xx" where xx was a sequentially increasing digit. For example an atom labelled

[c] The δ-value is typically a fraction of the electron density found in a light atom peak. However, the peak heights – and hence the value chosen for the threshold – are affected by grid size, data resolution and the thermal parameters.

O1 in the subcell model would be transformed to give the unique atoms O1_1, O1_2 *etc.* This retention of numbering scheme enabled the quick identification of atom types, especially when trying to label Os as bridging or "free" in the input files.

The *cif* containing information about the structure following the transformation process was saved and used to generate a list of the ideal bonds and angles within the structure for later manipulation. A *.l5* file was generated using the local FORTRAN 77 routine *topasreader.*[19] This *.l5* file was used to generate a description of the atomic positions as a macro, as follows, using the local routine *l5totopas.*[20] Each of the macro lines (A1-A3) describes each of the atomic coordinates (xyz) with a name, a refining value (val), and the ideally calculated position (val2). Each site line then uses each of the 3 macros to enable refinement of the atomic positions with the ability to return to the original positions easily.

```
macro A1(param,val,val2) {x param val }
macro A2(param,val,val2) {y param val }
macro A3(param,val,val2) {z param val }
site P1 A1(xP1, 0.237, 0.230) A2(yP1, 0.952, 0.936) A3(zP1, 0.070, 0.061) occ P 1 beq !bval 3
```

Finally the generated bonds and angles information was used to generate restraints for each of the polyhedra within the structure using the local routine *top_to_rest_2.*[21] This ensured that the refinement could be restrained using known bond length/angle data for each of the central atoms in the polyhedra.

Bond length and angle restraint values were determined using a combination of chemical knowledge of the polyhedral arrays and bond valence sum calculations. From previous work and literature sources (Chapter 1), P_2O_7 groups are well known to exhibit differing P-O bond lengths for the two types of bond within them, namely the $P\text{-}O_{bridging}(\text{-}P)$ and $P\text{-}O_{terminal}$ bonds. The terminal bonds are ~1.5 *Å*; the bridging bonds are longer at ~1.58 *Å*.

Similarly Mo-O bond lengths are known to have different values depending on their connectivity. A free Mo=O bond is known to be ~ 1.65 *Å*. Mo-O(-P) bonds are typically 1.98 *Å*; Mo-O(-Mo) bonds range in length from 2.15 to 2.7 *Å* depending on the length of the octahedral chain within the system.[22]

In order to try and refine many different starting models (for the initial *xyz* positions of all the atoms), and hence to discover the global minimum – the true structure solution – in each unit cell with varying symmetry, an input file was written to allow simulated annealing of the positions. This involved modifying each of the macro lines above with additional code to enable randomisation of the *xyz* positions:

```
macro A1(param,val,val2) {x param val }  val_on_continue=val2+Rand(-x,x)
```

It was then possible to refine the atomic coordinates to convergence, randomise their positions by addition of a random value between ± *x* and re-refine/randomise the positions for a set number of iterations or until a good solution had been found.

2.3 Instrumentation

Routine sample checks were performed on the Siemens d5000 or Bruker d8 diffractometers described below. VT experiments have been carried out on the d8 diffractometers with either furnace or cryochamber attachments. Experimental methods and sample preparation are also outlined.

Powder diffraction data recorded over the course of these experiments have been used to analyse sample purity and also to investigate changes in the materials synthesised with temperature or changing sample environment. As a first step the identification of the materials was carried out in Bruker's EVA software.[23] Where these compounds have been positively identified using the Powder Diffraction File (PDF) database[24] the 6 digit label is included in the text. More detailed analysis of the sample has been undertaken using Rietveld refinement.

2.3.1 Siemens d5000 powder diffractometers

Two Siemens d5000 diffractometers have been used. One is permanently in flat-plate reflection geometry, denoted "d5" in this thesis, and the second, the "d6," is permanently in capillary transmission mode geometry. Both machines are controlled using Bruker's XRD Commander software.[25]

The d5 is an automated diffractometer operated at 40 kV 40 mA. A $CuK_{\alpha 1,2}$ source produces X-rays which first pass through a Soller slit and secondly either a fixed one degree or a variable 6 mm (v6) or 20 mm (v20) divergence slit before illuminating the sample. The diffracted beams pass through a second Soller slit and entering an energy dispersive Sol-X detector. Standard scans have been run using a 2θ range of 10-90 ° 2θ, with either fixed one degree or variable 6 mm slits and a step size of 1 s. Longer scans for Rietveld refinements have been recorded over the range 5-120 ° 2θ with a longer time per step of 7.5 s.

Samples were prepared for the d5 by grinding to give a finely powdered material. Many of the materials investigated experience preferred orientation when run as a bulk powder. To reduce this effect samples were sieved through an 80 mesh sieve onto a silicon disc smeared with Vaseline to act as an adhesive. The silicon discs were specially cut along the 511 plane that is systematically absent so that the discs didn't add peaks to the scans recorded.

The d6 is fitted with a Ge(111) crystal monochromator that provides strictly $CuK_{\alpha 1}$ radiation. The X-rays pass through fixed 0.5 mm divergence slits. A Braun PSD-50M linear position sensitive detector (PSD) with automated step size 0.0144 ° detects the diffracted intensity from the sample.

Samples were prepared for capillary measurement as follows. Compounds were ground to form a finely mixed powder, and then packed into a 0.5 mm diameter glass capillary tube. The capillaries were tapped during the preparation process to ensure adequate packing, and then flame sealed. The glass capillaries were then mounted and centred in the beam; capillaries were rotated during data collection.

2.3.2 Bruker AXS d8 Advance X-ray powder diffractometers

Two Bruker diffractometers operated at 40 kV and 40 mA have been used during the course of this research. The "d8" provides strictly $CuK_{\alpha 1}$ radiation using a Ge(111) crystal monochromator. The X-rays pass through a fixed Soller slit and a fixed 1 ° divergence slit. A Vantec linear PSD, with minimum step size of 0.0085 °, detects the diffracted intensity.

The "d9" also has a Cu tube providing $CuK_{\alpha 1,2}$ radiation, Soller slits and incident variable divergence and antiscatter slits. The d9 does not have a monochromator fitted, but a Ni filter removes all CuK_{β} radiation from the beam. The detector on this machine is a Lynx-Eye detector, containing 192 silicon strip detectors to provide very high resolution data. Both machines are controlled using Bruker's XRD Commander software.[25]

VT studies have been carried out on samples to examine the possible occurrence of phase transitions, chemical reactions and reduction chemistry in an H_2 gas environment. These experiments were carried out on either the d8 or the d9 using one of the furnace or cryochamber attachments outlined in the following sections; use of these attachments has enabled experiments to be carried out between 16 and 1473 K on lab-based machines.

2.3.2.1 Use of an Anton Paar HTK1200 furnace

The Anton Paar HTK1200 furnace (HTK1200) has been used to conduct high temperature XRD experiments on the d8. Samples can be heated from room temperature to a maximum temperature of 1473 K in a range of sample environments. The standard environment used to investigate the presence of phase transitions within materials was under air. In this thesis the sample chamber has also been flushed with N_2 or a 5 % H_2/Ar gas mixture supply; a vacuum pump also enables experiments to be carried out *in vacuo*.

Samples were prepared for experiments by grinding and sprinkling onto amorphous SiO_2 discs smeared with vacuum grease and mounted within the furnace. The furnace control is integrated with Bruker's XRD Commander software,[25] and can be programmed either in step/scan mode, where the furnace heats the sample to temperature and then records an XRD pattern, or in heat/scan mode, where the furnace ramps at a constant rate recording scans in a continual loop. Furnace data have been calibrated through the use of internal standards, as outlined above. The sample height was set by measuring the position of a known reflection. The height was then offset by -0.2 mm to ensure the sample remained within ± 0.2 mm of the ideal position over the whole temperature range studied.

2.3.2.2 Use of a PheniX cryostat

Low temperature experiments have been carried out using an Oxford Cryosystems PheniX, a helium powder cryostat between 16 and 300 K. Samples were prepared for PheniX experiments by grinding and sprinkling them on either an Al sample holder or a silicon disc smeared with Vaseline and mounted within the attachment. The sample chamber was then evacuated and cooled by a closed circuit refrigeration system.

The temperature control for experiments was controlled by the Cryopad Software,[26] in conjunction with Bruker's XRD Commander to control the diffractometer.[25] As such, there was no direct control of the temperature for each scan, and so continual loops were programmed to collect diffraction data while cooling at a constant rate. The local FORTRAN routine, *phenixlogfiles*, was used to extract the average temperature for each scan.[27]

Calibration of the PheniX data was undertaken by one of two methods. The first involved modeling the peaks arising due to the Al sample holder as a Pawley phase in refinements to compare the refined cell parameter with that known for Al. The second method involved including a standard material in the sample preparation stage and then modeling that phase during Rietveld analysis, as outlined above. The data recorded on the PheniX throughout this thesis have been found to be well temperature calibrated, and hence no corrections have been applied. Graphs showing the calibration data are included alongside the results for each experiment.

2.3.3 Single crystal diffractometer

Single crystal data were recorded using a Bruker AXS Smart 6000 Diffractometer, equipped with a Mo source. Temperature was controlled using an Oxford Cryosystems Nitrogen Cryostream 600, and can be deemed accurate to ± 0.1 °. Further details about data collection are given in the tables within the text. The raw data were collected with the SMART software.[28] Data were integrated within the SAINT software package.[29] Files of unit cell information and *hkl*, intensity and errors were output using the XPrep software.[29]

2.3.4 Station 16.2_{SMX} at the Synchrotron Radiation Source (SRS), Daresbury

Single crystal synchrotron experiments in this thesis were undertaken at Station 16.2_{SMX} at the SRS, Daresbury. This station is optimised with high-flux, monochromatic radiation for single crystal diffraction. It is fitted with a Bruker-Nonius Apex II CCD area detector. Station 16.2_{SMX} has a fixed wavelength of ~ 0.82 Å. Data were collected using the Bruker Apex II software.[30]

2.3.5 Use of the Enraf-Nonius Crystal Heater (FR559)

The Enraf-Nonius Crystal Heater (Hothead) is a crystal heater designed to attach onto a standard single crystal goniometer for investigating crystal structures from room temperature up to 973 K. The Hothead was developed in the 1970s and (beyond the standard goniometer head components) comprises an electrically heated resistance wire, a flowing gas supply and a thermocouple, as pictured, Figure 2.1.[31] A single gas flow supply, from *e.g.* an aquarium pump, provides both a hot and a cold flow through the hothead. The cold gas is necessary to encase the hot air flowing around the crystal to minimise the effects of draughts within the laboratory.

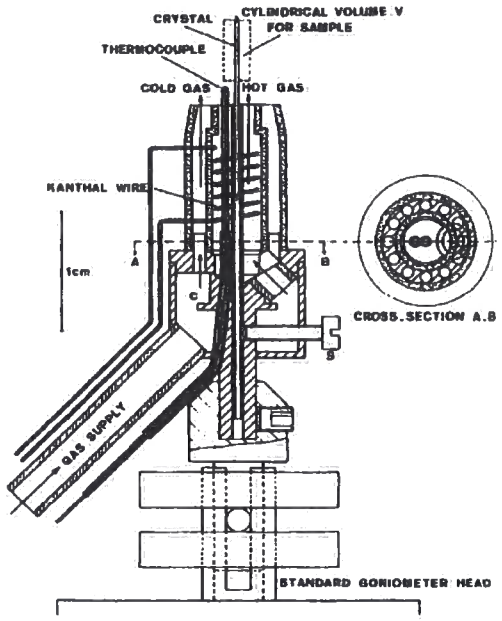

Figure 2.1 A schematic of the hothead, taken from F. Tuinstra *et al.*, *J. Appl. Cryst.*, 1978, 11, 257-259.

The Hothead was used in this thesis to study the phase transition and high temperature structure of $(MoO)_2P_4O_{13}$ (Chapter 5) both at the SRS at Daresbury (on station 16.2_{SMX}) and also on the Bruker Smart 6000 diffractometer detailed above. Crystals were selected and glued onto a pulled quartz fibre. Quartz was preferred over glass or other fibres due to its low thermal expansion. Pulled fibres were used in preference to pulled capillaries as a fibre could be selected of the correct thickness for the crystal under study.

2.3.5.1 Methodology for experiments at the SRS, Daresbury

Initial development time with the Hothead was used to investigate potential adhesives for this high temperature work. Experiments with both Araldite® and Araldite® Rapid led to the observation that the glues charred and eventually lost their functionality above 523 K and 573 K respectively. A ceramic based cement called Fortafix Autostic FS was an alternative. This adhesive is chiefly used for high temperature applications such as in kitchen hob units or oven spaces. Despite the cement being crystalline in nature (composed of several Mg/Ca/Al containing silicates) and hence giving rise to some powder rings in certain orientations of the diffractometer in the single crystal frames, it was used as it had a maximum working temperature of greater than 1300 K. For the small quantities required, *i.e.* to hold the quartz fibres in the metal pips and to affix small crystals to the ends of the fibres, the cement was sticky enough to act as an adhesive and also dried in a short amount of time without the need for any complicated dehydrating curing methods. The mounted goniometer head is shown in Figure 2.2.

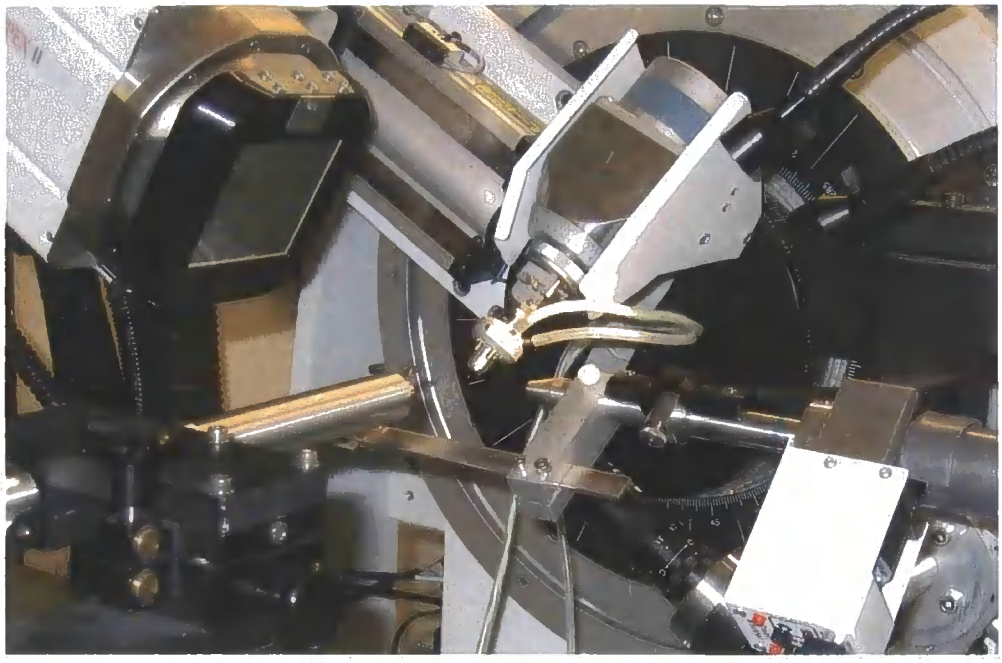

Figure 2.2 Photo of the Hothead goniometer mounted on the diffractometer at Daresbury.

Once the goniometer was mounted in the diffractometer the wires were positioned out of the way, and a suitable collection strategy for the Hothead devised. Normal diffractometer collision positions could no longer be assumed to be correct while using this setup due to the presence of the Hothead. With the addition of a ceramic element, a plastic shield and a thermocouple onto the end of the goniometer, shadowing/extra diffraction arising from the crystalline components could be seen during collection. Two ways to deal with the shadowing were used, the first required the user to manually find the positions of the shadowed/unusable frames before data collection and to programme the software to only collect the usable frames, the second relied on finding the positions after data collection and only integrating the data in the usable frames. Another problem when designing a data collection strategy was the presence of the wires. Although the wires could be taped out of the way onto the main diffractometer circle, it was necessary to leave sufficient slack that the circles could move, but not enough that the wires could fall into the path of the beam or onto the Hothead. Data collection strategies also needed to record appropriate amounts of reciprocal space (with redundancy as required) while ensuring the Hothead and all its components (thermocouple, plastic shielding and trailing wires) did not crash into any of the diffractometer components (collimator and detector). To these ends the suggested collection strategy with set detector distance/angle and varying the Φ/Ω positions were manually explored to check the slack/positioning of the wires and to check for crashing potential. Initially the Hothead was fixed so that the two wires came out at the Φ=0 position. The phi circle was then moved to its first position (Φ=90 deg) and the omega circle swept to discover the maximum and minimum positions possible. This was then repeated with the Φ=120 and Φ=300 positions. Once the maximum coverage had been determined on the diffractometer the wires were fixed to the diffractometer base circle.

2.3.5.2 Methodology for experiments in Durham

The hothead was initially positioned as a normal goniometer head on a Bruker AXS Smart 6000 Diffractometer (Section 2.3.3). However, it was found that the Hothead would not pass underneath the collimator on the machine, thus vastly reducing the amount of reciprocal space that could be probed. As the goniometer height could not be reduced to correct for this, an alternative approach was employed. This made use of a vertical goniometer mount, *i.e.* with the χ angle equal to 0. This attachment is pictured in Figure 2.3.

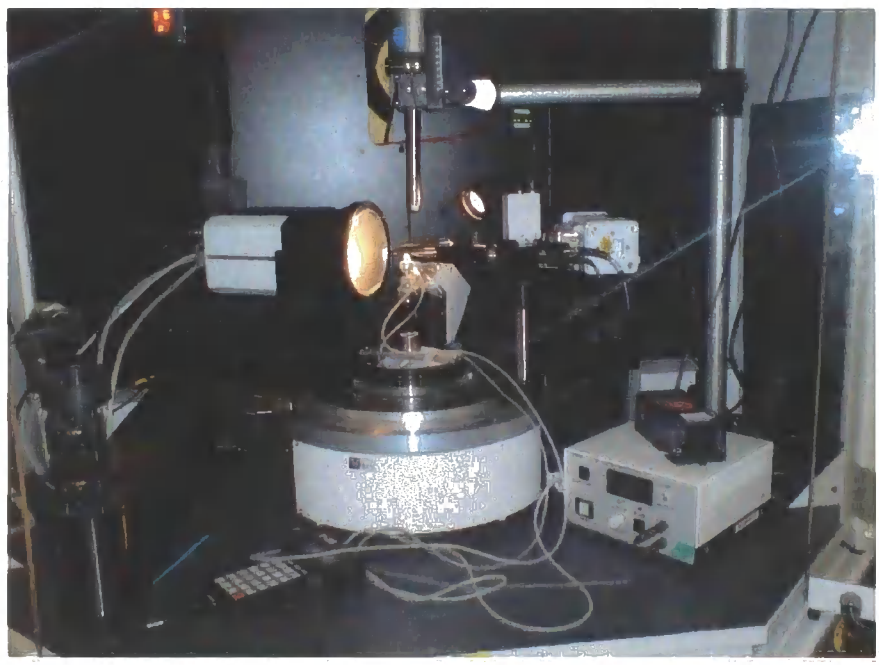

Figure 2.3 Photo of the Hothead goniometer mounted on the diffractometer in Durham.

This arrangement has several advantages. It enables the use of the hothead without the need to carefully discover the new crash limits that were needed for each of the circles in each Φ position. The simpler set-up also negates the need to worry about trailing wires during the data collection. Due to the better positioning of the shielding and the heating element with respect to the detector, no shadowing of the reflections was observed. These advantages are counterbalanced by the reduction in data collected at different Φ angles. In practice, the data collection takes place at a fixed Φ angle, though this cannot be called a specific Φ angle relative to the diffractometer circles, as would occur in normal data collection.

2.3.6 Beamlines ID11/ID31 at the European Synchrotron Radiation Facility (ESRF)

ID11 is a materials science beamline; it has a tunable energy from 23-140 keV and high flux, making access highly competitive for *e.g.* time resolved diffraction studies. Experiments on this beamline involved recording short (~0.25 s) diffraction patterns on capillary samples to monitor the progress of a reaction, Chapter 7. The detector was an image intensifier, Frelon 2K CCD 2D detector with a dynamic range of 10^{14} and a minimum readout time of 20 ms. A double Laue-Laue monochromator is present on the beamline to enable the use of the high energy end of the spectrum. The

monochromator contains two bent Si(111) crystals that can be rotated for optimum flux. The wavelength used was ~ 0.2 Å.

A mirror furnace was used on ID11 to generate very high sample temperatures within a very short space of time for rapid data collection over short timescales, Figure 2.4. The furnace was constructed from a parabolic ceramic body with six openings. Three halogen lamps were used to heat the small space controlled by a Eurotherm controller. Platinum capillaries were filled with finely ground samples and positioned inside the furnace using systematic changes in temperature/time to investigate the reaction. Temperatures were calibrated from the Pt capillary and an Al_2O_3 standard material.

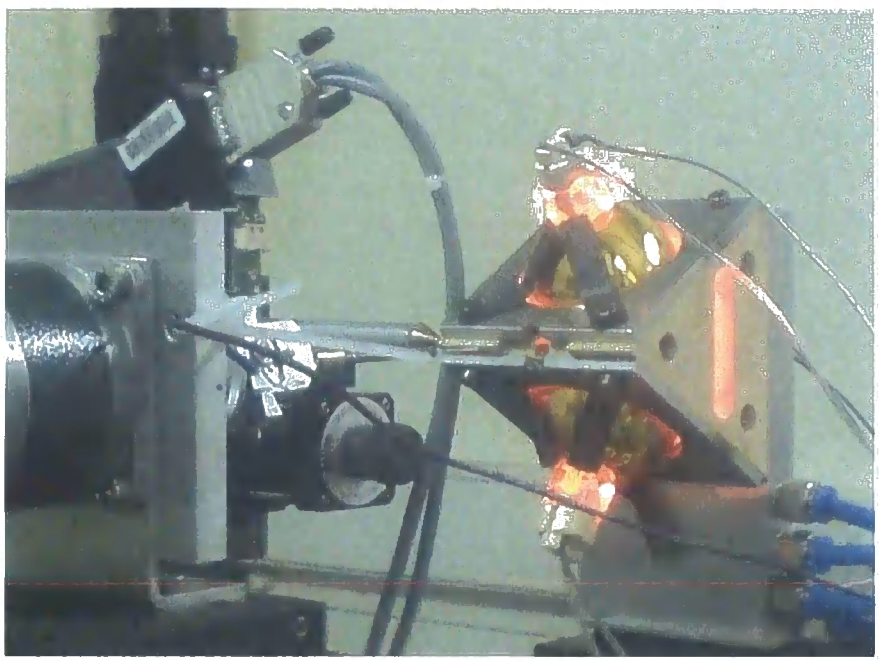

Figure 2.4 Photo of the mirror furnace. The collimator for the synchrotron radiation is visible to the left of the centre; Pt capillary in the centre of the picture.

ID31 is used to obtain high resolution powder diffraction patterns for structure solution and phase changes under evolving conditions. The beamline operates at energies between 5 and 60 keV, corresponding to λs of 2.48 to 0.21 Å. The radiation is produced from 3 ESRF undulators, passing through a double Si(111) monochromator. The detector bank contains 9 detectors spaced 2 ° apart, each with an individual Si(111) analyser crystal. Samples were recorded in spinning glass (ambient temperature) or quartz (variable temperature) capillaries. Samples were heated using the hot air blower to temperatures of 450 K.

2.3.7 HRPD at the ISIS Spallation Source, Didcot

All TOF data in this thesis were recorded at the High Resolution Powder Diffraction (HRPD) beamline at the ISIS spallation source at the Rutherford Appleton Laboratory near Didcot.[32,33] HRPD has a 100 K methane moderator that gives an incident flux between 0.5 and 12 Å. Neutrons are detected in 3 fixed positions, namely in backscattering (168 °), at 90 ° and at 30 °. The recent HRPD upgrade has seen the replacement of the old guide with the installation of a high-reflectivity supermirror guide. Flux

gains have been considerable; the new guide adds the ability to transmit shorter wavelength neutrons down to *d*-spacings of 0.3 Å. The high resolution of the machine in backscattering (10^{-4}) has been preserved.

To avoid frame overlap, that is where the slow neutrons from pulse 1 are overtaken by the fast neutrons of pulse 2, a series of choppers are used along the flight path of the neutrons. These ensure that the pulses are recorded individually with no interference to enable accurate determination of both the wavelength and hence *d*-spacings. The standard chopper frequency on HRPD is set to 50 Hz/5, where the ISIS frequency is 50 Hz. This frequency assures no frame overlap. The flux output of the spallation source is 200 mAhs. As such HRPD receives ~40 mAhs by virtue of the chopper frequency. This allows a TOF range of 100 ms to be recorded. For investigation of lower *d*-spacings, the TOF range can be increased to 200 ms by changing the chopper frequency to 50 Hz/10. Although this is to the detriment of neutron flux, the gain in TOF range and hence *d*-spacing can be essential to solving some problems, *e.g.* those of large superstructures. The 90 ° and backscattering banks at HRPD are ZnS scintillation detectors.

The instrument design on HRPD enables the user to investigate materials over a λ range of 0.3 to 12 Å and hence a d-spacing range of 0.3 to 6 Å (with variations in resolution between each of the banks). This, combined with the very high resolution available in backscattering enable the investigation of subtle phase transitions especially those seen in displacive phase transitions as detailed in this thesis.

Data were recorded at HRPD and the background due to the V can and the empty furnace were subtracted locally from standard scans.[34] The .gss and .asc files processed were converted to .xye files using the local routine Splithrpdgsas2.[35] During the same conversion routine the files were split into constituent 30 °, 90 ° and backscattering bank files, having filenames _30, _90 and _bs respectively.

The instrumental peakshape was calculated from ceria data by John S. O. Evans. The x-axis calibration coefficients, of the form given below, were refined using silicon data. Parameters difa and t_0 were refined for each structure to enable correction for potential minor shifts in peak positions over the tof range refined.

$$TOF\_sample\_peakshape = difa*d^2 + difc*d + t_0$$

2.3.8 BT1 at the National Institute of Standards and Technology (NIST)

All constant wavelength neutron data recorded in this thesis were recorded on beamline BT1 at the NIST Center for Neutron Research (NCNR) by Dr. Sarah Poulton and Dr. Mark Green. The NCNR is a reactor-source in Gaithersburg, Maryland.

Beamline BT1 at the NCNR is a high resolution powder diffractometer. Neutrons are detected using 32 ^{3}He detectors placed at 5 ° intervals to cover a 2θ range of 0-167 ° in a 13 ° scan. Two different monochromators were used during the course of this work with 15' collimation. The first was a Cu(311) monochromator, giving neutrons with a wavelength of 1.540 Å at good resolution. The

second was a Ge(311) monochromator that gave wavelengths of 2.079 Å and intensities three times higher than the Cu monochromator but with reduced resolution.

The recorded BT1 files were converted to .gsas files using the NIST programs proprep and gformat.[36] The .gsas files were locally converted to .xye files using Powder4.[37]

2.4 Other methods of characterisation

2.4.1 Electron diffraction

The interaction between electrons and matter is very strong; electron diffraction techniques only probe a thin layer at the surface of a material in reflection mode and for transmission geometry a much thinner layer is required.[38,39]

Bragg's law can be applied in the case of electron diffraction, but with some modifications compared to the cases above for X-rays and neutrons. The first modification is a simplification. The de Broglie wavelength of an electron is much smaller than that of, for example, a neutron. It follows that as the wavelengths are small, $\sin\theta$ is $\approx \theta$. Hence only small diffraction angles can be measured. Although this may sound problematic, in actual experiments it is not, as outlined below. Due to the much smaller size of the electrons' wavelengths when compared to the size of the unit cell, the size of the Ewald sphere in reciprocal space is much bigger than the crystal lattice. As such a large number of reflections can be "seen" at a single Bragg angle.[d]

In this thesis, electron diffraction has been used to discover the relationship between a sublattice and a superlattice. The presence of a superlattice structure within a crystal contributes extra reflections to the diffraction pattern which cannot be indexed using the sublattice. The new superlattice peaks lead to the discovery of the true superlattice in real space by relation to the sublattice peaks. For example, a superlattice peak that can be indexed to be k=0.5 requires a doubling of the real b axis to correctly index the superlattice peaks occurring along that direction in the crystal.

Electron diffraction patterns were recorded on a Philips EM 430 Transmission Electron Microscope (TEM) operating at 300 kV.

2.4.2 Nuclear Magnetic Resonance (NMR)

Nuclear Magnetic Resonance (NMR) techniques are used to probe the interactions present in a material when placed within a magnetic field. Thus the differing electronic environments of atoms within a crystal structure enable the local structure of a material to be studied. This is in contrast to the long-range order probed by X-ray diffraction techniques.

In the solid state there are anisotropic interactions present which are cancelled out in solution state NMR due to tumbling. Several of these interactions are found to be proportional to $(1\text{-}3\cos^2\theta)$, and

[d] This arises from the fact that only infinite crystals give "point" diffraction. As the sample size in one direction is so small, the discrete maxima become elongated in that direction, that is parallel to the beam direction.

can be averaged to zero by spinning the sample at the so-called magic angle of 54.7 ° to the applied magnetic field, B_o.

Several materials in this thesis have been investigated by ^{31}P solid-state NMR. Phosphorus has 100 % natural abundance and high receptivity ($6.63x10^{-2}$ relative to ^{1}H). It is also a spin ½ nuclei. NMR spectra have been recorded on a Varian Infinity Plus 500 MHz spectrometer in the Department of Chemistry, Durham by Anne Soleilhavoup.

1D spectra were recorded using a single pulse, consisting of a single pulse, acquisition time and a recycle delay. 2D INADEQUATE spectra were recorded to investigate through-bond J-coupling interactions present within the structure.[40] The spectra recorded (discussed in Chapter 4) highlight pairs of atoms that are present within a P_2O_7 group, with their resonances appearing on the same horizontal line in the presentation used.

2.4.3 Second Harmonic Generation (SHG)

It is possible to use a very intense light source, *e.g.* a laser, to investigate whether a crystal exhibits inversion symmetry, *i.e* whether it is centrosymmetric or acentric.[41]

In a material that is centrosymmetric, it can be shown that the electric polarisation, *P*, is linearly dependent on the applied electric field, Equation 2.10, where *a* is a constant. In an acentric material this is not so, and it is necessary to use the relationship given in Equation 2.11, where both a_1 and a_2 are constants. The electric field can be described in terms of a wavevector, Equation 2.12, where t is the time and ω the angular frequency.

$$P = aE \tag{2.10}$$

$$P = a_1E + a_2E^2 \tag{2.11}$$

$$E = E_O \sin\omega t \tag{2.12}$$

Substitution of Equation 2.12 into Equation 2.11, leads to Equation 2.13, such that the crystal generates a wave with double the frequency of the incident radiation; this is Second Harmonic Generation (SHG).

$$P = a_1E_O \sin\omega t + \frac{a_2}{2}E_O^2 - \frac{a_2}{2}E_O^2 \cos 2\omega t \tag{2.13}$$

In the case of many inorganic solids, the electric field interacts most strongly with the most polarisable atoms, *i.e.* the oxygen atoms. If follows from this that even if the heavier atoms are arranged centrosymmetrically, the acentric lighter atoms are still able to generate an SHG signal, making this test sensitive to small departures from centrosymmetry. The experimental setup used is described in reference 42.[42]

2.4.4 Infrared spectroscopy

All infrared (IR) spectra were recorded on a Perkin Elmer Spectrum 100 FTIR instrument over the range 450-4000 cm^{-1} with a KBr disc. The background calibration was carried out using an identical KBr disc and calibration checked for the KBr "sample" to yield no transmission. Each pellet was made using 0.40(2) g dried KBr with 2 % sample by mass to ensure equi-sized pellets for comparison.

2.4.5 Thermal methods

Analysis of some compounds was undertaken by two different thermal methods. The applications and practicalities of each are outlined below.

2.4.5.1 Differential Scanning Calorimetry (DSC)

In this technique samples are heated at a specified rate, *e.g.* 10 K/min, to a specified temperature. The instrument monitors the amount of heat being taken up (endothermic)/given out (exothermic) by the sample with respect to an inert reference material, when a constant heating rate is maintained. The input/output from the sample is plotted against temperature, and from this graph phase transitions can be identified, assuming that the change in enthalpy is detectable. DSCs were carried out on a Perkin Elmer Pyris 1 Differential Scanning Calorimeter.

2.4.5.2 Thermogravimetric Analysis (TGA)

This second type of thermal analysis heats a sample of known mass at a constant rate, and measures the change in mass, typically as a % change, over time and temperature. This technique is useful to quantify changes in composition of samples, *e.g.* loss of H_2O, NH_3 or P_2O_5. This method has been used to investigate chemical reaction pathways, and it can also highlight phase transitions if they are accompanied by a mass loss, for example loss of P/O content. TGAs were carried out using a Perkin-Elmer Pyris 1 Thermogravimetric Analyzer.

2.5 Synthetic methods

Several different synthetic methods have been employed during the synthesis of the materials investigated in this thesis. These are high temperature synthesis, or the "churn and burn" technique, hydrothermal syntheses and solution state methods.

The high temperature methods can be used for thermodynamically stable materials that form on heating an intimate mixture of the reactants to high temperatures. These syntheses have been carried out in alumina or platinum crucibles, sealed in quartz tubes, or in a few cases in a tube furnace under vacuum or gas flow.

The use of hydrothermal methods has enabled the formation of materials that would not withstand the high temperature routes, but would instead transform to other products on heating. Paar acid digestion autoclaves have been the standard apparatus employed.

2.6 References

1. S. E. Lister, *Negative Thermal Expansion Materials, 4th Year Project Report*, University of Durham, 2004.
2. G. M. Sheldrick, *SADABS*, University of Göttingen, Germany, 1996.
3. W. Clegg, *Crystal Structure Determination*, Oxford University Press, 1993.
4. ed. R. A. Young, *The Rietveld Method*, Oxford University Press, 1993.
5. H. M. Rietveld, *J. Appl. Crystallogr.*, 1969, **2**, 65-71.
6. A. A. Coelho, *TOPAS Academic: General Profile and Structure Analysis Software for Powder Diffraction Data*, Bruker AXS, Karlsruhe, 2004.
7. P. Thompson, D. E. Cox and J. M. Hastings, *J. Appl. Crystallogr.*, 1987, **20**, 79-83.
8. C. J. Crossland, *Solvothermal routes to New Chalcogenide Materials, PhD Thesis*, University of Durham, 2004.
9. K. G. Lyon, G. L. Salinger, C. A. Swenson and G. K. White, *J. Appl. Phys.*, 1977, **48**, 865-868.
10. K. Wang and R. R. Reeber, *Phil. Mag. A*, 2000, **80**, 1629-1643.
11. J. P. Cline, *Standard Reference Material 640c - Silicon Powder Line Position and Line Shape Standard for Powder Diffraction*, Gaithersburg, Maryland, USA, 2000.
12. J. S. O. Evans, *Multitopas, Fortran 77 routine*, Durham, 1999.
13. J. S. O. Evans, *Multitopas_files, Fortran 77 routine*, Durham, 1999.
14. A. A. Coehlo, *Appl. Cryst.*, 2002, **36**, 86-95.
15. *International Tables for Crystallography, Volume A*, Dordrecht, Holland and Boston, USA, 1983.
16. G. Oszlányi and A. Sütő, *Acta Crystallogr., Sect. A*, 2004, **60**, 134-141.
17. H. Gies, *Science*, 2007, **315**, 1087-1088.
18. B. J. Campbell, H. T. Stokes, D. E. Tanner and D. M. Hatch, *J. Appl. Cryst*, 2006, **39**, 607-614.
19. J. S. O. Evans, *Topasreader, Fortran 77 routine*, Durham, 1999.
20. J. S. O. Evans, *I5totopas, Fortran 77 routine*, Durham, 1999.
21. J. S. O. Evans, *top_to_rest_2, Fortran 77 routine*, Durham, 1999.
22. G. Costentin, A. Leclaire, M. M. Borel, A. Grandin and B. Raveau, *Rev. Inorg. Chem.*, 1993, **13**, 77-101.
23. Bruker AXS, *Diffrac^{plus} Basic Evaluation Package: EVA 10.0*, 2004.
24. Powder Diffraction File, *International Centre for Diffraction Data*, Pennsylvania, 1998.
25. Bruker AXS, *Diffrac^{Plus} XRD Commander v2.3: Software for Controlling Bruker Diffractometers*, Karlsruhe, 2000.
26. Oxford Cryosystems, *Cryopad v 1.482*, Oxford, 2007.
27. J. S. O. Evans, *phenixlogfile, Fortran 77 program*, Durham, 1999.
28. *SMART V5.625*, Bruker AXS, Madison, WI, USA, 2005.
29. *SAINT V6.02*, Bruker AXS, Madison, WI, USA, 2005.
30. Bruker AXS, *Apex II v2.1.4: Software for Controlling Bruker Diffractometers*, Karlsruhe, 2007.
31. F. Tuinstra and G. M. Fraase Storm, *J. Appl. Cryst.*, 1978, **11**, 257-259.
32. R. Ibberson, W. I. F. David and K. S. Knight, *The High Resolution Neutron Powder Diffractometer (HRPD) at ISIS - A User Guide*, ISIS Crystallography, Didcot, 1992.

33. C. C. Wilson, *Single crystal neutron diffraction from molecular materials*, World Scientific, London, 2000.
34. P. G. Radielli, T. Proffen and L. C. Chapon, *Ariel 4.0*, ISIS Facility, Oxford, UK, 2008.
35. J. S. O. Evans, *Splithrpdgsas2, Fortran 77 routine*, Durham, 2007.
36. NIST, *User's Guide*, 2008, http://www.ncnr.nist.gov/programs/crystallography/guide/.
37. N. Dragoe, *Powder4 v1.5b*, Orsay, France, 2004.
38. P. J. Goodhew and F. J. Humphreys, *Electron Microscopy And Analysis*, Taylor and Francis, London, 1988.
39. M. H. Loretto, *Electron Beam Analysis of Materials, 2nd Edition*, Chapman and Hall, London, 1994.
40. A. Lesage, M. Bardet and L. Emsley, *J. Am. Chem. Soc.*, 1999, **21**, 10987-10993.
41. D. McKie and C. McKie, *Essentials of Crystallography*, Blackwell Scientific Publications, Oxford, 1986.
42. K. M. Ok, E. O. Chi and P. S. Halasyamani, *Chem. Soc. Rev.*, 2006, **35**, 710-717.

3. Dehydration Reactions of $MoO_2 \cdot H_2O \cdot PO_3OH$ and the *in-situ* Identification of two New Molybdenum Phosphates

3.1 Introduction

This chapter describes studies on the dehydration of $MoO_2 \cdot H_2O \cdot PO_3OH$. This material was initially prepared as a precursor to $(MoO_2)_2P_2O_7$, whose structure is the subject of Chapter 4. During the investigation, the dehydration was found to be more complex than first thought. This chapter describes the identification and characterisation of two new molybdenum phosphates discovered during this work.

The compound $MoO_2 \cdot H_2O \cdot PO_3OH$ was first isolated by Schulz in 1955,[1] and described as an orthophosphate. Thermogravimetic analysis (TGA) revealed that it lost one mole of water between 423 – 498 K and half a mole of water between 498 and 573 K, to form a product containing pyrophosphate groups. This led to the formulation of this material as $MoO_2 \cdot HPO_4 \cdot H_2O$. On leaving a heated solution of MoO_3 and H_3PO_4 under ambient conditions for several weeks, a second crystalline phase was obtained, having a total of three H_2O molecules within the structure. This material was only briefly mentioned by Schulz, stating that it readily lost 1.5 moles of water below 373 K, to form the phase under investigation here.

The structure of $MoO_2 \cdot HPO_4 \cdot H_2O$ was solved by Kierkegaard in the monoclinic space group $P2_1/m$,[2] and was described as consisting of corner-sharing MoO_6 octahedra and PO_4 tetrahedra, such that each octahedron shared three corners with tetrahedra, and each tetrahedron shared three corners with Mo octahedra. The polyhedra form 1D chains of alternating P and Mo polyhedra as pictured in Figure 3.1a. The chains form along [010] and are held together by H bonding. The positions of the H atoms could not be located by Kierkegaard, but by consideration of the O ion environments, proton affinities and bond distances he concluded that all the protons must form Mo-OH type bonds, resulting in the assignment of the structure as $Mo(OH)_3PO_4$. The material was studied using IR and ^1H NMR by Glemser and coworkers.[3,4] An IR band at ~ 1625 cm^{-1} was assigned as arising from a water molecule scissor motion,[3] and led the authors to conclude that the true formula/structure was actually as described by Schulz.

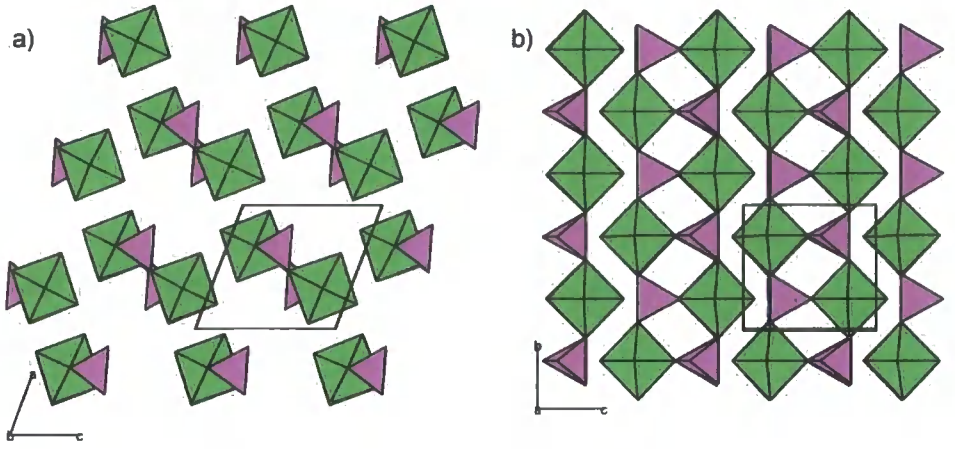

Figure 3.1 The structure of $MoO_2{\cdot}H_2O{\cdot}PO_3OH$. a) View along [010] shows the chains in the structure that are held together by H bonding, and b) the *bc* plane with alternating MoO_6 octahedra and PO_4 tetrahedra forming chains in the [010] direction.

Later structural investigations were carried out by Weller *et al.* (1989)[5] and Biot *et al.* (2001).[6] They used powder neutron and X-ray studies respectively to accurately locate the positions of the H atoms. Although the latter study failed to find the positions of the H atoms from the X-ray data, Biot *et al.* used bond-length-strength calculations to place the atoms. Both groups concluded that the correct formulation should be $MoO_2{\cdot}H_2O{\cdot}PO_3OH$.

The descriptions of the dehydration process of this material in the literature are conflicting. Schulz described it as occurring in two distinct steps, as outlined above.[1] She described the intermediate material as having the composition $MoO_2{\cdot}PO_3OH$, being an orthophosphate containing a P-OH group. Kierkegaard repeated this dehydration study and found a single dehydration step, and described the powder photograph recorded after heating $MoO_2{\cdot}H_2O{\cdot}PO_3OH$ at 498 K as not being identical to the precursor, suggesting that the "complicated diffuse picture" was probably a mixture of both $MoO_2{\cdot}H_2O{\cdot}PO_3OH$ and the fully dehydrated product $(MoO_2)_2P_2O_7$. Further study by Gopalakrishnan[7] found that the hydrated precursor loses one mole of H_2O at 498 K and the resulting XRD pattern – different to the precursor – could be indexed on a tetragonal cell with a = 6.27 and c = 4.91 Å. The phase could be formulated as $MoO_2(HPO_4)$, as proposed by Schulz.[e] Gopalakrishnan suggested that this phase could undergo a topotactic dehydration to a layered material similar to $VOPO_4{\cdot}2H_2O$.[8] None of these phases have been formally identified or structurally characterised within the literature to this author's knowledge.

Schulz claimed there are two forms of the dehydrated material, a stable and an unstable one (with respect to rehydration). The unstable form is prepared on heating the hydrate, $MoO_2{\cdot}H_2O{\cdot}PO_3OH$ between 573 and 773 K, and is light blue in colour. This form of the material is said to rehydrate within

[e] The accurate positions of the H atoms were not known when this paper was published. As such the authors cited both $MoO(OH)PO_4$ and $MoO_2(HPO_4)$ as potential formulas. Following the publications by Weller *et al.* and Biot *et al.*, the formulation as $MoO_2(HPO_4)$ appears to be the correct one.

3 weeks when left in contact with the atmosphere. The stable polymorph is not hygroscopic and forms on heating the unstable form up to 873 K. Confusingly, Schulz states that the stable polymorph can be formed at lower temperatures, but is then also blue in colour.

The structure of the final dehydrate, $(MoO_2)_2P_2O_7$, was solved by Kierkegaard,[9] in space group *Pnma*. It has been described as being composed of Mo ions in octahedral coordination and P ions in tetrahedral coordination. Every MoO_6 octahedron shares two Mo-O vertices with two other MoO_6 octahedra, forming zigzag chains in the *xz* plane. Three vertices of the octahedron are linked to P_2O_7 groups, and one Mo-O bond is "free". The PO_4 tetrahedra pair up to form P_2O_7 groups. The 6 vertices of the P_2O_7 group are linked to MoO_6 octahedra, these double tetrahedra are in eclipsed conformations, such that each eclipsing pair of P-O bonds forms bonds with the same MoO_6 octahedral chain, thus linking 3 chains together. The structure of this material is investigated further in Chapter 4.

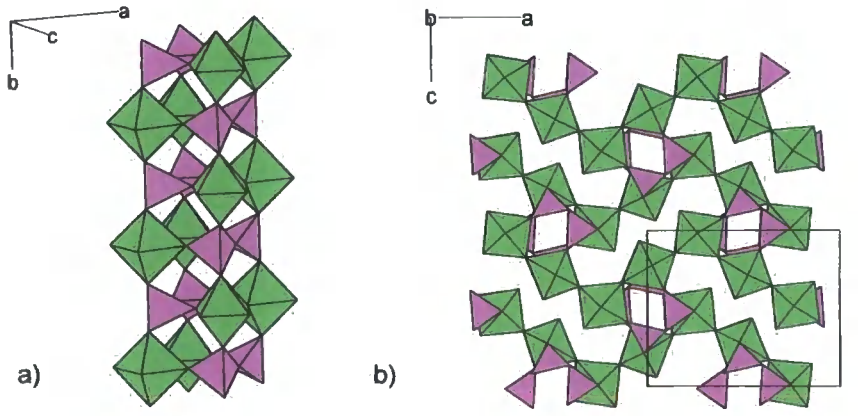

Figure 3.2 The structure of $(MoO_2)_2P_2O_7$. (a) The 2D chains of P_2O_7 groups linking MoO_6 octahedra along [010]. (b) The 3D connectivity of the structure showing the zigzag chains.

This chapter outlines the work that has been undertaken on the areas described above to try and unravel this somewhat confused literature. These studies involved *in-situ* variable temperature diffraction studies where both temperature and time have been varied. It was also necessary to develop new methodologies to analyse these data, and further experiments were carried out to enable isolation and structure solution of intermediates phases.

3.2 Synthesis and Rietveld analysis

This investigation began with the synthesis of the hydrated molybdenum phosphate, $MoO_2{\cdot}H_2O{\cdot}PO_3OH$. Two routes have been used to synthesise this material. The first (solution-state) route was described by Kierkegaard.[2] A typical synthesis (SEL234) involved dissolving 7.5 g MoO_3 (52 mmol, Alfa Aesar, 99.95 % metals basis) in 22.5 cm^3 85 % H_3PO_4 (331 mmol, Aldrich) at approximately 453 K. The solution was then cooled to room temperature, 200 cm^3 HNO_3 was added and the solution refluxed for 12 hours. The solution was again cooled and micro crystals of the title compound precipitated from the solution. These crystals were filtered off, and washed with acetone

before being left to dry in air. The yield was 11.93 g, 94.8 %. Samples prepared using this method contain little or no MoO_3 impurity.

The second method[6] was a hydrothermal synthesis. A typical synthesis (SEL214) involved heating 2.48 g MoO_3 (17 mmol, Alfa Aesar, 99.95 % metals basis) with 1.77 cm^3 H_3PO_4 (26 mmol, Aldrich) in a Teflon-lined autoclave, at 453 K for 12 hours. The resulting solid was washed with demineralised water and dried in air. The yield was 2.68 g, 65 %. Samples prepared using this method contained MoO_3 as an impurity, between approximately 5 and 15 % by Rietveld analysis. Successful syntheses were confirmed by comparison of the PXRD patterns with the PDF (11-0333).[10]

Figure 3.3 shows the Rietveld analysis of sample SEL234, a pure sample of $MoO_2{\cdot}H_2O{\cdot}PO_3OH$ prepared by the solution state method. 20 parameters were refined in this analysis, including 6 coefficients of a Chebychev polynomial to model the background, a sample height parameter, 4 lattice parameters of $MoO_2{\cdot}H_2O{\cdot}PO_3OH$, 3 isotropic displacement factors – one for each atom type, 4 parameters used to define the TCHZ peak shape,[11] a scale parameter and a parameter to describe axial divergence. A final R_{wp} value of 5.31 % was obtained. The difference curve (shown in grey) shows the good fit between the structural model (Kierkegaard)[2] and the recorded data. No peaks due to MoO_3 are present in this scan. Selected refinement details are given in Table 3.1. The Topas input file is included in the E-appendix.

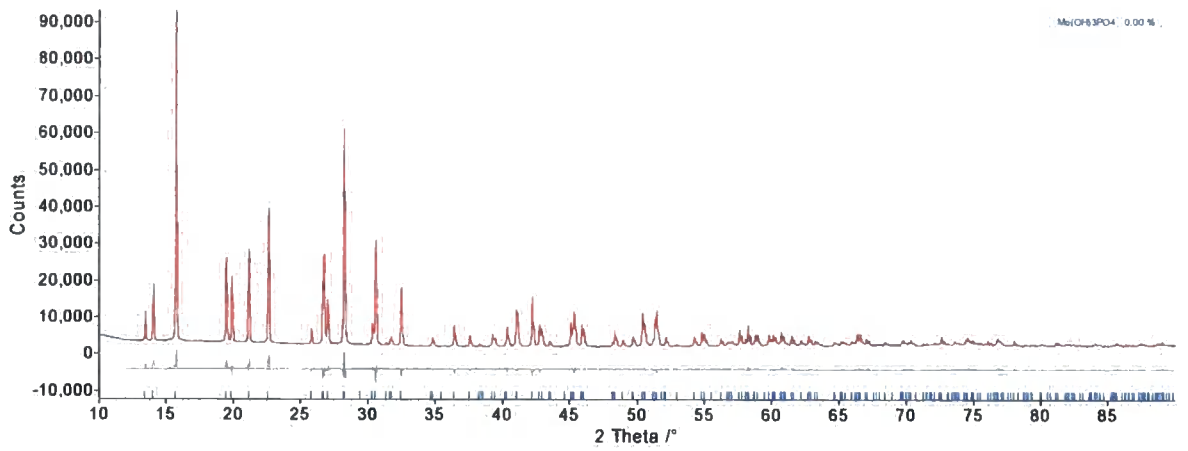

Figure 3.3 Rietveld analysis of SEL234, pure $MoO_2{\cdot}H_2O{\cdot}PO_3OH$ (d9_02374); R_{wp} 5.31 %. The figure shows the experimental data in blue, the calculated pattern in red and the difference plot in grey. Tick marks (in blue) show the predicted positions of the peaks.

Table 3.1 Selected refined values, crystallographic and data collection parameters for d9_02374.

Space Group	$P2_1/m$	2θ range /°	10-90
a /Å	6.7427(1)	2θ step size /°	0.02
b /Å	6.3371(1)	Time per step /s	2.5
c /Å	7.0439(1)	R_{wp} /%	5.31
β /°	110.1378(8)	R_{Bragg} /%	3.64
Volume /Å^3	823.06(4)	GOF	3.22
Number of parameters	20		

3.3 *In-situ* studies of the dehydration reaction

From the literature it was known that $MoO_2{\cdot}H_2O{\cdot}PO_3OH$ could be dehydrated to form $(MoO_2)_2P_2O_7$;[9] however in our hands, following the preparation method for $(MoO_2)_2P_2O_7$ in the literature yielded an amorphous blue solid and not the desired crystalline powder.

Following these unsuccessful *ex-situ* attempts to synthesise the dehydrated phase, the reaction was followed *in-situ* in a Bruker d8 diffractometer, equipped with an Anton Paar HTK1200 furnace attachment. A sample of the hydrated precursor, $MoO_2{\cdot}H_2O{\cdot}PO_3OH$, was sprinkled onto an amorphous quartz disc smeared with Vaseline as adhesive and then mounted in the furnace. The diffractometer was programmed to heat the sample from 303 to 1023 K recording a 30 minute XRD pattern every 10 K from 10 to 90 ° 2θ.

3.3.1 Visual inspection of the data

The initial set of scans is shown in Figure 3.4. This figure suggests that the known hydrated phase loses water to eventually give the known dehydrated phase at 873 K (highlighted in blue). It can also be seen from Figure 3.4 that the reaction does not proceed directly from the first known compound to the second. Instead multiple phases are present over the course of the dehydration reaction. Due to the conflicting (or lacking) information in the literature about the composition of these phases, an investigation was planned to discover their identity. Analysis of the variable temperature data would yield information about the time and temperature dependence of the existence and stability of both these known and as yet unknown phases. This would then reveal both *in-situ* and *ex-situ* synthetic routes to each phase; *in-situ* routes would enable the collection of good quality diffraction data for indexing and structure solution, *ex-situ* routes would allow bulk synthesis for application of further characterisation techniques.

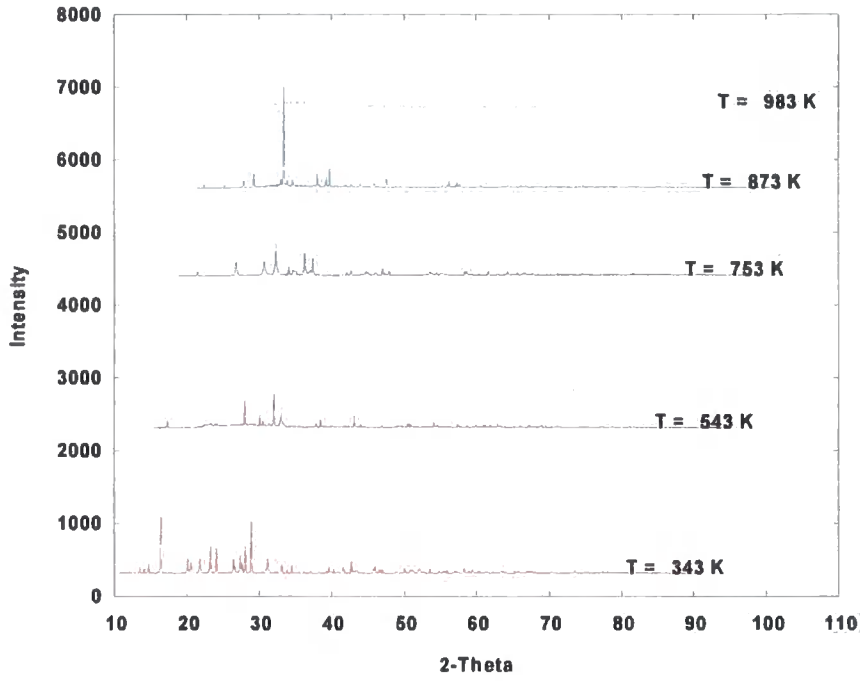

Figure 3.4 Initial *in-situ* dehydration of $MoO_2{\cdot}H_2O{\cdot}PO_3OH$ (SEL191, d8_03228), heating from 303 to 1003 K. The hydrated precursor is shown in red, unknown phases 1 and 2 are shown in purple and black respectively, the known dehydrate, $(MoO_2)_2P_2O_7$, is in blue and the amorphous high temperature products are in brown. Set temperatures are displayed for each phase highlighted. Data are offset in x and y for clarity.

All samples of $MoO_2{\cdot}H_2O{\cdot}PO_3OH$ prepared at the time these experiments were undertaken contained MoO_3 as an impurity. Hence, these two phases co-exist as the starting reactants in the dehydration reactions. Visual inspection of the *in-situ* dehydration reaction (against set temperatures) shows that the intensity of the $MoO_2{\cdot}H_2O{\cdot}PO_3OH$ peaks begin to decrease above 423 K. At the same time the background intensity rises, and, following the complete disappearance of the known hydrated phase, the XRD patterns show a minor new crystalline phase appears, unknown 1 (UNK1). The significant increase in background intensity indicates that a significant amorphous component is present within this temperature range. UNK1 is seen most clearly in range 25 (Figure 3.5).

On further increasing the temperature peaks due to UNK1 decrease in intensity; the background intensity also decreases and a second new phase crystallises, unknown 2 (UNK2), above 700 K. This phase is most clearly seen in range 46 at 763 K, Figure 3.5. As the temperature is increased again the known phase $(MoO_2)_2P_2O_7$ appears; UNK2 and $(MoO_2)_2P_2O_7$ co-exist over the temperature range 773 – 813 K. Above this temperature the main phase present is $(MoO_2)_2P_2O_7$. On heating above 933 K all crystalline phases disappear and only a very broad peak is present. The peaks arising from the impurity phase, MoO_3, disappear before 873 K; this phase is known to volatilise at this temperature.[12]

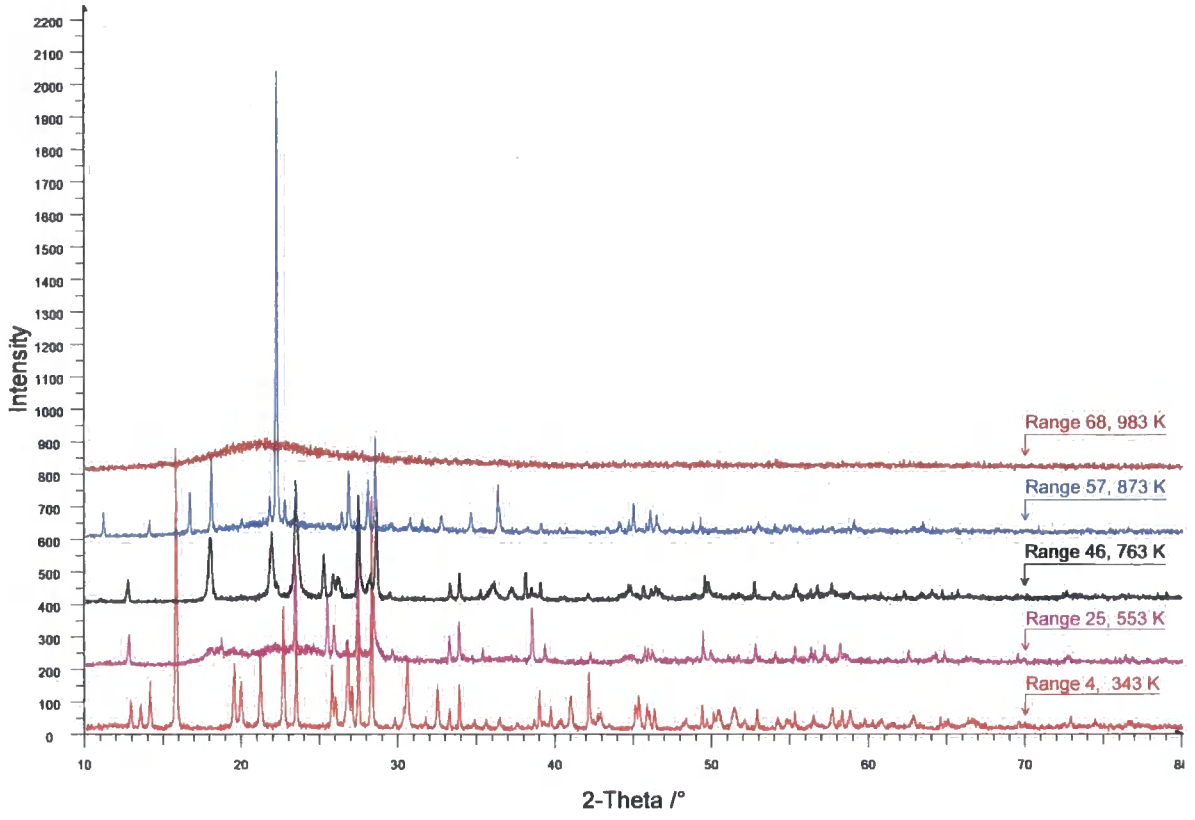

Figure 3.5 The five distinct phases found on heating a sample of $MoO_2{\cdot}H_2O{\cdot}PO_3OH$. The initial hydrate decomposes to form two unknown phases (UNK1 and UNK2) most clearly visible in ranges 25 and 46 respectively, finally forming the known dehydrated phase, $(MoO_2)_2P_2O_7$ in range 57 before further heating destroys all crystalline material. Scan colours are carried forward from Figure 3.4. The impurity, MoO_3 was present in the scans recorded up to 873 K.

The progression of the dehydration reaction is shown schematically in Equation 3.1:

$$MoO_2{\cdot}H_2O{\cdot}PO_3OH + MoO_3 \rightarrow UNK1 + MoO_3 + \text{amorphous material} \rightarrow$$
$$UNK2 + MoO_3 \rightarrow (MoO_2)_2P_2O_7 \rightarrow \text{final amorphous product} \qquad (3.1)$$

This experiment was repeated with a maximum heating temperature of 823 K, with scans recorded on cooling back to room temperature as well as on heating to check this synthetic route for use in *ex-situ* work, Figure 3.6. The final scan on cooling to room temperature is the crystalline compound initially targeted, $(MoO_2)_2P_2O_7$.

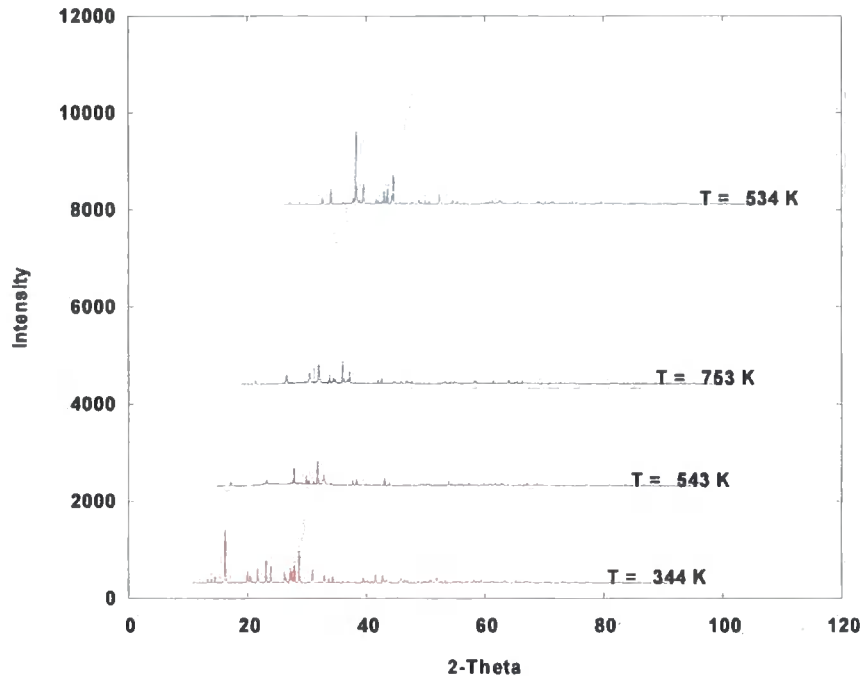

Figure 3.6 Scans recorded on heating a sample of $MoO_2{\cdot}H_2O{\cdot}PO_3OH$ (SEL191, d8_03230) from 303 K up to 823 K and then cooling back to 303 K. Scan colours are carried forward from Figure 3.4. Scans are offset in x and y for clarity.

Initial *ex-situ* attempts to synthesise $(MoO_2)_2P_2O_7$, using the information gained from the *in-situ* experiments, led to the belief that there were two different but very similar forms of this material as hinted by Schulz.[1] The XRD patterns from samples prepared with different heating times showed similar peak positions but with varying intensities that could not be modeled using the known structure, even with the addition of preferred orientation corrections. Further investigation of the dehydration reaction (as discussed above) showed that the two phases were in fact very different, but the initial syntheses of $(MoO_2)_2P_2O_7$ often gave a mixed phase product also containing UNK2, even though the dehydration investigations shown in Figures 3.4 and 3.6 seemed to show a single-phased product when heated under the same conditions.

In order to better understand the phase evolution, *in-situ* experiments were carried out to monitor the phase transformation between UNK2 and the known dehydrated compound. As such, samples of the hydrated precursor material were heated to 773 and 793 K, following the heating pattern outlined above, and then held at a final temperature, recording many scans immediately one after each other to follow the reaction at that temperature. The analysis is described in detail in Sections 3.3.2 and 3.3.3 for the data recorded in d8_03342 at a final holding temperature of 793 K; results for the dataset with a holding temperature of 773 K are given for comparison following the explanation of data analysis.

3.3.2 Methodology

Over the course of the dehydration reaction, many different phases are seen, as described in Section 3.3.1. Some of these are known and previously characterised phases and some are new, unknown

phases. In order to extract useful information from the diffraction data it is important to be able to model the different phases using the information that is available about each of them.

For the known, fully characterised phases – $MoO_2{\cdot}H_2O{\cdot}PO_3OH$, MoO_3 and $(MoO_2)_2P_2O_7$ – full Rietveld analysis could be undertaken as the lattice parameters and atomic coordinates are known for each of them and available from the published *.cif* files.[6,9,13]

A pseudo-voigt peak was introduced to model the increasing background intensity arising from the formation of an amorphous compound during the early stages of the reaction. The peak position, intensity and fwhm were allowed to refine during the refinements. The fwhm was restrained to remain broad over the refinements so that it could not refine to fit a sharp Bragg reflection. The total intensity under this peak gives an indication of the ranges and time/temperature intervals during which the amorphous compound is present during the reaction.

Initially when analysis was undertaken nothing was known about the two phases UNK1 and UNK2; neither cell parameters nor any information about cell contents. Hence it was not possible to use either Pawley fitting or Rietveld analysis. The only known information about these phases were the positions, intensities and fwhms of each peak. Knowledge about the increasing and decreasing intensities of the peaks would yield information about the stability of the phases, and provide information for *ex-situ* synthesis or *in-situ* isolation and hence hopefully lead to the discovery of their composition. Two slightly different methods were used to model the peaks using individual peak fitting, these differed in the way the peaks were allowed to refine within the whole pattern fitting process.

The first method used for UNK1 involved introducing a set of peaks with individual, refining peak positions and fwhms with a fixed ratio of intensities and an overall scale parameter. This ensures that only the whole phase can be present – with a positive scale factor – or none of it – with a scale of zero. The peak intensity ratios and positions were freely refined using range 25 of the data file d8_03342 and then varied with an overall scale term for other ranges. For this to work properly small shift limits were applied to each of the peak positions, calculated knowing the shift in each of the peaks within the temperature ranges 470 to 770 K where the phase was present. This method allows quantitative phase analysis without knowledge of the structure provided all peaks belong to the same phase. The intensities for all the peaks within the phase could then be combined and used – alongside the scale parameter – to yield information about the appearance and disappearance of this phase within the dehydration experiment.

A second method was used to yield slightly more information about UNK2. Peaks were parameterised with individual positions, intensities and fwhms, as with the first method. The peak shape was modelled as a convolution of Gaussian and Lorentzian functions. A single overall Lorentzian term was refined; each peak had an individual Gaussian broadening term, such that the fwhm of each peak could be individually refined. A maximum fwhm of 0.2 deg was applied following visual inspection to ensure the peaks remained sharp throughout the analysis. Allowing the individual refinement of each peak's intensity (as opposed to the first - fixed ratio - method) enabled analysis of the occurrence and

disappearance of each peak individually to gain information for comparison with other phases. It also gives information about any extra peaks that were present alongside the known phase when the unknown phase had disappeared. As with the first method, the total intensity of this phase can be calculated by summing the intensity under each peak.

For phases that can be indexed, a Pawley refinement can be carried out using the indexed cell parameters. The total intensity arising from that phase can once again be calculated by summation of the intensity under each individual peak.

To be able to compare the total intensity present due to each phase during a reaction, however that phase is modelled, it is necessary to place each set of intensities on an absolute scale. Calculating the intensity from each phase that is not structurally characterised (modelled either with individual peaks or as a Pawley phase) has already been discussed. For the phases where the structure is known and has been characterised, it is necessary to calculate a relative intensity. In these data analyses this was done as follows. A Pawley refinement was carried out for each known phase in a scan range where that phase was the major phase. The intensity under all the peaks was summed. The value of intensity obtained for each phase from the Pawley fitting was then used as a scaling factor. The relative scale in each of the remaining refinements can be calculated by dividing the refined scale value in subsequent refinements by the value of the scale calculated in this one range. Multiplying the calculated intensity by the relative scale then gives a relative value of intensity for each phase that can be plotted against time, temperature or range number to monitor the progression of the reaction under investigation.

Due to the large number of parameters required to refine all the free variables within these refinements, it was necessary to ensure that values were constrained within appropriate limits. This is best explained by example with the phase specific lattice parameters. An example is given in Figure 3.7. This shows the free refinement of the lattice parameters of $MoO_2{\cdot}H_2O{\cdot}PO_3OH$ over the course of the first 50 ranges. The parameters follow a linear trend during refinement in the first 18 ranges, *i.e.* when the phase is present in the solid mixture. Following decomposition of the phase the parameters vary significantly. Knowing how the parameters refine in the first 18 ranges enabled the estimation of minimum and maximum limits for these parameters.

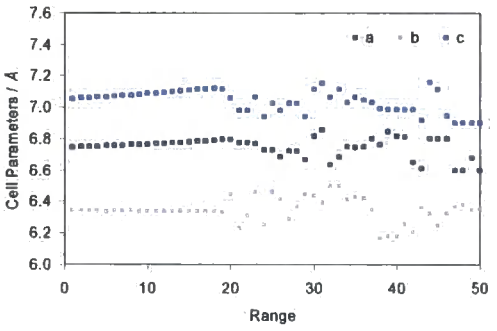

Figure 3.7 Variation in cell parameters of $MoO_2{\cdot}H_2O{\cdot}PO_3OH$ during free refinement. The phase is only present during the first 18 ranges of the dehydration experiment (from visual inspection), and during the first 18 ranges the parameters follow a linear trend. Following the dehydration of the phase the parameters vary significantly.

To avoid false minima the sample height was forced to have a linear dependence on temperature during refinements. This is known to be appropriate to this experimental setup.[14] The height was parameterised as given in the following Topas lines.

```
prm !te
prm !height_gradient -0.0003
prm height_intercept  0.07740`_0.00175 min 0.067 max 0.112
Specimen_Displacement(height,=height_gradient*te+height_intercept;:0)
```

The parameters '`te`', '`height_gradient`' and '`height_intercept`' are the set temperature, the gradient and intercept of the linear height function respectively. The parameter '`te`' is automatically introduced during the sequential refinements using the local FORTRAN routine *multitopas*.[15] The minimum and maximum limits set on the value for the variable '`height_intercept`' were used to ensure some freedom in the refining height parameter. The limits were calculated by comparing the upper and lower limits of the refined height parameter over the ranges recorded at constant temperature.

This methodology has enabled the extraction of useful information about previously unknown phases from diffraction data. The following section outlines the analysis undertaken and the results obtained.

3.3.3 Data analysis using sequential whole pattern fitting

A total of 104 parameters were refined in each of these sequential whole pattern fitting refinements *via* command files written using the local Fortran program Multitopas,[15] over the 2θ range 10-45 ° 2θ. The methods outlined in Section 3.3.2 were employed. One fit from each of the four main sections of the dehydration experiment is given in Figure 3.8.

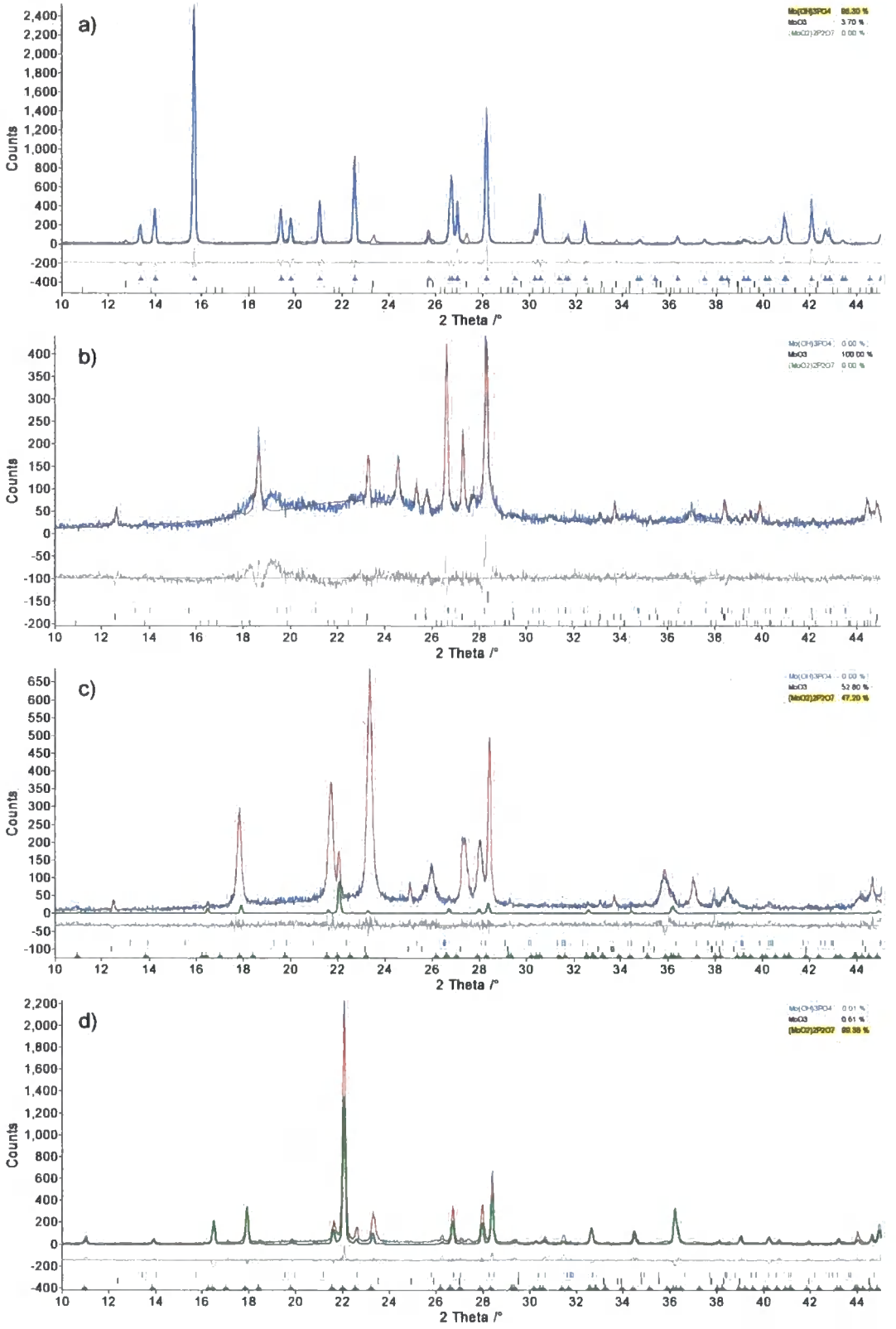

Figure 3.8 Plots of the fit in each of the four main regions of the dehydration reaction, d8_03342. a) Range 1 is $MoO_2{\cdot}H_2O$-PO_3OH and MoO_3, b) range 25 is UNK1 (with large amorphous background), c) range 46 is mainly UNK2, with some $(MoO_2)_2P_2O_7$, d) range 249 is the known phase, $(MoO_2)_2P_2O_7$. R_{wp}s for the ranges (a-d) are 18.43, 19.44, 17.29 and 19.46 %. The main phase in each range is highlighted where possible. The figure shows experimental data in blue, calculated pattern in red and difference plot in grey.

For the three known phases, Rietveld analysis was carried out to obtain phase specific information. For $MoO_2{\cdot}H_2O{\cdot}PO_3OH$, a total of 8 parameters were refined. These included 4 lattice parameters, a scale term and 3 isotropic temperature parameters – one for each atom type within the phase. An 8th order spherical harmonic was also used to model some preferred orientation present in this phase. The terms of this correction were refined for the first range and then fixed for the duration of the experiment as the direction of preferred orientation should not change during the course of the reaction. The impurity, MoO_3, was modelled using 6 parameters. These included 3 lattice parameters, a scale term and 2 isotropic temperature parameters – one for each atom type within the phase. For $(MoO_2)_2P_2O_7$, a total of 7 parameters were refined. These included 3 lattice parameters, a scale term and 3 isotropic temperature parameters – one for each atom type within the phase.

An overall TCHZ peak shape was used for each of these known phases. This was the preferred method over phase-specific peak shapes due to the possibility of peaks becoming very broad over the course of the sequential refinements and thus causing the calculated phase percentages to be incorrect. A Lorentzian size term was added to each phase to allow for some individual peak width differences between the phases. The peak shape was allowed to refine in range 1 for the phases $MoO_2{\cdot}H_2O{\cdot}PO_3OH$ and MoO_3 and then each of the 4 refined parameters u, v, w and y were fixed (*i.e.* used as an empirical instrumental function) for the other ranges. For each known phase in the experiment a size term was allowed to refine between values of 1000 to 10000 nm, ensuring that the phase was only present within the refinement when it refined to a suitable value, *i.e.* during the ranges where the phase was present in the sample mixture. A single parameter was refined to describe axial divergence in each range of the experiment.

For UNK1 and UNK2, the cell parameters were unknown during this initial data analysis, and so the two methods outlined in Section 3.3.2 were applied. UNK1 was modelled using the fixed-ratio method. This phase was parameterised in this data analysis in terms of 13 peaks, and hence 13 positions, 13 fwhms and one scale term were refined for this phase.

UNK2 was modelled using the free-intensity model as it was believed from initial syntheses that there was some similarity between UNK2 and $(MoO_2)_2P_2O_7$. For this reason the 15 peaks found within the scans of the unknown and known phases were parameterised with individual positions, intensities and fwhms, a total of 45 parameters. This method would allow for comparison between the phases. It also would give information about any extra peaks that were present alongside UNK2 when it had disappeared; these may be due to a superstructure of the fully dehydrated phase, $(MoO_2)_2P_2O_7$, the existence of which is proposed in the literature.[9]

The background was described using 5 parameters. Two parameters modelled a linear Chebychev polynomial across the entire 2θ range; the remaining 3 parameters introduced a Pseudo-Voigt peak, used to model the increasing amorphous content during the early stages of the dehydration. The peak position, intensity and fwhm were allowed to refine during the refinements. The fwhm was constrained within the limits 4.5 – 12 °, such that the peak remained broad and could not refine to fit a sharp Bragg reflection.

Initial inspection of the height variation with temperature on free refinement of parameters is given in Figure 3.9a). Scans were recorded every 10 K from 303 to 793 K, ranges 1-49, and then a further 200 scans were recorded at 793 K, ranges 50-249. Figure 3.9 shows that the refined height initially varied erratically over the course of the sequential refinements, and not linearly with temperature as expected.[14]

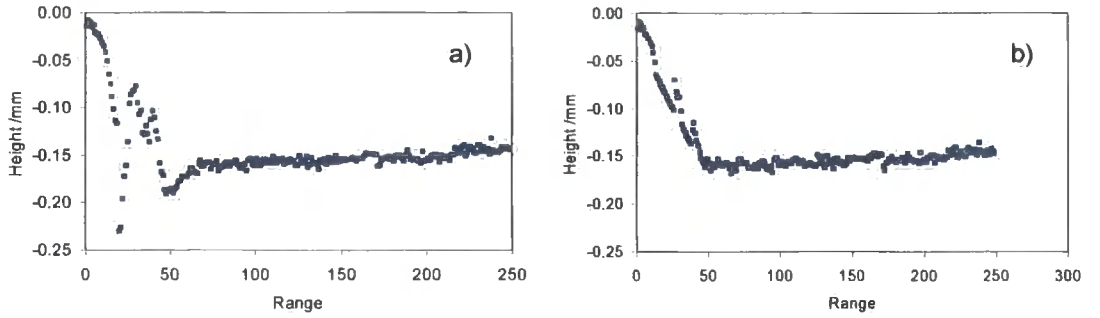

Figure 3.9 The refining height parameter during a) free refinement and (b) following the application of limits. The temperature is constant from range 50 onwards. The widest variation in a) is seen in ranges 15 to 40 where MoO_3 is the only known phase an present in very small concentration; b) the height has a clear temperature dependence where limits have been used to ensure a linear variation with temperature.

Regression analysis was undertaken to obtain the best fit straight line through the values occurring along the line of linear variation with temperature, Figure 3.10. These were taken to be from the first 12 ranges, where the main phases were $MoO_2{\cdot}H_2O{\cdot}PO_3OH$ and MoO_3, and the average height value of the constant temperature scans, where the main phase was $(MoO_2)_2P_2O_7$. The height was then parameterised as described above. The variation in the height parameter with and without limits is shown in Figure 3.9.

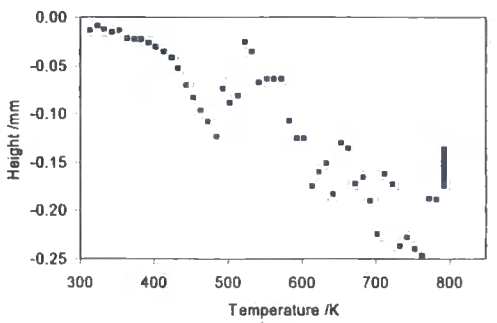

Figure 3.10 Changing height on free refinement (navy blue squares) and regression analysis (purple line) to determine suitable boundaries on the height parameter.

Figure 3.11 shows the calculated R_{wp} for each of the sequential refinements. It can be seen that for most of the 30 minute data collections, an R_{wp} of ~ 18 % was achieved. The increase over ranges 13 to 27 is due to the increased non-linear background that was difficult to model; this was due to the increasing amorphous content within the sample mixture.

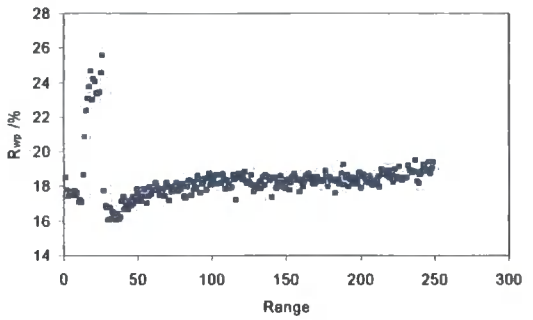

Figure 3.11 The calculated R_{wp}s for each range in the sequential refinements. A value of approximately 18 % was achieved for all the scans, except over the ranges 13 to 27 due to the difficulty modelling the background arising from increased amorphous content within that set of scans.

Of most interest from this data analysis was information about the presence and absence of phases within the dehydration reaction, so that this information could be used for *ex-situ* synthesis and further Rietveld analysis. The graphs in Figure 3.12 show the information obtained from this analysis for each of the known phases. The range numbers where the phases are present are indicated by the positive values of their scale parameters, given in Figure 3.12d). The cell parameters for each phase are seen to vary linearly with increasing temperature within the temperature range where each phase is present.

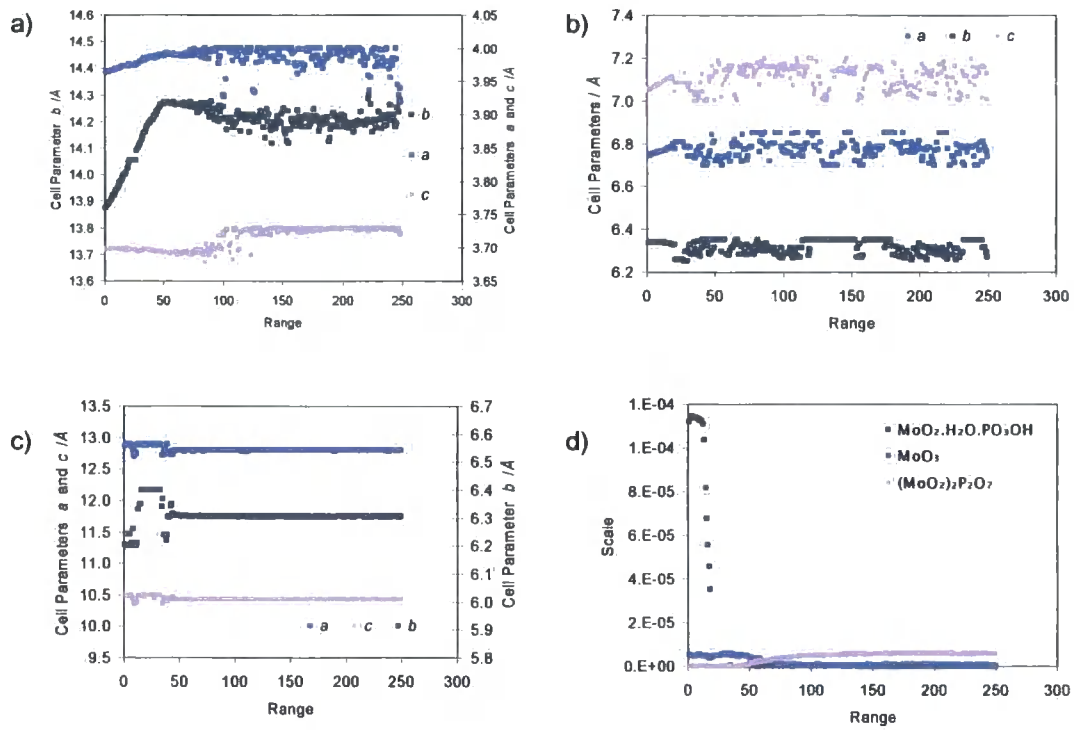

Figure 3.12 The cell parameters from Rietveld refinement of each of the known phases, a) MoO_3, b) $MoO2{\cdot}H_2O{\cdot}PO_3OH$ and c) $(MoO_2)_2P_2O_7$. d) The calculated scale parameter highlights the regions where these phases are present. The lattice parameters are seen to vary linearly with temperature during the ranges where the scale parameter has a non-zero value.

A graph showing the variation in the intensity under the "amorphous" peak and its fwhm is given in Figure 3.13. The intensity increases over the ranges 12 to 55 where the presence of the amorphous content within the scans has been previously noted. The peak is broad over the course of the sequential refinements, remaining in the range 8 to 10 degrees while the peak intensity is large. The intensity returns to a small value outside those range values, and the fwhm remains approximately constant. An example of the fit using this background peak is shown in range 25 in Figure 3.8. The broad peak used gives an indication of the increased background intensity only, and does not perfectly model the background in the ranges 12 to 55; however, a better model is outlined in Section 3.4 where further structural analysis is undertaken for UNK1.

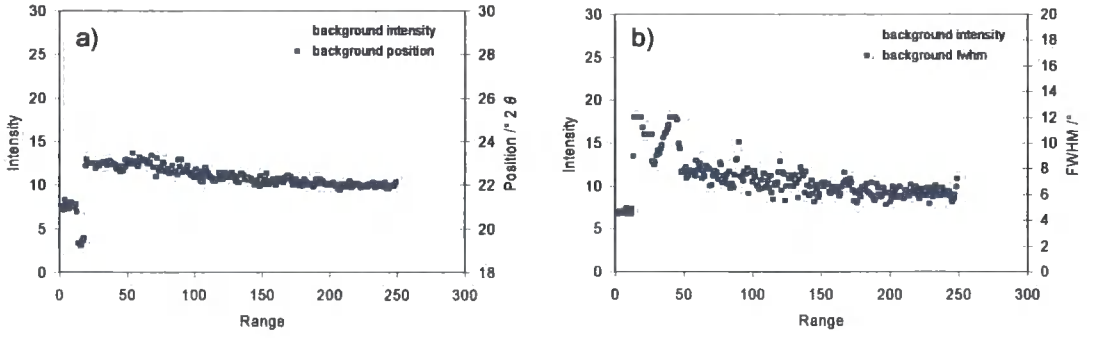

Figure 3.13 Graphs showing intensity, position and fwhm of the peak used to model the amorphous content over the course of the dehydration. The intensity (purple line) is seen to increase during the ranges with high background due to increased amorphous content. a) The position of the peak (blue squares) remains approximately constant throughout the whole dehydration. b) The fwhm of the peak (blue squares) is broad to model the intensity due to the amorphous phase present within the solid mixture.

Summation of the intensity under the peaks for the unknown phases UNK1 and UNK2 has provided information about when these phases are present in the dehydration reaction, Figure 3.14. It is clear that as UNK1 disappears UNK2 forms.

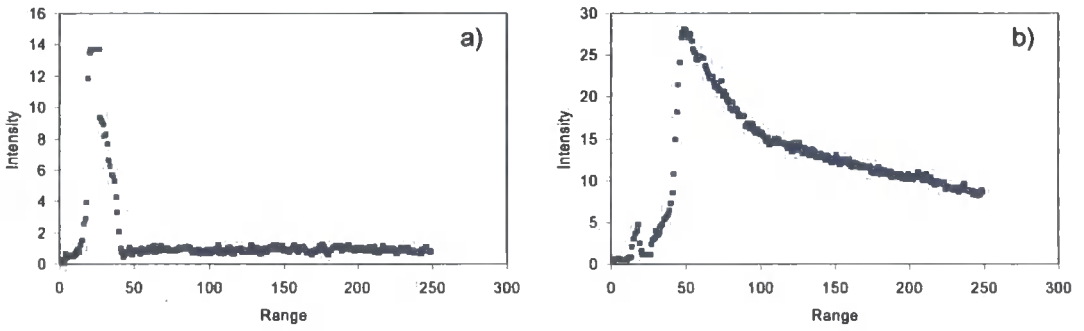

Figure 3.14 Graphs showing the intensity under the modelled peaks for each of the unknown phases, a) UNK1 and b) UNK2. These graphs provide information on the presence and formation/disappearance of the phases over the full range of the dehydration reaction. The small amount of calculated intensity to the left of the main part in the graph for UNK2 is due to an overlap of one of the modelled peaks with the background due to the amorphous content over those ranges.

Plotting the individual intensity of each peak modelled for UNK2 against range reveals that although the majority of the peaks follow the trend shown for that phase in Figure 3.14, three peaks out of the fifteen used to describe that phase follow a different trend, increasing in intensity at a similar rate shown for the known phase, $(MoO_2)_2P_2O_7$, and hence are likely to be from that phase. These peaks are close in 2θ to the positions of peaks from the known phase. This suggests that these three anomalous peaks may be simply "mopping up" minor errors in the Rietveld fit caused, for example, by preferred orientation.

To give an indication of the stable range/temperature regions of each of the known phases, and hence allow further synthesis – both *in-situ* and *ex-situ* – a graph showing phase intensities against range and temperature was needed. Pawley refinements were carried out for each of the known phases in the range of maximum intensity for each phase, *i.e.* range 1 for $MoO_2{\cdot}H_2O{\cdot}PO_3OH$ and MoO_3, and in range 249 for $(MoO_2)_2P_2O_7$.

The intensity under the phase's peaks could then be summed to give a total intensity for that phase in that range. Intensity versus range information was calculated using the scale parameter determined for each phase during the sequential Rietveld refinements. For UNK1 and UNK2 the intensity information can be taken directly from that plotted in Figure 3.14. The graph showing the total intensity of each of the known and unknown phases against range is given in Figure 3.15a).

The information given in Figure 3.15a was described qualitatively from visual inspection at the beginning of this section, but has now been quantified from whole pattern fitting to confirm the phase presence with time and range and temperature throughout the reaction. Clearly the starting hydrate decomposes and both a minor crystalline phase (UNK1) and an amorphous phase are formed, then UNK2 begins to form and just as it reaches its maximum intensity the known dehydrated phase increases in intensity. At the end of the 249th scan UNK2 has nearly all disappeared and the known dehydrated phase is almost present at constant scale, indicating no new formation of that material.

There is a slight dip seen in the intensity beyond the 220th range. No change is seen in UNK2 at this point. It is unknown what gives rise to this phenomenon.

Analysis was also undertaken on a similar set of data recorded with the same heating regime, but with a final temperature of 773 K. These data were used to gain more information about the transition between UNK2 and $(MoO_2)_2P_2O_7$. The data in this collection, d8_03337, were analysed using exactly the same procedure as described in this section for d8_03342. The final graph showing the intensity of each phase versus range is given in Figure 3.15b). Due to the reduced final temperature, it is clear from visual inspection that the rate at which UNK2 is converting to the known phase is slower. Only one hundred scans were recorded at 773 K (due to time constraints), unlike the 200 recorded in the experiment at 793 K. Hence the final scan is not at the end of the conversion process. It is still clear from these data that the transformation is slower at this reduced temperature, as would be expected.

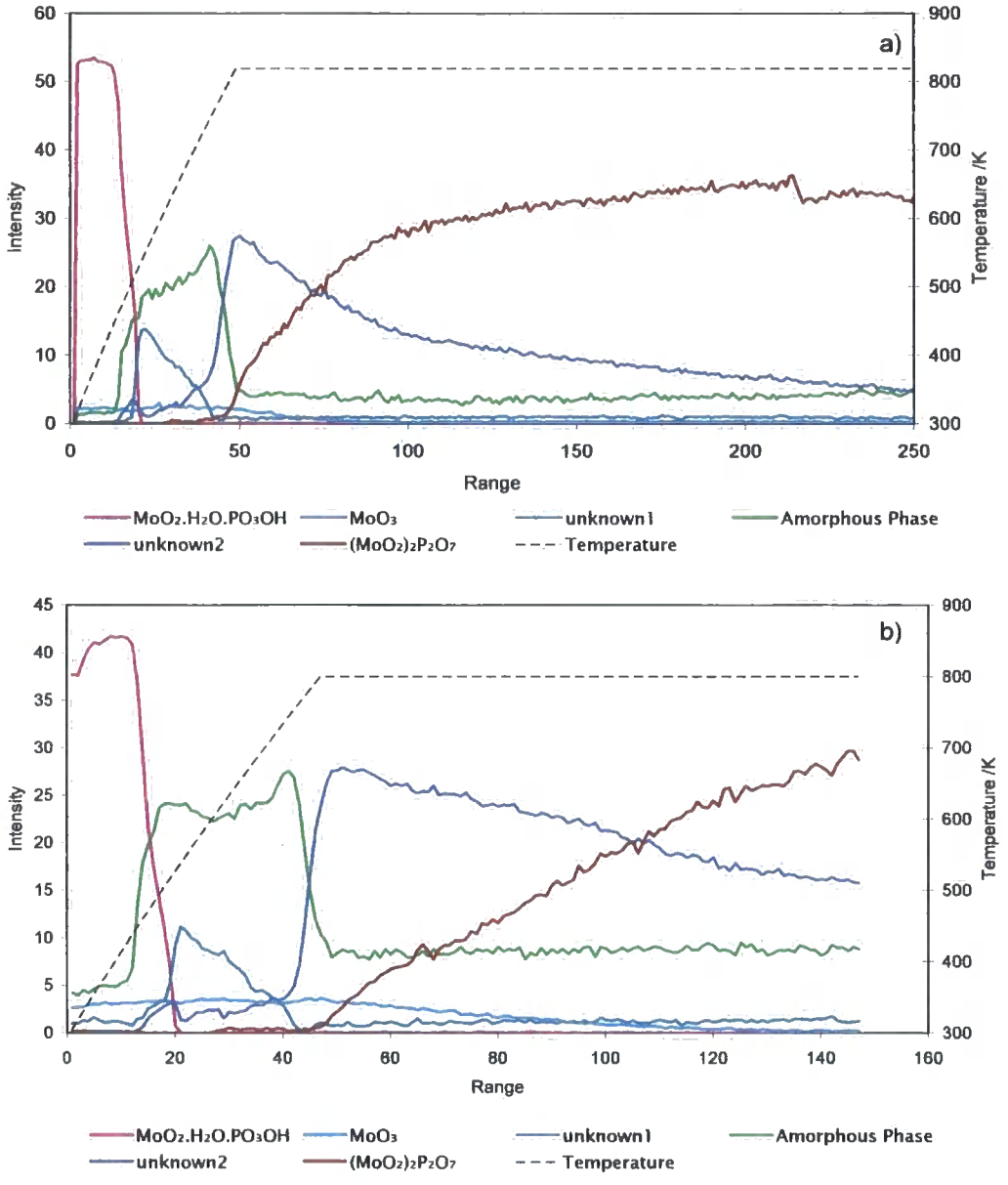

Figure 3.15 Progression of the dehydration from the starting hydrate, $MoO_2{\cdot}H_2O{\cdot}PO_3OH$ (with MoO_3 impurity), to UNK1 and an amorphous phase, through to UNK2 and finally forming $(MoO_2)_2P_2O_7$. a) Scans were recorded for 30 minutes every 10 K from 313 to 793 K (ranges 1-49) and then 200 constant scans were recorded while the temperature was held at 793 K (ranges 50-249) to monitor the formation of the known phase, d8_03342. b) Scans were recorded for 30 minutes every 10 K from 313 to 773 K (ranges 1-47) and then 100 constant scans were recorded while the temperature was held at 773 K (ranges 48-147) to watch the formation of the known phase, d8_03337.

This experiment also allows one to determine an optimal procedure for isolating UNK2. By heating to 773 K and rapidly cooling back to room temperature it should be possible to prepare an essentially phase pure sample of this material, Section 3.5.1.

The initial input files in each of the sequential analyses and the spreadsheets containing further analysis of the information output from the refinements are given in the E-Appendix.

3.3.4 Results from infrared spectroscopy

Infrared spectra were recorded on each of the phases formed during the dehydration of $MoO_2{\cdot}H_2O{\cdot}PO_3OH$. Samples of each material were synthesised following the synthetic methods given in this chapter. 13 mm pellets were prepared from 0.4 g dried KBr and 2 % (by mass) of each sample. The pellets were stored in a desiccator under vacuum before use. Spectra were recorded on a Perkin-Elmer Spectrum 100 FTIR instrument. A spectrum of a KBr pellet (prepared and recorded at the same time) was subtracted from each scan as background calibration. The IR spectra for each of the samples are given in the following figures.

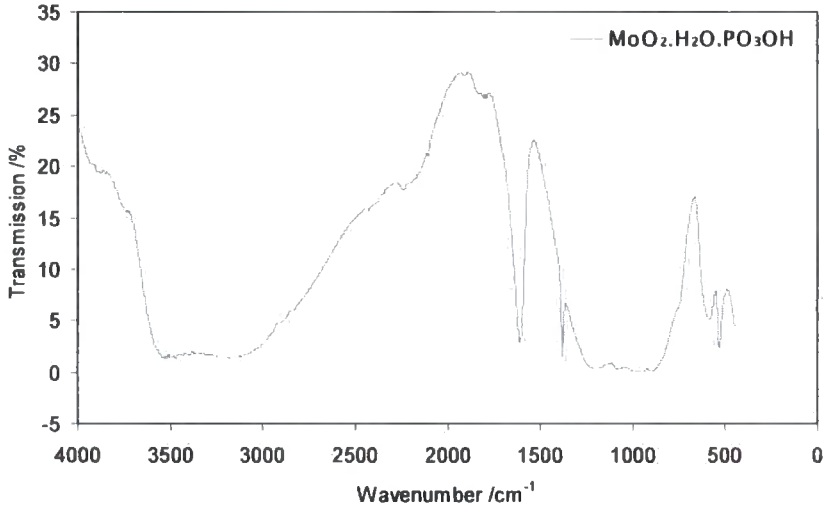

Figure 3.16 IR spectrum for sample SEL320, $MoO_2{\cdot}H_2O{\cdot}PO_3OH$. Peak maxima were at 3533, 1610 and 1383 cm^{-1}.

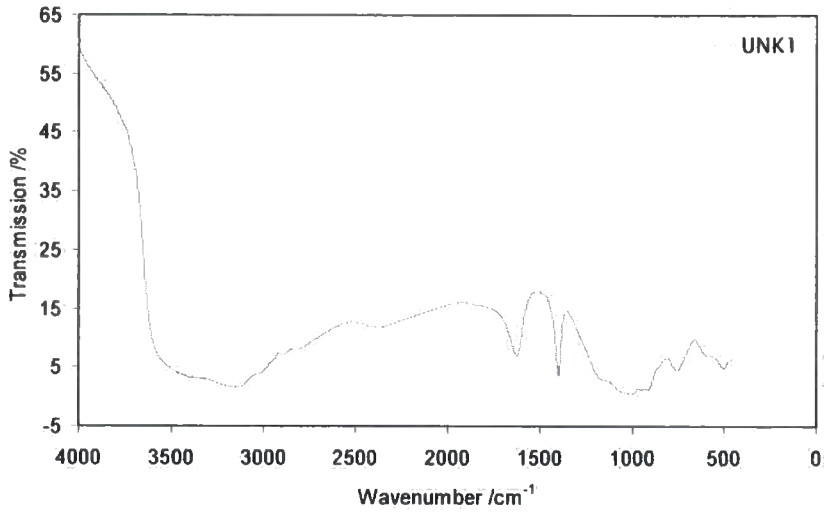

Figure 3.17 IR spectrum for sample SEL323, UNK1. Peak maxima were at 3159, 1621 and 1399 cm^{-1}.

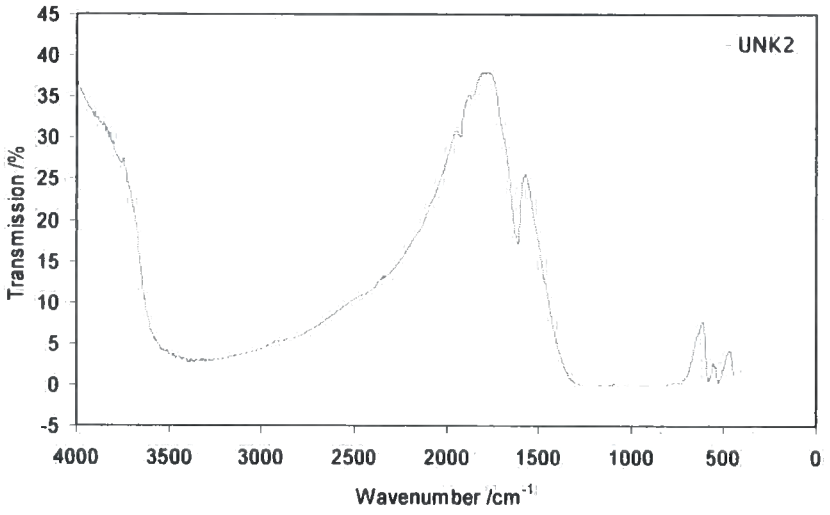

Figure 3.18 IR spectrum for sample SEL321, UNK2. Peak maxima were at 3396 and 1619 cm^{-1}.

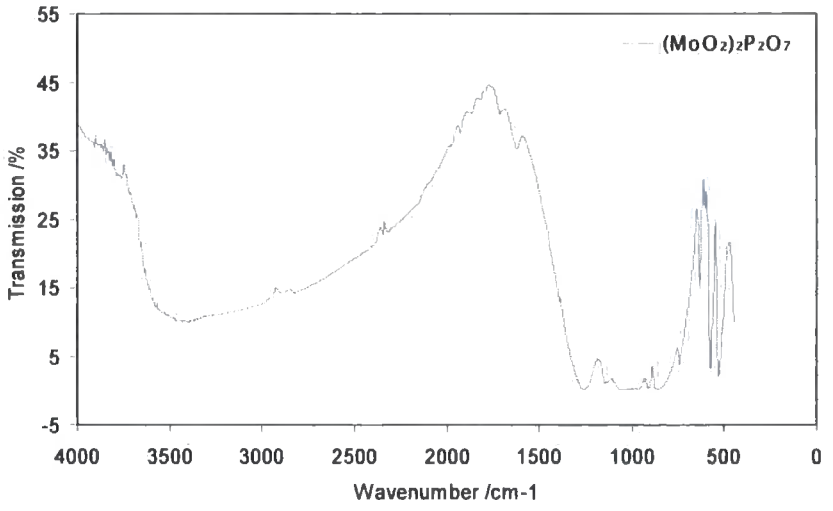

Figure 3.19 IR spectrum for sample SEL322, $(MoO_2)_2P_2O_7$. Peak maxima were at 3423 and 1623 cm^{-1}.

IR frequencies found in similar phosphate materials found in the literature are listed in Table 3.2. These data have provided additional information about the composition of the two unknown phases discovered during the dehydration reaction.

Table 3.2 IR frequencies arising within phosphate containing materials.

Wavenumber /cm^{-1}	Peak	Assignment
3300	Broad	O-H stretch[16]
1640	Sharp	O-H bend[16]
~1400	Sharp	P-OH deformation[17]

It is noted that the four materials gave rise to poor quality IR spectra, despite care taken to prepare dry pellets and remove any background contribution that may arise from the KBr absorbing water during the preparation process. Nevertheless, each spectrum does contain features that can be assigned to their compositions. Each spectrum contains a broad band centred approximately in the region 3500-3150 cm^{-1}; this arises primarily due to O-H stretches. In the final phase, $(MoO_2)_2P_2O_7$, there are no OH groups present (this has been confirmed by TGA analysis), and it must be concluded that the broad stretch is due to surface absorbed water. The sharp peak at ~1600 cm^{-1} in each spectrum has been assigned to an O-H bend, but this could also be due to absorbed water in the pellet. The final feature in both $MoO_2{\cdot}H_2O{\cdot}PO_3OH$ and UNK1 has been assigned by Corbridge and Lowe[17] to be a P-OH deformation. This latter assignment leads to the conclusion that these latter two materials contain P-OH moieties, whereas UNK2 and $(MoO_2)_2P_2O_7$ do not, their O-H stretches and bends arising due to absorbed water. These assignments were essential as extra chemical information during the structure solution process for the two unknown materials.

3.3.5 Results from thermal analysis techniques

Chemical information about the dehydration process was also obtained from the thermal techniques, Thermogravimetric Analysis (TGA) and Differential Scanning Calorimetry (DSC); both of these methods are outlined in Section 2.4.5.

The TGA trace is shown in Figure 3.20. It is clear from the trace that the material loses mass from room temperature up to approximately 800 K, above which temperature the material is stable with respect to mass loss. The initial mass loss between 300 and 400 K was believed to be due to absorbed water in the sample, as the TGA trace plateaus after this point; all of the absorbed water was removed by 400 K. Our material does not follow a two-step dehydration in this trace as indicated by some authors in the literature.[1,7] The total mass loss from the structure (excluding the absorbed water) is 11.7 %. The predicted mass loss for complete dehydration (Equation 3.2) is 11.2 %.

$$2\ MoO_2{\cdot}H_2O{\cdot}PO_3OH \rightarrow (MoO_2)_2P_2O_7 + 3\ H_2O \qquad (3.2)$$

The excess 0.5 % not predicted could be due to either excess absorbed water or due to minor MoO_3 impurities. The latter is known to volatilise above 873 K.

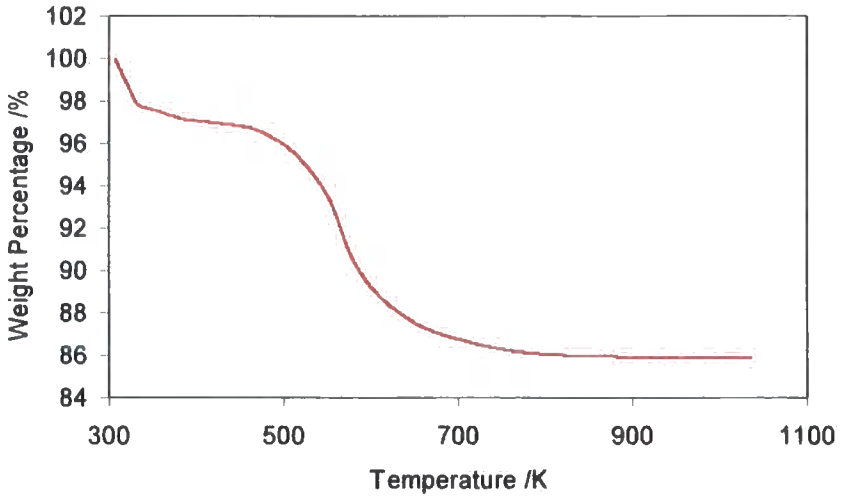

Figure 3.20 The TGA trace recorded on 13.4 mg $MoO_2{\cdot}H_2O{\cdot}PO_3OH$, SEL320. The material was heated at 10 K/min from 300 to 1073 K.

In order to better understand the changes occurring with respect to temperature on dehydration, the TGA trace was differentiated, this is given in Figure 3.21. There are three regions of change within this graph. The first, below 400 K, is due to the loss of absorbed water in the material. From visual inspection and whole pattern refinements in Section 3.3, the progression of phases through the dehydration reaction was discovered. In Figures 3.15a) and Figures 3.15b), the dehydration process proceeds directly from one phase to the next on increasing temperature. However, this simple picture does not account for the fact that the dehydration reaction is not instantaneous. This is seen most notably in the formation of UNK1 as the phase is poorly crystalline and there is a large amorphous

background present within the scans, implying that the precursor phase does not simply lose all of its water content to form UNK1, but that the process may be gradual. These observations aid our understanding of Figure 3.21. The material loses water molecules between 400 K and 700 K. The material UNK1 begins to form above 423 K and then transforms to UNK2 above 700 K. Thus the material UNK2 was believed to be free of H_2O and OH moieties, having an empirical formula identical to that of the final phase, $(MoO_2)_2P_2O_7$. This is in agreement with the IR data.

Due to the lack of a distinct two-step dehydration process, it was not possible to directly gain information about the composition of UNK1 from the TGA data. However, the IR data support the material containing P-OH groups. Further data were required about this phase to fully identify it.

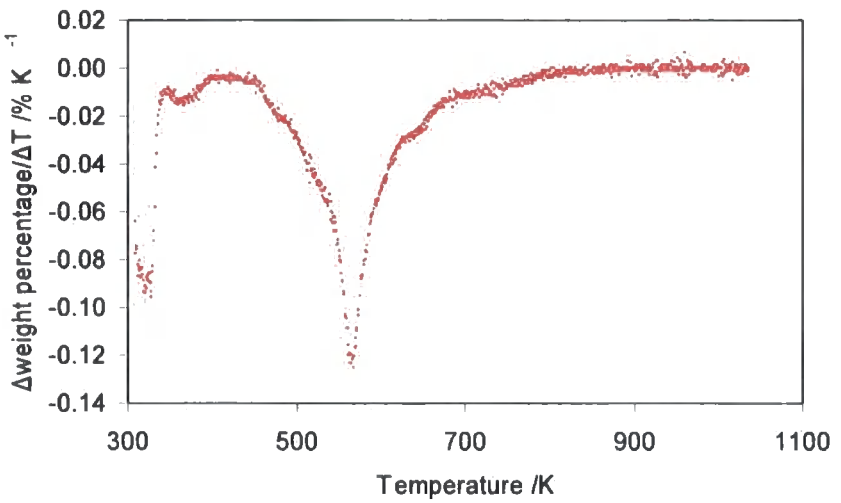

Figure 3.21 The differentiation of the TGA trace recorded $MoO_2{\cdot}H_2O{\cdot}PO_3OH$, SEL320. Data were rebinned after every 5th data point □approximately every 0.8 K.

The DSC trace, also recorded on SEL320, is shown in Figure 3.22. The graph shows two very clear thermal events with maxima at 336 and 556 K. These have been assigned to the loss of absorbed water and the loss of the structural water from the precursor to the UNK2 phase. A small event is seen at 640 K; however, no evidence is seen for this in either the TGA or diffraction data.

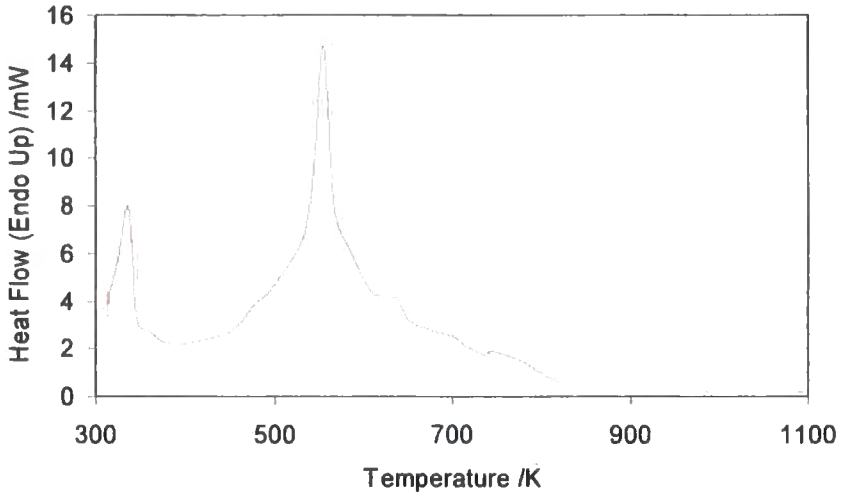

Figure 3.22 The DSC trace recorded on $MoO_2{\cdot}H_2O{\cdot}PO_3OH$, SEL320. The sample was heated at 10 K/min from room temperature to 823 K.

3.4 Structure determination of β-$MoOPO_4$, UNK1

3.4.1 Synthesis

UNK1 was found to exist during the temperature ranges 483 to 713 K on heating (collecting 30 minute scans every 10 K, d8_03342). The phase was initially isolated *in-situ* by repeating the dehydration reaction up to the 25th scan and then cooling back to room temperature, d8_03324. Twenty 30 minute scans were recorded to check the stability of the phase on standing for ten hours at room temperature. This experiment showed that the phase could be quenched back to room temperature and that it did not decompose on standing or form other phases on cooling. A 12 hour scan, d8_03357, was recorded (Figure 3.23) and the phase did not decompose during this time period. The large background, seen during the temperature ranges 483 to 713 K over the course of the whole dehydration process in d8_03342, was again present.

Direct synthesis conditions for UNK1 were initially investigated *in-situ*. A sample of the hydrated precursor was heated to 523 K at 2 K/min and continuous 30 minute scans were recorded to watch for ideal time and temperature conditions to isolate the phase *ex-situ*. It was seen that only the desired phase formed over these conditions, and no decomposition was seen over 16 hours (d8_03379). Using known temperature calibration offsets of the HTK furnace,[18] a sample of UNK1 (SEL233) was synthesised by heating 0.479 g $MoO_2{\cdot}H_2O{\cdot}PO_3OH$ (1.98 mmol, SEL214) in an alumina crucible at 5 K/min to 553 K, and holding at that temperature for 60 minutes. The yield was 0.4359 g. The sample was cooled *in-situ* to room temperature and the crucible contained a pale blue powder. The identity of this material was confirmed by comparison with previously recorded scans of this phase; a small quantity of MoO_3 was also present alongside the final product phase.

It was predicted from the IR data in Section 3.3.4, that UNK1 contained only P-OH groups and no H_2O molecules. This is equivalent to the loss of one mole of water, or a mass loss of 7.4 %, from the precursor phase, $MoO_2{\cdot}H_2O{\cdot}PO_3OH$. The percentage mass loss during this synthesis was 9.0 %.

It is noted that on preparation of this phase from the hydrated precursor without any MoO_3 impurity, the phase is less crystalline, and only 3 main peaks can typically be discerned above the background noise, particularly with the large amorphous content present in the XRD pattern. These peaks have *d*-spacings at 1.57, 3.14 and 4.28 Å; the first two are clearly from a related set of *hkl* reflections.

3.4.2 Indexing and structure solution

To aid the indexing and structure solution process, an XRD pattern of UNK1 was recorded in capillary mode on the d6. This ensured that preferred orientation was minimised. The data collection parameters are listed in Table 3.3. Peak fitting for UNK1 was performed in TOPAS Academic;[19] the MoO_3 impurity was modelled as a Rietveld phase. Nineteen peaks were assigned to UNK1 and modelled using a PV peak shape. The best cell obtained during this process was a monoclinic cell with cell parameters:

a = 7.4077 Å b = 7.2128 Å c = 7.2805 Å β = 61.651 ° FOM 20.0

The indexing software suggested a C-centred cell; this was confirmed by the presence of the reflection condition (*hkl*) $h+k$ = 2n. A search was undertaken in the ICSD[20] to discover whether a known cell of this size existed with a possible related structure. Searching against the indexed cell revealed a similar cell for ε-$VOPO_4$[21] having lattice parameters:

a = 7.2659(3) Å b = 6.8934(2) Å c = 7.2651(3) Å β = 115.3396(13) °

The structure of this phase had been solved in space group *Cc*. A Pawley fit using the indexed cell parameters in this space group was carried out to check the ability of this cell to account for all the peaks assigned to UNK1, Figure 3.23. 192 parameters were used to model the phases in this refinement. This included 17 general parameters (15 coefficients of a Chebychev polynomial to model the background, 1 parameter to model axial divergence and 1 parameter to model the zero error), 10 parameters for the impurity phase MoO_3 (3 lattice parameters, 2 isotropic displacement parameters, a scale parameter and 4 peak shape parameters) and 165 parameters to model the Pawley phase UNK1 (4 lattice parameters, 4 peakshape parameters and 157 refining peak intensities). The final R_{wp} value for this refinement was 2.99 %. The input file for this refinement is included in the E-appendix.

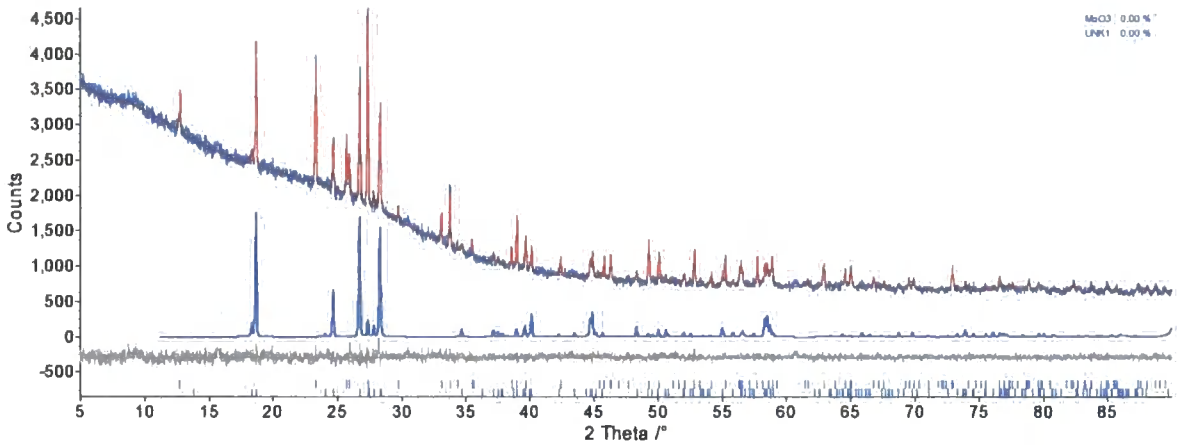

Figure 3.23 Pawley fit in space group *Cc*, d6_00480, R_{wp} 2.99 %. The figure shows the experimental data in blue, the calculated pattern in red and the difference plot in grey; the Pawley fit of UNK1 is shown highlighted in blue. The positions of the predicted peaks are given by the tic marks at the bottom of the figure.

The atomic coordinates of $VOPO_4$ were taken as starting coordinates for structure solution, with the V (N.B. formally V^{5+}) replaced by a Mo ion. The structure was initially refined using bond distance and angle restraints. The Mo-O distances were restrained to be 1.9 *Å* ± 0.3. The PO_4 tetrahedron was refined to be a regular polyhedron with P-O distances of 1.5 *Å*. The P atom is found on a general position in ε-$VOPO_4$ and so free rotation and translation of the PO_4 group was permitted. Once the polyhedra had found stable positions *via* simulated annealing, individual atomic coordinates were refined. For this final refinement, a total of 64 parameters were refined. This included 23 general parameters (21 coefficients of a Chebychev polynomial to model the background, 1 parameter to model axial divergence and 1 parameter to model the zero error), 10 parameters for the impurity phase MoO_3 (3 lattice parameters, 2 isotropic displacement parameters, a scale parameter and 4 peak shape parameters) and 31 parameters to model the Rietveld phase β-$MoOPO_4$ (4 lattice parameters, a scale term, 4 peakshape parameters, 3 isotropic displacement parameters and 19 atomic coordinates).[f] The final refinement is shown in Figure 3.24, R_{wp} 3.12 %. Selected refinement details are given in Table 3.3, fractional coordinates are given in Table 3.4 and bond lengths are given in Table 3.6. The input file for this structure solution is included in the E-appendix.

[f] The nomenclature for the phase β-$MoOPO_4$ was chosen to distinguish it from the known phase α-$MoOPO_4$.

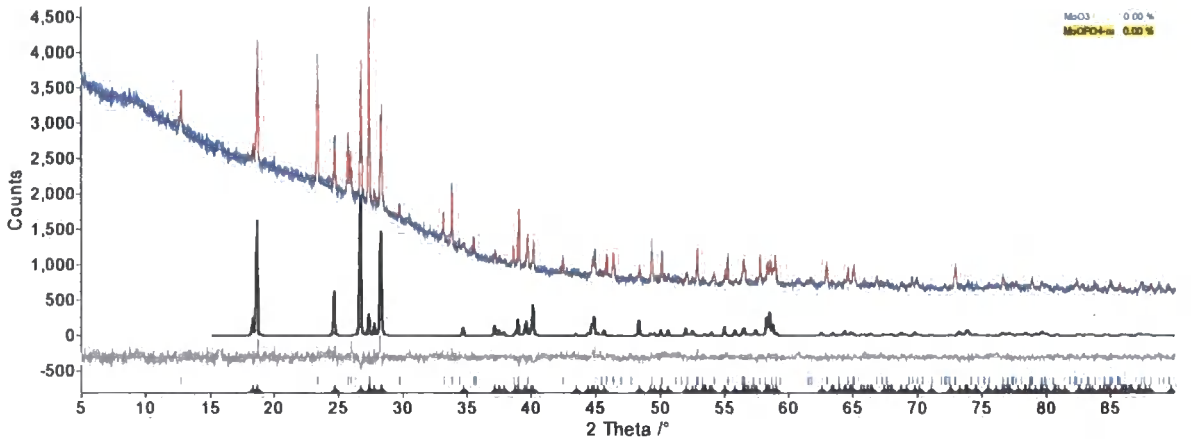

Figure 3.24 Final Rietveld refinement for the structure solution of β-$MoOPO_4$, UNK1; d6_00480, R_{wp} 3.12 %. The figure shows the experimental data in blue, the calculated pattern in red and the difference plot in grey.

Table 3.3 Selected refined values, crystallographic and data collection parameters for d6_00480.

Space Group	*Cc*	2θ range /°	10-90
a /Å	7.4050(6)	2θ step size /°	0.017
b /Å	7.2085(4)	Time per step /s	8.5
c /Å	7.2880(5)	R_{wp} /%	3.12
β /°	118.35(3)	R_{Bragg} /%	2.1
Volume /$Å^3$	342.35(4)	GOF	1.16
Number of parameters	64		

Table 3.4 Fractional coordinates for β-$MoOPO_4$, UNK1.

Atom Label	Atom Type	x	y	z	Occ	B_{iso} /$Å^2$
Mo1	Mo	0.5	0.2546(37)	0.5	1	6.26(34)
P1	P	0.2132(65)	0.5978(25)	0.2091(75)	1	1.00(59)
O1	O	0.728(14)	0.3326(42)	0.723(13)	1	1.00(58)
O2	O	0.058(12)	0.4979(97)	0.043(17)	1	1.00(58)
O3	O	0.430(11)	0.522(11)	0.423(13)	1	1.00(58)
O4	O	0.0932(67)	0.7547(87)	0.2965(68)	1	1.00(58)
O5	O	0.2773(82)	0.8000(66)	0.1527(88)	1	1.00(58)

3.4.3 Comparison of the structure of β-$MoOPO_4$, UNK1 with known materials

The crystal chemistry of the $XOPO_4$ series of materials is complex. Many structural types are known to exist. To enable comparison of structure types more easily, a list of common materials of each type

is given, alongside its space group and lattice parameters in Table 3.5. The structures and phase transitions are described in more detail below.

Table 3.5 Overview of the structure types of $XOPO_4$ materials, their space groups and cell parameters. Standard uncertainties are quoted where present in the original papers.

Structure Type	Space Group	Cell Parameters (*abc* /Å, β/°)
α-$NbOPO_4$[22]	*P4/n* → *P4/nmm*	*a*=6.3873(10) *c*=4.1037(8)
β-$NbOPO_4$[23]	$P2_1/c$ → *Pnma*	*a*=13.097 *b*=5.280 *c*=13.228 β=120.334
α_I-$VOPO_4$[24]	*P4/n*	*a*=6.20 *c*=4.11
α_{II}-$VOPO_4$[25]	*P4/n*	*a*=6.014(7) *c*=4.434(2)
β-$VOPO_4$[26]	*Pnma*	*a*=7.770(3) *b*=6.143(3) *c*=6.965(3)
ε-$VOPO_4$[27]	$P2_1/n$	*a*=7.265 Å *b*=6.877 Å *c*=7.260 Å β=115.35 °
ε-$VOPO_4$[21]	*Cc*	*a*=7.2659(3) Å *b*=6.8934(2) Å *c*=7.2651(3) Å β=115.3396(13) °

For the phosphates of Nb and Ta, two types are known, but the chemistry within each group of materials exhibits a rich number of modifications and phase transitions between phases.[28,29] Both structural types are composed of chains of corner sharing XO_6 octahedra that are linked together by PO_4 tetrahedra to form 3D structures. The first type of these materials the α-form is a tetragonal phase built up of chains of XO_6 octahedra joined together by trans linkages along the *c*-axis.[22,30] The 3D structure of the material is completed by PO_4 tetrahedra corner sharing with four different chains within the material. The structure of this phase was originally proposed from single crystal data for $NbOPO_4$ by Kierkegaard and Longo[22] and independently by Kaiser *et al.*,[30] in space group *P4/n*. Later work by Sleight and co-workers discovered a second-order phase transition, occurring at 473 K, above which the low temperature *P4/n* structure becomes dynamically disordered, and the symmetry of the material increases.[31] The high temperature form of this material is in space group *P4/nmm*. Below the phase transition all lattice parameters exhibit positive thermal expansion; above the phase transition the *a* and *b* cell parameters show negative thermal expansion. This has been described as occurring due to the rocking motion of the corner shared polyhedra within the structure.

The β-form of the material consists of XO_6 octahedra joined together through cis linkages, forming zigzag chains through the 3D structure.[23] The material was first characterised at room temperature in the monoclinic space group $P2_1/c$. A first order phase transition was discovered at 565 K between the low temperature monoclinic form and the high temperature orthorhombic form of $NbOPO_4$.[32] The unit cell volume halves following this phase transition and the high temperature orthorhombic cell can be described as a subcell of the monoclinic superstructure. The thermal expansion of this material was studied from room temperature up to 973 K by both X-ray and neutron diffraction techniques. NTE is shown by the *a* cell parameter over the entire range studied; above the phase transition NTE is seen in all three cell parameters. Quenching of the high temperature orthorhombic phase below the phase transition was not possible in this study, although it was described as being possible due to the first

order nature of the transition. However, the transition is displacive, not reconstructive, and thus unlikely to have a high energy barrier to transformation. The isolation by Serra *et al.* of the orthorhombic phase at room temperature[33] is believed to be due to impurities of non-stoichiometry.

A phase transition from β-$TaOPO_4$ to α-$TaOPO_4$ has been discovered by heating the compound to temperatures between 773 and 1773 K under pressures of 25-60 kbar.[29]

When X=Mo, only the alpha phase of the material was previously known, being isostructural with α-$NbOPO_4$.[34] However, the MoO_6 octahedra are distorted in the direction of the chains; there are four bonds of 1.974(23) Å, a short bond at 1.663(26) Å and a long bond at 2.630(26) Å. The structure can be described in terms of 5 coordinate polyhedra along the chain direction or corner sharing octahedra with alternating short and long Mo-O bonds. This is consistent with the characteristic variation in bond lengths normally seen for materials containing Mo(V).[35] Both the α- and β- forms of $WOPO_4$ have been synthesised.[36] The tetragonal α-form was synthesised by heating a sample of the monoclinic β-form at 1173 K and 6 GPa. The assignment of the structures of the two W containing materials as the α- and β- forms isostructural to related materials was on the basis of the comparison between the powder diffraction patterns and cell indexing. The materials were not fully structurally characterised, but a later investigation by IR supported these conclusions.[37]

The chemistry of the related vanadium phases are of interest due to their use as catalysts and lithium battery materials. The α-/β- nomenclature for these phases is not equivalent to the Ta/Nb phases described above (except for the two α- forms). There are many known polymorphs of $VOPO_4$; some are known to have only slight differences between them. For example, in the α_I- and α_{II}-$VOPO_4$ phases,[24,25] both materials consist of parallel chains of VO_6 octahedra linked together by PO_4 tetrahedra. By considering the atomic positions of the corner-sharing oxygen atoms and the P as unchanged between the two structures, the structural differences between the two phases arise from the relative positions of the V ion: in the α_I-phase the vanadium atom is on the same side of the chain as the phosphorus and on the opposite side in the α_{II}-phase.[25] This latter phase is isostructural with the alpha type tetragonal phases discussed above. This material – as well as $MoOPO_4$ – can be thought of as a pseudo-layered structure due to the presence of one very long X-O bond along the chain direction. Tachez *et al.* note in their discussion of the polymorphism of these phases that the formation of either phase is dependent on the preparation method.[25] In the case of the α_{II}-phase (and hence the tetragonal Mo, Nb and Ta analogues discussed above), the synthesis is carried out at high temperature; conversely, in the case of the α_I-phase, the material is formed by low-temperature dehydration of a hydrated precursor.

ε-$VOPO_4$ was first synthesised by heating a sample of $V^{III}PO_4.H_2O$ under a flow of oxygen at a maximum temperature of 823 K. by Lim *et al.*.[27] They indexed the powder pattern to a C-centred monoclinic cell with lattice parameters:

a = 7.265 Å b = 6.877 Å c = 7.260 Å β = 115.35 ° [no esds given]

It is noted that this cell can be transformed to an A-centred orthorhombic cell, where this cell is half the volume of the cell known for the material β-$VOPO_4$. Increasing the synthesis temperature led to the formation of the latter compound, but the two phases – β- and ε-$VOPO_4$ – had distinct powder patterns. The structure of the new ε-phase was solved in space group $P2_1/n$, however no results were published about the structure in this paper, although it was suggested that the material had a structure that was intermediate between the hydrate and the β-phase. A later paper compared the structure obtained in space group $P2_1/n$ with a structure obtained in space group Cc.[21] Both structures are composed of chains of trans- corner sharing VO_6 octahedra parallel to [101], with the characteristic long-short-long alternation of V-O bonds along the chain direction, due to the formation of short vanadyl bonds in this direction. The chains are joined together by PO_4 tetrahedra such that the VO_6 octahedra tilt away from the chain direction by forming two V-O-P bonds with the same regular tetrahedron. The remaining two P-O bonds are linked to two other chains. In the *Cc* model the O-V=O bonds in parallel chains all point in the same direction, however, in the $P2_1/n$ model the O-V=O chains lie antiparallel in adjacent chains. Girgsdies *et al.* claim that the *Cc* model is less distorted on free refinement of atoms. Both the β- and ε-$VOPO_4$ structures are different to the α-/β- Nb/Ta phases.

Selected bond lengths from the refinement of the new phase β-$MoOPO_4$ are given in Table 3.6. It can be seen that the bond distances calculated for the Mo-O bonds within this compound do not follow the characteristic variation in bond lengths normally seen in Mo^V compounds, and the octahedra are distorted along the chain. These surprising bond lengths required further investigation, Section 3.4.4.

Table 3.6 Selected bond distances and BVS for Mo and P in β-$MoOPO_4$. It is noted that the data quality is poor, leading to very unreliable Mo-O bond lengths.

Mo-O1 (1) /Å	1.789(72)	P-O2 /Å	1.409(82)
Mo-O2 /Å	1.862(75)	P-O5 /Å	1.645(64)
Mo-O4 /Å	1.910(60)	P-O3 /Å	1.712(75)
Mo-O3 /Å	2.005(82)	P-O4 /Å	1.736(78)
Mo-O1 (2) /Å	2.160(66)	Mo BVS /vu	4.66[38]
Mo-O5 /Å	2.420(75)	P BVS /vu	4.04[39]

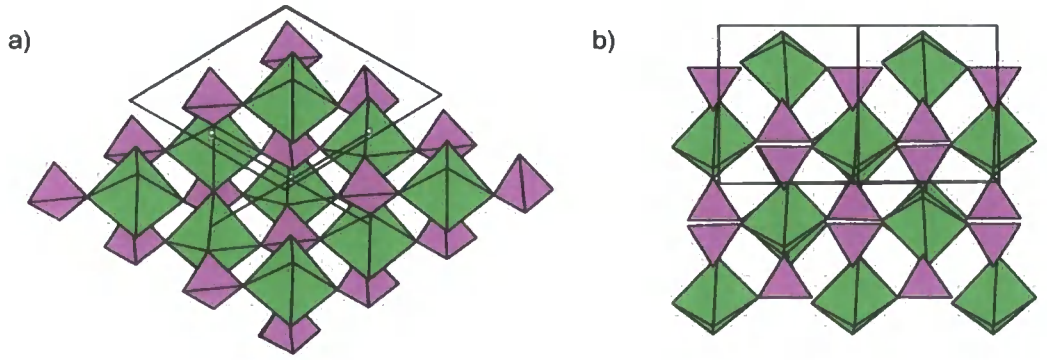

Figure 3.25 The structure of β-$MoOPO_4$. a) Chains of MoO_6 octahedra along [101], top to bottom in this picture. b) View down [101] showing chains of MoO_6 linked together by PO_4 tetrahedra.

3.4.4 Further investigation into the structure of "UNK1"

Despite the reasonable fit of this model to the XRD data, there are some inconsistencies. The IR and TGA results from Sections 3.3.4 and 3.3.5 point to the structure containing P-OH groups. The refined bond lengths are unusual. Finally the oxidation state of the Mo atom is +5 wheras SQUID data implied that the material was diamagnetic, *i.e.* that the material contained Mo in the +6, d^0 oxidation state.

These pieces of evidence suggest $MoO_2.PO_3OH$, as previously predicted by Schulz and Gopalakrishnan, as a more likely composition.[1,7] This formula would require breaking of an Mo-O-P linkage and the formation of both an Mo=O and a P-OH bond, thus introducing an extra O atom into the structure. An alternative possibility is the presence of Mo vacancies, perhaps accompanied locally by OH groups, $Mo_{1-x}O(PO_{4-y}(OH_y))$. It is, however, possible that the OH peak observed in the IR data is associated with the significant amorphous component present.

From the good fit of β-$MoOPO_4$ to the X-ray data, it's likely that the heavy metal positions are at least approximately correct. In fact deletion of the P atoms from the refinement does not change the appearance of the calculated pattern greatly, showing the data are relatively insensitive to the P positions due to the low crystallinity of the phase and the poor XRD data obtainable. For ease of construction of a new model, the *Cc* unit cell was transformed to a related A-centred orthorhombic cell (lattice parameters *a* 12.62 Å, *b* 7.21 Å and *c* 7.54 Å, having twice the volume), and the symmetry was reduced to *P*1. This structure was used as a starting point from which to build a new model. By consideration of the dehydration pathway, detailed in Section 3.7, an Mo-O-P linkage was broken and the MoO_6 octahedral chains were straightened to allow the introduction of a P-OH group into the structure.

By consideration of both the precursor and final structures and the H-bonding present in the precursor, two models were proposed. One model (1) contained the P tetrahedra within the layers in the structure, and the second model (2) contained the tetrahedra inverted from that position, to enable H-bonding with the molybdenyl bond of the MoO_6 octahedron in an adjacent layer. On inspection the space group of both these new structures was *Pm*11. The polyhedra in the structures were idealised so that it could investigated for potential higher symmetry and unit cells in Cerius2.[40] This software

predicted a smaller orthorhombic cell; however, on Pawley fitting of this cell, it was discovered that this smaller unit cell does not predict all of the reflections observed. The two potential UNK1 structures (1 and 2) are shown in this smaller cell for structural visualisation purposes only, Figures 3.26 and 3.27. The *cif* files for these approximate models are given in the E-Appendix.

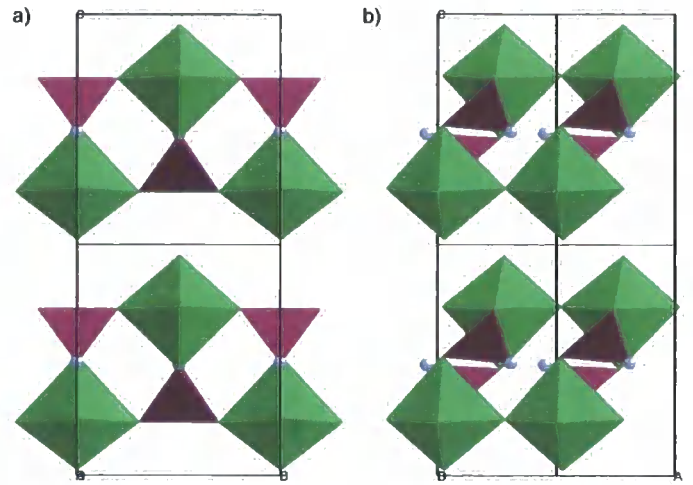

Figure 3.26 Possible structure of $MoO_2.PO_3OH$ (1). View a) down [100], b) down [010]. The PO_4 groups in this model are contained within the layers, *c.f.* Figure 3.27. The P-OH group is indicated by a grey sphere.

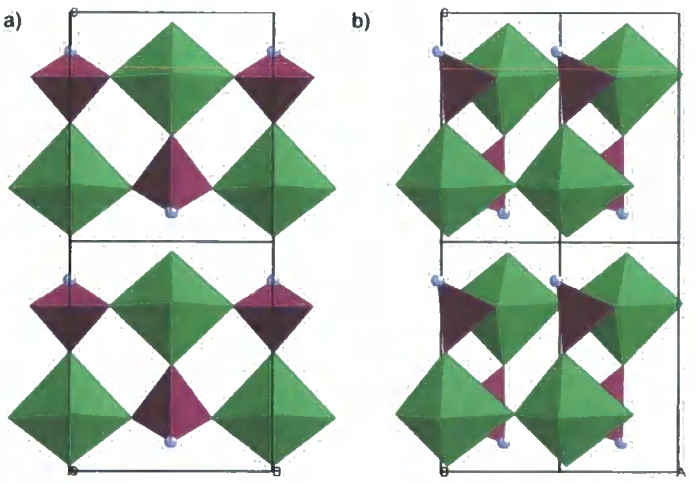

Figure 3.27 A possible structure of $MoO_2.PO_3OH$ (2). View a) down [100], b) down [010]. The PO_4 groups in this model are directed out of the layers, *c.f.* Figure 3.26. The P-OH group is indicated by a grey sphere.

The atomic coordinates of this proposed model were used to simulate the diffraction pattern for the phase against the capillary data, d6_00480. A total of 41 parameters were refined. This included 23 general parameters (21 coefficients of a Chebychev polynomial to model the background, 1 parameter to model axial divergence and 1 parameter to model the zero error), 10 parameters for the impurity phase MoO_3 (3 lattice parameters, 2 isotropic displacement parameters, a scale parameter and 4 peak

shape parameters) and 8 parameters to model the $MoO_2.PO_3OH$ phase (4 lattice parameters, a scale term and 3 isotropic displacement parameters; the peakshape was fixed to be the same as the MoO_3 phase). The final refinement is shown in Figure 3.28, R_{wp} 3.66 %.

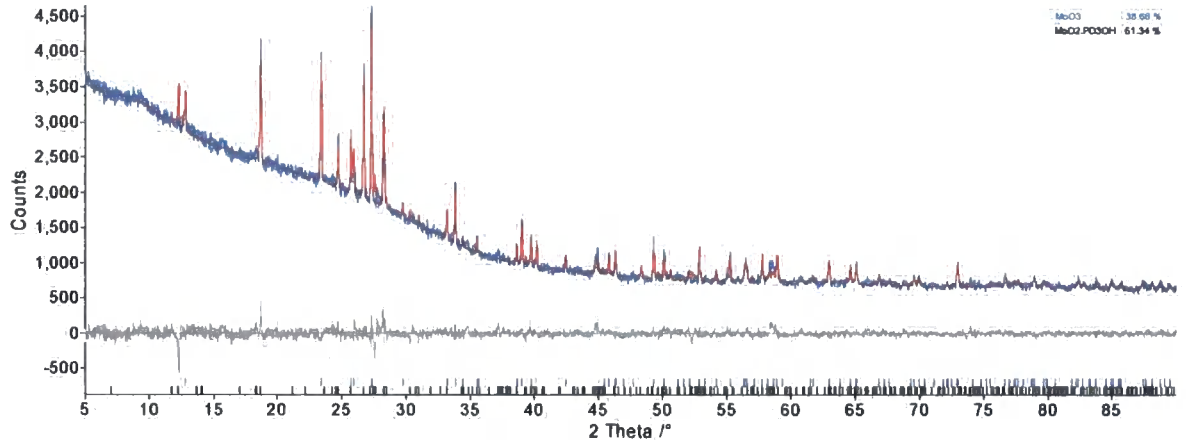

Figure 3.28 Comparison of the calculated pattern for the structural model of $MoO_2.PO_3OH$ with the experimental data, d6_00480; R_{wp} 3.66 %. The figure shows experimental data in blue, calculated pattern in red and difference plot in grey.

It has not been possible to refine the atomic positions in this model due to time constraints. Further refinement would involve the use of rigid bodies as the data quality is not sufficient to be able to freely refine the coordinates of the individual atoms. These models are included here as possible structures of UNK1 only. Further discussion of the dehydration mechanism is given in Section 3.7. That these various models give a reasonable fit to the X-ray data confirms that determination of P/O positions is very hard. Further neutron data would be required though a definitive answer would still be hard to achieve. We will therefore use the $MoO_2.PO_3OH$ model which is consistent with IR and magnetic data in further discussion of the transformation chemistry of this phase.

3.5 Identity and structure determination of β-$(MoO_2)_2P_2O_7$, UNK2

3.5.1 Isolation and synthesis

UNK2 was found to exist during the temperature ranges 703 to 793 K on heating (collecting 30 minute scans every 10 K). Figures 3.15a) and 3.15b) both show that UNK2 is the main phase during range number 46 and so phase isolation was carried out *in-situ* by repeating the previous dehydration reaction up to the 46th range and then cooling back to room temperature, d8_03371. This experiment confirmed that the phase could be isolated back at room temperature. A 12 hour scan was then recorded, d8_03372, and used to index the phase. This *in-situ* synthesis was performed on a sample that was made using a hydrothermally prepared sample of $MoO_2{\cdot}H_2O{\cdot}PO_3OH$, *i.e.* one that contained some MoO_3 impurity.

The synthesis of a bulk sample of this material was required to enable further characterisation by ^{31}P NMR and FTIR methods. Direct synthesis conditions for UNK2 were initially investigated *in-situ*. A sample of the hydrated precursor was heated straight to 753 K at 2 K/min and continuous 30 minute

scans were recorded to watch for ideal time and temperature conditions to isolate the phase *ex-situ*. However, it was noted that following the direct heat to temperature, UNK2 formed alongside α-$(MoO_2)_2P_2O_7$, and there was no time period at this temperature (following the direct 2 K/min heating) when only UNK2 was present. These conditions were repeated using final temperatures of 733 and 713 K, and at both of these reduced temperatures α-$(MoO_2)_2P_2O_7$ again formed alongside UNK2. Control over the heating rate is therefore crucial for isolation of phase pure UNK2. *Ex-situ* synthesis was therefore carried out using an overall heating rate that was equivalent to the time spent approaching 763 K in the ramp/scan/ramp *in-situ* experiments as follows: 0.2049 g of $MoO_2{\cdot}H_2O{\cdot}PO_3OH$ (0.85 mmol, SEL225) was heated in an alumina crucible to 793 K at a rate of 0.33 K/min. Once the sample had reached 793 K it was held at temperature for 0.1 hours and then cooled *in-situ*. The synthesis produced a very pale blue powder; the yield was 0.17 g. This final mass equated to an overall mass loss of 17 %. The total loss of water from the structure is equal to a mass loss of 11.2 %. The excess mass loss is again believed to be due to absorbed water by the sample.

3.5.2 Indexing

Peak fitting was performed in TOPAS Academic.[19] Twenty five peaks were assigned to UNK2 and modelled with a position, intensity and refining TCHZ peak shape. These peaks were used for indexing as described in Section 2.2.4. The MoO_3 impurity was modelled as a Rietveld phase. The best solution from indexing gave a cell with the following lattice parameters:

a = 16.2437 Å b = 3.8913 Å c = 6.2840 Å $\alpha=\beta=\gamma$= 90 ° FOM 8.42

A Pawley fit was undertaken using these cell parameters in the lowest symmetry orthorhombic space group, *P*222, Figure 3.29.[41] Altogether 293 parameters were refined. These included 23 global parameters, (21 coefficients of a Chebychev polynomial to model the background, a sample height parameter and one parameter to model axial divergence), 24 parameters to model the MoO_3 phase (3 lattice parameters, 2 isotropic displacement parameters □ one for each atom type, 4 parameters used to define the TCHZ peak shape, a scale parameter and 14 coefficients of an 8th order spherical harmonic used to model preferred orientation), and 239 terms to model UNK2. These were 3 lattice parameters, 4 parameters used to define the TCHZ peak shape and 232 intensities for the predicted reflections.

Comparing the peakshape of the highlighted UNK2 Pawley phase with those of the MoO_3 impurity, it is clear that the former phase is much broader and different peaks have different widths, with the *00l* reflections being sharpest. To model this anisotropic strain broadening a further 7 parameters were used. These were 5 parameters to model a 4th order spherical harmonic correction (sh2), a Lorentzian strain broadening term and a strain broadening scale term. The anisotropic strain broadening was modelled as given in the following Topas lines.

```
Str ai n_L( @  0. 11785)
pr m scal e_sh2   0. 99933   l or_f whm = ( scal e_sh2)  ( sh2)  Tan( Th) ;
```

The fwhms of each peak in the Pawley fit (dependent on tan θ) were scaled to the coefficients of the spherical harmonic, sh2. The final Rietveld refinement is given in Figure 3.30, the R_{wp} was 3.17 % and all the peaks within the XRD pattern were accounted for. The input file for this refinement is included in the E-appendix.

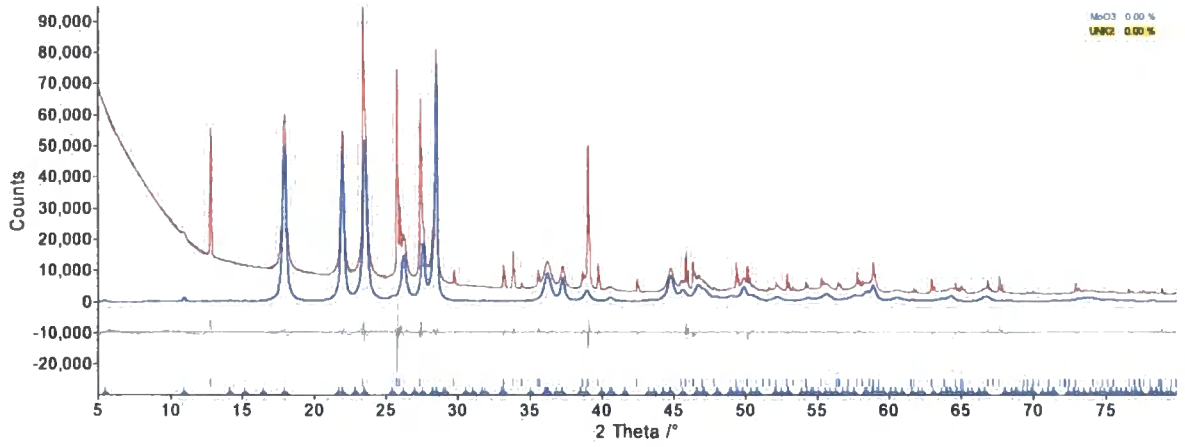

Figure 3.29 Pawley fitting of a sample of UNK2, SEL237 in space group *P*222 (with some MoO_3 modelled as a Rietveld phase) in d9_02380. The R_{wp} for this fit was 3.17 %. The figure shows experimental data in blue, calculated pattern in red and difference plot in grey.

3.5.3 Initial space group determination

To determine the space group the list of *hkl* and intensity information obtained from the Pawley fit in TOPAS were used to determine systematic absences. The reflections that were present were: (*hkl*) *h*+*k* = 2n, (*0kl*) *k* = 2n, (*h0l*) *h* = 2n, (*hk0*) *h*+*k* = 2n, (*h00*) *h* = 2n, (*0k0*) *k* = 2n, and (*00l*) *l* = 2n. These reflection conditions arise from space group $C222_1$. However, to check this assignment, the calculated list of *hkl*s and intensities were inspected by the program ExtSym.[42] This program seeks to quantify the likelihood of an extinction symbol using Bayesian probability theory. The most likely extinction symbols returned by the program were $C\text{--}2_1$ *and* $Cc\text{--}$. The former symbol is in agreement with the assignment made from inspection of the systematic absences. The latter symbol varies from the first by the extra reflection condition (*0kl*) *l* = *2n*, and leads to the possible space groups $Ccm2_1$, *Ccmm* and *Cc2m*.

In order to check the assignment of this space group, the input file from a Pawley fit was performed in space group $C222_1$. Altogether 174 parameters were refined; this reduction in parameters occurs as the $C222_1$ phase predicts only 113 intensities compared to 232 for *P*222. The final R_{wp} for this fit was 3.27 %, similar to that using *P*222 despite using 119 fewer parameters. The input file for this refinement is included in the E-appendix.

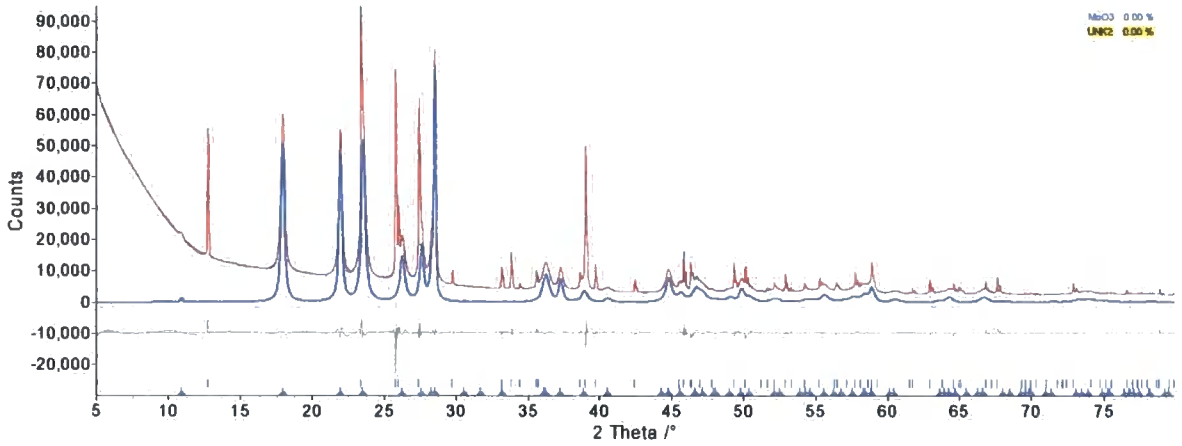

Figure 3.30 Pawley fitting of SEL237, a sample of UNK2 in space group $C222_1$ (with some MoO_3 modelled as a Rietveld phase) in d9_02380, R_{wp} 3.27 %. The figure shows experimental data in blue, calculated pattern in red and difference plot in grey.

3.5.4 Second harmonic generation and unit cell contents

A sample of UNK2 was sent to Prof. P. Shiv Halasyamani at the University of Houston to undergo Second Harmonic Generation (SHG) testing, Section 2.4.3. The SHG test returned a negative result, that is, no SHG was detected. Although this is a non-definite result, it was presumed (in a first instance) that this negative test implied that the material had a centrosymmetric lattice type. Space group $C222_1$ is not centrosymmetric. One of the maximal non-isomorphic supergroups of $C222_1$ is centrosymmetric, space group *Cmcm*. Of the space groups with extinction symbol *Cc*–, only space group *Ccmm* is centrosymmetric, related to *Cmcm* by switching of the axes. This space group was taken as a starting point for real space annealing of the structure.

From IR and TGA measurements, the structure of UNK2 was known to not contain any H_2O or OH moieties. The material was also found to rehydrate to the fully hydrated precursor, $MoO_2{\cdot}H_2O{\cdot}PO_3OH$, within a couple of weeks. This finding suggests that UNK2, hereon designated β-$(MoO_2)_2P_2O_7$ to distintuish it from the known, α- phase, is the phase Schulz found to be the unstable form of $(MoO_2)_2P_2O_7$.[1] Further confidence in this conclusion was found by noting that the unit cell volume for UNK2 (~396 $Å^3$) was approximately half that for α-$(MoO_2)_2P_2O_7$ (827 $Å^3$). As such the total unit cell contents for the unknown material were believed to be $Mo_4P_4O_{22}$.

3.5.5 Structure solution and true space group determination

To facilitate structure solution, data were collected on both beamline ID31 at the ESRF and on HRPD at ISIS to give increased intensity and resolution data. Due to the metastable nature of the material, it was not possible to obtain the data on exactly the same sample; however, care was taken to ensure that the synthesis of each sample was the same.

Diffraction patterns were recorded on ID31, as outlined in Table 3.7. In order to obtain better statistics at lower *d*-spacings, four scans were recorded over two different 2θ ranges, and then normalised and summed together. The first set of scans was recorded over the 2θ range 0-35, and the second set of

scans was recorded between 10-35 ° 2θ. Diffraction patterns were recorded on HRPD at ISIS, as outlined in Table 3.8. A 15 mm cylindrical can was filled to a depth of 30 mm and loaded onto the candlestick for ambient temperature neutron diffraction.

Table 3.7 Data Collection parameters for data recorded at ambient temperature on a sample of UNK2, SEL317, at station ID31, ch2627_sel317_295K.xye.

Data Collection Parameters	Values
λ / Å	0.35285(8)
Maximum 2θ Range /°	0-35
Total Length of Scans /min	120
Temperature /K	295
Number of scans	8
Data Bin Size /°	0.004

Table 3.8 Data collection parameters for data recorded at ambient temperature on a sample of UNK2, SEL321, at HRPD, ISIS, HRP39707.xye.

Data Collection Parameters	Values
TOF range /μs	30-130
Sample Environment	Candlestick
Temperature /K	300
Data recorded /μAh	116.96

In order to begin solving the structure of UNK2, initial files were prepared to allow simulated annealing of the heavy metal positions within the unit cells in space group *Ccmm*. Annealing experiments were carried out using a variety of cell contents with Mo/P, 2Mo/P, Mo/2P and 2Mo/2P atoms to allow atoms to adopt Wyckoff sites of different multiplicity. After 1000 iterations with different cell contents no solution refined to give a model which satisfied the unit cell contents, *i.e.* no atoms refined to special positions from these partial models. It was also very hard to see how it would be possible to position the MoO_6 or PO_4 polyhedra within the size and symmetry requirements of the unit cell.

During the ExtSym investigation above, the third space group (in order of probability) was *Pcan*. This space group allows pseudo C-centering due to the 4c special position having the extra reflection condition (*hkl*) *h+k* = 2n. Simulated annealing was attempted in this space group. Atoms refined to special positions and so fulfilled the required cell contents Mo_4P_4. Rigid MoO_6 and PO_4 were introduced using fixed central positions and refining tilt angles. Following 1000 simulated annealing iterations the arrangement of the polyhedra with the lowest R_{wp} was chemically sensible, having a corner sharing polyhedral structure as predicted for the structure. Oxygen atoms that had refined to the same position on the corner-sharing positions were merged. Whilst appearing plausible this structure had two problems. Firstly intensity was predicted for absent *001* and *003* reflections.

Secondly P atoms were in trigonal pyramidal PO_5 coordination though with an elongated P displacement parameter. Inspection of the model showed, however, that a related model could be built in $C222_1$, which contained octahedral MoO_6 and P_2O_7 groups disordered over two sites. This structure is shown in Figure 3.31.

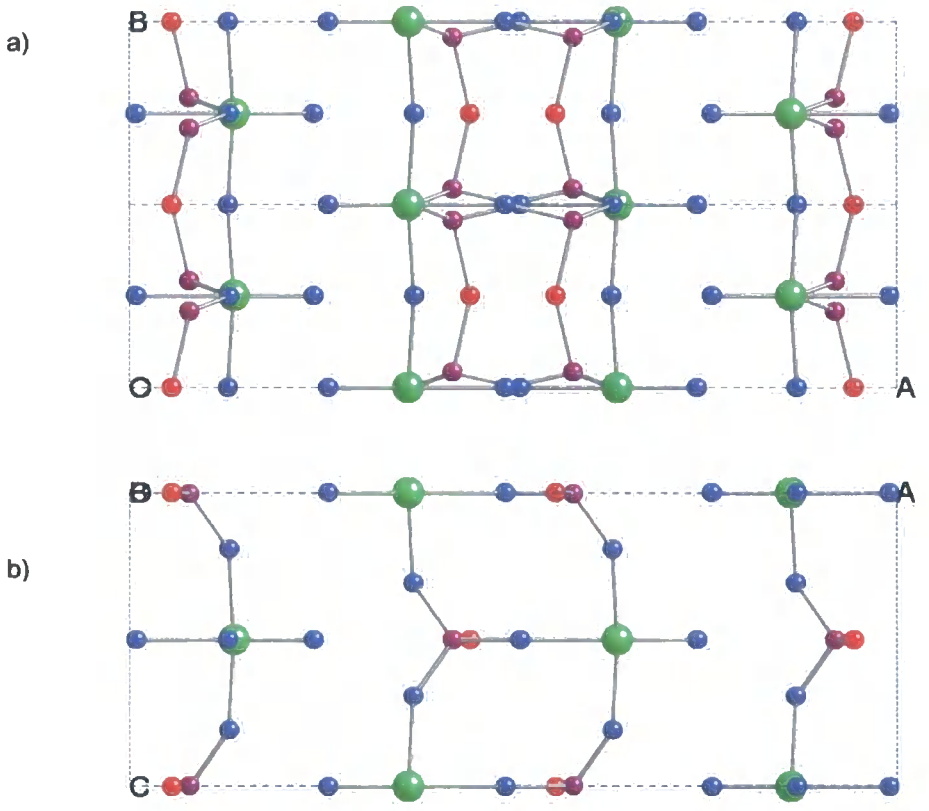

Figure 3.31 The structure of β-$(MoO_2)_2P_2O_7$. Mo atoms are shown in green, P atoms in purple, terminal O_t atoms in blue and bridging O_b atoms in red. Two unit cells along *b* are shown. a) View of β-$(MoO_2)_2P_2O_7$ down [001]. The layers between the chains and the double chains present in the layers are displayed. b) The MoO_6 chains are along [010]; the P_2O_7 groups link these chains together.

The structure is layered along [100] and is made up of MoO_6 and PO_4 units. The layers are shifted relative to each other by a translation of [½, ½, 0]. Each layer is composed of MoO_6 chains along [010] linked by the disordered P_2O_7 groups. A short molybdenyl (Mo=O) bond is directed into the layer, 2 Mo-O bonds form Mo-O-Mo chains, while the remaining 3 Mo-O bonds link to P tetrahedra above, below and perpendicular to the chain direction, such that a double chain forms. Two PO_4 tetrahedra share a corner (O_b) to form a P_2O_7 unit. The remaining 6 vertices are corner shared with the MoO_6 chains. The purple P atom and the red bridging O atom have an occupancy of 0.5 such that adjacent P_2O_7 units aren't simultaneously present. This is discussed below.

This structural model was refined simultaneously against both the synchrotron and neutron data, Figure 3.32. A total of 107 parameters were refined. These included 35 overall parameters for both the synchrotron and neutron refinements (3 cell parameters, 11 refining coordinates, 7 isotropic

displacement parameters and 14 coefficients of an 8th order spherical harmonic to model the *hkl* dependent peakshape required to accurately model the phase). The remaining parameters described each of the individual datasets; these were 21 for neutron TOF backscattering (3 x-axis calibration terms, 12 background coefficients of a Chebychev polynomial, a scale term, 3 peakshape parameters, an absorption correction and a scaling term for the *hkl* dependent peakshape), 22 parameters for the TOF 90 deg bank data (as for the backscattering bank with an additional parameter to model the overall difference in the isotropic displacement parameters), and 29 parameters to model the synchrotron data (18 background coefficients of a Chebychev polynomial, a scale term, 6 peakshape parameters, 1 parameter to model axial divergence, a zero correction, a scaling term for the *hkl* dependent peakshape and 1 parameter to model the overall difference in the isotropic thermal displacement parameters). Selected refinement details are given in Table 3.9; the refinements are shown in Figure 3.32. The lowest overall R_{wp} found for these refinements was 4.24 %. Fractional atomic coordinates are given in Table 3.10. Bond lengths and bond valence sums are given in Table 3.11.

Table 3.9 Selected refined values, crystallographic and data collection parameters for the combined synchrotron and neutron refinement.

Space Group	$C222_1$	R_{wp} /%	4.246
a /Å	16.2247(13)	X-ray R_{Bragg} /%	2.143
b /Å	3.8951(3)	Neutron R_{Bragg} /%	2.663
c /Å	6.2785(5)	GOF	1.16
Volume /Å^3	396.78(5)	Number of parameters	107

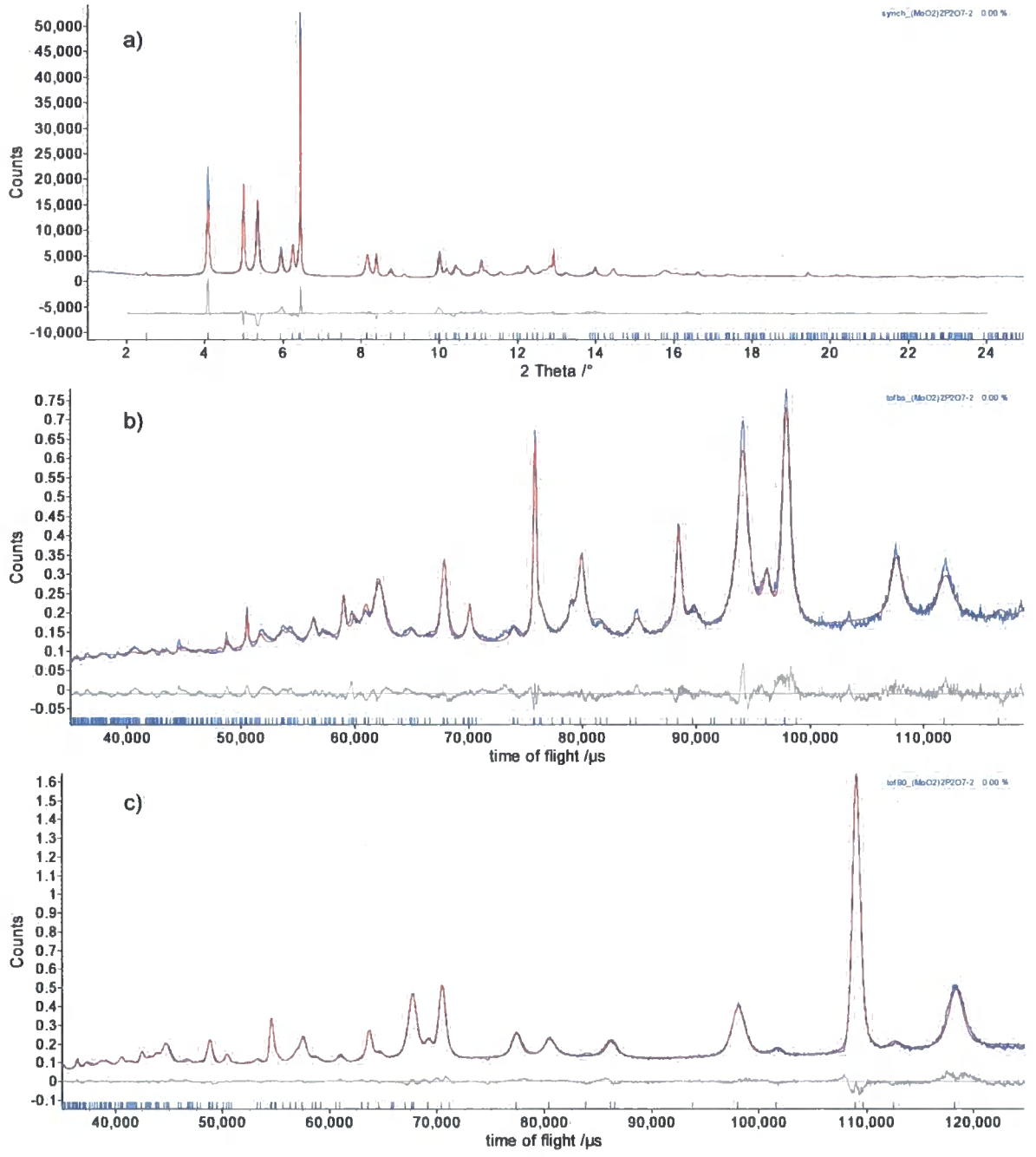

Figure 3.32 Rietveld fits of the structure solution of UNK2, β-$(MoO_2)_2P_2O_7$, against a) ID31 data, b) TOF-backscattering data and c) TOF-90° bank data. The final overall R_{wp} for these refinements was 4.24 %. Individual R_{wp}s for each data set were a) 9.1 %, b) 5.5 % and c) 3.7 %. Extra peaks arise from the V sample can in the backscattering data at ~ 52k, 60k, 73k and 104k μs. The figure shows experimental data in blue, calculated pattern in red and difference plot in grey.

Table 3.10 Atomic coordinates, occupancies and thermal displacement parameters for the solution to UNK2, β-$(MoO_2)_2P_2O_7$.

Atom Label	Atom Type	x	y	z	Occ	B_{iso} /Å^2
Mo1	Mo	0.3635(10)	0.0000	0.0000	1	6.78(3)
P1	P	0.5787(1)	0.0831(6)	0.0036(63)	0.5	3.35(3)
O1	O	0.3710(1)	0.5000	0.0000	1	8.06(3)
O2	O	0.4909(1)	0.0000	0.0000	1	5.89(3)
O3	O	0.3696(9)	-0.0011(1)	0.3073(2)	1	4.98(3)
O4	O	0.2598(1)	0.0000	0.0000	1	5.66(3)
O5	O	0.5565(3)	0.5000	0.0000	0.5	7.71(3)

The total cell contents were calculated to be $Mo_4P_4O_{22}$; the oxidation state of the molybdenum atom in this formula is +6. This empirical formula is identical to that of the final dehydrated phase and is consistent with the TGA/IR data. Calculated bond valence sum values for each of the metal atoms in the structure, agree very well with those expected. The bond lengths for the polyhedra fall in expected limits for these materials; these were refined without the addition of restraints or the use of rigid bodies. The P1-O5 bond distance is slightly long, but this may be due to the disorder in the structure affecting the ability of the refinement to accurately determine it.

Table 3.11 Bond lengths and bond valence sum values calculated for the solution to UNK2, β-$(MoO_2)_2P_2O_7$. BVSs were calculated using the values of Brese and O'Keefe.[39]

Central Atom	Apex Atom	Bond Length /Å	BVS /vu
Mo1	O4:1	1.6830(26)	6.13
	O3:1	1.9319(15)	
	O3:1	1.9319(15)	
	O1:0	1.95134(21)	
	O1:1	1.95134(21)	
	O2:0	2.0669(25)	
P1	O2:0	1.4617(30)	4.92
	O3:4	1.4904(32)	
	O3:5	1.5249(34)	
	O5:0	1.6636(29)	
O1	Mo1	1.95134(21)	1.77
	Mo1	1.95134(21)	
O2	Mo1	2.0669(25)	2.13
	P1	1.4617(30)	
O3	Mo1	1.9319(15)	2.17
	P1	1.5249(34)	
O4	Mo1	1.6830(26)	1.83
O5	P1	1.6636(29)	1.70
	P1	1.6636(29)	

3.5.6 An ordered model of the structure

To remove the disorder in the P_2O_7 groups it is necessary to double the *b*-axis to remove the 2-fold axes along [100]. Although there was no clear experimental evidence for this, an investigation into the ability of the structural model to order was undertaken. The disordered model was uploaded to the web-based resource ISODISPLACE.[43] Investigation into the modes present in the structure led to the conclusion that only symmetry-allowed site occupancy modes *DT1* and *DT2* vary P and O5 (bridging oxygen) atom occupancies to give an ordered model. The propagation of these modes through the structure leads to two distinct possible ordering patterns, Figure 3.33. An X-ray pattern was simulated for each of these models to compare them with the synchrotron data obtained at ID31. These patterns are shown in Figure 3.34.

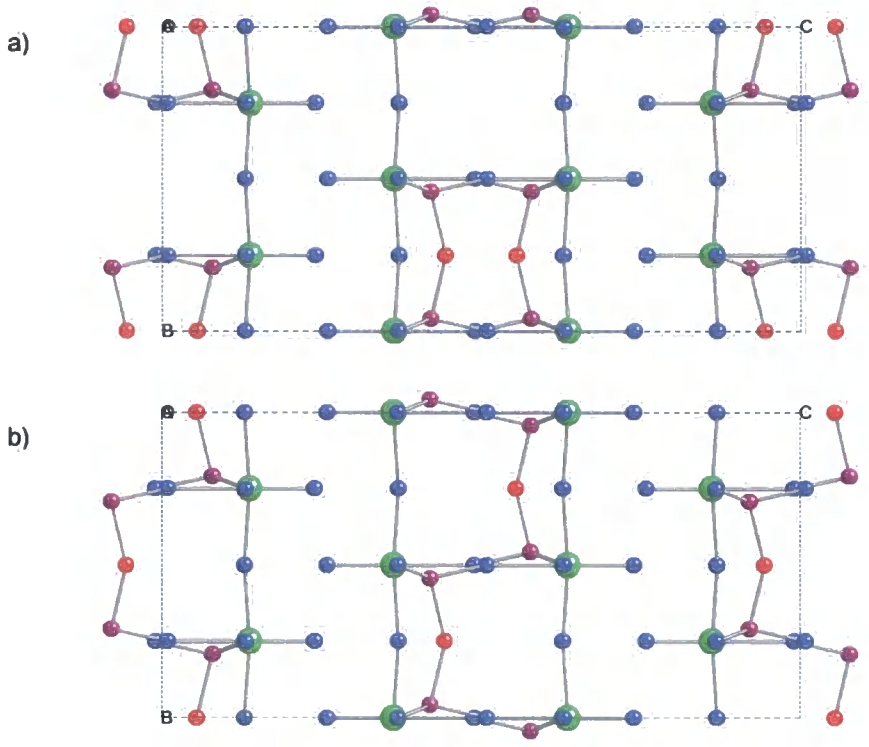

Figure 3.33 The possible ordering patterns in β-$(MoO_2)_2P_2O_7$. a) The *DT1* model, space group *P*2. b) The *DT2* model, space group $P2_1$.

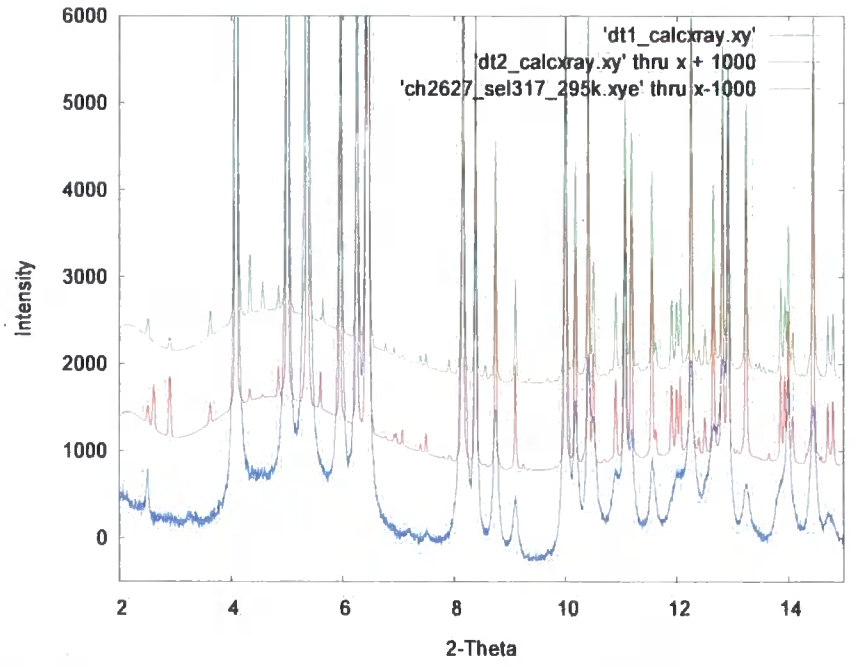

Figure 3.34 The simulated patterns for each of the ordering models of β-$(MoO_2)_2P_2O_7$; *DT1* in red, *DT2* in green, synchrotron data recorded at ID31 in blue. This figure shows the normalised data zoomed to 13 % of their total intensities.

It is clear in the simulated patterns that only weak extra peaks would arise due to ordering. There do appear to be some very weak but broadened peaks present in the synchrotron data that are not accounted for by the disordered model (*c.f.* the tic marks in Figure 3.31a); these peaks are only just visible above the noise in the baseline, and as such no definite conclusions can be reached. However, local order within the chains may be masked by disorder between the layers as they can shift relative to each other. This was hinted at in both the broad nature of the weak ordering peaks and also in the ability of these stacking faults to explain the *hkl* dependent peak shape required to fit the data. By structural comparison between this material and the final phase, α-$(MoO_2)_2P_2O_7$, the DT1 ordering mode is proposed as the more likely underlying ordered structure. This is further discussed in Section 3.7.

3.6 Rietveld analysis of the dehydration reaction

Following the structure solution of each of these unknown phases, it is now possible to undertake full Rietveld analysis of the variable temperature data discussed earlier and compare the information obtained from this method compared with that based on intensity fitting for unknown phases. A five phase Rietveld refinement was performed. A total of 49 parameters were refined in each of these sequential Rietveld refinements over the 2θ range 10-45 ° 2θ. For each of the two new phases suitable minimum and maximum limits were applied to the cell parameters. The overall peak shape and refining Lorentzian size terms were added. A 4th order spherical harmonic preferred orientation correction was required for β-$MoOPO_4$, coefficients were determined in range 25 and fixed for other refinements; a 4th order spherical harmonic correction was added to the β-$(MoO_2)_2P_2O_7$ phase to model the *hkl* dependent peakshape, the coefficients were refined in range 46 and then fixed for other refinements. For $MoO_2.H_2O.PO_3OH$ and α-$(MoO_2)_2P_2O_7$ a 4th order spherical harmonic preferred orientation correction was fixed using range number 1 and range 249 respectively. One fit from each of the four main sections of the dehydration experiment is given in Figure 3.35; this figure should be compared with the refinements shown in Figure 3.8. The input file, output file and spreadsheet containing all the data are included in the E-Appendix.

The phase percentages and relative scales against range number are given in Figure 3.36. The latter graph plots the data as scale*Z*M*V to allow comparison between different phases.[9] The approximate law of conservation of diffracted energy states that "the total energy diffracted by a particular specimen under particular experimental conditions is roughly constant. Therefore, anything done to alter the physical condition of the specimen does not alter the total amount of diffracted energy but only its distribution in space. This law is not at all rigorous but it does prove helpful in considering many diffraction phenomena."[44]

[9] Z: Number of formula units per unit cell, M: molar mass, V: Volume.

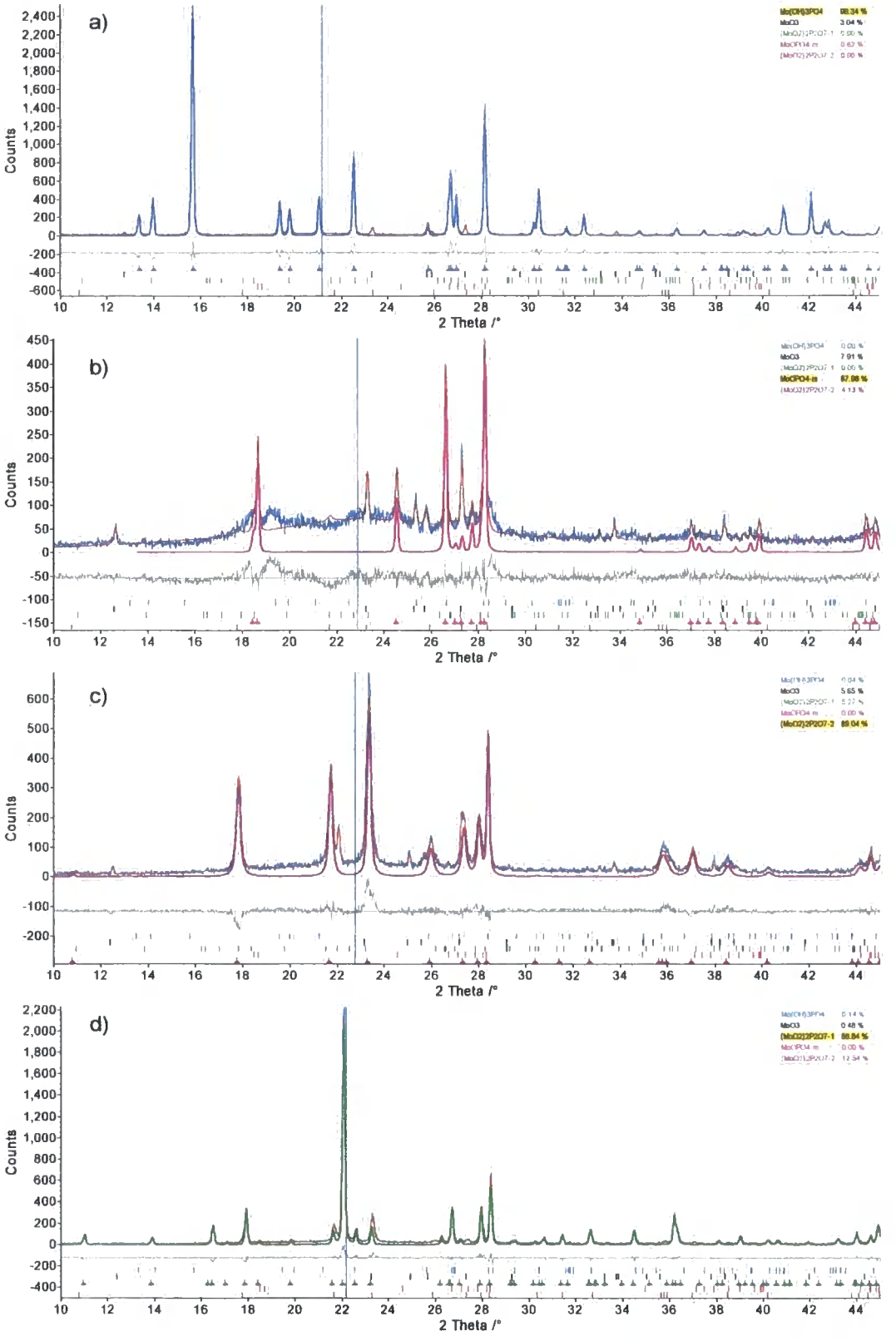

Figure 3.35 Plots showing the fit in each of the four main regions of the dehydration reaction, d8_03342. a) Range 1 is $MoO_2{\cdot}H_2O{\cdot}PO_3OH$ and MoO_3, b) range 25 is β-$MoOPO_4$ (with large amorphous background), c) range 46 is mainly β-$(MoO_2)_2P_2O_7$, with some α-$(MoO_2)_2P_2O_7$, d) range 249 is α-$(MoO_2)_2P_2O_7$. R_{wp}s for the ranges (a-d) are 19.44 %, 20.80 %, 19.48 % and 18.53 %. The main phase in each range is highlighted. The figure shows experimental data in blue, calculated pattern in red and difference plot in grey.

This approximate law states that in each range in the refinements, the total sum of the relative scales should be equal throughout the analysis if the contents of the material does not change. However, on heating this system, mass loss due to water occurs and there is also a buildup of amorphous intensity during the phase evolution of β-$MoOPO_4$. The latter point will cause the relative scale of β-$MoOPO_4$ to be reduced compared to the fully hydrated phase. Further study would require the addition of a known mass of a standard material to "spike" the data analysis.

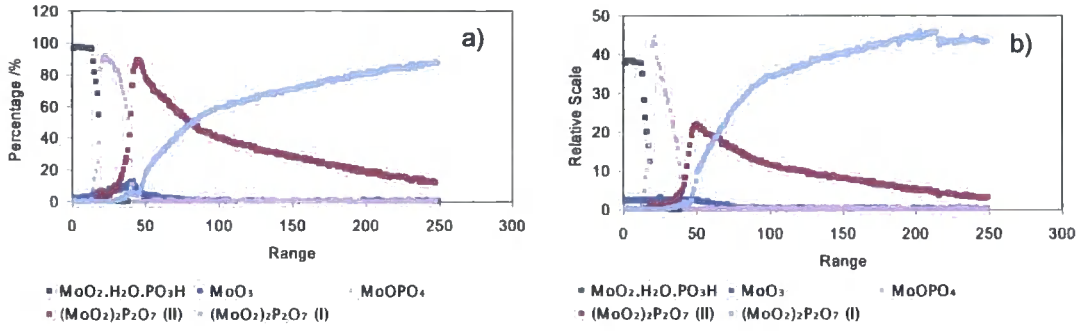

Figure 3.36 Phase evolution graphs from the Rietveld analysis. a) The phase percentages as calculated during refinement. b) The relative scales of each phase in the refinement.

Figure 3.36b) – the full Rietveld analysis of the dehydration – can be compared directly with Figure 3.15a) – the whole powder pattern fitting approach. The two methods give comparable results, the former verifying the applicability of the method used in Section 3.3.

3.7 Structural transformation during the dehydration

Combining the information obtained from TGA/IR and diffraction experiments, Equation 3.3 presents a summary of the known and postulated phases in the dehydration reaction.

$$MoO_2{\cdot}H_2O{\cdot}PO_3OH \rightarrow MoO_2.PO_3OH \rightarrow \beta\text{-}(MoO_2)_2P_2O_7 \rightarrow \alpha\text{-}(MoO_2)_2P_2O_7 \qquad (3.3)$$

With these phases in mind, a discussion of the dehydration mechanism is possible. Table 3.12 includes the constituents of each of the phases, alongside the type of bonding for each of the metal atoms, to highlight the changes occurring.

Table 3.12 Information about each of the main phases observed during the dehydration reactions. Each phase is subdivided into its bonding constituents. Empirical formulae are included scaled to contain 2 Mo atoms for ease of comparison.

Name	$MoO_2{\cdot}H_2O{\cdot}PO_3OH$	$MoO_2.PO_3OH$	β-$(MoO_2)_2P_2O_7$	α-$(MoO_2)_2P_2O_7$
Empirical Formula	$Mo_2P_2O_{10}(OH)_2.2H_2O$	$Mo_2P_2O_{12}H_4$	$Mo_2P_2O_{11}$	$Mo_2P_2O_{11}$
Mo=O	2	1	1	1
Mo-OH_2	1	0	0	0
Mo-O(-Mo)	0	2	2	2
Mo-O(-P)	3	3	3	3
P-O-(P)	0	0	1	1
P-O-(Mo)	3	3	3	3
P-OH	1	1	0	0

From this table, it is possible to rationalise the changes in the structures that occur during the dehydration reaction. These changes are shown pictorially in the following figures. The first reaction is believed to occur by loss of the H_2O molecules, resulting in the formation of Mo-O-Mo chains throughout the structure, Figure 3.37.

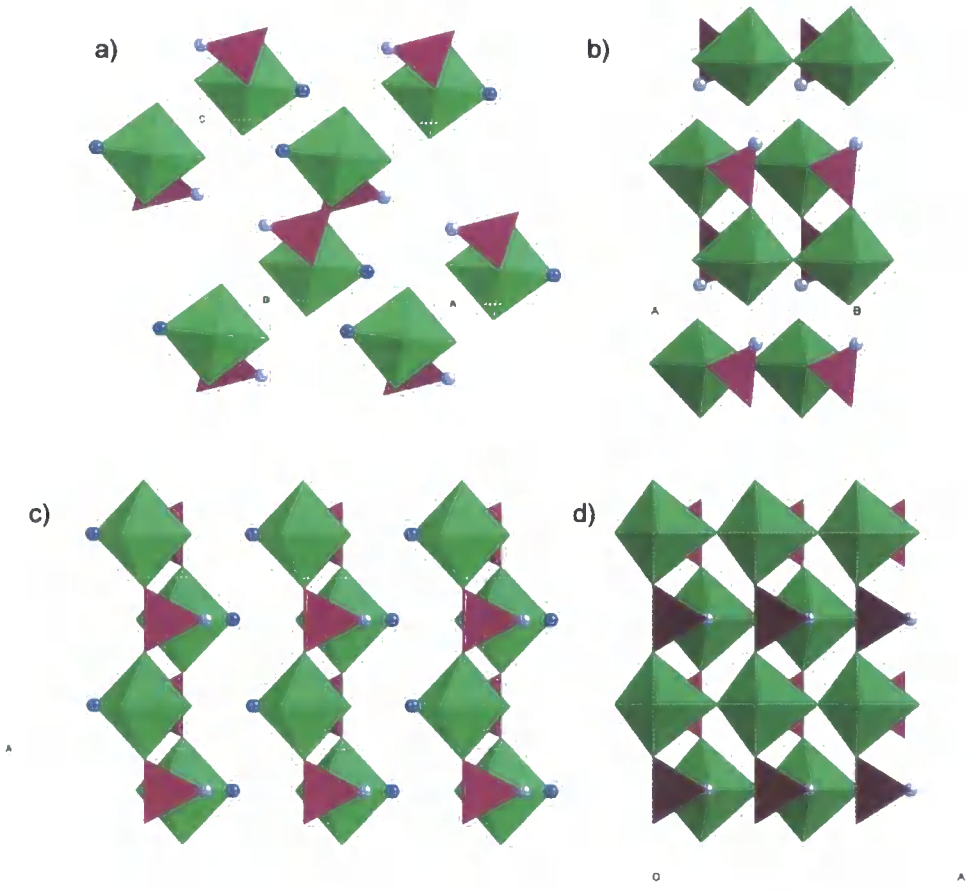

Figure 3.37 Polyhedral representation of the dehydration and loss of H_2O from a+c) $MoO_2{\cdot}H_2O{\cdot}PO_3OH$ to form b+d) $MoO_2.PO_3OH$ looking down two sets of potentially related axes in their structures. Mo-centred octahedra are shown in green, P-centred tetrahedra are given in purple. H atoms are not displayed for ease of viewing. Mo=O groups are given in royal blue; P-OH groups are shown in grey.

This reaction is a low temperature reaction, taking place at 553 K. This implies that there is likely to be relatively little rearrangement of the atoms within the structure. The proposed mechanism is consistent with these observations, requiring only slight movements of the chains relative to each other. $MoO_2.PO_3OH$ is known to rehydrate to $MoO_2{\cdot}H_2O{\cdot}PO_3OH$. This points toward this reaction being topotactic in nature, with the structure of the precursor controlling the structure of the subsequent phase.

The transformation from $MoO_2.PO_3OH$ to β-$(MoO_2)_2P_2O_7$ occurs by condensation of the P-OH groups to form P_2O_7 groups, Table 3.12. Two processes must occur at this transition. Firstly MoO_6 octahedra within the double chains must move relative to one another and secondly two P-OH groups condense to form a P-O-P linkage and water. These processes presumably happen simultaneously (the latter driving the former) though the transition has been broken down into two stages, Figure 3.38.

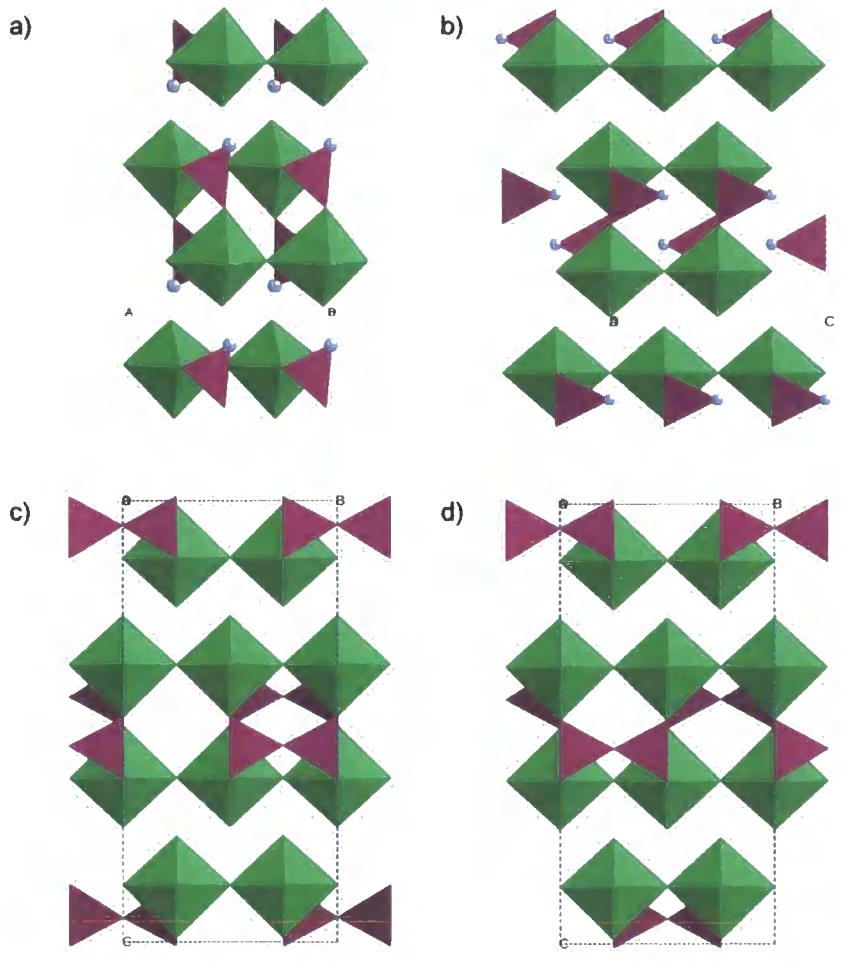

Figure 3.38 Polyhedral representation of the condensation of P-OH groups in a) $MoO_2.PO_3OH$, via a rearrangement in b), to form P_2O_7 groups in c) DT1 β-$(MoO_2)_2P_2O_7$ and d) DT2 β-$(MoO_2)_2P_2O_7$ looking down potentially related axes in their structures. Mo-centred octahedra are shown in green, P-centred tetrahedra are given in purple; the P-OH groups are shown in grey.

This proposed method is consistent with the belief that the overall disordered structure of β-$(MoO_2)_2P_2O_7$ is ordered within individual chains. The two ordering mechanisms (DT1 and DT2 from Section 3.5.6), can both arise from this dehydration mechanism by differing local condensation of P_2O_7 groups within the chains. There is no conclusive evidence for either of these ordering patterns forming in preference to the other; however, they are both possible mechanistically.

The structures of β-$(MoO_2)_2P_2O_7$ and α-$(MoO_2)_2P_2O_7$ are compared in Figure 3.39. They both contain chains of MoO_6 octahedra that are linked by P_2O_7 groups; however, in the more stable phase these chains are not linear, they have adopted a zigzag pattern within the structure. This is therefore a reconstructive transition. α-$(MoO_2)_2P_2O_7$ is presumably more stable from the known higher stability (~years) of this phase with respect to rehydration. The structure of this phase is considered in more detail in Chapter 4.

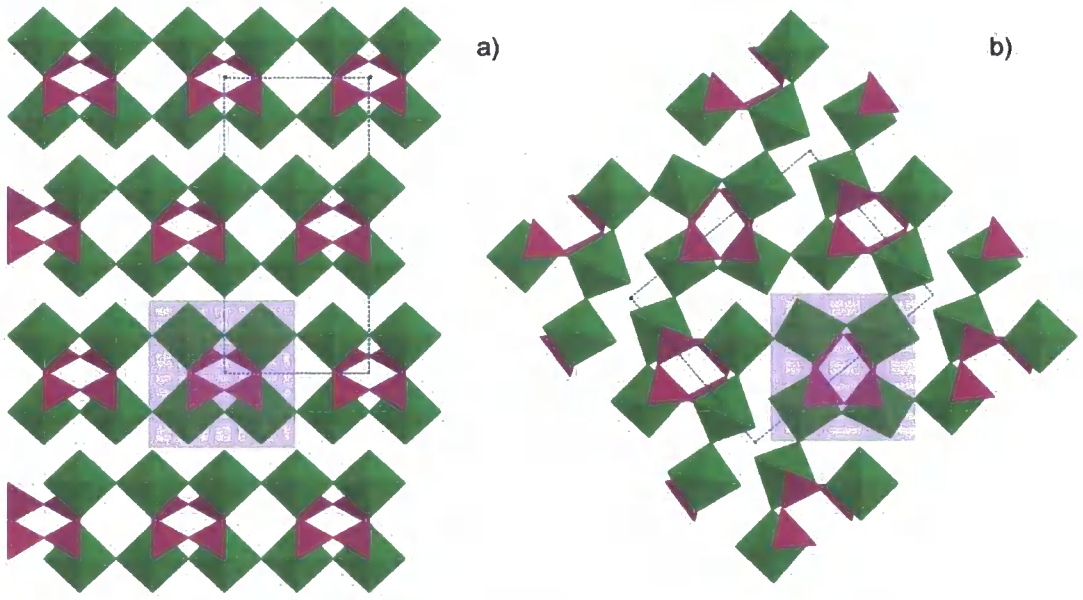

Figure 3.39 Comparison of the structures of a) β-$(MoO_2)_2P_2O_7$ (DT1) and b) α-$(MoO_2)_2P_2O_7$. Mo-centred octahedra are shown in green, P-centred tetrahedra are given in purple.

3.8 Isolation of α-$(MoO_2)_2P_2O_7$

As described in Section 3.3.1, early syntheses of $(MoO_2)_2P_2O_7$ led to the belief that there were two very similar forms of this material, as hinted at by Schulz.[1] The stable α- phase was eventually isolated *ex-situ* as follows.

2.247 g of $MoO_2{\cdot}H_2O{\cdot}PO_3OH$ (9.29 mmol, SEL313) was ground in an agate pestle and mortar and transferred to an alumina crucible. The powder was heated at 5 K/min to 923 K, and held at that temperature for 48 hours, then being cooled in the furnace to room temperature. The synthesis produced a creamy coloured powder, with a powder pattern shown in Figure 3.40. The yield was 1.633 g, 81.8 %. The successful synthesis was confirmed by comparison of the PXRD patterns with the PDF (74-1380).[10]

Figure 3.40 shows initial Rietveld analysis undertaken on this phase. 28 parameters were refined in this analysis, including 15 coefficients of a Chebychev polynomial to model the background, a sample height parameter, a parameter to model axial divergence, 3 lattice parameters of the phase α-$(MoO_2)_2P_2O_7$, 3 isotropic displacement parameters – one for each atom type, 4 parameters used to define the TCHZ peak shape and a scale factor. A final R_{wp} value of 7.37 % was obtained. The difference curve in Figure 3.40 (shown in grey) shows a reasonable – but not perfect – fit between the structural model (Kierkegaard)[9] and the experimental data. Selected refinement details are given in Table 3.13. The input file for this refinement is included in the E-appendix. As discussed in Chapter 4 this model is only an approximation of the true room temperature structure.

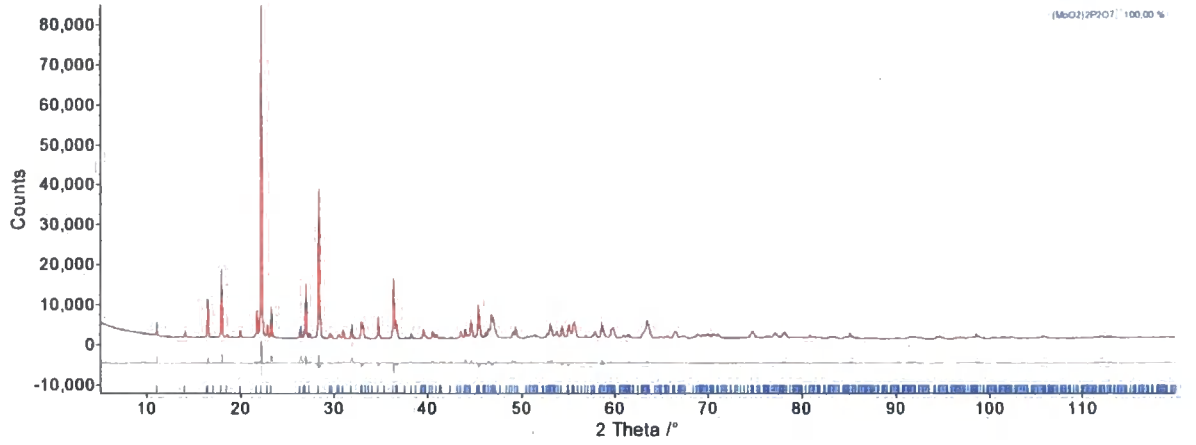

Figure 3.40 Rietveld analysis of SEL315, α-$(MoO_2)_2P_2O_7$, d9_02843, R_{wp} 7.37 %. The figure shows experimental data in blue, calculated pattern in red and difference plot in grey.

Table 3.13 Selected refined values, crystallographic and data collection parameters for d9_02843.

Space Group	*Pnma*	2θ range /°	5-120
a /Å	12.5859(4)	2θ step size /°	0.02
b /Å	6.3055(1)	Time per step /s	1.5
c /Å	10.3696(3)	R_{wp} /%	7.37
Volume /Å^3	822.94(4)	R_{Bragg} /%	5.27
Number of parameters	28	GOF	3.62

3.9 Conclusions

The material α-$(MoO_2)_2P_2O_7$ has been prepared by dehydration of the precursor $MoO_2{\cdot}H_2O{\cdot}PO_3OH$. The structure of the former material is the subject of Chapter 4 of this thesis. The investigation into the dehydration reaction of $MoO_2{\cdot}H_2O{\cdot}PO_3OH$ has led to the discovery of two new phases. The reaction proceeds as follows:

$$MoO_2{\cdot}H_2O{\cdot}PO_3OH + MoO_3 \rightarrow \beta\text{-}MoOPO_4 + MoO_3 + \text{amorphous material}$$
$$\rightarrow \beta\text{-}(MoO_2)_2P_2O_7 + MoO_3 \rightarrow \alpha\text{-}(MoO_2)_2P_2O_7 \rightarrow \text{final amorphous product} \quad (3.1)$$

A novel approach was used to analyse the diffraction data from these sets of experiments, in order to extract information from these data without knowledge of the atomic structure or cell parameters. This peak fitting approach has enabled the calculation of phase evolution graphs. These graphs – combined with further experiments, have led to the successful isolation of both of the unknown phases both *in-situ* and *ex-situ*.

β-$MoOPO_4$ has been successfully indexed to a monoclinic cell with lattice parameters:

a = 7.4077 Å b = 7.2128 Å c = 7.2805 Å β = 61.651 ° FOM 20.0

This structure was believed to be similar to ε-$VOPO_4$, and structure solution of this new molybdenum phosphate was carried out using the known vanadium phosphate phase as an initial structural model. Analytical data have suggested that this solution does not fully describe the phase; IR and TGA data suggest the phase contains P-OH groups and SQUID data have shown the phase to be diamagnetic (Mo^{VI}). A structure has therefore been derived from this by introducing P-OH bonds giving the formula $MoO_2.PO_3OH$. This structure has been used to discuss qualitatively the mechanism of the dehydration pathway.

Isolation of β-$(MoO_2)_2P_2O_7$ has led to successful indexing of the phase to a monoclinic cell with lattice parameters:

a = 16.2437 Å b = 3.8913 Å c = 6.2840 Å $\alpha=\beta=\gamma$= 90 ° FOM 8.42

Analysis of the systematic absences from this phase led to the assignment of space group $C222_1$ to this phase. Further investigation led to the solution of the structure as being a disordered phase, with formula $(MoO_2)_2P_2O_7$, *i.e.* the same formula as the final dehydrated product. This phase, β-$(MoO_2)_2P_2O_7$, is unstable with respect to dehydration.

The whole powder pattern modelling that was undertaken was repeated following the structure solution of the unknown materials using a Rietveld-only approach to compare the results from the two methods. The results found for the latter more conventional approach agreed very well with those obtained from the whole pattern approach required when there was no structural information about several phases. This has proven the ability to gain useful information from the whole powder pattern method.

A mechanism for the dehydration reaction has been proposed which is consistent with all experimental information available.

3.10 References

1. I. Schulz, *Z. Anorg. Allg. Chem.*, 1955, **281**, 99-112.
2. P. Kierkegaard, *Acta Chem. Scand.*, 1958, **12**, 1701-1714.
3. O. Glemser, *Angew. Chem.*, 1961, **73**, 785-805.
4. O. Glemser, H. K. Hofmeister and E. Schwarzmann, *Z. Anorg. Allg. Chem.*, 1960, **312**, 50-52.
5. M. T. Weller and R. G. Bell, *Solid State Ionics*, 1989, **35**, 79-84.
6. C. Biot, A. Leclaire, M. M. Borel and B. Raveau, *Z. Kristallogr.*, 1997, **212**, 792-794.
7. J. Gopalakrishnan, *Proc. Ind. Nat. Sci. Acad. A: Phys. Sci.*, 1986, **52**, 48-66.
8. H. R. Tietze, *Aust. J. Chem.*, 1981, **34**, 2035-2038.
9. P. Kierkegaard, *Ark. Kemi*, 1962, **19**, 1-14.
10. Powder Diffraction File, *International Centre for Diffraction Data*, Pennsylvania, 1998.
11. P. Thompson, D. E. Cox and J. M. Hastings, *J. Appl. Crystallogr.*, 1987, **20**, 79-83.
12. S. E. Lister, Unpublished work, 2006.
13. L. Kihlborg, *Ark. Kemi*, 1963, **21**, 357-364.
14. S. Allen and J. S. O. Evans, Unpublished work, 2000.

15. J. S. O. Evans, *Multitopas, Fortran 77 routine*, Durham, 1999.
16. D. E. C. Corbridge and E. J. Lowe, *J. Chem. Soc.*, 1954, 493-502.
17. D. E. C. Corbridge and E. J. Lowe, *J. Chem. Soc.*, 1954, 4555-4564.
18. S. Allen, *Thermoresponsive Behaviour of AM_2O_8 Materials, Ph. D. Thesis*, University of Durham, 2003.
19. A. A. Coelho, *TOPAS Academic: General Profile and Structure Analysis Software for Powder Diffraction Data*, Bruker AXS, Karlsruhe, 2004.
20. ICSD, Fachinformationszentrum, Karlsruhe, 2003.
21. F. Girgsdies, W.-S. Dong, J. K. Bartley, G. J. Hutchings, R. Schlögl and T. Ressler, *Solid State Sci.*, 2006, **8**, 807-812.
22. J. M. Longo and P. Kierkegaard, *Acta Chem. Scand.*, 1966, **20**, 72-78.
23. A. Leclaire, H. Chahboun, D. Groult and B. Raveau, *Z. Kristallogr.*, 1986, **177**, 277-286.
24. B. Jordan and C. Calvo, *Can. J. Chem.*, 1973, **51**, 2621-2625.
25. M. Tachez, F. Theobald and E. Bordes, *J. Solid State Chem.*, 1981, **40**, 280-283.
26. R. Gopal and C. Calvo, *J. Solid State Chem.*, 1972, **5**, 432-435.
27. S. C. Lim, J. T. Vaughey, W. T. A. Harrison, L. L. Dussack, A. J. Jacobson and J. W. Johnson, *Solid State Ionics*, 1996, **84**, 219-226.
28. E. M. Levin and R. S. Roth, *J. Solid State Chem.*, 1970, **2**, 250-261.
29. J. M. Longo, J. W. Pierce and J. A. Kafalas, *Mater. Res. Bull.*, 1971, **6**, 1157-1165.
30. U. Kaiser, G. Schmidt, R. Glaum and R. Gruehn, *Zeit. Anorg. Allge. Chem.*, 1992, **607**, 113-120.
31. T. G. Amos, A. Yokochi and A. W. Sleight, *J. Solid State Chem.*, 1998, **14**, 303-307.
32. T. G. Amos and A. W. Sleight, *J. Solid State Chem.*, 2001, **160**, 230-238.
33. D. L. Serra and S.-J. Hwu, *Acta Crystallogr., Sect. C*, 1992, **48**, 733-735.
34. P. Kierkegaard and M. Westerlund, *Acta Chem. Scand.*, 1964, **18**, 2217-2225.
35. G. Costentin, A. Leclaire, M. M. Borel, A. Grandin and B. Raveau, *Rev. Inorg. Chem.*, 1993, **13**, 77-101.
36. N. Kinomura, M. Hirose, N. Kumada, F. Muto and T. Ashida, *J. Solid State Chem.*, 1988, **77**, 156-161.
37. E. J. Baran, I. L. Botto, N. Kinomura and N. Kumada, *J. Solid State Chem.*, 1990, **89**, 144-146.
38. F. Zocchi, *Solid State Sci.*, 2000, **2**, 383-387.
39. N. E. Brese and M. O'Keeffe, *Acta Crystallogr., Sect. B*, 1991, **47**, 192-197.
40. *Cerius2, v 3.8*, Molecular Simulations Inc., Cambridge, England, 1998.
41. G. S. Pawley, *J. Appl. Cryst.*, 1981, **14**, 357-361.
42. A. Markvardsen, W. I. F. David, J. C. Johnston and K. Shankland, *Acta Crystallogr., Sect. A*, 2000, **57**, 47-54.
43. B. J. Campbell, H. T. Stokes, D. E. Tanner and D. M. Hatch, *J. Appl. Cryst.*, 2006, **39**, 607-614.
44. B. D. Cullity, *Elements of X-ray Diffraction*, 2nd Edition, Addison Wesley, London, 1978.

4. Structures and Phase Transitions of α-$(MoO_2)_2P_2O_7$

4.1 Introduction

The product formed on complete dehydration of $MoO_2 \cdot H_2O \cdot PO_3OH$ was first isolated by Schulz and formulated as $(MoO_2)_2P_2O_7$.[1] Schulz claimed that there are two forms of this material, a stable and an unstable one (with respect to rehydration). The unstable form was said to be prepared on heating the hydrated precursor, $MoO_2 \cdot H_2O \cdot PO_3OH$, to temperatures between 573 and 753 K. A more stable polymorph, which was not hygroscopic, formed on heating up to 873 K. Chapter 3 described the solution of the hygroscopic material β-$(MoO_2)_2P_2O_7$. This chapter focuses on the final stable phase α-$(MoO_2)_2P_2O_7$.

The structure of α-$(MoO_2)_2P_2O_7$ was described in Section 3.1 as having two unique Mo and two unique P atoms in space group *Pnma*.[2] These metal atoms are in octahedral and tetrahedral coordination geometry respectively, Figure 3.2. The MoO_6 octahedra form chains in the *ac* plane; Mo1 forms a para-linkage across 3 MoO_6 octahedra, and Mo2 forms a cis-linkage; these create zigzag chains through the structure. Of the remaining vertices three form an Mo-O-P linkage, and the remaining Mo-O vertex is "free". The P_2O_7 groups are in an eclipsed conformation, with all six vertices linking to MoO_6 octahedra.

The bond lengths for each of the Mo and P polyhedra (as given in the original paper) are given in Tables 4.1 and 4.2. The errors were quoted to be a few tenths of an *Å*.

Table 4.1 Bond lengths within MoO_6 octahedra in α-$(MoO_2)_2P_2O_7$, as given in reference 2.

Central Polyhedral Atom	Vertex Atoms (Connecting Atom)	Bond Length /*Å*
Mo1	O2 (P2)	1.87
	O4 (P1)	1.89
	O6 (Mo2)	2.09
	O7 (Mo2)	1.94
	=O9	1.83
Mo2	O1 (P1)	1.97
	O3 (P2)	2.09
	O6 (Mo1)	1.86
	O7 (Mo1)	2.17
	=O8	1.83

It is clear from these values that the Mo=O "free" bond is the shortest as expected. However, in the Mo1 octahedron there are 4 short bonds, one medium and 1 long with an average bond length of 1.91 *Å* and a bond valence sum of 6.09. The Mo2 octahedron has 2 long, 2 medium and 2 short bonds, an average of 1.984 *Å* and a bond valence sum of 5.11. The Mo atoms in the material have a nominal charge of +6; the bond length spreads are far from characteristic for typical Mo phosphate materials.

Table 4.2 Bond lengths within PO_4 tetrahedra in α-$(MoO_2)_2P_2O_7$.

Central Polyhedral Atom	Vertex Atoms (Connecting Atom)	Bond Length /Å
P1	O5 (P2)	1.60
	O1 (Mo1)	1.59
	O4 (Mo1)	1.46
P2	05 (P1)	1.59
	O2 (Mo1)	1.61
	O3 (Mo2)	1.54

The P-O bond lengths calculated for this structure have values far from characteristic of P_2O_7 groups in other materials. In a typical structure, the bridging bonds – in a P-O-P linkage – are longer than the other P-O-Mo bonds, in a ratio of approximately 1.58:1.5 Å. The P-O-P bond angle is 140.94 °; this is consistent with bond length/angle trends in molybdenum phosphates (Section 5.4).[3]

Kierkegaard described the structure as being an idealised one, as "some of the light atoms should be slightly displaced in order to give an explanation of very weak zones, indicating a *b* axis being four times that of the sublattice cell."[2]

Synthesis of α-$(MoO_2)_2P_2O_7$, which forms as either a white or pale blue powder, was described in Chapter 3. This chapter investigates the true structure of this material and the phase transitions it undergoes.

4.2 Variable temperature studies of α-$(MoO_2)_2P_2O_7$

4.2.1 Low temperature study of α-$(MoO_2)_2P_2O_7$

A sample of α-$(MoO_2)_2P_2O_7$ (SEL243) was prepared for VT XRD with a small quantity of aluminium powder as internal standard. The finely ground powder was mounted using a small quantity of Vaseline as an adhesive on a silicon disc then mounted into the sample holder of the Oxford Cryosystems PheniX. Continuous twenty minute scans were recorded as the PheniX cooled from 300 K to 18 K at a rate of 12 K hr^{-1} (d9_02442). The same heating and data collection rate were used on warming from 18 to 300 K (d9_02443). Twenty minute scans were recorded from 10 to 90 ° 2θ, with a step size of 0.02 ° 2θ.

For each XRD pattern recorded a total of 35 parameters were refined. These included 17 global parameters (12 background parameters, one parameter to model axial divergence and a sample height displacement parameter), 11 parameters for α-$(MoO_2)_2P_2O_7$ (3 cell parameters, 3 isotropic displacement parameters - 1 each for each atom type, 4 parameters to describe a TCHZ peak shape used and a scale parameter), and 7 parameters for the aluminium internal standard (1 cell parameter, a scale parameter, a single isotropic displacement parameter and 4 parameters to describe a TCHZ peak shape). The peak position, intensity and fwhm of a Gaussian peak were used to model a small

quantity of amorphous background, arising from the Vaseline. The Rietveld refinement of the first dataset is shown in Figure 4.1. The published model gives a reasonable fit to the data; however, it is far from perfect. The seed input file for the refinements and the spreadsheets containing the values of all the refined parameters are included in the E-Appendix.

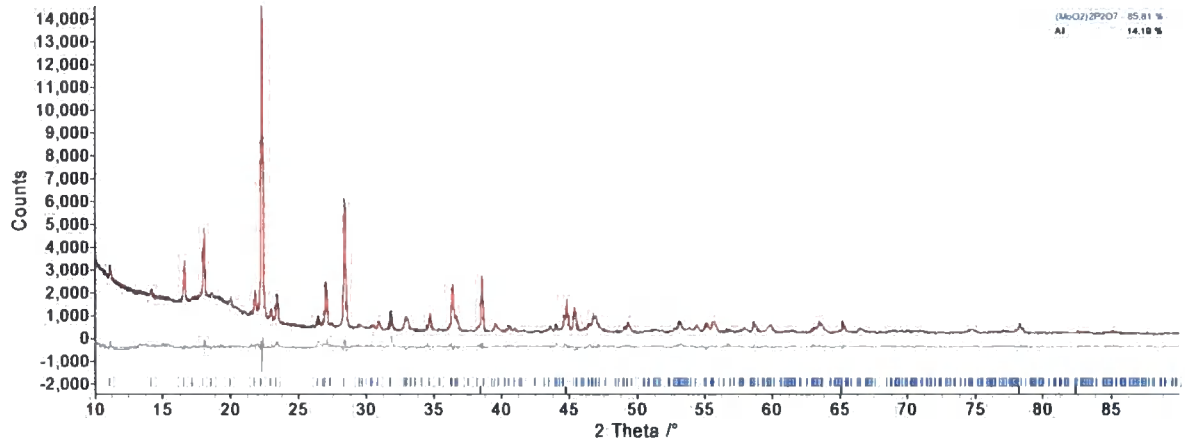

Figure 4.1 Rietveld fit of α-$(MoO_2)_2P_2O_7$ (SEL243), in d9_02442(1). The R_{wp} for this fit was 6.752 %. The figure shows the experimental data in black, the calculated pattern in red and the difference plot in grey. Tick marks (in blue) show the predicted positions of the peaks.

The temperature calibration of the PheniX was checked by comparing the refined values of the cell parameter of the internal standard (Al powder) with literature data.[4] Figure 4.2 shows experimental data from this experiment compared to thermal expansion data calculated by Wang and Reeber. A constant offset of 0.0017 Å (calculated by least squares refinement) was applied to the literature data. Excellent agreement is observed between experimental and literature data (particularly in the gradient) suggesting that the differences between the sample holder and PheniX thermocouple temperature are negligible.

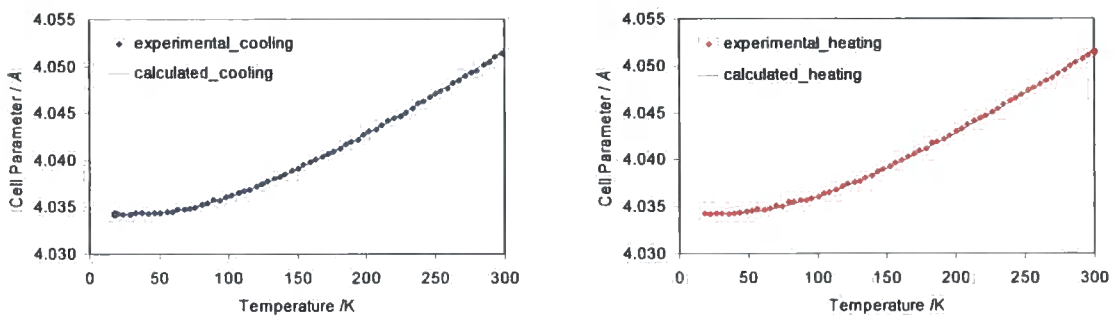

Figure 4.2 Al cell parameter on heating and cooling.

Graphs showing the variations in the volume and lattice parameters of α-$(MoO_2)_2P_2O_7$ over the temperature range 18 – 300 K are given in Figure 4.4, alongside those refined from data recorded on the high temperature stage.

4.2.2 High temperature study of α-$(MoO_2)_2P_2O_7$

The changing cell parameters of the material were also investigated from room temperature up to a temperature just below the decomposition temperature of the material. A small quantity of α-$(MoO_2)_2P_2O_7$ (SEL243) was prepared for XRD together with a small quantity of Al_2O_3, as an internal standard, on an amorphous silica disc smeared with a small amount of Vaseline to act as an adhesive. This sample was then mounted in the alumina sample holder in the high temperature attachment on the d8. Scans were recorded from 10 to 90 ° 2θ using an Anton Paar HTK1200 furnace attachment (HTK1200) on a Bruker d8 Advance diffractometer. Temperature intervals of 10 K were employed, heating from 313 to 693 K, then cooling from 695 to 315 K; a total of 78 scans.

For each data set a total of 31 parameters were refined. These included 11 global parameters (9 background parameters, a sample height correction and 1 parameter to model axial divergence), 11 parameters to model the α-$(MoO_2)_2P_2O_7$ structure (3 cell parameters, 3 isotropic displacement parameters, 4 parameters to model the TCHZ peak shape used and a scale parameter) and 9 parameters to model the Al_2O_3 included as a reference material (2 cell parameters, 2 isotropic displacement parameters, 4 parameters to model the TCHZ peak shape and a scale parameter). The peak position, intensity and fwhm of a Gaussian peak were used to model a small quantity of amorphous background, arising from the Vaseline. The R_{wp} for this refinement in range number 1 was 15.8 %; the calculated and recorded patterns are given in Figure 4.3. The parameters that were refined during this analysis are presented graphically in the following sections. The seed input file for the refinements undertaken and the spreadsheets containing the values of all the refined parameters are included in the E-Appendix.

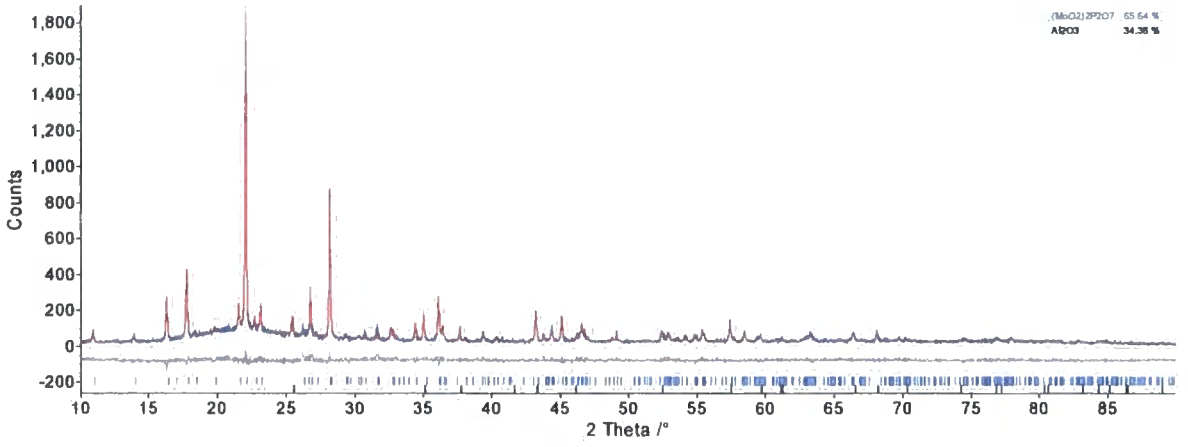

Figure 4.3 The Rietveld fit of α-$(MoO_2)_2P_2O_7$ (SEL243), in scan d8_03413(1). The R_{wp} for this fit was 15.80 %. The figure shows the experimental data in blue, the calculated pattern in red and the difference plot in grey.

Figure 4.4 shows the lattice parameters and cell volume over the range 16 to 753 K. Each graph shows the data for both the heating (red) and cooling (blue) cycles. The *y* scale axes on the graphs for the *a*, *b* and *c* cell parameters have been scaled to show the relative changes. Percentage changes for the lattice parameters *a*, *b* and *c* over the whole temperature range are 1.94 %, 0.05 %

and 0.61 % respectively. There is good agreement between the refined values for the lattice parameters on heating and cooling, with only very slight hysteresis. The data from the PheniX and HTK1200 measurements are in excellent agreement.

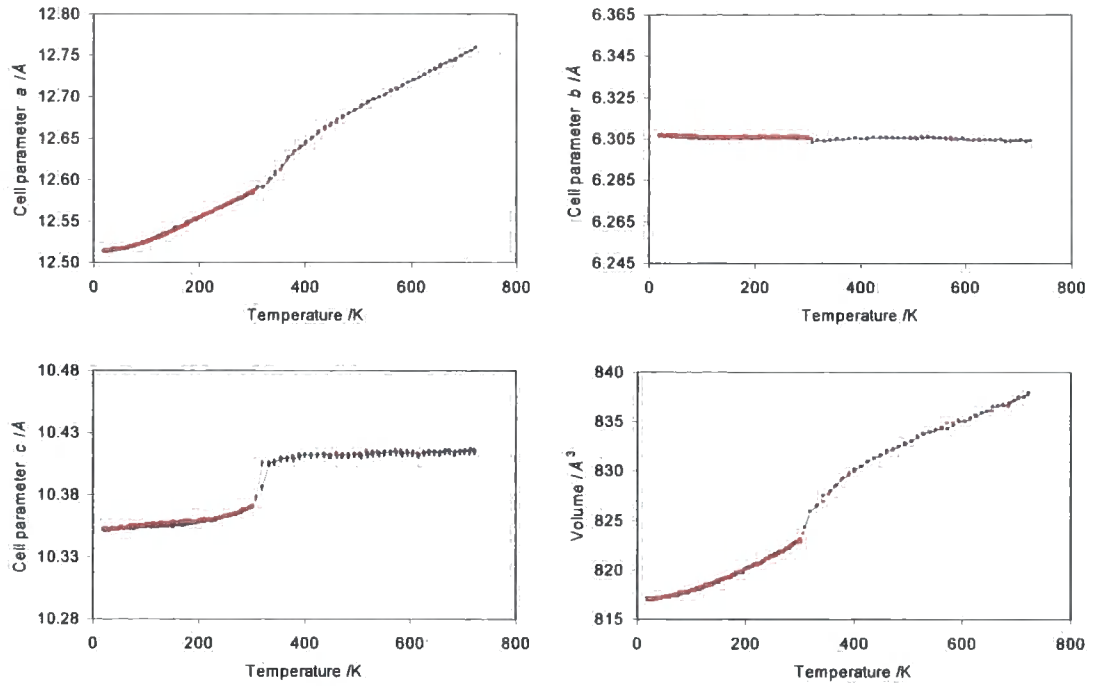

Figure 4.4 Changes in unit cell parameters with increasing (red) and decreasing (blue) temperature from the low temperature PheniX data (■) and the HTK1200 (●) experiments. The same % change scale is shown for each graph. Standard uncertainties are plotted; they are typically less than 0.0009 Å for cell parameters, and less than 0.1 Å^3 for the volumes.

The clear discontinuity visible in the *c* parameter suggests a first order transition occurs. However, the changes in the *a* parameter and the volume are more gradual, suggesting more complex behaviour.

In order to obtain values for the volume thermal expansion coefficients for the data, the data were fitted using a Bezier algorithm to allow numerical differentiation. The thermal expansion coefficients were calculated as defined in Equation 1.2. The calculated values of α_V for both the low and high temperature data sets are plotted in Figure 4.5. α-$(MoO_2)_2P_2O_7$ is found to undergo positive thermal expansion over the whole temperature range studied.

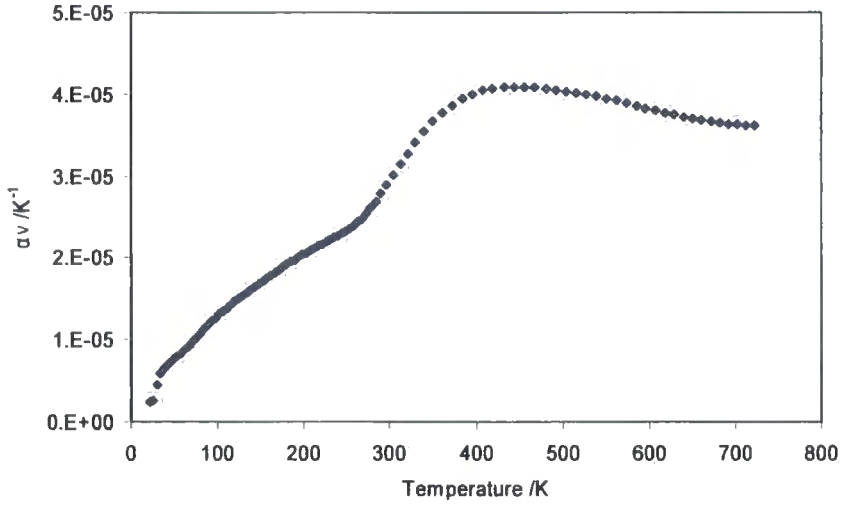

Figure 4.5 Thermal expansion data calculated for α-$(MoO_2)_2P_2O_7$ over the temperature range 18 – 753 K. Data points have been included over the whole range of data available. Values at extreme edges of data are derived from a smaller number of data points and are therefore less reliable.

4.2.3 VT study of α-$(MoO_2)_2P_2O_7$ using synchrotron data

Relatively rapid data collections were performed on a sample of α-$(MoO_2)_2P_2O_7$ (SEL315) at beamline ID31 at the ESRF to gain more accurate cell parameters for the material to determine the cell metric more precisely on increasing temperature through the phase transition. The sample was prepared in a 0.7 mm quartz capillary and mounted in the diffractometer; data were recorded using a wavelength of 0.35285(8) Å, calibrated using a Si standard. Diffraction patterns were recorded as detailed in Table 4.3. Further experimental details are given in Section 2.3.6.

Table 4.3 Data collection parameters for variable temperature data recorded at the ESRF on station ID31.

Variable	Values
2θ /°	1-31
Scan Length /min	10
Temperature Range /K	200 – 450
Heating Range /Khr^{-1}	36
Temperature Range /K scan^{-1}	6

A seed input file was written to refine cell parameters and unit cell volume using the subcell model across the whole temperature range. A total of 22 parameters were refined including 13 global parameters (9 coefficients of a Chebychev polynomial to model the background, a zero error and 1 parameter to model axial divergence) and 9 parameters to model the α-$(MoO_2)_2P_2O_7$ subcell (3 lattice parameters, 1 isotropic displacement parameters – 1 for each atom type, a scale factor and 4 parameters to describe the TCHZ peak shape). The Rietveld fit for range number 1 is given in Figure 4.6.

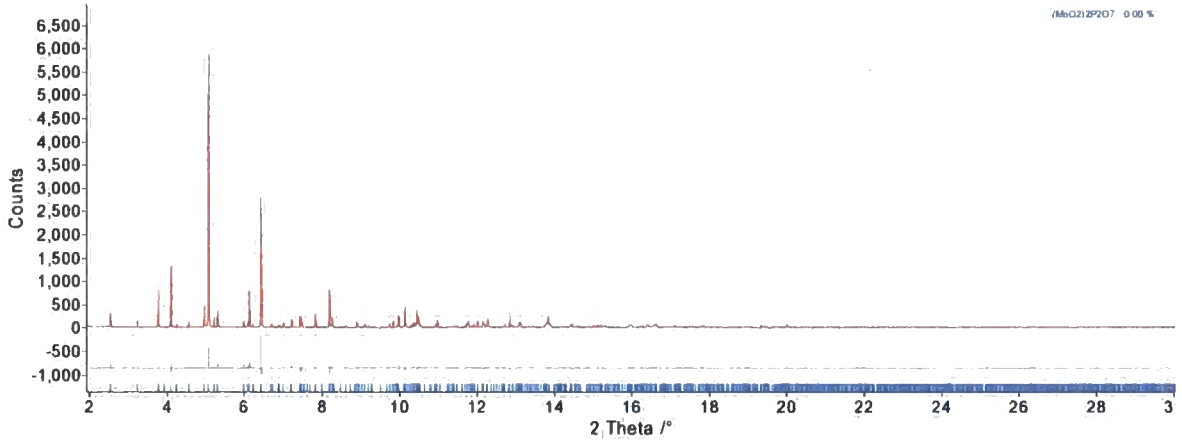

Figure 4.6 The Rietveld fit of of α-$(MoO_2)_2P_2O_7$ (SEL315), in scan ch2627_sel315_ramping_0001.xye. The R_{wp} for this fit was 17.81 %. The figure shows the experimental data in blue, the calculated pattern in red and the difference plot in grey.

This subcell model is seen to fit the data reasonably well. Refined cell parameters are given in Figure 4.7.

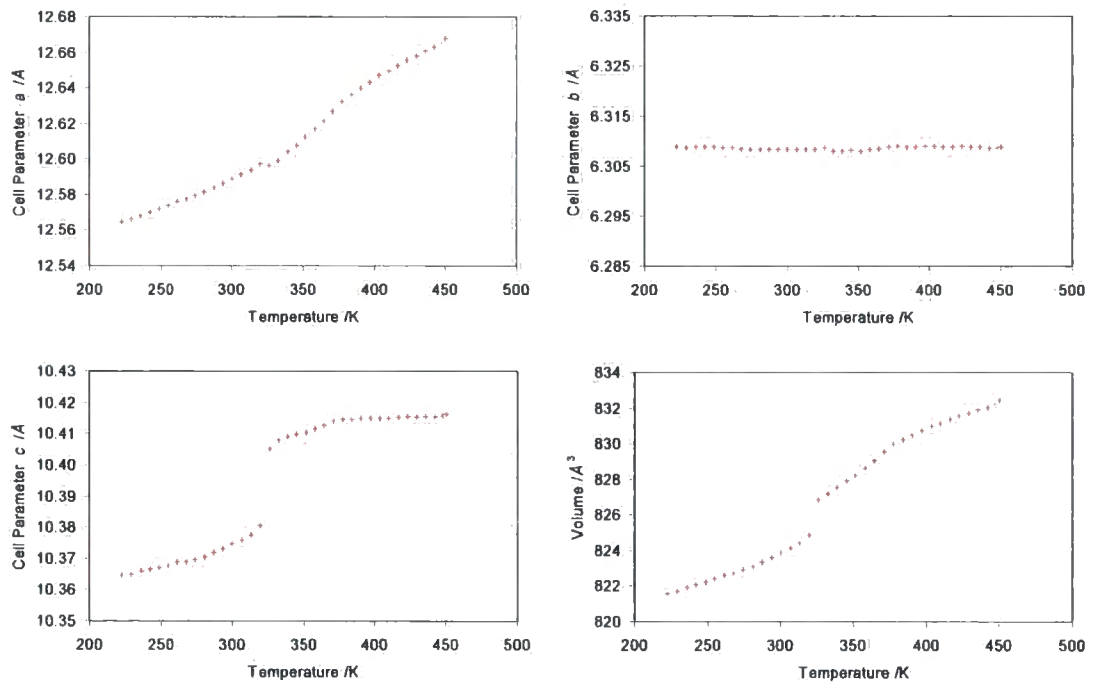

Figure 4.7 Changes in unit cell parameters with increasing temperature from data recorded at ID31, at the ESRF. The same % change scale was used for each of the *a*, *b* and *c* lattice parameter graphs. Standard uncertainties are plotted; they are typically less than 0.0002 Å for cell parameters, and less than 0.02 Å for the volumes.

The changes in cell parameter with temperature imply that two transitions occur. A first phase transition at 325 K appears to be first order, and the second at approximately 377 K appears to be

more second order in nature. This second phase transition was not clearly visible in the lab X-ray data.

There are slightly inconsistencies in some refined values at T=325 K (most notably in the *a* cell parameter in Figure 4.7). As a first order process the two phases can exist simultaneously at this temperature. Figure 4.8 compares the peak positions of certain reflections present below, at and above 325 K. A clear shift in 2θ is noted between the scan at low temperature (in blue) and the one at highest temperature (in red). The intermediate scan (in green) shows extra peaks indicating the presence of a two phase region at 325 K.

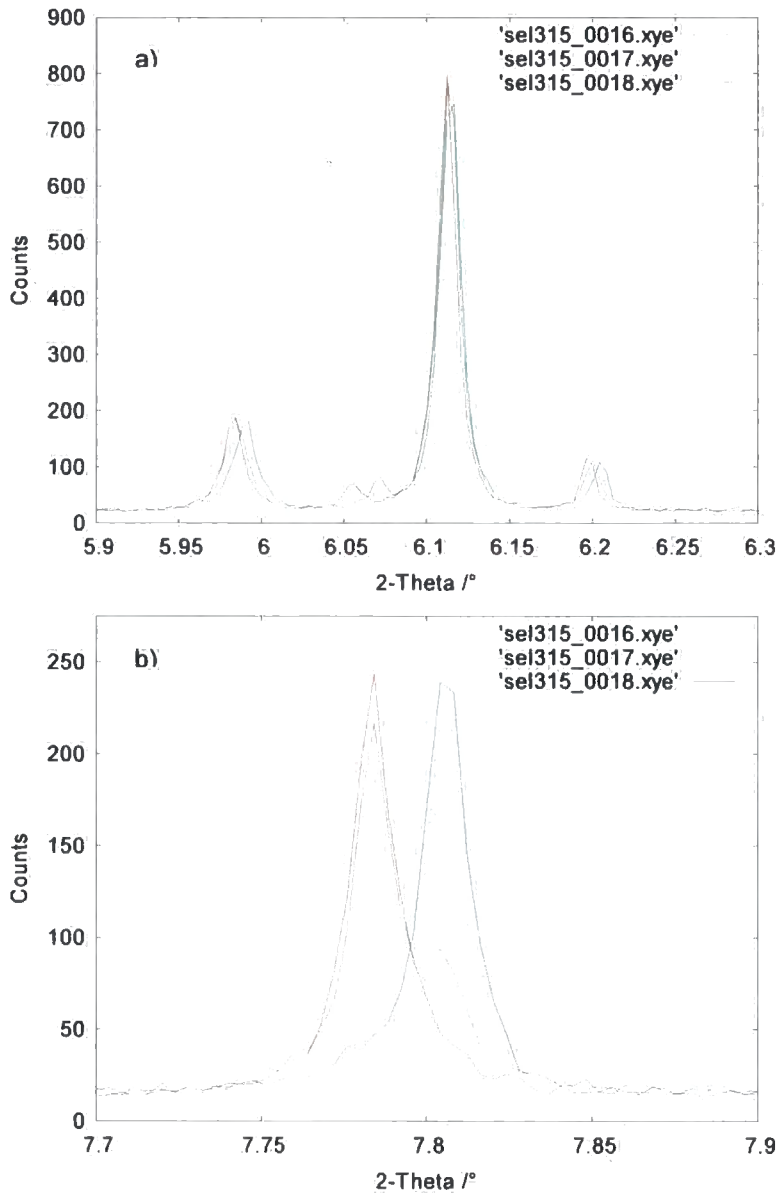

Figure 4.8 Comparison of individual peaks in the scans immediately below (16, blue), during (17, green) and above (18, red) the phase transition at 325 K. Peaks are indexed using the subcell model. a) The 311, 302, 020 and 400 reflections are shown. b) The 004 reflection.

4.2.4 1D and 2D ^{31}P solid state NMR studies

From VT powder diffraction studies two phase transitions have been suggested in α-$(MoO_2)_2P_2O_7$. However, due to the dominance of the heavy molybdenum atoms within the structure, and the very small changes observed in the XRD, little information is available about the structure below the phase transition.

α-$(MoO_2)_2P_2O_7$ contains three elements that can be probed by solid state Magic Angle Spinning NMR. ^{95}Mo is a quadrupolar nucleus with low receptivity and hence not an ideal nucleus for study by NMR. Due to the low natural abundance of ^{17}O – and the need to isotopically enrich the material – it was decided to initially investigate the structure using ^{31}P NMR. This was done in collaboration with Anne Soleilhavoup from the solid state NMR group in Durham. Experiments were undertaken using the conditions and pulse sequences described in Section 2.4.2.

In the published subcell model,[2] there are two crystallographically unique P atoms in P_2O_7 groups which are formed by corner sharing a $P1O_4$ and a $P2O_4$ tetrahedron through an O5 corner. The remaining 3 vertices of the PO_4 units corner-share with MoO_6 octahedra. As such it would be expected that the two unique P atoms would have similar chemical shifts. A series of VT 1D and 2D ^{31}P studies were carried out on a sample of α-$(MoO_2)_2P_2O_7$, SEL251. These are shown in Figure 4.9 (1D) and Figures 4.10a) and 4.10b) (2D), labelled with the set temperatures on the controller. The real temperatures have been determined to be accurate to ± 5 K from experiments undertaken with a $PbNO_3$ standard.

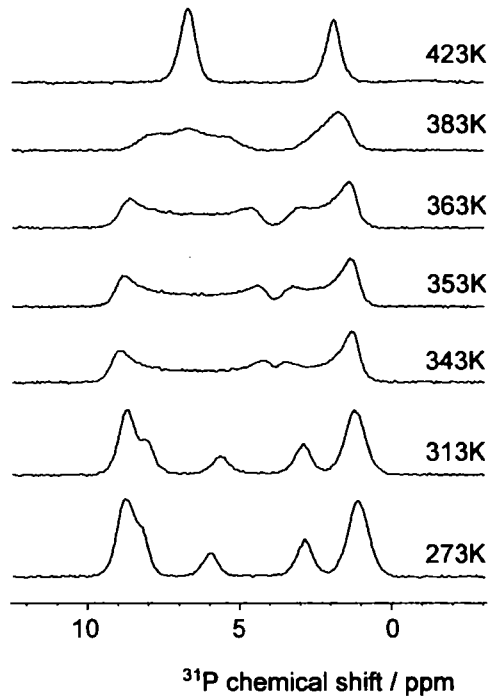

Figure 4.9 VT 1D ^{31}P NMR data recorded on α-$(MoO_2)_2P_2O_7$ (SEL251) recorded with the sample spinning at 5 kHz.

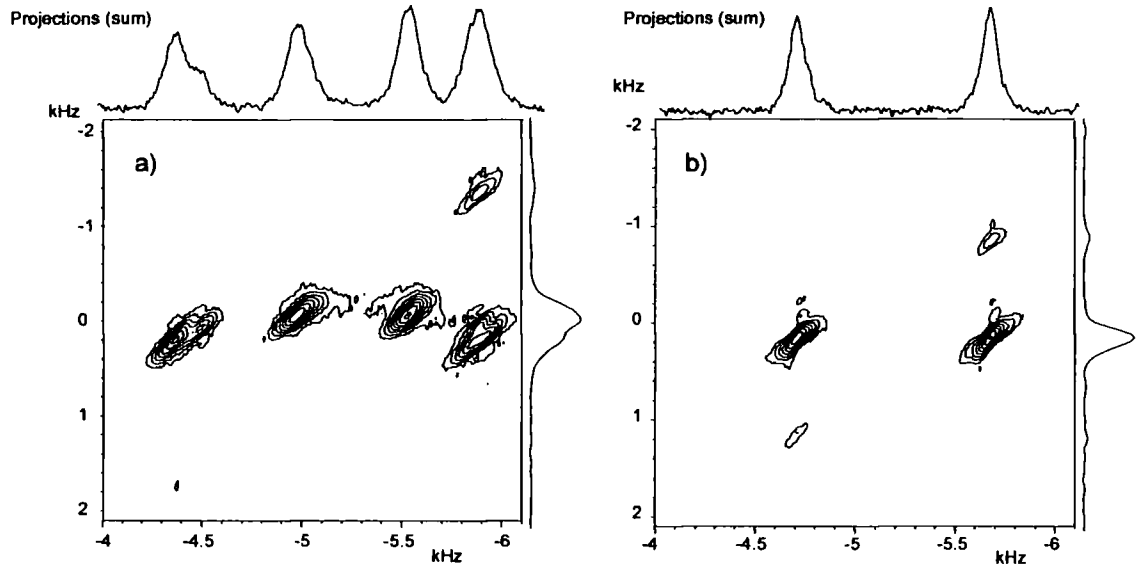

Figure 4.10 2D INADEQUATE experiments on α-$(MoO_2)_2P_2O_7$ (SEL251) at a) 273 K and b) 423 K. The sample was spun at a speed of 15 kHz.

These spectra clearly show that the number of P environments within the structure changes as a function of temperature. From the patterns recorded at 423 K (above both phase transition temperatures), there are two P resonances present in both the 1D (Figure 4.9) and 2D (Figure 4.10b)) NMR spectra. Analysis of the intensity of the 1D signals with mixing time, τ, gave identical through-bond J-couplings to 2 decimal places (14.60 Hz), suggesting they couple to each other. The 2D spectrum confirms the coupling between these two P atoms. This leads to the conclusion that the two resonances arise from 2 P atoms within a P_2O_7 group. This is entirely consistent with the subcell structural model proposed by Kierkegaard.[2] Reintroduction of the dipolar coupling between two equivalent P sites by rotational resonance leads to the weak autocorrelations (resonances on the diagonal) in the INADEQUATE experiments.

On cooling to 273 K the spectra are more complicated. There are 5 resonances with varying intensity. These peaks were deconvoluted (Figure 4.11) into the 5 different peaks and are labelled a-e for discussion. The approximate intensity ratio of a:b:c:d:e is 2:1:1:1:3. J-couplings were calculated for each of these peaks from spin-echo measurements. These are given in Table 4.4.

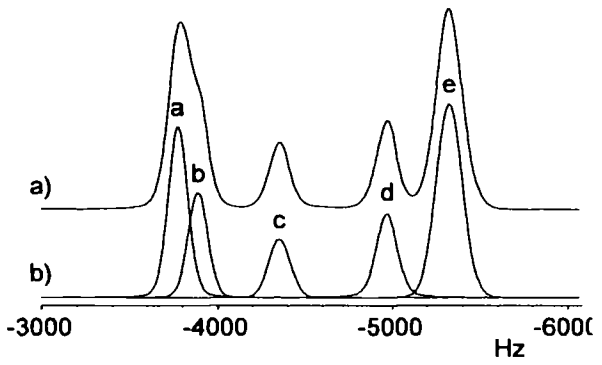

Figure 4.11 The deconvolution of the 1D ^{31}P NMR spectrum of α-$(MoO_2)_2P_2O_7$ at 273 K.

Table 4.4 Values of the P-P J-coupling calculated for the resonances present in the 1D spectrum at 273 K.

Signal	J-Coupling /Hz
a	10.3(5)
b	9.1(5)
c	29.2(5)
d	29.8(5)
e	11.8(5)

From this table, the signals a/b/e and c/d were found to have essentially identical J-coupling values. The data are therefore consistent with the presence of 4 P_2O_7 groups, 3 $O_3P_{a/b}$-O-P_eO_3 groups and one O_3P_c-O-P_dO_3 group, with the former three groups being structurally very similar.

The intermediate temperature spectra are discussed further in Section 4.5.

4.3 High temperature structure refinement

The variable temperature studies performed using X-ray and neutron diffraction data and ^{31}P solid state NMR, have provided evidence for the formation of a low temperature superstructure. The published model[2] for α-$(MoO_2)_2P_2O_7$ provides a starting point from which to be able to solve the superstructure, and this will be described in Section 4.4.

The ^{31}P NMR data have indicated that the high temperature structure contains 2 unique P atoms, as contained in the subcell model, originally published by Kierkegaard. The bond lengths and angles originally reported for this material are, however, far from characteristic for MoPO species. Individual synchrotron, neutron and a combined synchrotron/neutron refinement were performed to determine the high temperature structure more precisely.

4.3.1 High temperature synchrotron data

Data were recorded on a sample of α-$(MoO_2)_2P_2O_7$ (SEL315) at 423 K, on beamline ID31 at the ESRF. The data were recorded on the same sample as used to record the variable temperature data (Section 4.2.3). Data processing was as described in that section. Diffraction patterns were recorded

as outlined in Table 3.7. In order to obtain better statistics at lower *d*-spacings, four scans were recorded over two different 2θ ranges, and then normalised and summed together. The first set of scans was recorded over the 2θ range 0-35 ° 2θ, and the second set of scans was recorded between 10-35 ° 2θ.

Table 4.5 Data collection parameters for the high temperature data recorded on α-$(MoO_2)_2P_2O_7$ (SEL315), at the ESRF on station ID31, ch2627_sel315_423K_long.xye.

Data Collection Parameters	Values
λ /Å	0.35285(8)
Maximum 2θ Range /°	0-35
Total scan time /min	120
Temperature /K	423
Number of scans	8

A total of 78 parameters were refined over the range 2-30 ° 2θ. These included 14 global parameters (12 background coefficients, a zero error and 1 parameter to describe axial divergence) and 36 parameters to model the subcell phase (3 lattice parameters, 28 atomic coordinates, scale parameter, 13 atomic displacement parameters, 4 peak shape parameters, and 15 parameters to define an *hkl* dependent peak shape, including 1 scale parameter and 14 coefficients of an 8^{th} order spherical harmonic function). The final fit had an R_{wp} of 7.85 %. The magnitude of the extra peak width convolution from the *hkl* dependent spherical harmonic function was between 0 and 0.02 ° fwhm for the various reflections.

4.3.2 High temperature neutron data

Data were recorded on a sample of α-$(MoO_2)_2P_2O_7$ (SEL311b) sent to beamline BT-1, the high resolution neutron powder diffractometer at the NCNR, for investigation into the high temperature structure. A Cu(311) monochromator with a 90° take-off angle, λ = 1.5403(2) Å, and in-pile collimation of 15 minutes of arc were used. Data were collected over the range of 3-168 ° 2θ with a step size of 0.05 °. A scan was recorded in the CCR at 500K. These details are summarised in Table 4.6. Data processing information is given in Section 2.3.8.

Table 4.6 Data collection parameters for high temperature data recorded at NIST on station BT1, MoOPO058.xye.

Data Collection Parameters	Values
λ /Å	1.5403(2)
2θ Range /°	3-168
Total scan time /hrs	7
Temperature /K	500

A total of 82 parameters were refined over the 2θ range 3-165 °. These included 17 global parameters (15 background coefficients, a zero error and 1 parameter to model axial divergence) and 21 parameters to model the subcell phase (3 lattice parameters, 28 atomic coordinates, a scale parameter, 13 isotropic displacement parameters, 4 peak shape parameters). The remaining 16 parameters were used to model the peaks arising in the scan file from an aluminium heat shield as a Pawley phase that was positioned around the sample can to better maintain sample temperature (1 lattice parameter, 4 peak shape parameters, 11 intensities). Two 0.1 ° regions of the scan were excluded from the refinement; this exclusion did not significantly alter the quality of the fit. The final fit had an R_{wp} of 6.48 %.

4.3.3 Combined high temperature refinements using synchrotron and neutron data

The input files that were used for each of the individual synchrotron and neutron refinements were used as the starting components for a combined refinement. All of these input files are included in the E-Appendix. The data sets used for these refinements were recorded at 423 K (synchrotron) and 500 K (neutron). Figure 4.7 indicates that the structure above the second phase transition at 377 K doesn't change. Hence, the assumption that the atomic coordinates are the same within both data sets is reasonable, with slight differences due to thermal expansion being accounted for in the two sets of cell parameters for each of the data sets. However, the differing temperatures between the data sets will have an effect on the thermal displacement parameters for each set of data. To this end, an additional line was added to the refinement of the synchrotron data as follows:

```
Fix_Biso (p2,0)
```

This macro serves to scale the peaks within the X-ray component by addition or subtraction of a constant value to the thermal parameters determined predominantly from the neutron data.

A total of 104 parameters were refined. For the X-ray model a total of 22 parameters were refined, including 12 background coefficients, a zero error, 1 parameter to describe axial divergence, 3 lattice parameters, a scale parameter and 4 peakshape parameters. The X-ray model also included a fixed 8^{th} order spherical harmonic to describe an *hkl* dependent peak shape, as described in Section 4.3.1. A total of 41 parameters were used to describe the model of the neutron data set, these included 15 background coefficients, a zero error and 1 parameter to describe axial divergence, 3 lattice parameters, a scale parameter and 4 parameters to model the peakshape. An additional 16

parameters were required to model the peaks arising from the aluminium heat shield (1 lattice parameter, 11 intensities and 4 parameters to model the peakshape). There were 28 atomic positions and 10 isotropic displacement parameters refined.

Data sets were weighted so that they gave an approximately equal contribution to the final R_{wp}. It was concluded from these results that the optimal value for the x parameter in the weighting equation was 4. This value ensured the overall R_{wp} was calculated from approximately equally weighted X-ray and neutron data sets. This value has hence been used in all subsequent refinements unless indicated otherwise.

The model was initially refined over the same d-spacing range in each data set. The atomic positions were randomised after each convergence of the model and re-refined; a total of 10,000 iterations were carried out to ensure the global minimum had been found. Following the simulated annealing, the 2θ ranges for both datasets were extended in order to obtain more accurate atomic coordinates. The value calculated for the parameter p2 (the U_{iso} scaling term included in the synchrotron data refinement) during simulated annealing was zero within a standard uncertainty. This parameter was fixed to be zero. The new 2θ ranges were 2-34 ° (synchrotron) and 5-140 ° (neutron). The Rietveld fits for the model to the synchrotron and neutron data is given in Figures 4.12, 4.13 and 4.14.

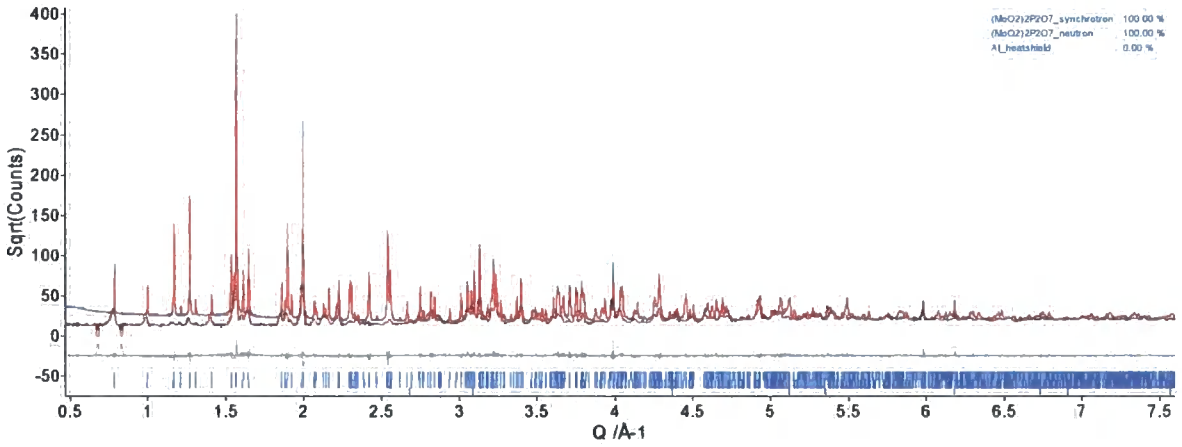

Figure 4.12 Refinement of both the synchrotron and neutron data sets using refined coordinates over a larger d-spacing range. The range 0.5 to 7.5 $Å^{-1}$ in Q is shown. The overall R_{wp} for this fit was 7.57 %. The figure shows the experimental synchrotron data in blue, the experimental neutron data in black, the calculated patterns in red and the difference plots in grey.

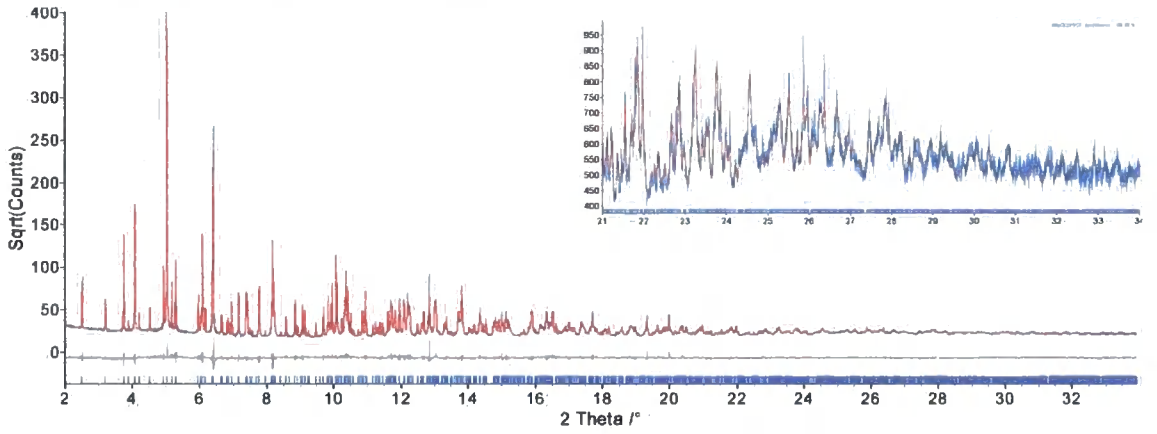

Figure 4.13 Fit of the model to the synchrotron data set. Inset: The 2θ range 21-34 °. The R_{wp} for this fit was 8.15 %. The figure shows the experimental data in blue, the calculated pattern in red and the difference plot in grey.

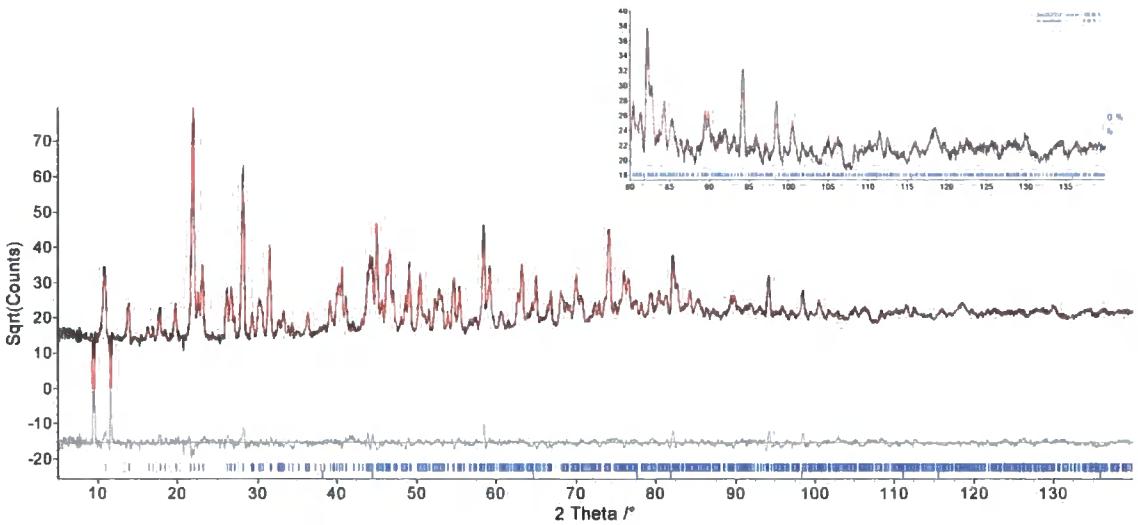

Figure 4.14 Fit of the model to the neutron data set. Inset: The 2θ range 80-140 °. The R_{wp} for this fit was 6.64 %. The figure shows the experimental data in black, the calculated pattern in red and the difference plot in grey.

The quality of the model's fit to the data out to large 2θ values indicates that this model is a good description of the high temperature structure. Table 4.7 contains selected refinement details for each of the synchrotron, neutron and combined refinements. Table 4.8 contains the atomic coordinates and Tables 4.9 and 4.10 contain the bond lengths and P-O-P bridging angles.

Table 4.7 Selected refinement details for the high temperature structure of α'-$(MoO_2)_2P_2O_7$.

	Synchrotron	Neutron	Combined	
Section	4.3.1	4.3.2	4.3.3	
a /Å	12.6576(1)	12.6774(4)	12.6581(1)	12.6794(5)
b /Å	6.3095(1)	6.3052(2)	6.3097(1)	6.3059(2)
c /Å	10.4162(1)	10.4122(3)	10.4164(1)	10.4139(4)
Volume /Å^3	831.86(1)	832.28(4)	831.94(1)	832.64(5)
Space Group	*Pnma*	*Pnma*	*Pnma*	
Number of Parameters	78	82	104	
R_{wp} /%	7.85	6.48	7.57	
GOF	2.85	1.492	3.28	
R_{Bragg} /%	3.38	3.52	3.92	4.22
2θ range /°	2-30	5-165	2-34	5-140
Temperature /K	423	500	423	500

Table 4.8 The refined structural parameters for the high temperature structure of α'-$(MoO_2)_2P_2O_7$. B_{iso} values quoted are from the 500 K neutron refinement.

Atom Label	Atom Type	*x*	*y*	*z*	Occ	B_{iso} /Å^2
Mo1	Mo	0.9979(1)	0.25	0.2234(1)	1	0.86(22)
Mo2	Mo	0.2511(1)	0.25	0.0152(1)	1	0.90(26)
P1	P	0.6575(3)	0.25	0.9908(3)	1	0.91 (70)
P2	P	0.9710(3)	0.25	0.6912(3)	1	1.02(71)
O1	O	0.2741(3)	0.5570(6)	0.0244(4)	1	2.22(87)
O2	O	0.0307(3)	0.5556(6)	0.2258(3)	1	1.40(77)
O3	O	0.8938(5)	0.25	0.5812(6)	1	3.22(16)
O4	O	0.5955(5)	0.25	0.1080(6)	1	2.36(13)
O5	O	0.0855(5)	0.25	0.6291(7)	1	3.45(15)
O6	O	0.1631(4)	0.25	0.1389(5)	1	1.42(12)
O7	O	0.3859(5)	0.25	0.1880(5)	1	2.33(12)
O8	O	0.1715(5)	0.25	0.8870(6)	1	3.76(18)
O9	O	0.4506(4)	0.25	0.4249(5)	1	2.16(12)

Table 4.9 Bond lengths and bond valence sum values calculated from the published model and the models refined using the neutron and synchrotron data both individually and in the combined refinement described above. Standard uncertainties for the published model were not calculated as the coordinates themselves were not refined. BVSs were calculated using the values of Brese and O'Keefe.[5]

Central Atom	Apex Atom	Published Model Bond Length /Å	Synchrotron Bond Length /Å	Neutron Bond Length /Å	Combined Bond Length /Å
Mo1	O9:1	1.835	1.6561(92)	1.663(10)	1.6565(56)
	O7:1	1.950	1.7030(93)	1.692(10)	1.6930(59)
	O2:0	1.858	1.9802(59)	1.9727(59)	1.9716(38)
	O2:1	1.858	1.9802(59)	1.9727(59)	1.9716(38)
	O4:1	1.898	2.1355(96)	2.135(11)	2.1482(61)
	O6:0	2.080	2.2434(81)	2.2739(97)	2.2717(55)
	BVS /vu	6.04	6.29	6.31	6.32
Mo2	O8:0	1.842	1.674(98)	1.688(12)	1.6737(66)
	O6:0	1.884	1.7246(85)	1.6903(94)	1.7043(55)
	O1:1	1.957	1.9486(57)	1.9553(56)	1.9603(38)
	O1:0	1.957	1.9486(57)	1.9553(56)	1.9603(38)
	O3:1	2.107	2.098(11)	2.078(12)	2.0689(68)
	O7:0	2.185	2.4662(97)	2.4942(99)	2.4827(59)
	BVS /vu	5.06	6.08	6.19	6.19
P1	O1:4	1.588	1.463(10)	1.461(12)	1.4524(69)
	O1:5	1.588	1.5117(62)	1.511(14)	1.5022(42)
	O4:0	1.605	1.5117(62)	1.5115(68)	1.5022(42)
	O5:1	1.644	1.539(12)	1.5115(68)	1.5466(77)
	BVS /vu	3.98	5.22	5.32	5.31
P2	O3:0	1.548	1.460(11)	1.524(13)	1.5004(41)
	O5:0	1.599	1.4747(61)	1.5320(73)	1.5004(41)
	O2:4	1.610	1.4747(61)	1.5320(73)	1.5061(42)
	O2:5	1.610	1.619(12)	1.552(13)	1.5892(77)
	BVS /vu	4.15	5.27	4.82	4.99

Table 4.10 P-O-P bond angles calculated from the published model and the models refined using the neutron and synchrotron data both individually and in a combined refinement described above. Standard uncertainties for the published model were not calculated as the coordinates themselves were not being refined.

Bond Angle /°	Published Model	Synchrotron	Neutron	Combined
P1-O5-P2	141.0	147.2(8)	155.2(9)	150.2(5)

This refined model has given a good fit to the data and the bond distances are found to be chemically sensible. The distributions of bond lengths in the polyhedra for the published model were described in Section 4.1. For the refined model a new pattern has emerged with both of the Mo centred octahedra, having 2 short bonds, 2 medium and 2 long bond lengths. MoO_6 octahedra are known to be distorted due to the displacement of the metal ion away from the centre of the octahedron.[6]

This distribution of bond lengths can be rationalised due to the zigzag nature of the Mo octahedral chain. A short portion of the chain is reproduced in Figure 4.15. The shortest bond in each of the octahedra is to the terminal oxygen (O8 and O9). The bonds opposite to O8 and O9, namely Mo2-O7 and Mo1-O4 respectively, are "long" bonds. However, these two lengths differ significantly between the two octahedra, being 2.4827(59) and 2.1482(61) *Å* respectively. The former bond is part of the Mo-O-Mo backbone, whereas the latter bond is perpendicular to the Mo chain, forming an Mo-O-P linkage. These structural differences are the origin of the significant differences between these two long bond lengths.

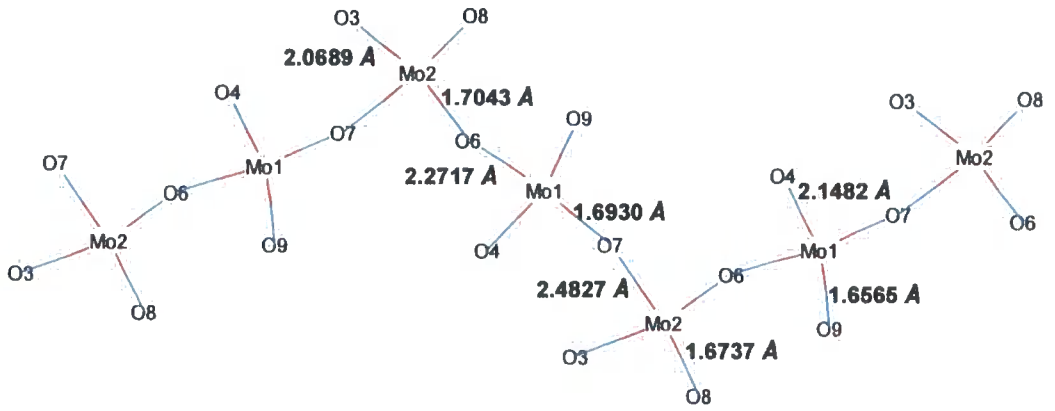

Figure 4.15 A labelled 2D section of the MoO_6 chain structure in α-$(MoO_2)_2P_2O_7$. The chains are in the *ac* plane.

These differences in the Mo octahedra containing a double Mo=O bond are discussed in a review of such structures by Costentin and coworkers.[7] They state that the Mo atom is displaced out of the basal plane towards one of the oxygens, forming a short (~1.65 *Å*) molybdenyl bond. The bond "opposite" the short bond is longer, with lengths varying from ~ 2.15 *Å* in a Mo-O-P arrangement, 2.40 *Å* in a Mo-O-Mo double octahedral arrangement and between 2.7 and 2.9 *Å* for chains of molybdenum octahedra. Our refined values are consistent with these findings. Within the *ac* plane of the structure, the Mo-O bond lengths within the zigzag chain are found to alternate long/short along its length. The presence of a longer Mo-O bond length causes the next O-Mo bond length to be shorter to maintain the bond valence on the O atom. The short Mo2-O6 bond also causes the Mo2-O3 bond to be longer. The remaining two bonds on each of the octahedra are medium length (Mo1-O2 and Mo2-O1), not pictured.

The bond valence sums for the refined model are much improved over those from the published structural model. The refined model is also consistent with the ^{31}P solid state NMR results in Section 4.2.4. All the input files and the bond lengths calculated for this model are included in the E-Appendix.

4.3.4 Combined low temperature refinements using the high temperature model

Following successful refinement of the high temperature structure, the atomic coordinates were used to investigate their ability to model the low temperature data. A comparable scan was recorded at the ESRF and NIST on the same samples at 250 K. Data collection parameters are given in Tables 4.11 and 4.12.

Table 4.11 Data collection parameters for low temperature data recorded at the ESRF on station ID31, ch2627_sel315_250K_long.xye.

Data Collection Parameters	Values
λ /Å	0.35285(8)
Maximum 2θ Range /°	0-35
Total Length of Scans /min	120
Temperature /K	250
Number of scans	8

Table 4.12 Data collection parameters for low temperature data recorded at NIST on station BT1, MoOPO054.xye.

Data Collection Parameters	Values
λ /Å	1.5403(2)
Maximum 2θ Range /°	3-168
Total Length of Scans /hrs	7
Temperature /K	250

The input file used in Section 4.3.3 was used to refine the model, fixing the coordinates of the high temperature solution to enable direct comparison. A total of 73 parameters were refined. The parameter used to model the neutron axial divergence was fixed to the value refined during the high temperature refinements. The overall R_{wp} for this fit was 9.60 %. The final refinements are given below in Figures 4.16 and 4.17 for direct comparison with Figures 4.13 and 4.14.

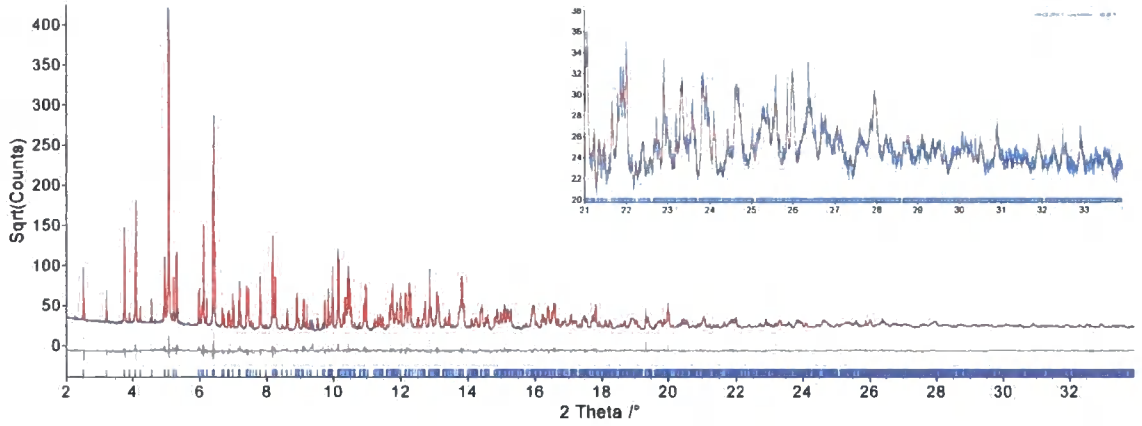

Figure 4.16 The fit of the model to the low temperature synchrotron data set. Inset: The 2θ range 21-34 °. The R_{wp} for this fit was 9.29 %. The figure shows the experimental data in blue, the calculated pattern in red and the difference plot in grey.

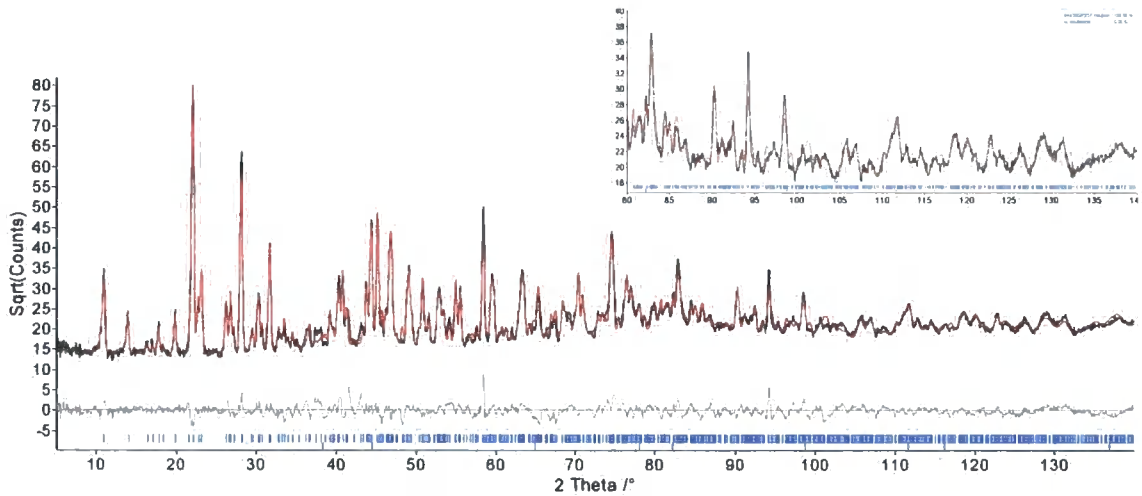

Figure 4.17 The fit of the model to the low temperature neutron data set. Inset: The 2θ range 80-140 °. The R_{wp} for this fit was 10.20 %. The figure shows the experimental data in black, the calculated pattern in red and the difference plot in grey.

The R_{wp}s for the high temperature *vs.* low temperature data are 8.15/9.29 % (synchrotron) and 6.64/10.20 % (neutron). It is evident from the figures above and the increased R_{wp} values for each of the individual/overall refinements that the model does not describe the low temperature data recorded as well as the high temperature data.

4.4 Superstructure identification and structure solution

4.4.1 *In-house* X-ray studies

Evidence for the presence of a phase transition in this material has been obtained from three different methods, namely the discontinuities in variable temperature data (both X-ray, neutron and solid state

NMR), a poor fit between the subcell model and the neutron diffraction data at low temperature, and the presence of extra peaks in the long synchrotron data collection.

From the temperature variation of the lattice parameter and NMR data, two phase transitions have been postulated within the material. A series of X-ray measurements were performed on the Bruker d8 diffractometer, d8_03559-03565, at 303, 313, 333, 353, 373, 423 and 304 K to further investigate this. The sample (SEL251) was prepared by grinding and sprinkling onto an amorphous silica disc smeared with Vaseline as adhesive and mounted into an Anton Paar HTK1200 furnace. The scans were recorded from 5-40 ° 2θ in order maximize signal-to-noise at larger *d*-spacings. A step size of 0.017 ° was used recording for 72 s per step; each scan was recorded over 47 hours. The scans are shown overlaid in Figure 4.18.

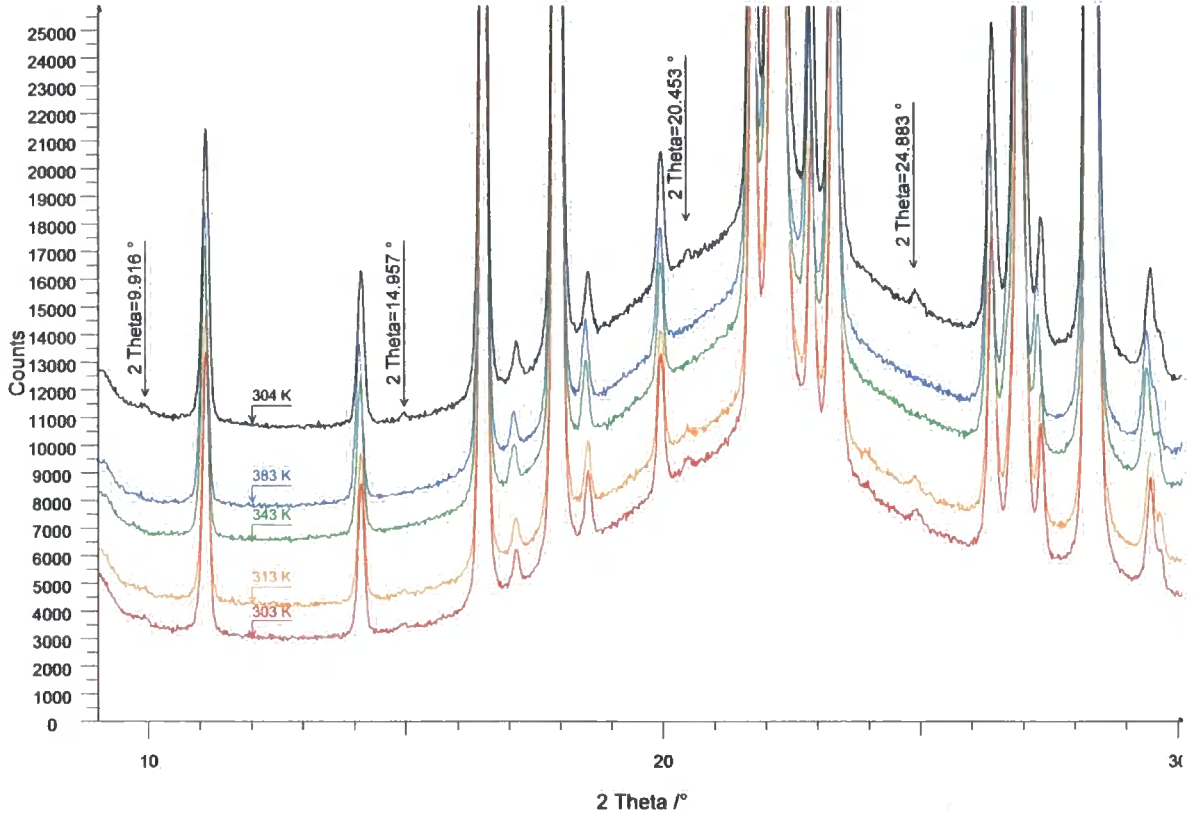

Figure 4.18 Powder diffraction patterns recorded between 303 K and 423 K; figure shows each of the scans offset in *y*, in the 9-30 ° 2θ region. The four peaks highlighted are superstructure peaks that disappear on heating from 303 to 423 K. The largest of these peaks has 0.25 % of the intensity of the most intense peak in the pattern.

Visual inspection of scans d8_03559 to d8_03565 shows the presence of 4 very weak peaks in the scans below the phase transition temperature (323 K), *i.e.* recorded at 303 and 313 K. At higher temperatures these peaks are absent; on cooling again to 304 K the peaks reappear. The peaks are weak but distinguishable above the background noise. The observation that peaks reappear on cooling indicates that they arise due to a superstructure forming below 323 K. If these peaks had been due to a volatile impurity the peaks would not reappear. The *d*-spacings and 2θ values ($CuK_{\alpha 1}$

radiation) for these peaks are given in Table 4.13; the positions of these peaks are not predicted by the subcell model.

Table 4.13 *d*-spacings and positions for superstructure peaks observed by X-ray and neutron diffraction on samples of α-$(MoO_2)_2P_2O_7$.

d-spacing /Å	2θ /° (Cu λ 1.5406 Å)	2θ /° (ID31 λ 0.3529 Å)	2θ /° (NIST λ 2.079 Å)
9.01	9.809	2.244	13.25
5.98	14.80	3.381	20.02
4.35	20.40	4.649	27.65
3.57	24.92	5.665	33.86

4.4.2 Electron diffraction studies

Electron diffraction patterns were recorded by Prof. RL Withers at Australian National University on a sample of α-$(MoO_2)_2P_2O_7$ (SEL244). Initial investigations revealed satellite reflections at:

$$G \pm m/4[2,\bar{1},0]^* \qquad (4.1)$$

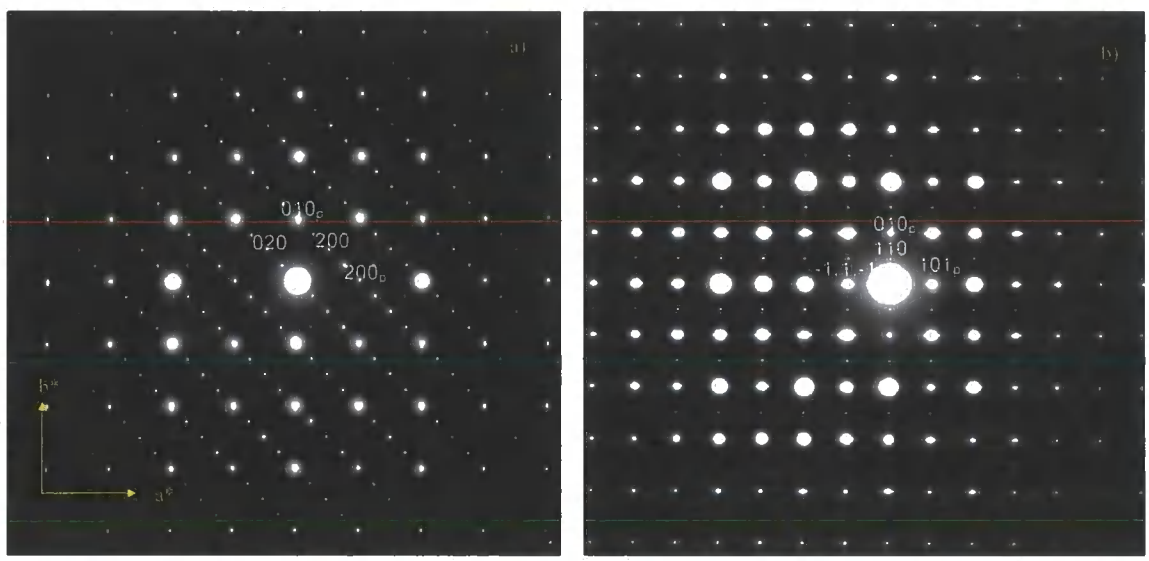

Figure 4.19 Electron diffraction patterns of α-$(MoO_2)_2P_2O_7$ with zone axes a) [001] and b) [1,-1,2], indexed with respect to both the *Pnma* parent sub-structure (labelled with the subscript p) and the supercell structure. Note the characteristic extinction condition F(*hk*0) = 0 unless *h*=2*n* in a), requiring the presence of an *a*-glide perpendicular to *c*.

These satellite peaks were indexed to a supercell, with the transformation matrix in Equation 4.2.

$$\begin{pmatrix} 1 & 2 & 0 \\ \bar{1} & 2 & 0 \\ 0 & 0 & 1 \end{pmatrix} \begin{pmatrix} a_{sub} \\ b_{sub} \\ c_{sup} \end{pmatrix} = \begin{pmatrix} a_{sup} \\ b_{sup} \\ c_{sup} \end{pmatrix} = \begin{pmatrix} 17.83\,Å \\ 17.83\,Å \\ 10.38\,Å \end{pmatrix} \qquad (4.2)$$

Pawley fits of both the subcell and supercell (in space group *P*2 for reasons described below) to the room temperature X-ray diffraction data of Figure 4.18 are shown in Figure 4.20. A total of 61 parameters were refined for the subcell Pawley fit: 18 background terms, a height correction and 1 parameter to model axial divergence, 3 lattice parameters, 4 TCHZ peak shape parameters and 34 parameters for the intensities of the subcell peaks within the range studied. This led to a final R_{wp} of 6.19 %. The Pawley fit using the supercell required 244 parameters. The extra 183 parameters were due to the intensities of the extra reflections not predicted in the subcell model. Figure 4.20a) shows the ability of the supercell to predict reflections at the positions of the extra reflections seen in the X-ray data. The R_{wp} is lower for this dataset, 2.981 %. The input files for these refinements are in the E-appendix.

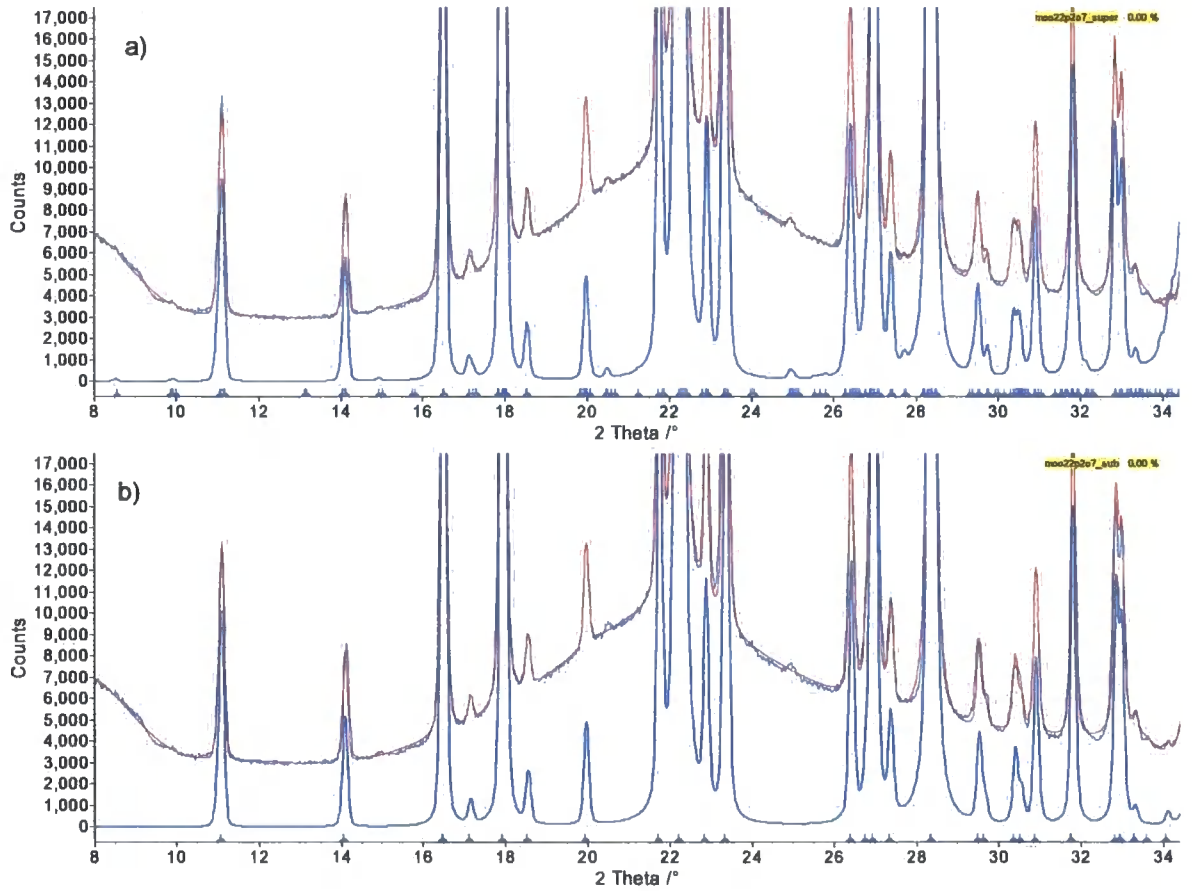

Figure 4.20 The Pawley fits of scan d8_03559. a) The new supercell derived from the electron diffraction data in space group *P*2 and b) the subcell model. Weak peaks at 2θ = 9.809, 14.80, 20.40 and 24.93 ° are all predicted by the supercell. The figure shows the experimental data in blue and the calculated pattern in red.

4.4.3 Choices of lattice type and space group

Following the cell determination, the next step in structure solution was to determine the space group. The systematic absences (*hk0*) *h*=2n in the electron diffraction suggested space group symmetry *P*–*a*. However, with the transformation matrix above, it's not possible to retain orthorhombic symmetry if standard group-subgroup relationships for a displacive phase transition are assumed.[8] For this

reason, reduction of the lattice symmetry from orthorhombic to monoclinic or triclinic must occur, though it's clear that β is approximately 90 ° from both electron and powder diffraction data. A full investigation of potential space groups was undertaken to check the assignment. Figure 4.21 shows the possible space groups, generated using the supergroup-subgroup theory contained within the ISODISPLACE web-based programme.[9]

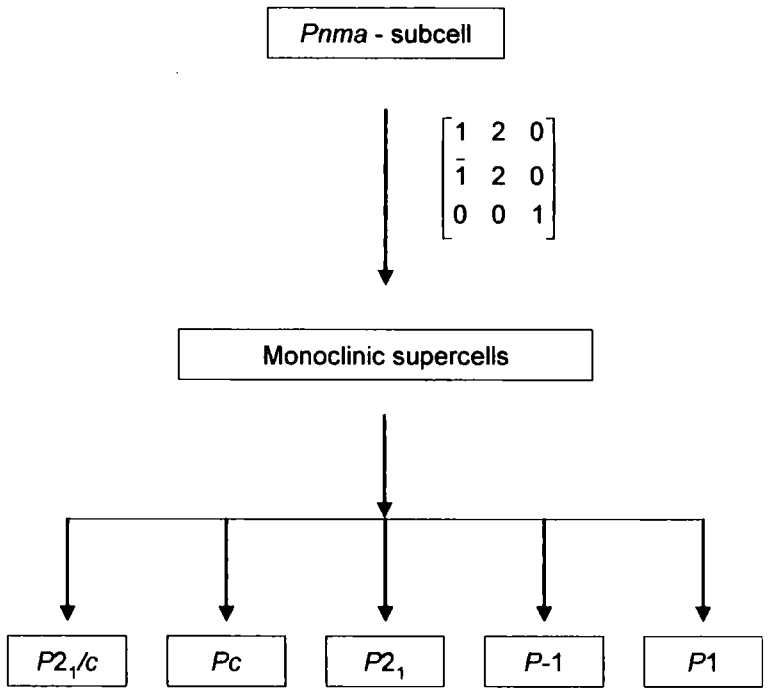

Figure 4.21 Space group "tree" constructed using the calculated transformation matrix.

By consideration of group theory alone, the reduction of symmetry from *Pnma* with the highest retention of symmetry is to the standard setting of $P2_1/c$ (equivalent to $P2_1/a$). It is clear from this tree that there are a large number of potential space groups for the low temperature phase. It became necessary to narrow down the number that would be investigated using the methodology described later in this chapter.

A sample of α-$(MoO_2)_2P_2O_7$ was sent to Prof. P. Shiv Halasyamani in the Chemistry Department at the University of Houston to undergo a Second Harmonic Generation (SHG, Chapter 2.4.3) test. The SHG test returned a negative result, that is, no SHG was observed. Although this is a non-definitive result, it was presumed (in the first instance) that this negative test implied that the material had a centrosymmetric lattice type. This reduced the possible number of space groups given in Figure 4.21 to space groups $P2_1/c$ and $P\bar{1}$. Results from electron diffraction suggest space groups $P2_1/c$ and Pc. Structure solution was therefore carried out initially in space group $P2_1/c$.

4.4.4 Superstructure model and structural refinement in $P2_1/c$

In the standard setting $P2_1/c$, the ac plane is 4 times larger than in the subcell model. The atomic coordinates for the structure in $P2_1/c$ were generated using ISODISPLACE,[9] from the high

temperature structure of Section 4.3.4. There are 8 Mo atoms, 8 P atoms and 44 O atoms present in the asymmetric unit. None of these atoms is on special positions.

An input file was written to restrain bond lengths and angles to allow simulated annealing of the structure, by randomising from the ideal high temperature structure positions. Restraints on terminal and bridging P-O bonds were 1.507 and 1.580 Å respectively. Restraints on the Mo-O bonds were as follows: short 1.65 Å, medium 1.99 Å and long 2.15/2.35 Å. The bond angles were restrained to be 90 and 180 ° in the octahedra and 109.47 ° in the tetrahedra; all restraints had sufficient weighting to retain sensible polyhedral geometry of the structure.

In order to check the plausibility of the structure in this space group initial distance least squares refinements were carried out using the "`only_penalties`" keyword in Topas. This allowed optimisation of the model by minimising the penalty functions applied to the structure. Refinements were performed using a simulated annealing approach in which coordinates were reset to the initial high symmetry values after each convergence. A geometrically sensible model in which all restraints were satisfied was achieved giving a lowest residual of 0.11 %. This information led to the conclusion that the restraints and penalty functions were chemically valid, and structure solution continued using the data as well as the penalties.

Powder diffraction patterns were recorded at 250 K at beamline ID31 at the ESRF and HRPD at ISIS. Data collection parameters are given in Tables 4.11 and 4.14. Refinements were carried out against both the X-ray and neutron data in conjunction with the restraints/penalties described above. The datasets were weighted to ensure they both contributed approximately equally to the refinement, as in Section 4.3.3.

Table 4.14 Data Collection parameters for low temperature data recorded at HRPD. ISIS, HRP39758.xye.

Data Collection Parameters	Values
TOF range /ms	30-130
d-spacing range /Å	0.62-2.70
Temperature /K	250
Data Recorded /μAh	200

A total of 235 parameters were refined during the simulated annealing experiments. These included 12 overall parameters for both datasets, 4 cell parameters, 3 isotropic displacement parameters – 1 for each atom type – and 5 coefficients of a 4th order spherical harmonic function to allow an *hkl* dependent peakshape and the η value for Gaussian/Lorentzian mixing. The peakshapes for the X-ray/neutron datasets were modelled with a TCHZ/TOF peakshape respectively. This was convoluted with the spherical harmonic function scaled to each of the datasets individually. 180 atomic coordinates were also refined. For the X-ray data 23 parameters were refined: 12 coefficients of a Chebychev polynomial to model the background, a zero error, 1 parameter to model axial divergence, a scale parameter, 6 parameters to model a TCHZ peakshape description and the

spherical harmonic scaling term/η ratio parameter. For the neutron data 20 parameters were refined, these were 9 coefficients of a Chebychev polynomial to model the background, an absorption correction, a scale parameter, 3 parameters to model the time of flight x-axis calibration, 1 parameter to model the TOF peakshape and the spherical harmonic scaling term/η ratio parameter described above. For the neutron data 3 parameters were used to model a small amount of intensity arising from the V sample can, namely a cubic lattice parameter, an isotropic displacement parameter and a scale parameter. The same TOF peak shape was used for the sample can as for the main phase under investigation.

Several thousand cycles of randomisation were performed using this file. After each convergence atomic coordinates were randomly moved by up to ± 0.05 (fractional coordinates), with a maximum/minimum limit of ± 0.1 from subcell-derived values. In $P2_1/c$ the model that fitted best to the data had an overall R_{wp} of 5.72 %, with R_{wp}s for each of the X-ray/neutron datasets of 8.48/3.73 % respectively. These fits are shown in Figures 4.22 and 4.23. Selected refinement details are given in Table 4.15.

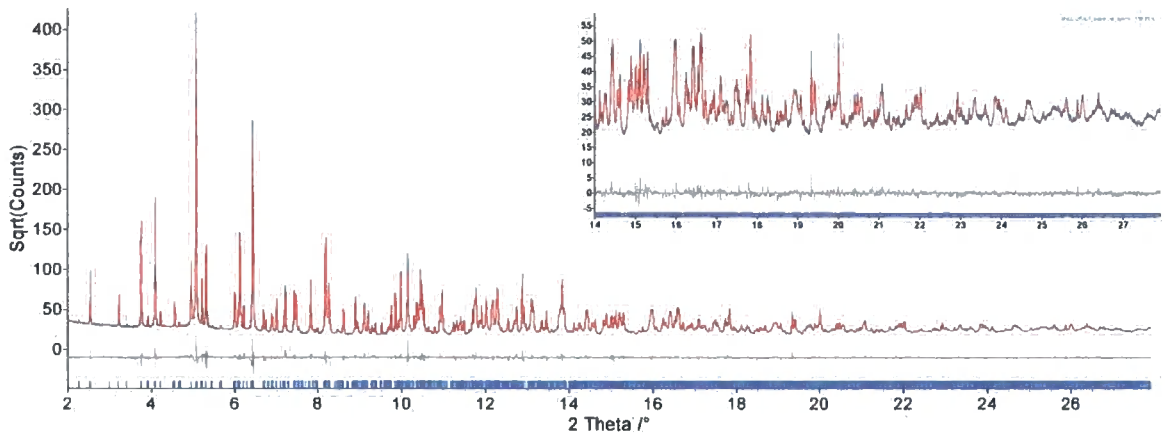

Figure 4.22 Rietveld fit of the superstructure model against the synchrotron data in space group $P2_1/c$. Inset: zoomed region 14-28 ° 2θ. Final R_{wp} for this refinement 8.48 %. The figure shows the experimental data in blue, the calculated pattern in red and the difference plot in grey.

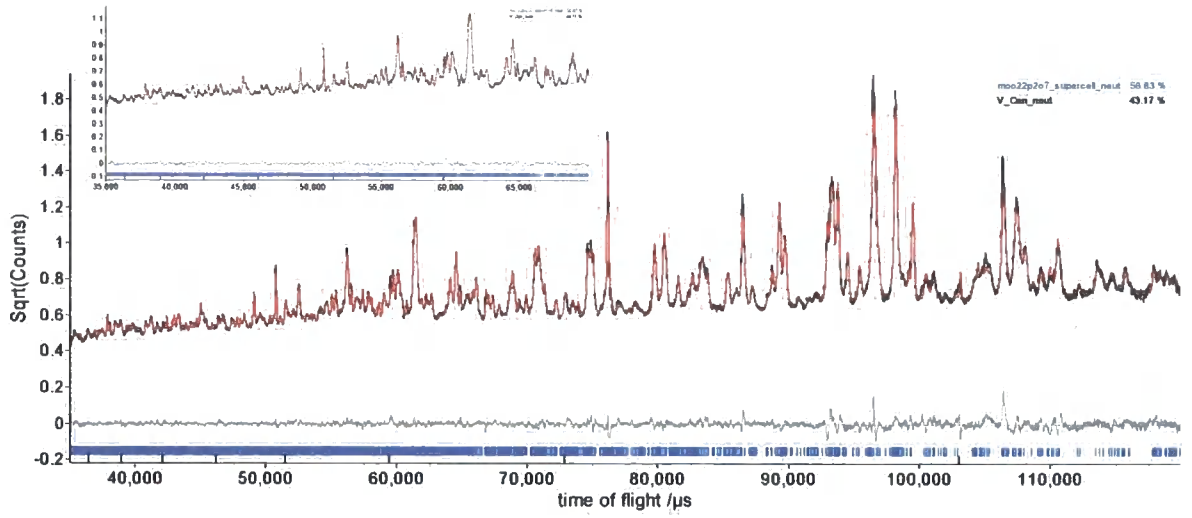

Figure 4.23 Rietveld fit of the superstructure model against the neutron data in space group $P2_1/c$. Inset: zoomed region 35000-70000 μs. Final R_{wp} for this refinement 3.73 %. The figure shows the experimental data in black, the calculated pattern in red and the difference plot in grey.

Table 4.15 Selected crystallographic data and refinement details from the combined X-ray and neutron refinement in space group $P2_1/c$.

Space Group $P2_1/c$			
a /Å	17.8152(3)	Overall R_{wp} /%	5.72
b /Å	10.3673 (1)	X-ray R_{wp} /%	8.48
c /Å	17.8092(3)	Neutron R_{wp} /%	3.73
β /°	90.2015(3)	X-ray R_{Bragg} /%	3.24
Volume /Å^3	3289.23(8)	Neutron R_{Bragg} /%	2.47
Number of Parameters	235	GOF	2.30

The model describes the diffraction data from both the X-ray and neutron experiments well. The magnitude of the extra *hkl* dependent fwhm convolution was between 0 and 0.05 ° for the various reflections. Bond lengths and angles were calculated for all the bonds present within the structure. Due to the large number present, these have not been tabulated but are shown graphically in Figures 4.24 and 4.25. Typical s.u.s for bond lengths were 0.016 Å and for bond angles 0.7 °. The mean values and e.s.d.s of the distributions of the bond lengths are given in Table 4.16. The final input file and spreadsheets of bond length/angle data are included in the E-Appendix.

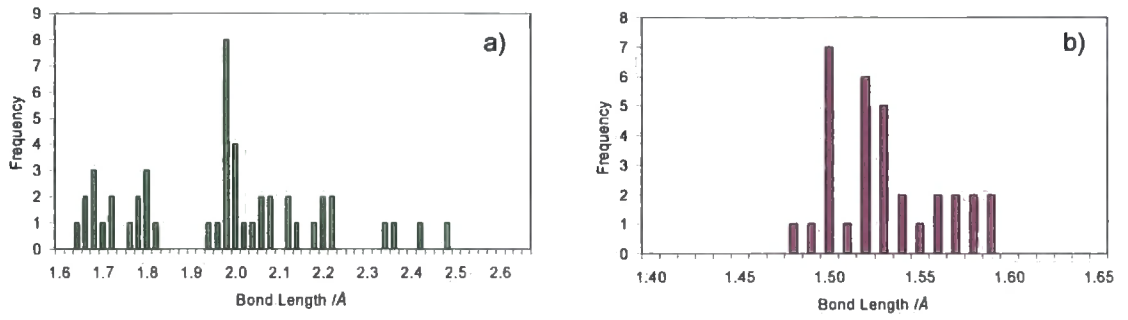

Figure 4.24 Bond lengths from the superstructure model in $P2_1/c$. a) Distribution of Mo-O bonds. b) Distribution of P-O bonds.

Table 4.16 Mean bond lengths and estimated standard deviations for the bond lengths in the $P2_1/c$ structure.

Bond Length	Value (e.s.d.) /Å
Mo-O (short)	1.668(26)
Mo-O (medium)	1.956(123)
Mo-O (long Mo1)	2.202(10)
Mo-O (long Mo2)	2.389(68)
P-O(-Mo)	1.511(17)
P-O(-P)	1.571(13)

At first glance the two histograms in Figure 4.24 do not seem to describe a well defined bond length distribution. The description of the bonding in the high temperature structure was outlined in Section 4.3.1. Based on the structure, the following distribution would be expected for the 48 Mo-O bonds: 8 short bonds (1.65 Å), 8 slightly longer than short bonds (~1.7 Å), 20 medium bonds (2 Å), 8 medium long bonds (2.15 Å) and 4 very long bonds (2.4 Å). This is the distribution that is observed in Figure 4.24a). The P-O bonds are known to be divided into the P-O_t and P-O_b bonds. Table 4.16 shows that these distributions have a mean of ~1.5 and 1.57 Å respectively; however, the distributions have spreads that cause them to overlap, as seen in Figure 4.24b). Bond valence sums are recorded in Table 4.17. Figure 4.25 contains information about the bond lengths and angles within each of the unique P_2O_7 groups within the superstructure.

Table 4.17 Bond valence sum calculations for each of the central atoms within the polyhedra. These were calculated using the values of Brese and O'Keefe.[5]

Central Atom	BVS /vu	Central Atom	BVS /vu
Mo1_1	5.79	P1_1	4.99
Mo1_2	6.09	P1_2	4.90
Mo1_3	5.77	P1_3	5.00
Mo1_4	6.03	P1_4	4.82
Mo2_1	5.99	P2_1	4.99
Mo2_2	5.97	P2_2	4.74
Mo2_3	6.03	P2_3	5.09
Mo2_3	6.12	P2_3	5.09

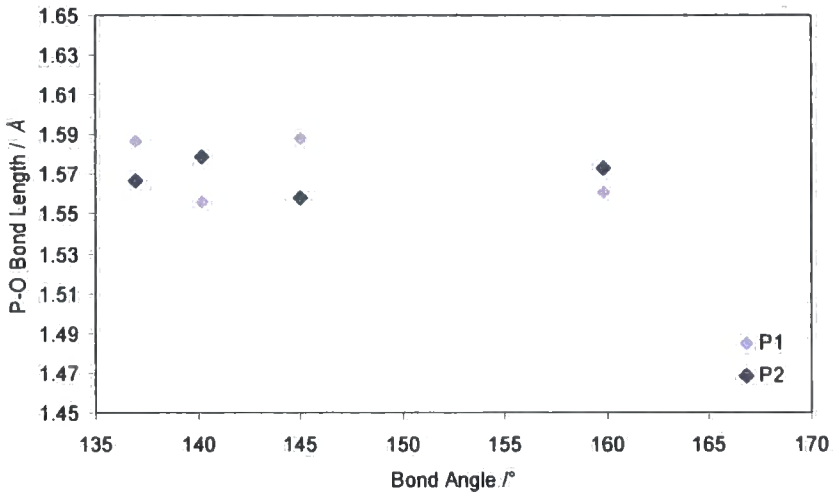

Figure 4.25 A scatter plot of the bond lengths and bond angles present within each of the 4 unique P_2O_7 groups within the structure. Type P1 and P2 atoms have been colour coded.

The P-O-P bond angles observed within the $P2_1/c$ structure have a distribution of 3:1, *i.e.* 3 at ~140 ° and 1 at ~160 °. This is the same distribution of P sites that was found from the ^{31}P NMR results in Section 4.2.4. It is also worth noting that DFT calculations, carried out by Anne Soleilhavoup, suggest that J couplings measured for $P_{a/b}$-O-P_e P_2O_7 groups correspond to P-O-P bond angles around 140 ° whereas P_c-O-P_d groups correspond to a bond angle closer to 180 °. These results are summarised in Table 4.18. The X-ray/neutron refinement is therefore entirely consistent with local information from NMR data.

Table 4.18 Calculated J-couplings of the P atoms within the 4 P_2O_7 groups in the $P2_1/c$ structure (in a slightly earlier modification of the structure).

P-O-P		J-coupling /Hz	
Distance /Å	Angle /°	Experimental	Theoretical
2.901	140		6.6(1)
3.020	141	~ 10(1)	6.6(1)
3.000	144		4.1(1)
3.100	158	~ 29(1)	19.3(1)

4.4.5 Superstructure model and structural refinement in $P\bar{1}$

From the initial consideration of the group theory of the transformation, a structural model was also constructed in space group $P\bar{1}$. In the $P\bar{1}$ model, there are twice as many unique atoms as compared to the $P2_1/c$ structure. Thus there are 16 Mo atoms, 16 P atoms and 88 O atoms present in the asymmetric unit. None of these atoms are on special positions. The process outlined for the $P2_1/c$ structure was followed to build and refine the model in $P\bar{1}$, but with an additional 180 atomic coordinates, two lattice parameters and 9 spherical harmonic coefficients. These refinements are included here for completeness. The model that fitted best to the data had an overall R_{wp} of 4.09 %, with R_{wp}s for each of the X-ray/neutron datasets at 4.86/2.60 % respectively. These fits are shown in Figures 4.26 and 4.27. Selected refinement details are given in Table 4.19.

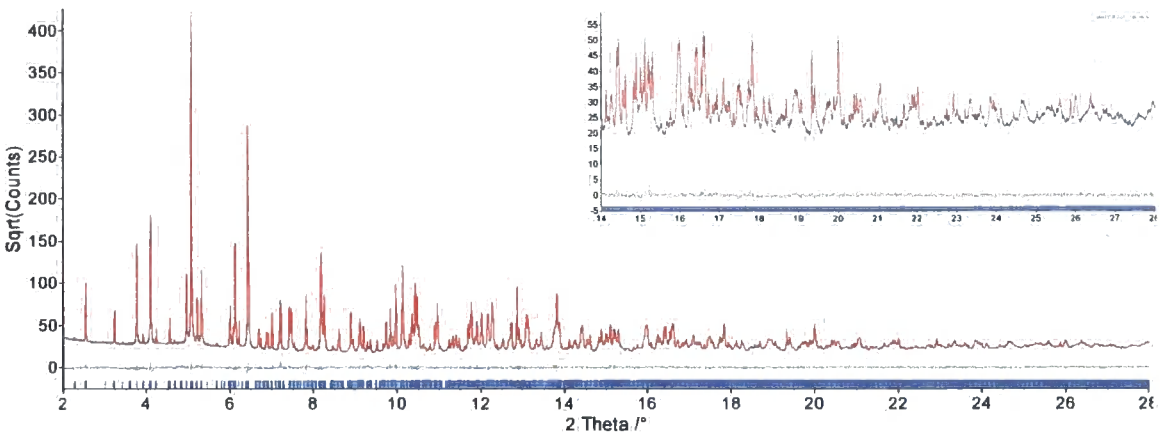

Figure 4.26 Rietveld fit of the superstructure model against the synchrotron data in space group $P\bar{1}$. Inset: zoomed region 14-28 ° 2θ. Final R_{wp} for this refinement pictured 4.86 %. The figure shows the experimental data in blue, the calculated pattern in red and the difference plot in grey.

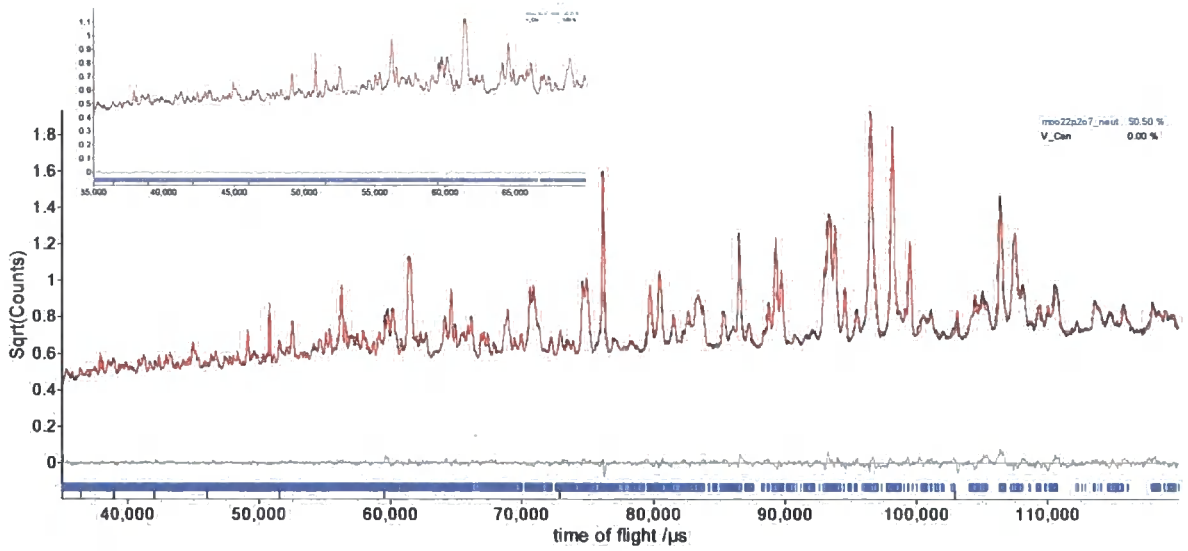

Figure 4.27 Rietveld fit of the superstructure model against the TOF data in space group $P\bar{1}$. Inset: zoomed region 35000-70000 μs. Final R_{wp} for this refinement pictured 2.60 %. The figure shows the experimental data in black, the calculated pattern in red and the difference plot in grey.

Table 4.19 Selected crystallographic data and refinement details from the combined X-ray and neutron refinement in space group $P\bar{1}$.

Space Group $P\bar{1}$			
a /Å	10.3674(1)	Overall R_{wp} /%	4.09
b /Å	17.8174(3)	X-ray R_{wp} /%	4.86
c /Å	17.8074(3)	Neutron R_{wp} /%	2.60
α /°	90.2017(3)		
β /°	90.0280(17)	X-ray R_{Bragg} /%	1.66
γ /°	89.9646(18)	Neutron R_{Bragg} /%	1.64
Volume /Å^3	3289.38(9)		
Refining parameters	427	GOF	1.65

The refined model gives a very good fit to the data. The bond lengths are shown in Figure 4.28. The mean values and e.s.d.s of the distributions are given in Table 4.20. The angles within the P_2O_7 groups are given in Figure 4.29. The final input file and spreadsheets of bond length/angle data are included in the E-Appendix.

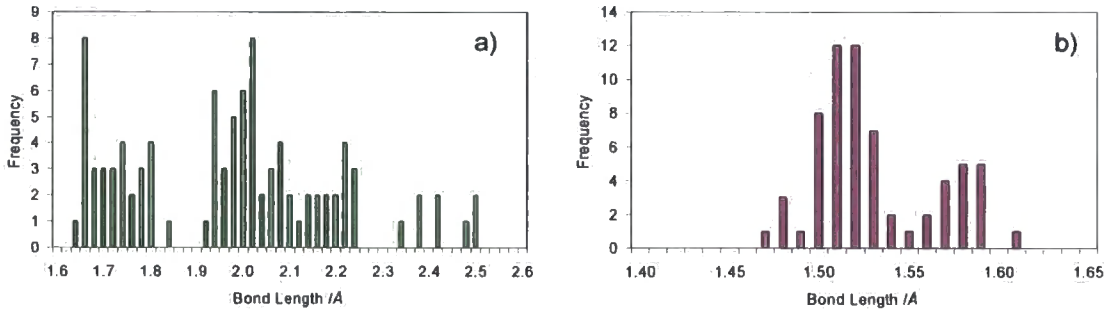

Figure 4.28 Bond lengths from the superstructure model in $P\bar{1}$. a) Distribution of Mo-O bonds. b) Distribution of P-O bonds.

Table 4.20 Mean bond lengths and estimated standard deviations for the bond lengths in the $P\bar{1}$ structure.

Bond Length	Value (e.s.d.) /Å
Mo-O (short)	1.665(20)
Mo-O (medium)	1.957(132)
Mo-O (long Mo1)	2.212(18)
Mo-O (long Mo2)	2.419(58)
P-O(-Mo)	1.510(17)
P-O(-P)	1.576(11)

The bond lengths and their distributions compare very closely with those from the high temperature *Pnma* and low temperature $P2_1/c$ structures. Bond valence sums are recorded in Table 4.21. Figure 4.29 contains information about the bond lengths and angles within each of the unique P_2O_7 groups within the superstructure.

Table 4.21 Bond valence sum calculations for each of the central atoms within the polyhedra. These were calculated using the values of Brese and O'Keefe.[6]

Central Atom	BVS /vu	Central Atom	BVS /vu	Central Atom	BVS /vu	Central Atom	BVS /vu
Mo1_1	6.04	Mo2_1	5.96	P1_1	4.99	P2_1	4.92
Mo1_2	6.09	Mo2_2	5.91	P1_2	4.91	P2_2	4.94
Mo1_3	5.98	Mo2_3	6.04	P1_3	4.87	P2_3	4.99
Mo1_4	6.31	Mo2_4	5.92	P1_4	4.95	P2_4	4.82
Mo1_5	6.02	Mo2_5	6.30	P1_5	4.99	P2_5	4.89
Mo1_6	5.96	Mo2_6	5.79	P1_6	5.06	P2_6	4.78
Mo1_7	5.74	Mo2_7	6.02	P1_7	5.01	P2_7	4.97
Mo1_8	5.96	Mo2_8	5.98	P1_8	5.13	P2_8	4.98

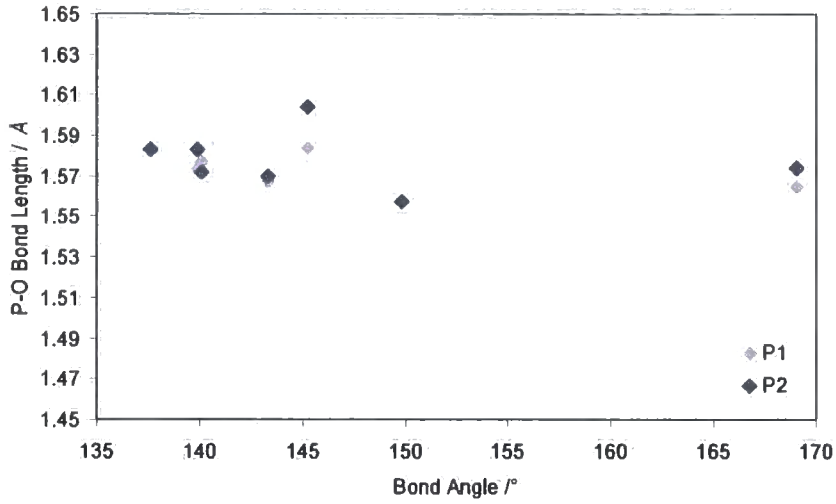

Figure 4.29 A scatter plot of the bond lengths and bond angles present within each of the 8 unique P_2O_7 groups within the structure. Type P1 and P2 atoms have been colour coded.

4.4.6 Comparison of the $P2_1/c$ and $P\bar{1}$ structures

The fits of the models to the X-ray and neutron data were given in Figures 4.22/4.23 ($P2_1/c$) and 4.26/4.27 ($P\bar{1}$). Both models gave a very good fit to the data. The $P\bar{1}$ structure gives a better fit to the data in terms of R_{wp} indices; however, there are 427 structural parameters in the former model as opposed to 235 parameters in the latter. It is therefore likely that the improved fit arises due to 3 factors: the increased structural flexibility possible; the lower metric symmetry which helps 'mop up' inadequacies in the peak shape model which is known to display significant strain anisotropy on these very high resolution instruments and the larger number of spherical harmonic terms describing peak width anisotropy in $P\bar{1}$.

A clear difference in the P-O-P bond angles was noted between the models. In the $P2_1/c$ structure, the P-O_b-P bond angles (Figure 4.25) were found to have a 3:1 small-large distribution and in $P\bar{1}$ a 7:1 distribution (Figure 4.29). The former distribution is consistent with experimental solid state ^{31}P NMR data. The structure is also consistent with electron diffraction data that pointed to a *c*-glide perpendicular to the *b* axis (transformed to a standard setting from an *a*-glide perpendicular to *c*).

The P-O-P bond angle in the only unique P_2O_7 group in the high temperature structure was found to be 150.2 ° from the combined refinements, Table 4.10. The low temperature structure has four unique P_2O_7 groups with bond angles as plotted in Figure 4.25. It appears from these data that the superstructure forms due to the preference for the P-O-P angles to be ~145 °.[10] However, for the majority of these bonds to have a favourable bond angle, one of them is forced to be larger. It is also worth noting that one P in the high temperature structure has a slightly high BVS; in the low temperature structure all are as expected.

4.5 Intermediate structure of α-$(MoO_2)_2P_2O_7$

From Figures 4.7 (cell parameters) and 4.9 (^{31}P NMR), it was apparent that the structure between 323 and 377 K was different to either the high or the low temperature structure. The marked change in gradient of the lattice parameters derived from the synchrotron data implied that the phase transition at 377 K was due to a second order phase transition. The changing resonances in the NMR imply that the material is different but do not give any clear information about the number of P sites that are present in this temperature range. Comparable diffraction patterns to those used for structure solution at high and low temperature were recorded at both ID31[h] and HRPD at 338 K. These are given in Figures 4.30 and 4.31 respectively.

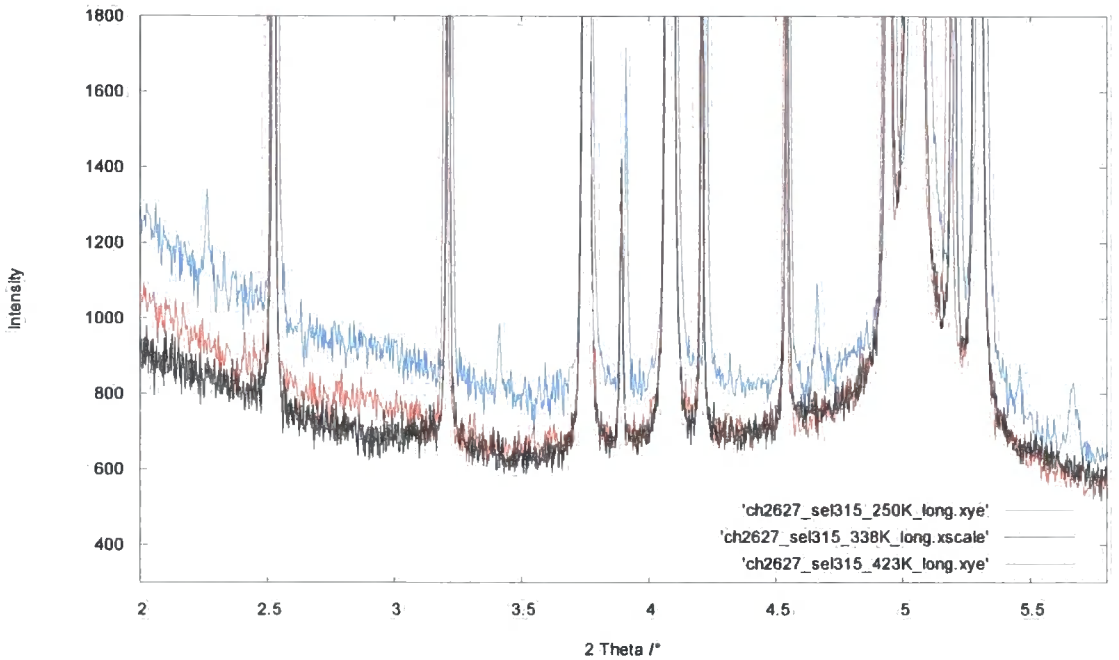

Figure 4.30 Diffraction patterns of α-$(MoO_2)_2P_2O_7$ (SEL315) on beamline ID31 at the ESRF. These were recorded at 250 K (blue), 338 K (black) and 423 K (red).

[h] The scan recorded on ID31 was recorded at a wavelength of 0.40282(6) Å. It has been converted here to have a wavelength equivalent to the other two scans recorded.

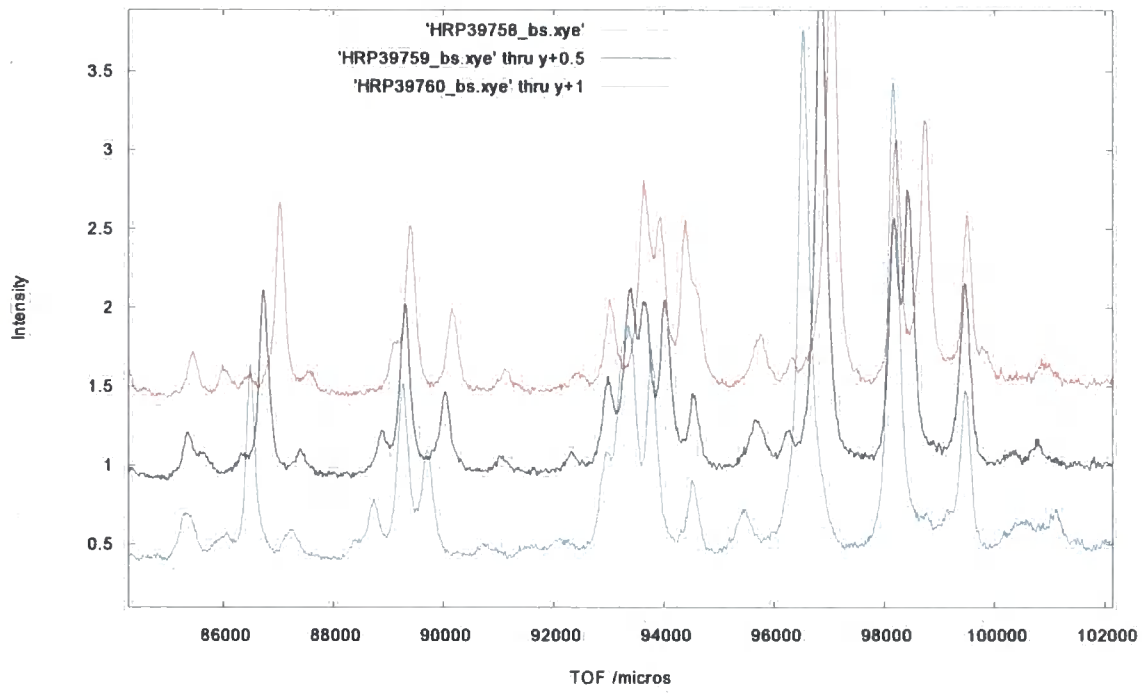

Figure 4.31 Scans of α-$(MoO_2)_2P_2O_7$ (SEL322) on the HRPD at ISIS. These were recorded at 250 K (blue), 338 K (black) and 423 K (red).

The superstructure peaks are clearly evident in the synchrotron data in Figure 4.30, but weak in the TOF data. There are no obvious differences (other than due to thermal expansion) between the data recorded at 338 K and 423 K in either the synchrotron or the neutron data. However, the marked change in the 1D NMR data, Figure 4.9, indicates that a fairly major change occurs within the structure at these intermediate temperatures.

The electron diffraction patterns in Figure 4.19 were all recorded at ambient temperature. However, one of these scans, Figure 4.32, is believed to be recorded at a slightly higher temperature due to beam heating. This EDP shows the presence of incommensurate satellite peaks that were not present in any of the other patterns recorded. It is believed that this figure hence shows evidence for this intermediate phase being incommensurate in nature. The extra satellite peaks are present along the parent a^* direction. No further investigation has been undertaken into this temperature region.

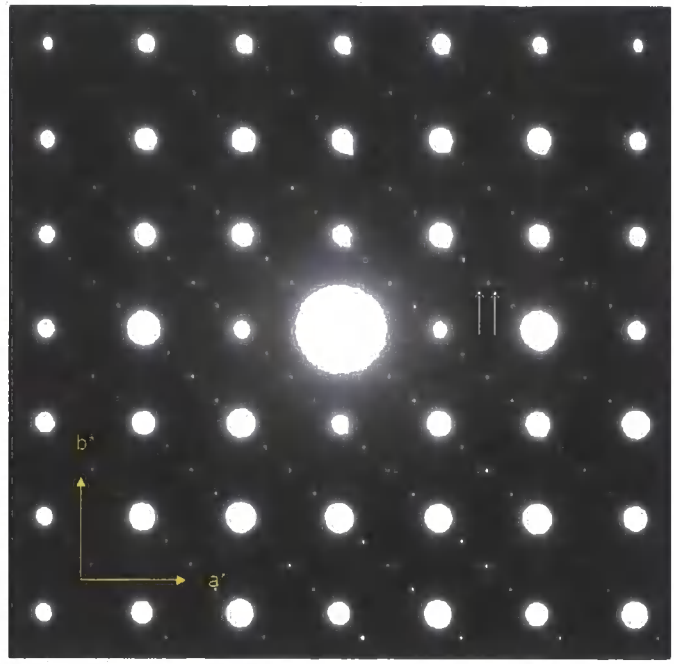

Figure 4.32 Electron diffraction patterns of α-$(MoO_2)_2P_2O_7$ with zone axis [001]. Incommensurate peaks are indicated by arrows.

4.6 Conclusions

VT X-ray data were recorded on the stable polymorph of α-$(MoO_2)_2P_2O_7$ in the lab over the range 16-753 K; these revealed the presence of two phase transitions. These were also observed in neutron and synchrotron data. VT 1D and 2D ^{31}P NMR data confirmed the temperature induced changes in the structure. Above 377 K, two peaks are present in the NMR data; these peaks arise from the P signals of the 2 P atoms present in a single crystallographically unique P_2O_7 group. Rietveld analysis of the high temperature subcell structure using combined refinement against synchrotron and neutron data has confirmed the structure to be similar to that published by Kierkegaard.[2] This new refinement contains more plausible bond lengths and angles for the polyhedra within the structure. This model does not give a good fit to the lower temperature data.

The low temperature structure (below 323 K) contains superstructure peaks that have been indexed to a cell with dimensions a ~17.83 Å, b ~17.83 Å and c ~10.38 Å from electron diffraction patterns. ^{31}P NMR has shown that the structure contains 5 discernible resonances; these have been attributed to at least 8 different P atoms, contained within 4 P_2O_7 units. Consideration of the group theory of the transformation led to the conclusion that the symmetry within the material was reduced from orthorhombic in the high temperature material, to monoclinic in the low temperature structure. SHG tests suggested the low temperature structure was centrosymmetric, leading to space groups $P2_1/c$ and $P\bar{1}$. The structure was investigated in these space groups using real space structure solution methods from the powder data. Both structures refined to give low R-factors (5.72 % R_{wp} in $P2_1/c$, 4.09 % R_{wp} in $P\bar{1}$) and gave very good fits to the data. Bond length distributions agreed well with those expected from the high temperature subcell model. P-O-P bond angles were found to be in a 3:1 distribution in the $P2_1/c$ structure and 7:1 in the $P\bar{1}$ model. The former is more consistent with the

NMR data; this space group also agrees with the extinction symbol *P--a* from the electron diffraction data.

At intermediate temperatures between 323 and 377 K, the XRD and neutron patterns do not contain the superstructure peaks present at lower temperatures. The NMR data imply that this phase is different to both the low and high temperature structure. NMR and electron diffraction data suggest this intermediate phase is incommensurately modulated.

4.7 References

1. I. Schulz, *Z. Anorg. Allg. Chem.*, 1955, **281**, 99-112.
2. P. Kierkegaard, *Ark. Kemi*, 1962, **19**, 1-14.
3. S. E. Lister, I. R. Evans, J. A. K. Howard, A. Coelho and J. S. O. Evans, *Chem. Commun.*, 2004, **22**, 2540-2541.
4. K. Wang and R. R. Reeber, *Phil. Mag. A*, 2000, **80**, 1629-1643.
5. N. E. Brese and M. O'Keeffe, *Acta Crystallogr., Sect. B*, 1991, **47**, 192-197.
6. A. F. Wells, *Structural Inorganic Chemistry (Fifth Edition)*, Clarendon Press, Oxford, 1984.
7. G. Costentin, A. Leclaire, M. M. Borel, A. Grandin and B. Raveau, *Rev. Inorg. Chem.*, 1993, **13**, 77-101.
8. *International Tables for Crystallography, Volume A*, Dordrecht, Holland and Boston, USA, 1983.
9. B. J. Campbell, H. T. Stokes, D. E. Tanner and D. M. Hatch, *J. Appl. Cryst*, 2006, **39**, 607-614.
10. M. O'Keeffe, B. Domenges and G. V. Gibbs, *J. Phys. Chem.*, 1985, **89**, 2304-2309.

5. Studies of $(MoO)_2P_4O_{13}$

5.1 Introduction

$(MoO)_2P_4O_{13}$ is a corner-sharing framework material containing Mo centred octahedra and P centred tetrahedra. Despite its simplistic formula, $(MoO)_2P_4O_{13}$ undergoes a phase transition between two complex phases. As a member of the 1Mo:2P family of compounds, this material was of interest as a possible precursor phase to MoP_2O_7; reduction of the parent phase would enable synthesis of the Mo phase related to the negative thermal expansion AM_2O_7 materials, Chapter 6. This chapter describes investigations into the various phases of $(MoO)_2P_4O_{13}$ using non-ambient diffraction methods.

The first description of a material that may have been $(MoO)_2P_4O_{13}$ was in 1955 by Schulz.[1] She prepared a green crystalline substance that she reported as $MoO_{3-x}\cdot P_2O_5$ with x predicted to be 0.2-0.3. For this compound to have been $(MoO)_2P_4O_{13}$, x would need to be 0.5. The structure was not solved at this time, but the crystals were indexed to a monoclinic cell with cell dimensions as given in Table 5.1, alongside those from other references to this composition in the literature. It seems likely that this material was $(MoO)_2P_4O_{13}$.

Table 5.1 Comparison of cell parameters for $(MoO)_2P_4O_{13}$ in the literature.

	Schulz[1,2]	Minacheva[3]	subcell[4]	supercell[5]
	(-)[i]	*Pb*[j]	$P2_1/c$	*Pn*
a /Å	≈ 16.7	8.288(2)	8.3068(8)	24.133 (2)
b /Å	≈ 19.3	19.529(5)	6.5262(6)	19.579(2)
c /Å	≈ 10.8	10.690(3)	10.7181(11)	25.109(2)
β /°	≈ 107.5	106.7(3)	106.7050(78)	99.962(3)
Vol /Å^3	≈ 3319.84	1657.18[k]	556(1)	11685(1)
Vol/Vol_{sub}	6	3	1	21
No. reflections used in solution	-	906	408	43783

A structure solution was reported by Minacheva *et al.* in 1979;[3] the cell parameters from this work are also given in Table 5.1. The two cells have some similarities, with almost identical *b* and *c* parameters and a halved *a* parameter in the Minacheva cell compared to Schulz's cell. Although the atomic coordinates were not refined in 1979 (due to pseudosymmetry effects), the paper did outline the coordination of the atoms within the structure. Each Mo atom is 6 coordinate octahedral and contains a molybdenyl group with one oxygen bound only to that Mo. The other five oxygens of the MoO_6 octahedron are shared with phosphorus tetrahedra, thus forming a 3D framework structure. Four phosphorus tetrahedra link together to form P_4O_{13} units, and share their remaining ten corners with

[i] The structure was never actually solved and the space group never determined to my knowledge.
[j] Although the structure was solved in space group *Pb*, the cell parameters have been given here as if in space group *Pc* for ease of comparison.
[k] The volume was not quoted in the paper, it has been calculated using standard trigonometry, no esd estimated.

molybdenum octahedra, resulting in the presence of P-O-P and P-O-Mo linkages. The connectivity is shown pictorially in Figure 5.1.

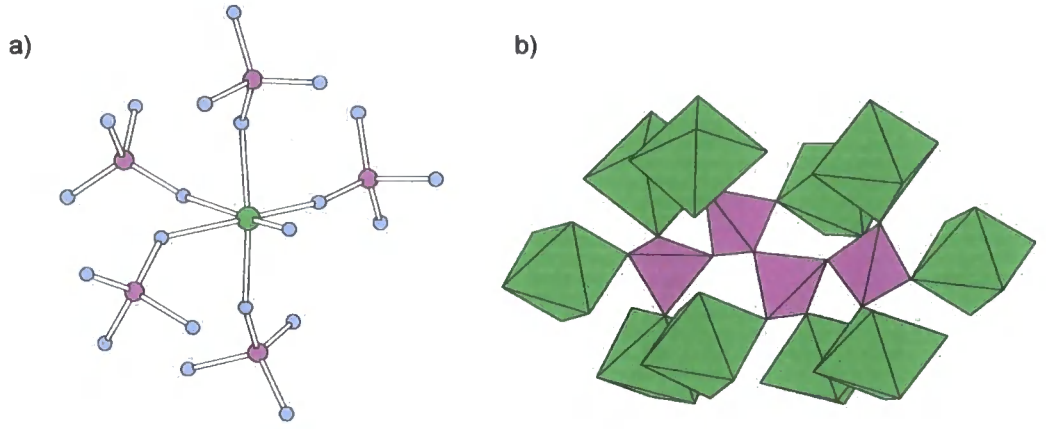

Figure 5.1 Structural connectivity in $(MoO)_2P_4O_{13}$. a) Skeletal representation of central MoO_6 octahedron surrounded by PO_4 tetrahedra; the free Mo-O bond is pointing forward. Mo atoms are illustrated in green, P atoms in purple and O atoms in grey-blue. b) Polyhedral representation of a P_4O_{13} group (PO_4 groups in purple) surrounded by MoO_6 groups (green).

An alternative structural model was published by Costentin *et al.* in space group $P2_1/c$, containing 11 atoms in the asymmetric unit.[4] This had the same structural connectivity as the structure published by Minacheva but it was refined in a much smaller cell and as such required fewer atoms in the asymmetric unit. For convenience this model will be referred to as the "subcell model". It is noted that this model gave an excellent agreement to the experimental data and refined to R/R_w 3.6/3.7 %.

We have recently shown that the true structure of this material is in fact far more complex than this subcell model. Single crystal experiments at 120 K showed that the true unit cell is 21 times larger than Costentin's published cell, containing 441 atoms in its asymmetric unit.[5] The presence of two very weak odd *0k0* reflections led to space group *Pn*.

The underlying connectivity within the three structure solutions is identical. It is clear from Table 5.1 that there are many similarities between the four unit cells that have been proposed; all have a volume that is an integer ratio of the smallest "subcell" model. In the subcell model the P_4O_{13} group is positioned on an inversion centre within the unit cell. This forces one of the P-O-P bond angles to be 180 °. In the other solutions present in the literature, these restrictions on the bond angle are removed due to the lowering of symmetry.

The true structure of this compound was solved from knowledge of the relationship between the unit cells of the incorrect subcell model and the new (true) supercell. As the two cells describe diffraction from the same crystal, the *d*-spacings of reflections present described using the subcell are a subset of those predicted for the supercell. It was, therefore, possible to relate the cells by comparing the assignment of different *hkl* indices to reflections observed at a given *d*-spacing. This allows the geometrical relationship between the two cells to be determined, and the transformation matrix

between them is given in Equation 5.1.[6] For reference, the two cells are shown side-by-side in Figure 5.2.

$$\begin{bmatrix} 3 & 0 & 1 \\ 0 & 3 & 0 \\ \bar{1} & 0 & 2 \end{bmatrix} \cdot \begin{bmatrix} a \\ b \\ c \end{bmatrix} = \begin{bmatrix} 3a+c \\ 3b \\ 2c-a \end{bmatrix} = \begin{bmatrix} a_{sup} \\ b_{sup} \\ c_{sup} \end{bmatrix} \quad (5.1)$$

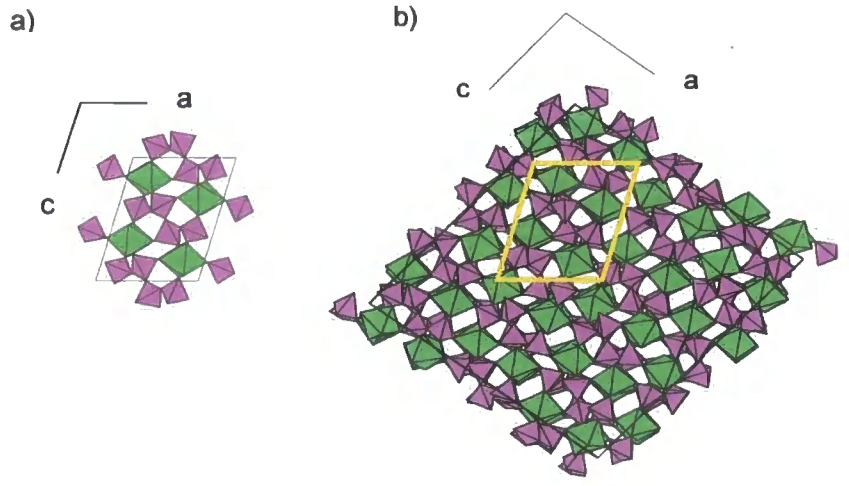

Figure 5.2 A polyhedral representation of $(MoO)_2P_4O_{13}$ showing a) the subcell model and b) the true low temperature structure viewed down [010].[5] MoO_6 octahedra are shown in green; PO_4 tetrahedra are in purple.

The starting coordinates for the superstructure refinement were then calculated by transforming the coordinates in the subcell model using the transformation matrix in Cryscon.[7] Suitable polyhedral restraints were written from knowledge of the local coordination environments for the atoms in the structure. A simulated annealing approach was then used in Topas to solve the structure.[8] Many cycles of randomisation and convergence were employed to find the best quality solution to the data. This model was then refined further in the Crystals software;[9] final R-factors were R/R_w 3.49/5.99 %.

Figure 5.3 shows the comparison between the refined thermal displacement parameters in the incorrect subcell model and the actual static displacement of the oxygen atoms in the supercell model, when folded back into the subcell unit. It is clear from this figure that the anisotropic thermal displacement parameters refined in the incorrect subcell structural model provide a remarkably good indication of the magnitude of static displacements present in the true superstructure.

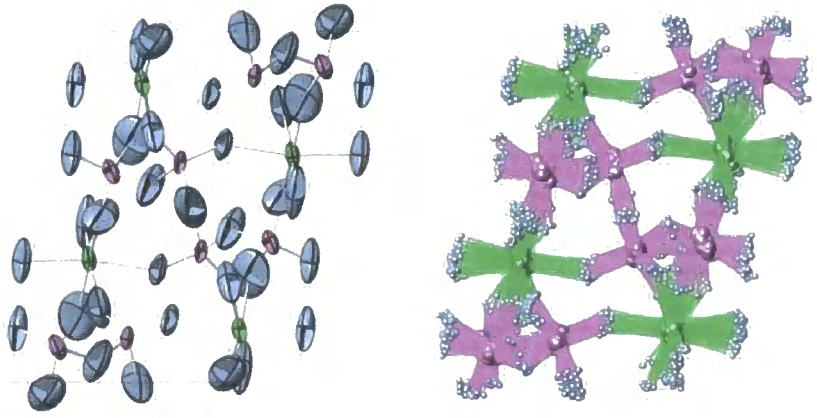

Figure 5.3 a) The refined thermal displacement parameters in the subcell model and b) the true static displacements in the supercell model, folded back into the subcell unit. This figure shows that the unusual thermal displacement parameters in the original structure solution are due to the true static displacements present in the complex superstructure.

Preliminary work also indicated a phase transition in the material at ~523 K by both powder XRD and Differential Scanning Calorimetry (DSC) measurements. It was initially believed that this phase transition could be the transformation from the *Pn* 21x superstructure to the simple $P2_1/c$ substructure. This chapter describes variable temperature diffraction experiments to probe the temperature-dependent structure of $(MoO)_2P_4O_{13}$. This has involved synchrotron X-ray and neutron studies at central facilities and in-house X-ray investigations using both single crystal and powder diffraction techniques.

5.2 Preparation of $(MoO)_2P_4O_{13}$

A sample of $(MoO)_2P_4O_{13}$ was prepared to investigate the structure using single crystal diffraction, and also to investigate the phase transitions and reduction chemistry. Sample SEL033 was prepared, using the method of Lezama,[10] shown in Equation 5.2.

$$MoO_3 + (NH_4)_2HPO_4 \rightarrow (MoO)_2P_4O_{13} \qquad (5.2)$$

1.4395 g MoO_3 (10 mmol, Alfa, 99.95 %) was added to 3.9616 g $(NH_4)_2HPO_4$ (30 mmol, Aldrich, 98+ %) and ground in an agate pestle and mortar to give an intimately mixed powder. This was transferred to a cylindrical (4 cm tall, 10 cm diameter) Pt crucible and heated as follows:

5 K/min → 523 K, held for 2 hours, then 2 K/min → 873 K for 6 hours, cooled in the furnace

The resulting green solid was washed from the crucible using demineralised water, and vacuum filtered. The solid was then dried at 353 K for an hour and scanned (d5_05483), yielding 2.1981 g $(MoO)_2P_4O_{13}$ (PDF 76-2079).[11] The preparation yields single crystals without the need for slow cooling from melt.

The solid formed was a mixture of crystalline $(MoO)_2P_4O_{13}$ and a glassy phase. The mixture could be separated once dried by passing it through an 80 mesh sieve. The crystalline components were small enough to pass through and the glassy parts were not. All experiments in this thesis have been undertaken using the crystalline product. Further grinding and heating of the glassy components did yield the crystalline material.

5.3 Rietveld refinement of $(MoO)_2P_4O_{13}$

To assess the phase purity of the sample described in Section 5.2 and confirm whether the bulk material has the same structure as single crystals, Rietveld analysis of the bulk material was undertaken. In previous work in this laboratory powder data were analysed using the subcell model for this structure.[6] Following the successful determination of the supercell structure (from data recorded at 120 K),[5] Rietveld analysis was undertaken on powder data using the supercell *cif* from the single crystal refinement.

5.3.1 Flat-plate characterisation

A sample of $(MoO)_2P_4O_{13}$ was prepared for XRD by thorough grinding of the solid and sprinkling the sample through an 120 mesh sieve onto a Vaseline-smeared silica disc. Diffraction data were collected for Rietveld refinement on the d8 at ambient temperature in the range 5 to 90 ° 2θ, with a step size of 0.017 °, collecting for a total of 15 hours, d8_03014.

A total of 26 parameters were refined in TOPAS Academic.[8] These included 14 global parameters (12 background parameters, a sample height correction and 1 parameter to describe axial divergence) and 12 parameters to model the $(MoO)_2P_4O_{13}$ structure (4 cell parameters, 3 isotropic displacement parameters – 1 each for each atom type, 4 parameters to parameterise a TCHZ peak shape used and a scale parameter). The refined cell parameters are presented in Table 5.2, alongside those from the low temperature single crystal structure solution. This refinement gave an R_{wp} of 14.02 %, and the calculated and recorded patterns are given in Figure 5.4.

Table 5.2 Refined parameters from Rietveld refinement of $(MoO)_2P_4O_{13}$.

	d8_03014 (ambient T)	Single Crystal (120 K)
a /Å	24.1304(3)	24.1134(6)
b /Å	19.5798(3)	19.5324(5)
c /Å	25.1168(3)	25.0854(6)
β /°	99.9937(9)	100.015(1)
Volume /Å^3	11687(1)	11685(1)

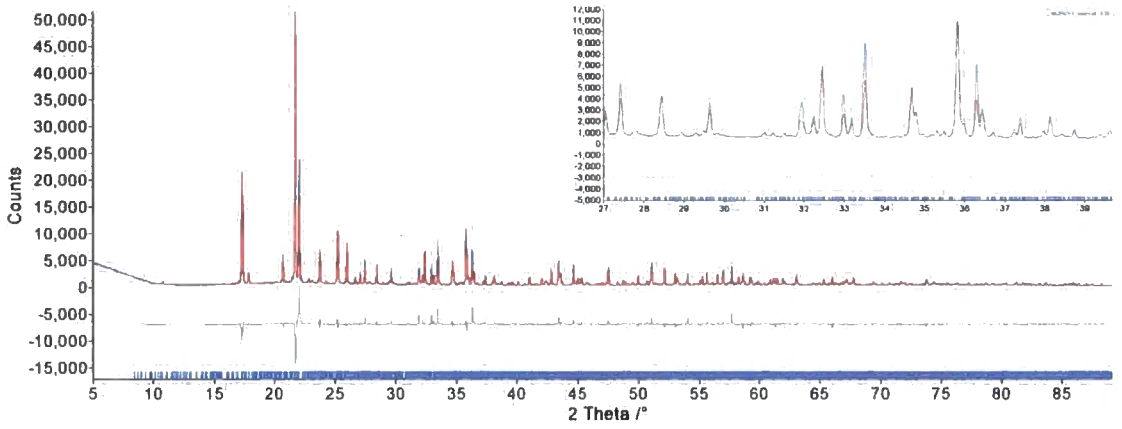

Figure 5.4 Powder data in d8_03014, R_{wp} 14.02 %. The recorded pattern (blue) has the pattern calculated from Rietveld analysis (red) superimposed over it. The lower grey trace indicates discrepancies between the recorded scan and the calculated pattern. Blue tick marks show the predicted peak positions for the model. Inset shows range 27-40 ° 2θ with ill-fitting intensities.

The quality of the fit given by this model in Figure 5.4 is not as good as expected from the quality of the model obtained in the low temperature single crystal refinement. At this point it was not known whether this was due to inherent differences between the structure of the polycrystalline and single crystal materials, or if these discrepancies were caused by preferred orientation or texture effects in the sample preparation. In order to trace the phenomenon giving rise to these discrepancies, a capillary measurement was undertaken and analysed.

5.3.2 Capillary characterisation

A sample of $(MoO)_2P_4O_{13}$ (SEL033) was prepared in a 0.5 mm glass capillary, as outlined in Section 2.3.1 to remove preferred orientation effects, and check the apparent inability of the low temperature structural model to fit the flat-plate powder data recorded on lab machines. Diffraction data were collected for Rietveld refinement on the d6 in the range 10 to 90 ° 2θ, with a step size 0.015 °, collecting for a total of 24 hours, d6_00082.

A total of 26 parameters were refined. These included 14 global parameters (12 background parameters, a zero point error correction, and 1 parameter to describe axial divergence) and 12 parameters to model the $(MoO)_2P_4O_{13}$ structure (4 cell parameters, 3 atomic displacement parameters – 1 each for each atom type, 4 parameters to parameterise a TCHZ peak shape used and a scale factor). A correction for absorption was made by fixing the isotropic displacement parameters to their average values found in the single crystal structure refinement, refining an absorption correction parameter, and then fixing the correction parameter and subsequently allowing the isotropic displacement parameters to refine. The ability of the low temperature model to fit the capillary data appeared visually to be much better than for the flat-plate data. This refinement gave an R_{wp} of 3.53 %, and the calculated and recorded patterns are given in Figure 5.5.

Table 5.3 Refined parameters from Rietveld refinement of $(MoO)_2P_4O_{13}$.

	Single Crystal (120 K)	d8_03014	Capillary Measurement
a /Å	24.1134(6)	24.1304(3)	24.1148(5)
b /Å	19.5324(5)	19.5798(3)	19.5673(5)
c /Å	25.0854(6)	25.1168(3)	25.1007(5)
β /°	100.015(1)	99.9937(9)	99.9963(15)
Volume /Å^3	11685(1)	11687(1)	11664(1)

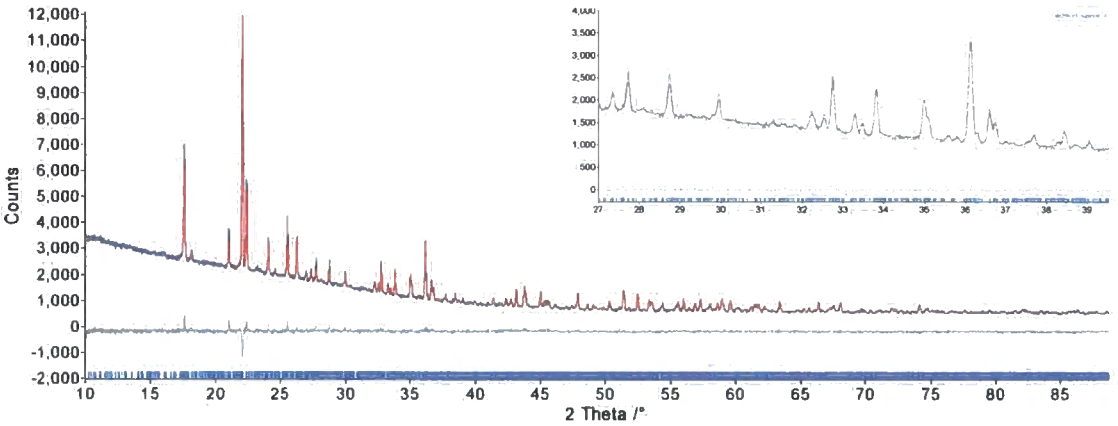

Figure 5.5 Rietveld refinement using capillary powder data on $(MoO)_2P_4O_{13}$ (SEL033) in d6_00082, R_{wp} 3.53 %. The figure shows the experimental data in blue, the calculated pattern in red and the difference plot in grey. Tick marks (in blue) show the predicted positions of the peaks.

By visually comparing Figures 5.4 and 5.5, it appears clear that the ability of the single crystal model to fit to the powder data is better for the capillary data. However, there is a much larger contribution from the background in the capillary sample than in the flat plate data. This has the effect of lowering the R_{wp} for the total pattern analysis. A better agreement factor for comparing the two Rietveld analyses is the GOF' as this residual factor is calculated with the contribution from the background removed when it is calculated, and allows for direct comparison between the two fits. The GOF's for the flat-plate and capillary measurements respectively were 4.43 and 1.243. These factors indicate that the ability of the fixed coordinate model to fit to the two datasets is much better for the capillary dataset than the data from the flat plate geometry. In turn it can be concluded that the flat-plate geometry data suffer slightly from texture arising due to the preparation of the powder, despite the samples having been prepared by sprinkling a small quantity of sample onto a Vaseline smeared disc.

Further evidence for this conclusion arises by comparing several powder diffraction scans recorded in flat-plate geometry, Figure 5.6. These scans have been normalised to enable comparison of the relative peak intensities throughout the 2θ range recorded.

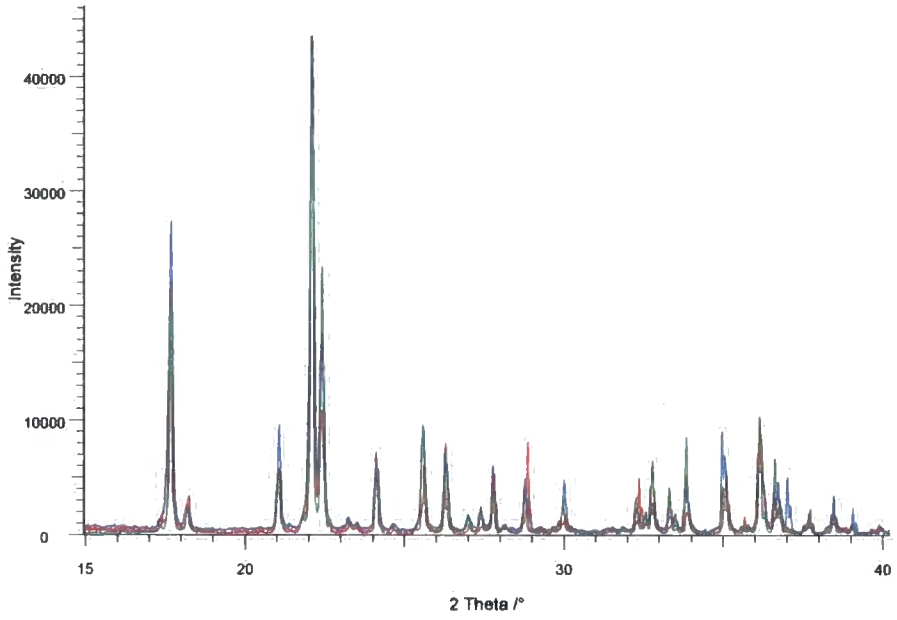

Figure 5.6 Flat-plate reflection geometry scans of sample SEL033. Scans have had their backgrounds subtracted and have been normalised onto the same intensity scale. Intensity ratios can be seen to vary across the 2θ range displayed. This provides evidence for the sample having texture in flat-plate scans.

It can be seen that the scans have differing relative intensity patterns. Addition of a spherical harmonic function to model preferred orientation in flat-plate samples gives a better fit to the data; though it is not possible to completely correct for these texture effects.

5.4 Room temperature single crystal structure determination of $(MoO)_2P_4O_{13}$

Structure determination using single crystal data collected at 293 K was undertaken to compare the room temperature structure with that solved at 120 K, to see if there were any major structural differences between the two temperatures.[5] The single crystal data collection method outlined in section 2.1.1 was followed for $(MoO)_2P_4O_{13}$ sample SEL033. Crystal information is given in Table 5.4. Data were collected on a Bruker AXS Smart 6000 Diffractometer (Section 2.3.3).

Table 5.4 Summary of the crystal data for $(MoO)_2P_4O_{13}$.

	120 K data	293 K data
λ (Mo Kα) /Å	0.71073	0.71073
Temperature /K	120	293
Chemical Formula	$(MoO)_2P_4O_{13}$	$(MoO)_2P_4O_{13}$
Molecular Weight /Daltons	555.766	555.766
Crystal Form	Irregular Prism	Irregular Prism
Crystal Size /mm^3	0.08 * 0.08 * 0.2	0.08 * 0.08 * 0.2
Crystal Colour	Green	Green

The room temperature structure refinement was carried out using the Oxford Crystals suite of programs.[9] Initial atom coordinates were imported to Crystals from a list 5 file containing the coordinates of the low temperature structure. Atomic coordinates, isotropic displacement parameters for each atom and an extinction parameter were all refined; a three parameter weighting scheme was also added. This gave an R_p of 3.25 % and an R_{wp} of 8.26 %, but with some large shifts/s.u.s (up to a maximum ratio of 8). Shift limiting restraints (SLR) were applied to *xyz* coordinates and displacement parameters (SLRs in Crystals set to 0.001 and 0.00001 respectively).[12] This led to convergence, and the unit cell data and other refinement details are given in Table 5.5, alongside data for the structure at 120 K.

For a structure of this size it is impractical to tabulate all the values of bond lengths and bond angles within the asymmetric unit. Data are therefore presented graphically in the form of several histograms for the data from the room temperature structure, and are also compared to the data from the 120 K structure. Full tabulations of distances and angles are included in the *cif*s in the E-Appendix.

Table 5.5 Summary of the single crystal refinements of $(MoO)_2P_4O_{13}$.

	120 K data	293 K data
Crystal System	Monoclinic	monoclinic
Space Group	*Pn*	*Pn*
a /Å	24.1134(6)	24.1332(20)
b /Å	19.5324(5)	19.5793(18)
c /Å	25.0854(6)	25.1091(20)
β /°	100.015(1)	99.962(3)
V /Å^3	11635.0(5)	11685.4(19)
Z	42	42
Calculated Density /gcm^{-3}	3.331	3.317
μ /mm^{-1}	2.934	2.921
Total number of reflections	451,577	216,594
Number of unique reflections	48,060	48,901
Criterion for Observed reflections	43,783 > 3*σ*	9,315 > 3*σ*
Number of refined parameters	1766	1766
Observations:Parameters Ratio	24.8	5.3
R /%	3.49	3.25
R_w /%	5.99	8.26
Goodness of Fit	0.8626	0.7905

The characteristic distribution of Mo-O bond lengths for Mo^V octahedra is expected to be that one bond is short, one long and four are of intermediate length.[13] The short bond corresponds to the "terminal" Mo-O bond. Figure 5.7a) shows the Mo-O bond distances for the 42 molybdenum atoms within the low temperature structure. It can be clearly seen that some of these are shorter and some longer, with the bulk of these bond lengths in the "central hump" of the histogram. The 3 distributions

contain 42:168:42 lengths, as expected for 42 molybdenum octahedra. Figure 5.7b) contains the equivalent data for the room temperature structure; the upper distribution overlaps slightly with the middle one. The distributions are more clearly separated at lower temperatures with the refined bond lengths having a smaller range. Typical s.u.s in a) are 0.004 *Å* and in b) 0.015 *Å*. The average values and the standard deviations of the distributions are given in Table 5.6.

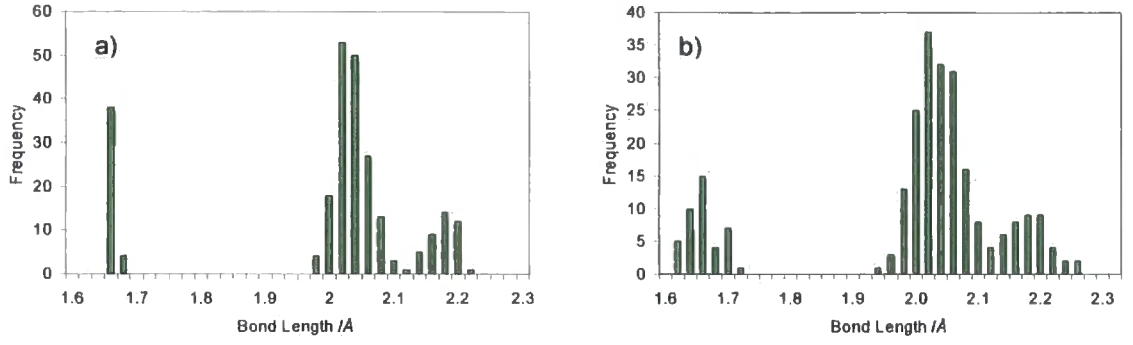

Figure 5.7 The Mo-O bond length data for the 252 bonds within both the 120 K (a) and 293 K (b) structure.

Table 5.6 Mean bond length and estimated standard deviations for the bond lengths in the data collections at 120 and 293 K.

	120 K	293 K
Bond Length	Value (e.s.d.) /*Å*	Value (e.s.d.) /*Å*
Mo-O (short)	1.653(5)	1.652(26)
Mo-O (medium)	2.025(25)	2.025(35)
Mo-O (long)	2.167(22)	2.172(35)
P-O	1.500(13)	1.497(39)
P-O_b	1.583(14)	1.583(36)

A scatter plot showing the correlation of bond distances at 120 and 293 K is shown in Figure 5.8. This highlights that there have been no major changes within the structure on heating as the same bonds that are short in the 120 K structure are short in the 293 K structure. The s.u.s are larger for the structure solved at higher temperature. The larger spread seen in the room temperature data is due to fewer observations >3σ in the data recorded (a fourfold decrease in the number used for model refinement, see Table 5.5). This is further discussed in Section 5.6.2.

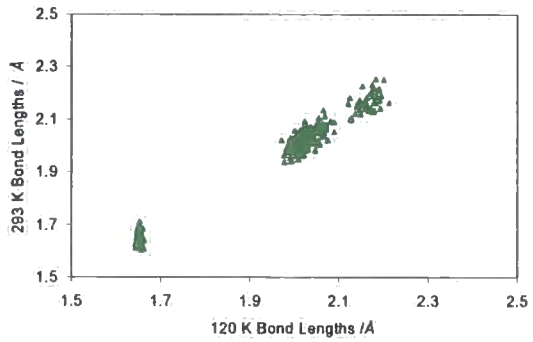

Figure 5.8 Correlation of Mo-O bond lengths in the 120 K and 293 K structures. Scatter plot clearly shows the correlation of the bonding distances in the structure at the two temperatures investigated. A line of best fit gives y=1.0083x-0.0156.

Figure 5.9 illustrates the spread of the P-O bond lengths within both structures. It is clear from the 120 K structure that there are two distinct types of P-O bonds, those linked to a Mo atom, and those to a second P atom. These are referred to as the terminal (O_t) and bridging (O_b) atoms from here on. These distributions are centred around 1.50 and 1.58 *Å* respectively. The distributions in the 293 K structure share the same mean (to 2 dp), but are clearly spread over a greater range as discussed for the Mo-O bonds. Typical s.u.s of individual distances in a) are 0.004 *Å* and in b) 0.016 *Å*. The average values and the standard deviations for the distributions are given in Table 5.6.

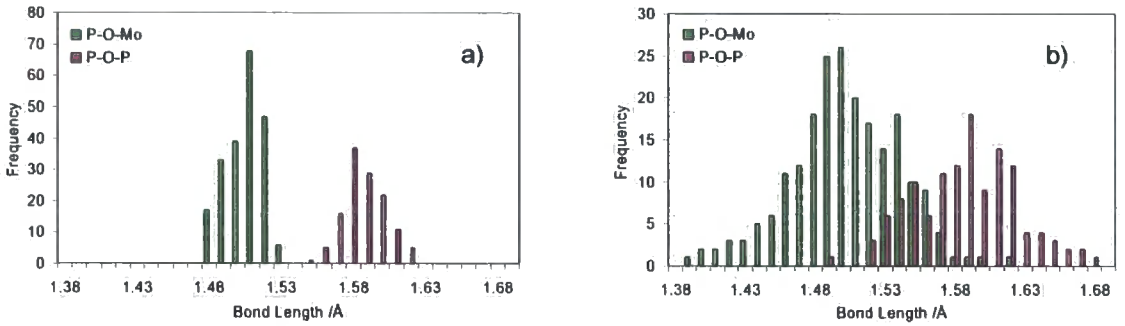

Figure 5.9 Histograms showing the distributions of P-O bond lengths dependent on type. a) The range of distances in the 120 K structure is much smaller than in b) the 293 K structure. The green columns show the data for the Mo-O-P bridges, and the purple columns indicate the P-O-P bridges.

Figure 5.10 shows the range of P-O-P bridging bond angles within the two structures. A typical s.u. for an individual bond angle is 0.3 ° in a) and 1 ° in b). Within the subcell model, the central P-O-P bond angle within the P_4O_{13} group is constrained to be 180 ° by symmetry, Figure 5.2. Superstructure formation normally occurs to allow P-O-P bonds to achieve their preferred angel of ~145 °.[14] Hence it may at first seem slightly odd that while most of the bonds lie in the range 126 – 164 °, several bonds have a bond angle greater than 170 °. The spreads of angles found for the two structures are displayed in Figure 5.11; the linear correlation plot between the two sets of bond angles indicate no major changes in the distributions of these angles on warming from 120 to 293 K.

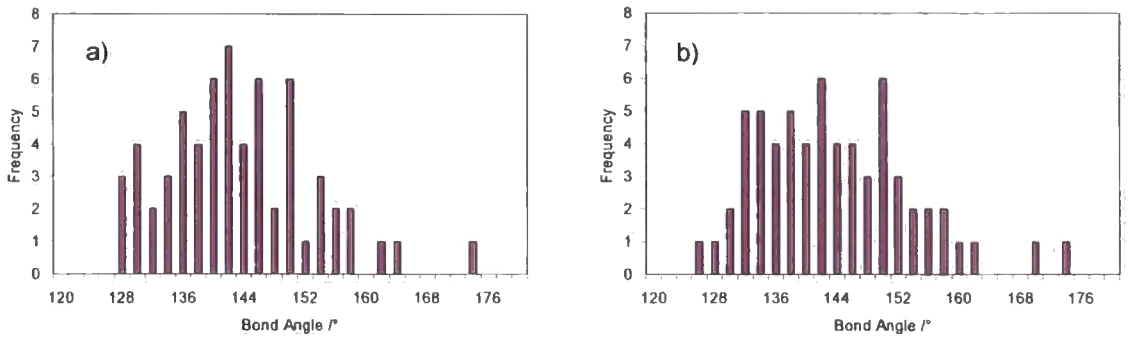

Figure 5.10 Histogram showing the P-O-P bond angles within low temperature (a) and room temperature (b) structures.

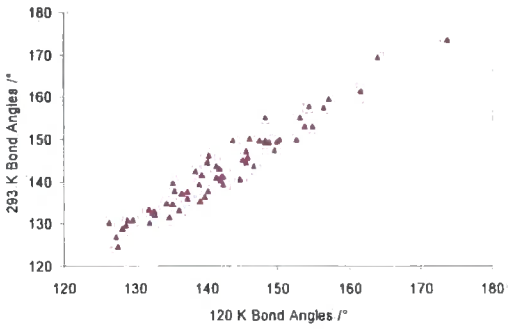

Figure 5.11 Graph showing the clear correlation between the P-O-P bond angles within the two structures. This indicates that no major changes occur in the crystal structure between 120 K and 293 K.

Figure 5.12 shows the relationship between the P-O_b-P bond lengths and P-O_b-P bridging bond angle. Typical s.u.s for bond lengths and angles are 0.004 *Å* and 0.3 ° at 120 K and 0.015 *Å* and 1 ° at 293 K. Particularly in the 120 K data it can be seen that bond length decreases as the angle approaches 180 °. As the bond angle tends to linear, there is better overlap between the O_b lone pair orbitals and orbitals on the P atoms. These are traditionally thought of as d-orbitals but are more likely to be P-O σ^* orbitals. Similar effects are observed in Si_2O_7 units and in cubic AM_2O_7 phases.[15-17]

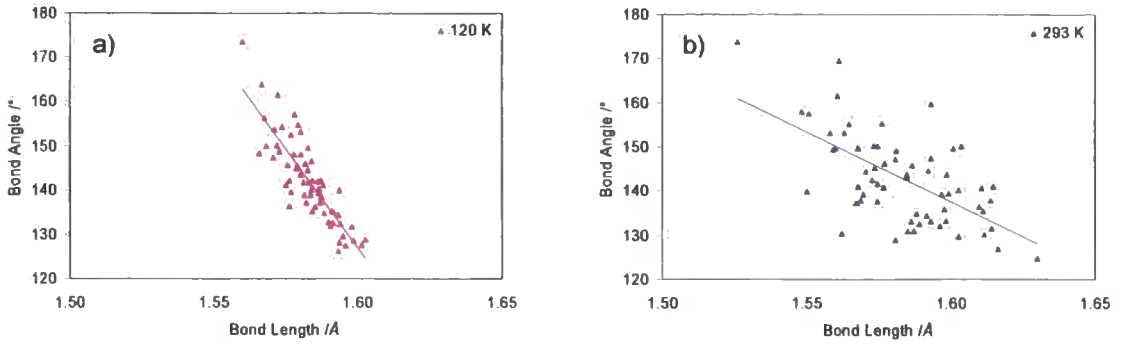

Figure 5.12 Scatter plots showing the strong correlation of bond length on bond angle for the P-O bonds within the structure. The lines of best fit for each dataset are shown. Best fit lines are a) y=-898x+1563 and b) y=-315x+642.

The isotropic displacement parameters refined for each atom are presented in Figure 5.13. The x-axis on each graph is identical; this shows the larger values and larger spread in temperature factors for the higher temperature structure. This is expected due to the increased energy of the system and the lower data quality of this data set. The average values and the standard deviations for the distributions are given in Table 5.7. The oxygen atoms show the largest values; this is because the oxygen atoms are lighter and in two-fold coordination, and hence less constrained within the structure, leading to larger isotropic displacement parameters.

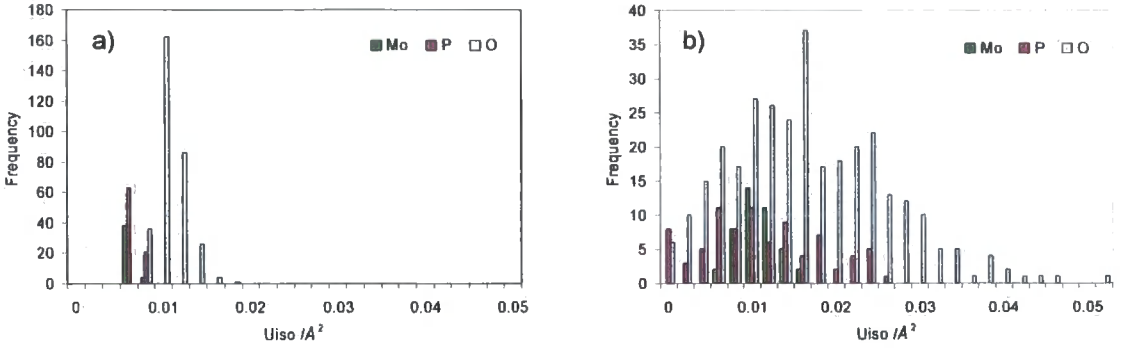

Figure 5.13 Histograms of isotropic displacement parameters for the low temperature (a) and room temperature (b) structures.

Table 5.7 Mean isotropic displacement parameters and estimated standard deviations in the data collections at 120 and 293 K.

	120 K	293 K
U_{iso}	Value (e.s.d.) /Å^2	Value (s.u.) / Å^2
Mo	0.00564(25)	0.00983(229)
P	0.00575(33)	0.01017(680)
O	0.00973(164)	0.01567(932)

This data analysis has shown that the structure at ambient temperature does not appear to differ vastly from the structure determined at 120 K. However, due to the increase in temperature and hence the increased energy within the compound, there are some slight differences, most notably in the U_{iso} values, as would be expected. Further comparison of the two structures is given in Figure 5.14.

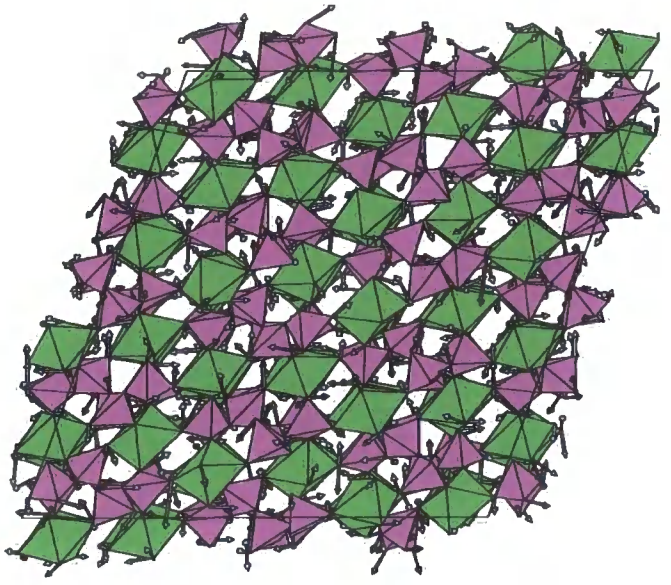

Figure 5.14 Diagram showing the structure of $(MoO)_2P_4O_{13}$ at low temperature, with green MoO_6 octahedra and purple PO_4 tetrahedra. The material is viewed down the [010] direction. The differences between the low temperature structure (pictured) and the room temperature model are displayed. The arrows indicate the atom positions in the room temperature structure; these have been scaled up by a factor of ten to aid viewing.

The average shifts for each atom type are given in Table 5.8. The largest shifts are for the O atoms, with smaller average displacements for P and Mo atoms.

Table 5.8 Average atomic shifts found for each of the atom types within $(MoO)_2P_4O_{13}$.

Atom Type	Shift /Å
Mo	0.0236
P	0.0342
O (- Mo)	0.0769
O (- P)	0.0715
O (central P_4O_{13})	0.0686

5.5 Variable temperature studies of $(MoO)_2P_4O_{13}$

5.5.1 Low temperature study of $(MoO)_2P_4O_{13}$

The low temperature behaviour of $(MoO)_2P_4O_{13}$ was studied between 16.4 and 300 K using the PheniX, Section 2.3.2.2. A sample of $(MoO)_2P_4O_{13}$ (SEL033) was ground with a small quantity of a silicon internal standard and prepared for XRD. Continuous twenty minute scans were run as the PheniX cooled from 300 K to 16.4 K at a rate of 17 K hr^{-1} (d8_03030). The same heating and data collection rate were used on warming from 16.4 to 300 K (d8_03031). Scans were recorded from 10 to 90 ° 2θ, with a step size of 0.017 ° 2θ.

For each XRD pattern recorded on both the cooling and heating cycles, a total of 74 parameters were refined. These included 13 global parameters (12 background parameters and 1 parameter to describe axial divergence), 38 parameters for the supercell model of $(MoO)_2P_4O_{13}$ (4 cell parameters, 3 isotropic displacement parameters – 1 each for each atom type, 6 parameters to describe a PV peak shape, a scale parameter and 24 parameters to model some preferred orientation with an 8th order spherical harmonic function[I]), 9 parameters for the silicon standard (1 cell parameter, a scale parameter, a single isotropic displacement parameter and 6 parameters to describe a PV peak shape), 1 height parameter was used for both the $(MoO)_2P_4O_{13}$ and the Si data. The remaining 13 parameters were used to model the Al sample holder. It was necessary to model this with a structure independent Pawley phase as the Al plate is textured due to the way it was manufactured.[18] Refined parameters were: 6 PV peak shape parameters, 5 parameters to model the intensity of the peaks, 1 height correction parameter and 1 cubic cell parameter. The first range of the cooling VTXRD experiment is shown in Figure 5.15; parameters were then refined sequentially using the local Fortran program *multitopas*.[19] The seed input file for the refinements undertaken and the refined parameters on the cooling data are included in the E-Appendix.

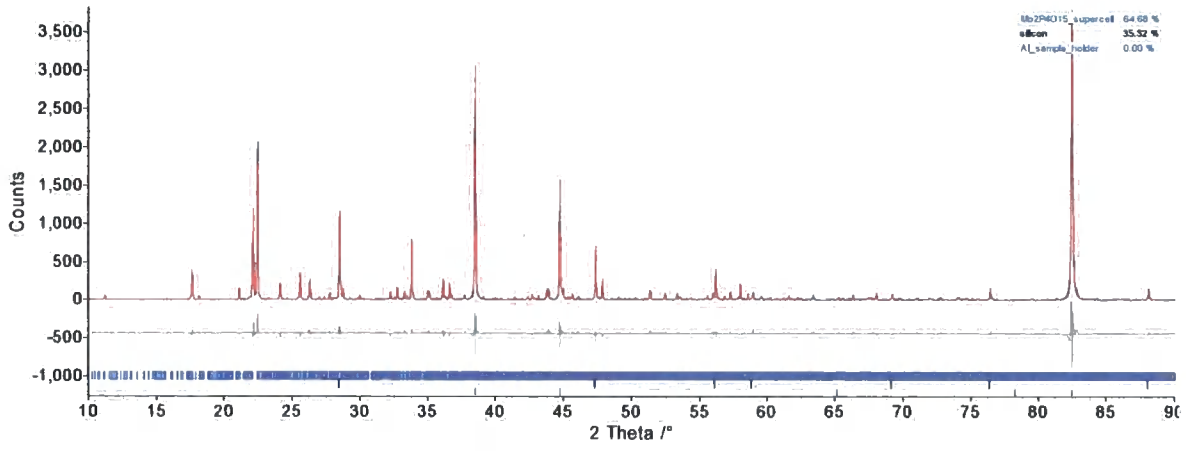

Figure 5.15 The diffraction pattern and Rietveld fit for d8_03030(1), R_{wp} 23.81 %. The figure shows the experimental data in blue, the calculated pattern in red and the difference plot in grey.

[I] The addition of the spherical harmonic function has enabled a better fit of the model to the diffraction data. Only the lattice parameters have been extracted from these measurements (not a full atomic coordinate model) and these do not correlate with spherical harmonic coefficients.

The temperature calibration of the PheniX was checked by comparing the values of the cell parameters for the two internal standards (Si and Al) with literature data.[m] Data from Wang and Reeber were used to calculate a theoretical cell parameter value for Al at each temperature.[20] Figure 5.16 shows data from this experiment compared to thermal expansion data calculated by Wang and Reeber. A constant offset of -4.379 * 10^{-5} Å (calculated by least squares refinement) was applied to the literature data. Excellent agreement is observed (particularly for the gradient) suggesting that the differences between the Al sample holder and PheniX thermocouple temperature are negligible; hence no temperature calibration was necessary for the PheniX data.

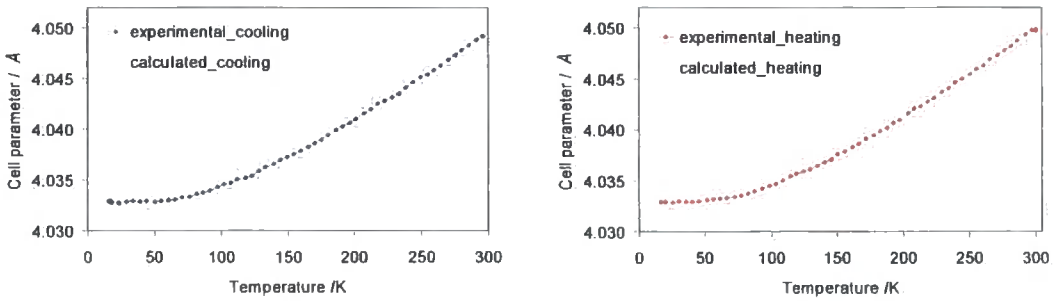

Figure 5.16 These graphs show the experimentally determined and theoretically calculated value for the Al cell parameter on cooling and heating.

For completeness, the graphs for the Si data are shown in Figure 5.17. Data were taken from Okada and Tokumaru (300-1500 K)[21] and Lyon *et al.* (6-340 K)[22] and normalised to fit to the NIST 640 C value of 5.4311946(92) Å[23] at 295.55 K.[24] An equation was calculated to fit the raw data to enable calculation of the Si lattice parameter at a given temperature. The refined values of the Si lattice parameter on heating and cooling were then extracted from the multiple refinement results and compared with calculated values obtained from the literature, Figure 5.17. The quality of the fit between the calculated and experimental cell parameters for Si is not as good as seen for the Al parameters above. The trend itself is apparent; the differences themselves are on a much smaller percentage scale due to the smaller thermal expansion exhibited by Si compared to Al.

[m] The position of the sensor detecting the set temperature may not represent the true temperature of the diffracted surface.

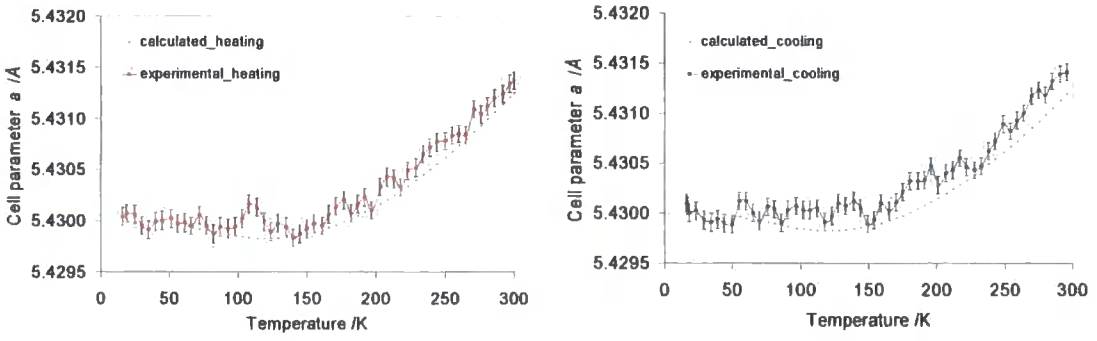

Figure 5.17 Calculated and experimental values of the Si lattice parameter on heating and cooling in the PheniX VT experiment.

Graphs showing the variations in the volume and lattice parameters of $(MoO)_2P_4O_{13}$ over the temperature range 16 □ 300 K recorded in the PheniX cryostat are given in Figures 5.24 and 5.27. The data are discussed alongside the results from the following high temperature study of $(MoO)_2P_4O_{13}$.

5.5.2 High temperature study of $(MoO)_2P_4O_{13}$

A sample of $(MoO)_2P_4O_{13}$ (SEL033) was examined using DSC, heating and cooling over the range 300 to 573 K at 10 K/min. The compound was found to undergo a phase transition at ~ 523 K, as illustrated in Figure 5.18.

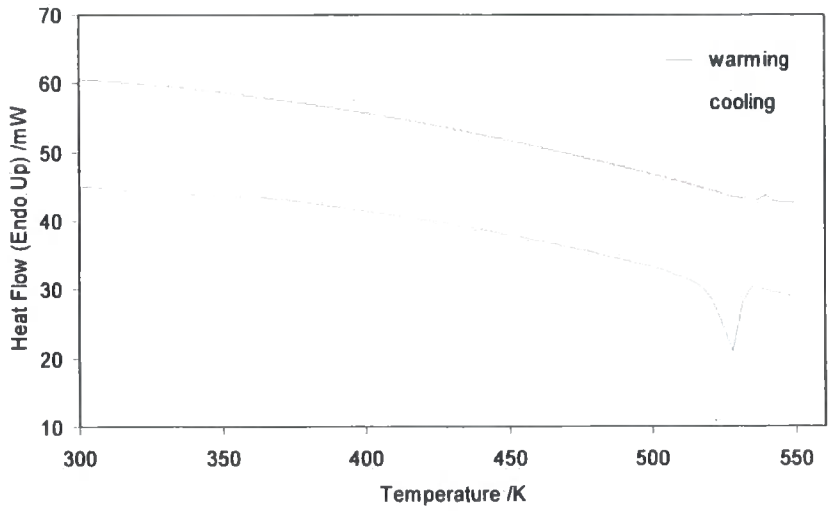

Figure 5.18 The DSC traces found on heating and cooling a sample of $(MoO)_2P_4O_{13}$. The sample was heated at a rate of 10 K/min from 298 to 573 K, and instrument cooled.

Following this discovery a small quantity of $(MoO)_2P_4O_{13}$ (SEL033) was mixed with an Al_2O_3 internal standard for high temperature VTXRD and mounted in the Anton Paar HTK1200 furnace attachment in the d8, Section 2.3.2.1. A 30 minute scan was undertaken before starting the variable temperature experiment, d8_03295. The data recorded were analysed using TOPAS Academic[8] in order to ensure

the relative quantities of $(MoO)_2P_4O_{13}$ and Al_2O_3 were acceptable, *i.e.* that the peak intensities for both phases were approximately equal, that there were no problems with preferred orientation for the molybdenum compound and that the signal-to-noise ratio was acceptable. There were no signs of preferred orientation in this XRD pattern, unlike samples prepared previously. This supports the earlier conclusion that there is some preferred orientation present in these samples as the addition of another material, in this case Al_2O_3, can remove this effect.

A total of 81 parameters were refined for this analysis. These included 20 global parameters (18 background parameters, a sample height correction and 1 parameter to describe axial divergence), 50 parameters to model the $(MoO)_2P_4O_{13}$ subcell structure (4 cell parameters, 30 atomic coordinates, 11 isotropic isotropic displacement parameters, 4 parameters to model the TCHZ peak shape used and a scale parameter) and 11 parameters to model the Al_2O_3 (2 cell parameters, 2 atomic coordinates, 2 isotropic displacement parameters, 4 parameters to model the TCHZ peak shape and a scale parameter). The final R_{wp} was 19.6 %; the calculated and recorded patterns are given in Figure 5.19.

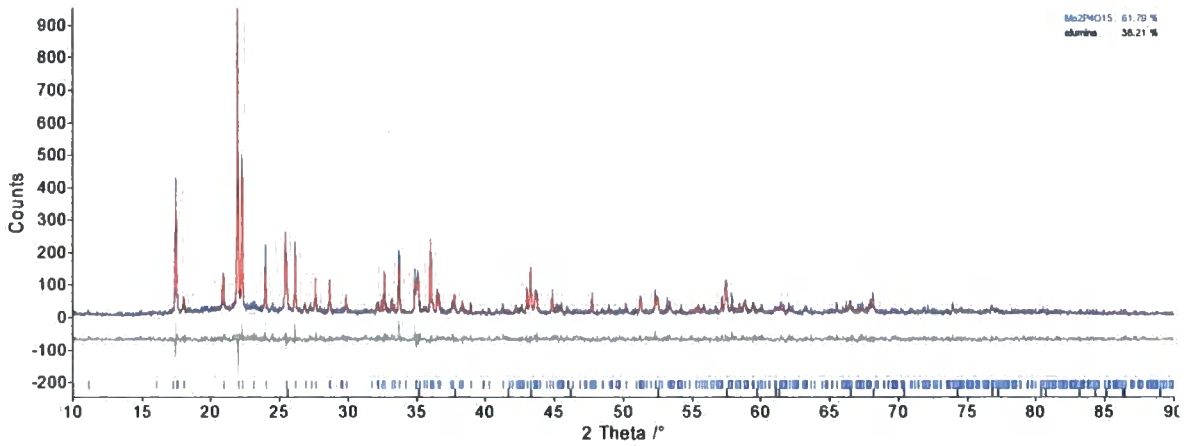

Figure 5.19 The Rietveld fit of scan d8_03295, R_{wp} 19.6 %, used to check the internal standard quantities and preparation before the variable temperature experiment. The figure shows the experimental data in blue, the calculated pattern in red and the difference plot in grey.

Scans were recorded from 10 to 90 ° 2θ in a Bruker d8 Advance diffractometer. Temperature intervals of 5 K were employed, heating from 308 to 693 K, then cooling from 695 to 315 K, and heating from 317 to 697 K with cooling from 699 to 319 K; a total of 309 scans. The scans from the first cycle of heating and cooling are plotted in Figure 5.20.

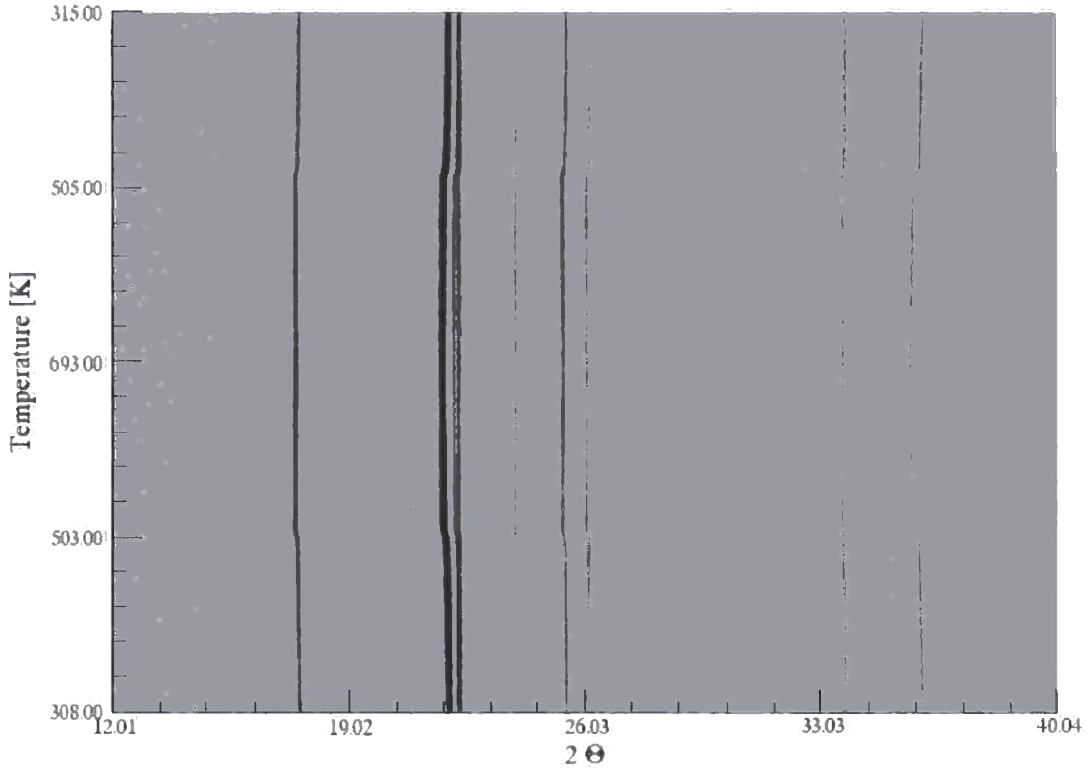

Figure 5.20 VT XRD patterns viewed as surface plots recorded on heating and cooling between 308 and 695 K, zoomed between 12 and 40 ° 2*θ*. The reversible phase transition is clearly seen between 514-531 K.

Visual inspection of these scans recorded reveals a clear shift in the positions of reflections on heating and cooling in the range 514 – 531 K. This is consistent with the phase transition discovered at 523 K by DSC. These variations are reversible on warming and cooling; they are highlighted in Figure 5.21 for the first warming cycle.

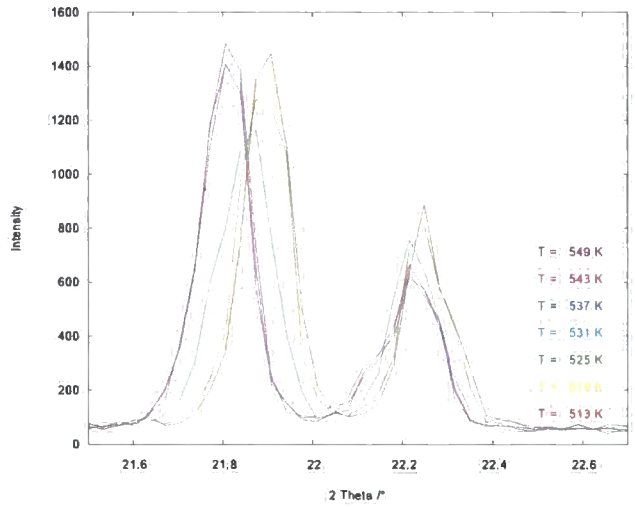

Figure 5.21 Range numbers 37 to 42 over the 2θ range 21.5-22.7 ° during the first heating cycle in d8_03297. The scans are colour labeled with their calibrated sample temperatures (calibration method outlined later in this chapter).

On first inspection the data of Figures 5.20 and 5.21 appear to show a splitting of the reflection at ~22.3 ° on warming. Peak splitting is normally associated with a lowering of metric symmetry. However, analysis of the overlapping reflections in the powder pattern reveals that the reflection at 22.3 ° 2θ is actually the combination of two overlapping Bragg reflections. Hence slight variations in the rates of change in unit cell parameters on heating causes one of these reflections to shift to lower angle. Figure 5.22 shows that this shoulder is caused by a reflection indexed to be the $1\bar{3}\,\bar{5}$ peak in the supercell model or the $1\bar{1}\,\bar{2}$ peak in the subcell model.

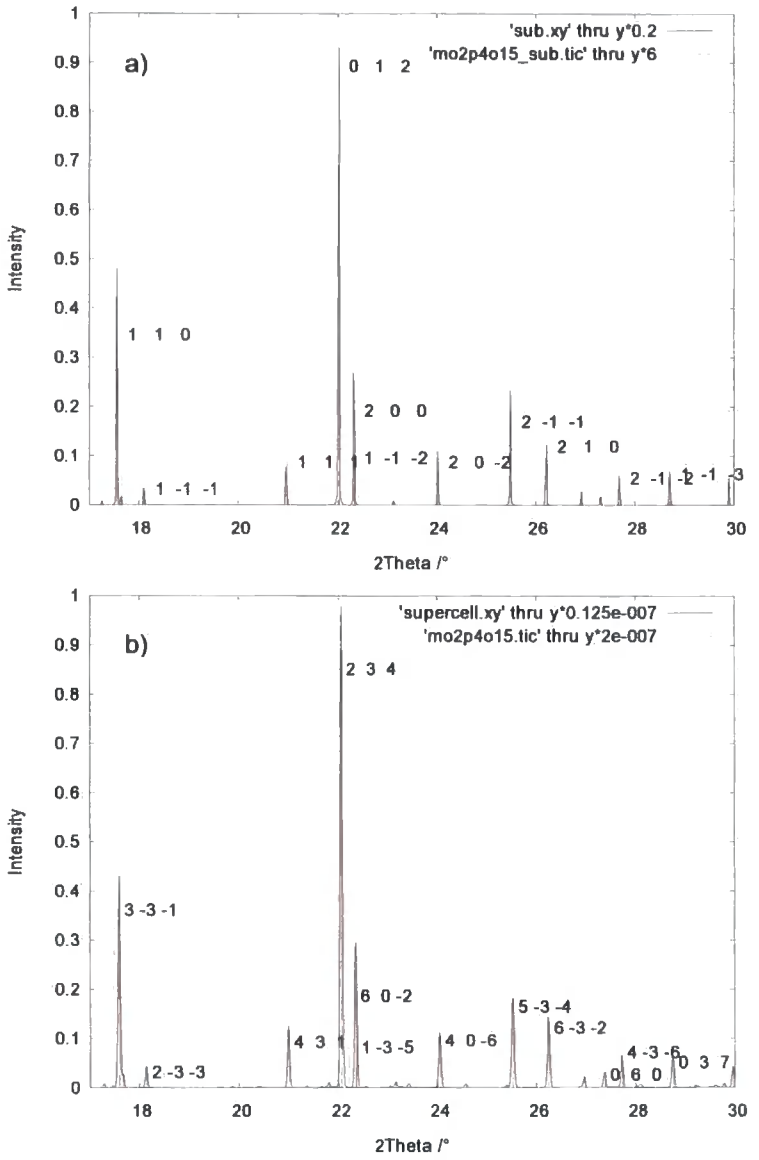

Figure 5.22 The calculated powder patterns overlaid with the *.dif* from the 120 K supercell *.cif* (a) and the subcell structure (b). Both scans have been normalised onto the same intensity scale. The most intense peaks have been annotated with their *hkl* values.

It was decided to use the subcell model for the sequential Rietveld refinements of the high temperature data. The cell parameters for the subcell were subsequently transformed to that of the supercell using simple trigonometry.

The input file for the refinement of the 30 minute data collection was used to write a seed input file for a set of sequential Rietveld refinements, using the local Fortran routine, *multitopas*.[19] Additional lines were added to the refinements so that the cell parameters and cell coordinates of both phases were randomly changed from their refined values at convergence and another round of least-squares performed using these new values. Minimum and maximum limits were applied to each cell parameter such that the randomisation could only change the values by ± 0.1 Å; similarly the atomic coordinates

were fixed to ± 0.05 Å. A total of 200 iterative cycles were performed on every data range, retaining the best converged result after the 200 iterations.

The temperature calibration of the HTK furnace was determined using the volume of the Al_2O_3 standard from Rietveld refinement. The most comprehensive analysis of the lattice parameters of Al_2O_3 was carried out by Taylor.[25] Taylor took the data available in the literature and normalized them to give lattice parameters *a* and *c* equal to 4.758 and 12.991 Å respectively at 26 °C. Regression analysis was performed over the temperature range 20 to 1232 °C using an equation of the form:

$$V = x_0(1 + x_1T + x_2T^2) \tag{5.3}$$

where the coefficients x_0, x_1 and x_2 have the values 254.53 $Å^3$, 19.6(5)x10^6 $°C^{-1}$ and 6.54(45)x10^9 $°C^{-2}$ respectively.[n] It is possible to use this equation as a method of temperature calibration.

Values obtained for the volume of Al_2O_3 in each sequential refinement were imported to Excel, alongside the set temperatures recorded for each scan. The refined values of the volume were then compared with the ideal volumes calculated using Taylor's equation,[25] and a corrected temperature calculated by solving Taylor's equation for each volume. Individual errors in these calculations were removed by fitting a polynomial expression through the calculated temperatures; the corrected temperatures were calculated using this polynomial expression. Differences between the corrected temperatures and those calculated purely using Taylor's equation will then be small but non-zero, as given in Figure 5.23. These corrected temperatures are then used as the sample temperature for each scan recorded.

[n] *Nota Bene*: The values of T in the above equation should be in °C.

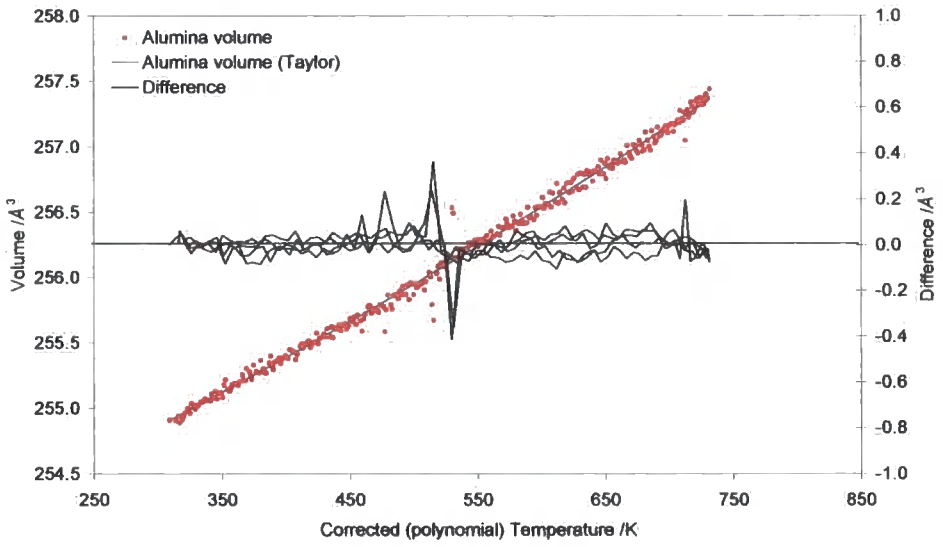

Figure 5.23 Differences between volumes calculated using Taylor's equation and a polynomial used to minimise individual errors in the use of Taylor's equation. The errors between the two approaches are small, being less than 0.4 $Å^3$ over the temperature range. The largest differences are seen immediately either side of the phase transition in $(MoO)_2P_4O_{13}$.

Figure 5.24 shows the unit cell volume data over the range 16 to 753 K. The supercell volume is known to be twenty-one times greater than the subcell volume, hence the volume data for the high temperature experiment have been scaled for comparison with the low temperature data. Data points from the low and room temperature single crystal measurements are also included. It is clear that all the data from the PheniX, HTK and single crystal measurements are in excellent agreement.

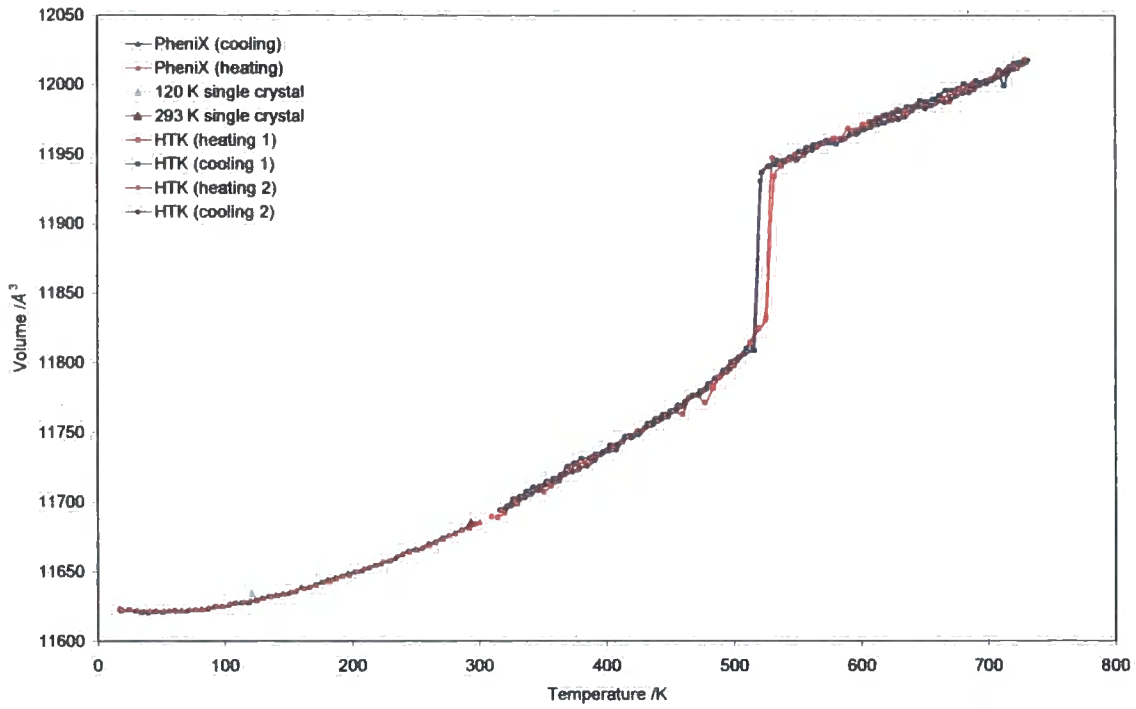

Figure 5.24 Volume expansion in $(MoO)_2P_4O_{13}$ from 16 □ 753 K, including data from high and low temperature powder XRD studies and single crystal structure refinements. The graph shows a smooth increase in volume with increasing temperature and the phase transition at 523 K. A slight hysteresis between high temperature heating and cooling datasets is visible.

The phase transition that was first seen by DSC is clearly visible in Figure 5.24, as the discontinuity in the volume of the unit cell at approximately 520 K, as expected for a first order transition. There is some hysteresis (~ 10 K) seen between the heating and cooling data; the average phase transition temperature value is in excellent agreement with the DSC measurement.

In order to obtain values for the thermal expansion coefficients, data were fitted using a Bezier function to allow numerical differentiation. The thermal expansion coefficients were calculated as defined in Equation 1.2. For most of the temperature range investigated, $(MoO)_2P_4O_{13}$ undergoes positive thermal expansion; however, below 80 K negative thermal expansion is observed. The calculated values of α_v for both the low and high temperature data sets are plotted in Figure 5.25.

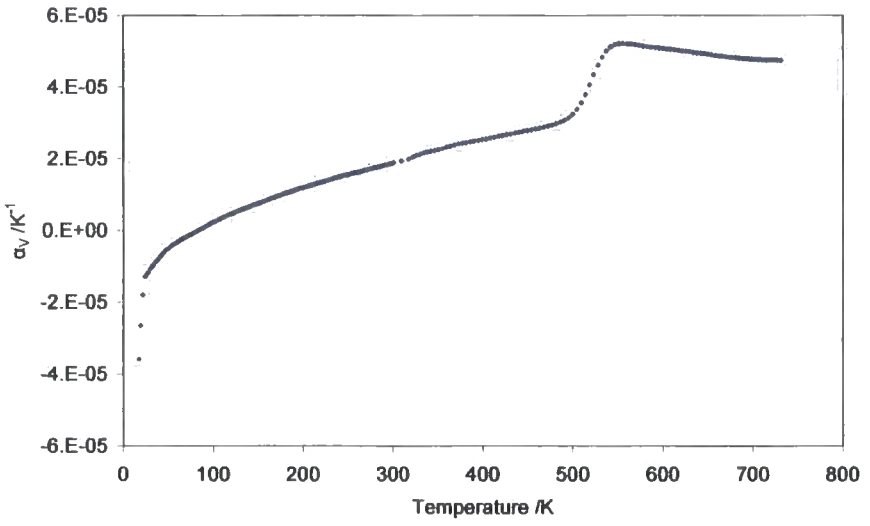

Figure 5.25 Thermal expansion data calculated for $(MoO)_2P_4O_{13}$ over the range 16 – 753 K. Values at extreme edges of data are derived from a smaller number of data points and are therefore less reliable. Negative thermal expansion is observed below 80 K.

To compare individual cell parameters over the whole temperature range, values derived using the subcell model have been transformed to equivalent supercell settings using the relationships given in Figure 5.26. The lengths *a'*, *c'* and *d'* were included to simplify the trigonometric equations. The definitions of these three lengths, as well as the equations used to obtain values for the supercell parameters from the subcell parameters, are given in the following Equations, 5.4 – 5.10.

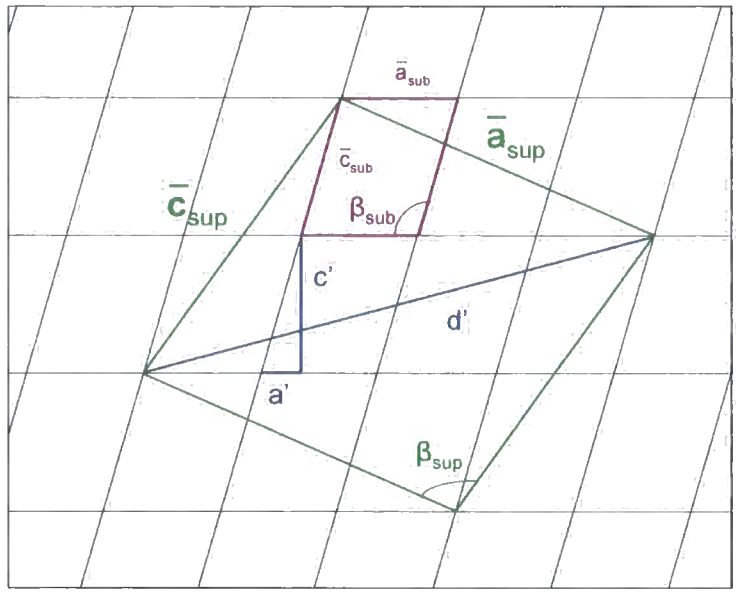

Figure 5.26 The relative orientations of the subcell and supercell unit cells in the *ac* plane. The grey dotted lines indicate the subcell lattice, with one unit cell highlighted in purple, and lattice parameters marked as a_{sub}, c_{sub} and β_{sub}. A supercell unit cell is then superimposed over the top of the subcell lattice in green, with lattice parameters a_{sup}, c_{sup} and β_{sup}. The *b* axis is directed out of the page, having unit length one for the subcell and three for the supercell. The origins of *a'*, *c'* and *d'* are explained in the text.

$$a' = c * \cos(180 - \beta) \tag{5.4}$$

$$c' = c * \sin(180 - \beta) \tag{5.5}$$

$$d' = \sqrt{(4a + a')^2 + c'^2} \tag{5.6}$$

$$a_{sup} = \sqrt{(3a - a')^2 + c'^2} \tag{5.7}$$

$$b_{sup} = 3b_{sub} \text{ (not pictured)} \tag{5.8}$$

$$c_{sup} = \sqrt{(a + 2a')^2 + 2c'^2} \tag{5.9}$$

$$\beta_{sup} = \cos^{-1}\left[\frac{d'^2 - c_{sup}^2 - a_{sup}^2}{2a_{sup}c_{sup}}\right] \tag{5.10}$$

Figure 5.27 shows the changes in the cell parameters of $(MoO)_2P_4O_{13}$ over the temperature range 16 – 753 K. Each graph shows the data for both the heating (red) and cooling (blue) cycles. The y scale axes on the graphs for the *a*, *b* and *c* cell parameters have been chosen to represent comparable relative changes. Percentage changes for the lattice parameters *a*, *b* and *c* over the whole temperature range are 0.58 %, 1.68 % and 1.0 % respectively. The *a*, *b* and *c* parameters all vary smoothly with temperature.

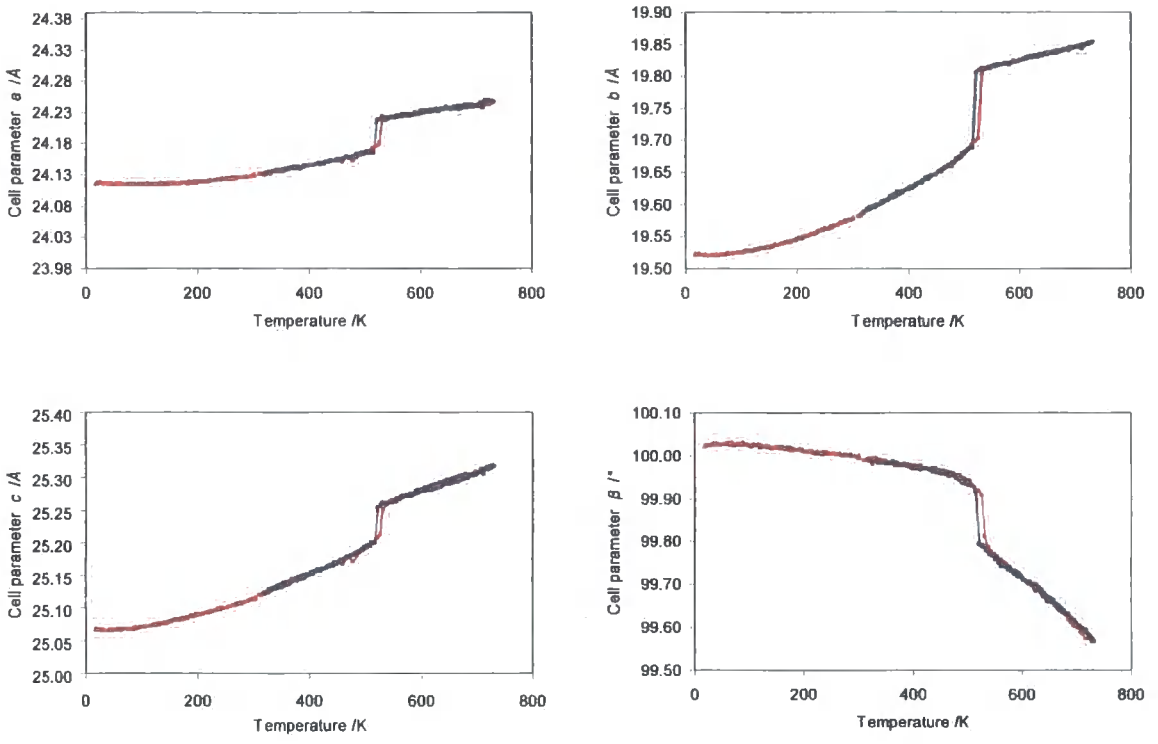

Figure 5.27 Changes in unit cell parameters with increasing (red) and decreasing (blue) temperature from the low temperature PheniX data (▲) and the high temperature furnace (■,●) experiments. The same % change scale is used for each graph.

5.6 High temperature single crystal structure determination

Following the discovery of the phase transition present within $(MoO)_2P_4O_{13}$, experiments were planned to solve the structure of the material at temperatures above the phase transition at 523 K. Due to the temperature of the phase transition being above that of standard equipment capabilities on most single crystal machines,[o] the use of an Enraf Nonius Crystal Heater (Hothead) was employed, as outlined in Section 2.3.5. High temperature measurements were carried out both at Station 16.2_{SMX} at Daresbury and in Durham; however, to ensure the crystals used for the data collections were of adequate quality, a room temperature data collection was also taken for comparison.

5.6.1 Data collection and analysis using the Hothead at Daresbury

Data collections were carried out using the Apex II software on Station 16.2_{SMX} at Daresbury.[26] Crystals were prepared and mounted on the Hothead and in the diffractometer as discussed in Section 2.3.5.1. Data were collected in short "matrix" collections (15 frames at 3 different φ positions) and also as longer "data" collections. Matrices collected at room temperature could be indexed to the known room temperature cell; however, the longer data collections could not be successfully refined, even when starting from the known low temperature structure.

[o] The ability to determine crystal structures between 77 and 500 K using a liquid nitrogen cryostream type attachment is currently standard on most single crystal diffractometers in research groups and at central facilities.

Data frames collected above the phase transition temperature of 523 K were compared with those collected at lower temperatures, Figure 5.28. The spot density decreases dramatically between the data collection at room temperature and at 573 K. Attempts to index the high temperature cell from these data were unsuccessful. Although the data would index to several different triclinic cells, none of these indexed all of the reflections satisfactorily.

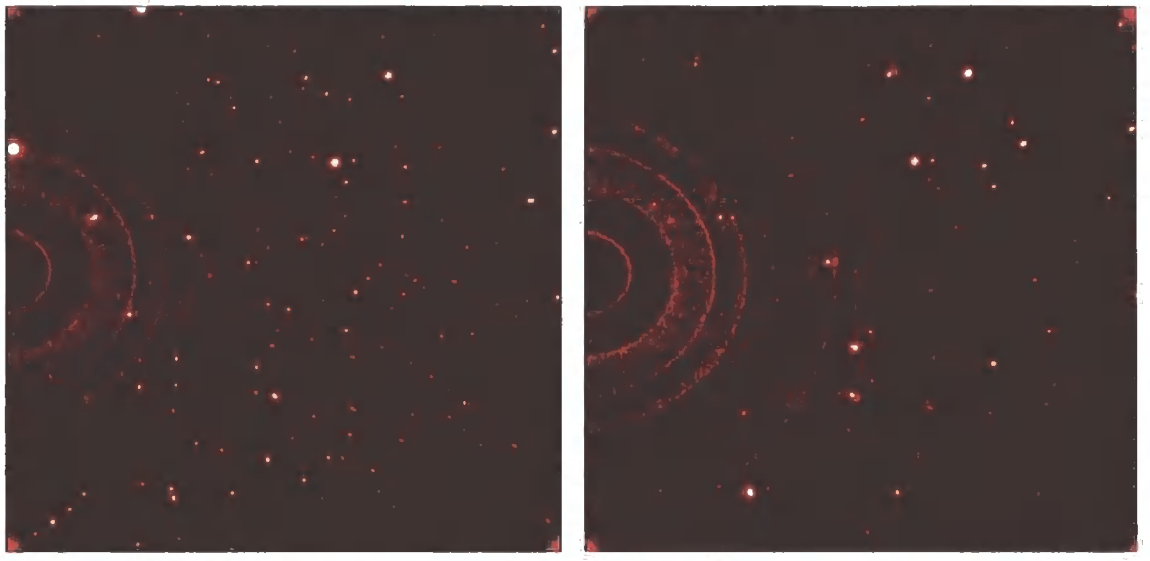

Figure 5.28 Single crystal frames recorded at a) ambient temperature and b) 573 K.

Data were also collected rapidly on warming to monitor the changing cell parameters with temperature. Short matrix collections were recorded from room temperature to 698 K in approximate 25 K steps. Collections had to be halted at this temperature due to an electrical fault on the Hothead.

Only collections up to – and including – the phase transition temperature, could be indexed to the known supercell unit. Though it was clear the structure remained more complex than the subcell model at all temperatures. By fitting the strongest reflections only with the subcell cell it was possible to follow the evolution of the cell volume with temperature, Figure 5.29.

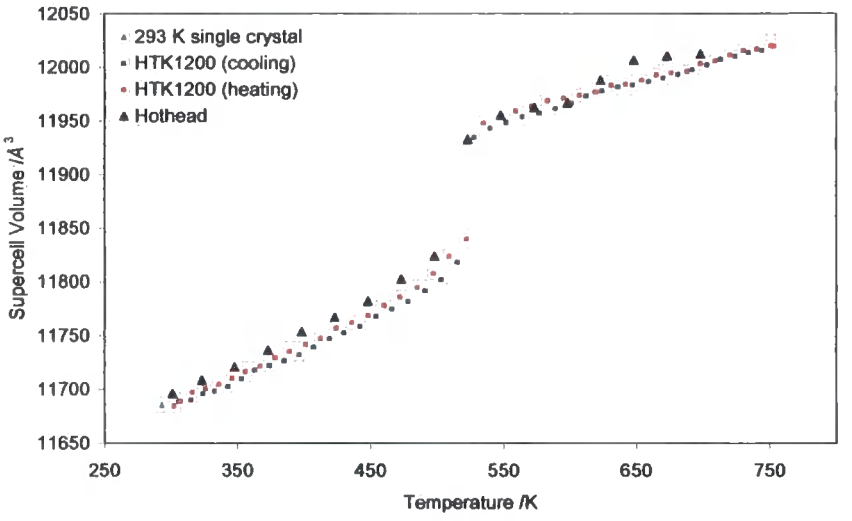

Figure 5.29 Graph showing the close agreement between the unit cell volumes from the Hothead single crystal experiments and the data from the high temperature powder experiments.

The data again show the phase transition between 500 and 525 K, as found from DSC and powder diffraction measurements. The volumes calculated from the VT single crystal experiment show the same trends and were found to agree with those found from powder diffraction experiments. However, the volumes from the single crystal experiments seem to imply that there is a third temperature region of interest for this material in-between the low and high temperature phases. This region between 525 and 625 K is investigated further in Section 5.7.1.

5.6.2 Data collection and analysis using the Hothead in Durham

Following several unsuccessful attempts to collect and analyse data recorded at the SRS, similar experiments were performed on a Bruker AXS Smart 6000 Diffractometer in Durham (section 2.3.5). Crystal testing was carried out on crystals of $(MoO)_2P_4O_{13}$ (SEL307a) at 120 K before any high temperature data collections were performed to ensure suitable crystals had been selected.

5.6.2.1 Room temperature data recorded on the Hothead

In order to compare the quality of the models derived from the Hothead experiments, specifically due to the reduced data redundancy present, the spreads in bond lengths were first calculated for one of the room temperature data collections (025dat, 30s/frame). Data collection proceeded as described in Section 2.3.5.2; data were collected over the full ω range possible in this set-up, details are given in Table 5.9.

Table 5.9 Data Collection procedure at 573 and 673 K using the Hothead. A full description of the experimental set-up is given in Section 2.3.5.2.

Fixed 2θ /°	-30
Initial ω /°	-30
$\Delta\omega$ /°	0.3
No. of frames	600
χ /°	0
φ /°	Constant
Collection Time/frame /s	10

The room temperature model was refined against the data recorded on the Hothead against F^2 using reflections having $I/\sigma(I) > 3$, refining scale, atomic positions, isotropic temperature factors and applying a 3 parameter optimal weighting scheme. Crystal information and a data refinement summary are given in Tables 5.10 and 5.11. The crystal used for this data collection was also used in the high temperature refinement at 573 K, Table 5.13.

Table 5.10 Summary of the crystal used in the room temperature collection 025dat.

λ (Mo Kα) /Å	0.71073
Temperature /K	573
Chemical Formula	$(MoO)_2P_4O_{13}$
Molecular Weight /Daltons	555.766
Crystal Form	Irregular Prism
Crystal Size /mm^3	0.22 * 0.14 * 0.04
Crystal Colour	Green

Table 5.11 Summary of the refinement data for the room temperature dataset recorded on the Hothead for $(MoO)_2P_4O_{13}$.

	293 K data
Crystal System	monoclinic
Space Group	*Pn*
a /Å	24.1291(10)
b /Å	19.5817(8)
c /Å	25.1108(10)
β /°	99.978(10)
V /Å^3	11685.1(8)
Z	42
Calculated Density /gcm^{-3}	3.317
μ /mm^{-1}	2.921
Total number of reflections	93,645
Number of unique reflections	48,060
Criterion for Observed reflections	20,209 > 3σ
Number of refined parameters	1766
Observations:Parameter ratio	11.4
R /%	4.75
R_w /%	11.49
Goodness of Fit	0.988

The following histograms give the bond length spreads for each of the atom types within the structure. Average bond lengths are given in Table 5.12, alongside the average bond length data from the standard room temperature refinement from Section 5.4.

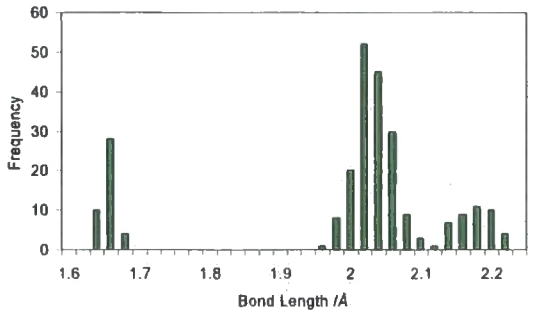

Figure 5.30 The Mo-O bond length data for the 252 bonds within the structure.

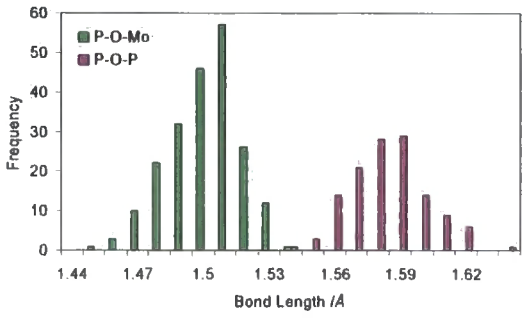

Figure 5.31 Histogram showing the distribution of P-O bond lengths dependent on type within the structure. The green columns show the data for the Mo-O-P bridges, and the purple columns indicated the P-O-P bridges.

Table 5.12 Mean bond length and standard deviations for the bond lengths in the data collection at room temperature.

	Standard Collection	Hothead Collection
Bond Length	Value (e.s.d.) /Å	Value (e.s.d.) /Å
Mo-O (short)	1.652(26)	1.647(11)
Mo-O (medium)	2.025(35)	2.022(26)
Mo-O (long)	2.172(35)	2.168(26)
P-O	1.497(39)	1.497(16)
$P\text{-}O_b$	1.583(36)	1.580(18)

Figures 5.30 and 5.31 show a clear splitting of the Mo-O and P-O bond lengths into their separate types for the data collection performed with the Hothead. By comparison with the same histograms for the standard collection (Figures 5.7b) and 5.9b)), these distributions are much more clearly separated, with smaller spread on each of the distributions. This information implies that despite the small amount of redundancy present within the Hothead data collections, the refinements are still of very good quality. Hence it can be concluded that the Hothead data collections are of satisfactory quality for structure solution and refinement. The *cif* from this refinement and the individual values for bond lengths and angles are given in the E-Appendix.

5.6.2.2 Initial data collection and structure solution

The same crystal as used at room temperature was heated to 573 K; an identical data collection strategy was used (300dat, 30s/frame). The data recorded were indexed to a triclinic cell, with cell parameters *a* 17.947(32) Å, *b* 19.864(3) Å, *c* 21.899(3) Å, α 72.421(3) °, β 78.174(4) °, γ 68.315(4) °, Volume 6877.2(19) $Å^3$. The data were integrated and analysis of the statistical distribution of the intensities led to the choice of the centrosymmetric space group, $P\bar{1}$. No absorption corrections could be made as the data collected had low redundancy.

The volume ratio between the room temperature structure and the high temperature unit cell was calculated to be ~ 1.75. This led to the calculation of the contents of the high temperature asymmetric unit to be 24 Mo, 48 P, 180 O; a total of 252 unique atoms. Attempts to solve the structure using Direct Methods in Sir92 failed.[27] This is not surprising giving the high pseudosymmetry present. Instead attempts were made to solve the structure using the charge flipping method (section 2.2.5).[28] The charge flipping input file written for Topas is included in the E-Appendix. Following several thousand iterations, the cloud with the lowest agreement index (0.7) was kept and the coordinates obtained by peak searching written into a new Topas file and a *cif* generated. Visual inspection of these results was able to show that this method had successfully found all 24 Mo and 48 P atoms; some of the expected 180 O atoms were also present forming metal-centred polyhedra.

This model was read into Crystals alongside the *ins* and *hkl* data files,[9] refinement was carried out against F^2, with symmetry equivalent reflections were merged. Successive cycles of difference Fourier map calculations and refinement of the scale and atomic positions yielded a structure containing MoO_6 octahedra and PO_4 tetrahedra with the same connectivity as known for the low temperature structure. For comparison, the low and high temperature structures are shown in Figure 5.32. The similarity between them is obvious.

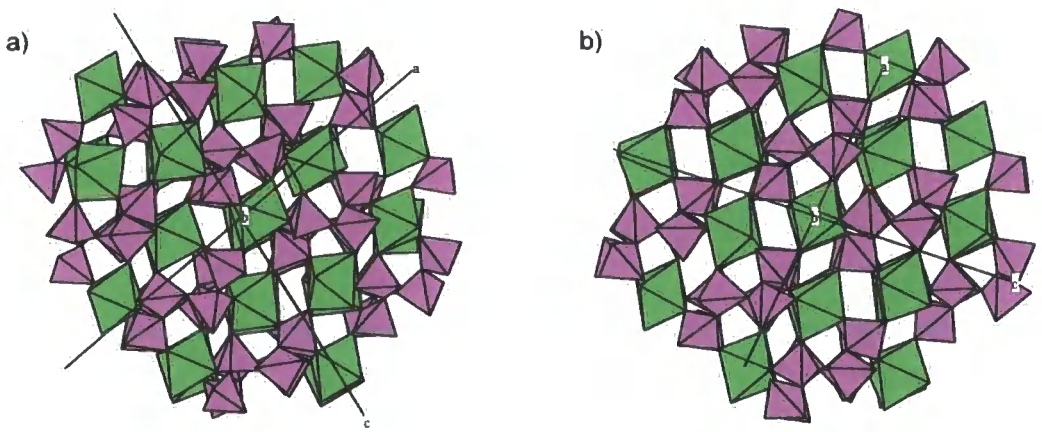

Figure 5.32 The structural connectivity for $(MoO)_2P_4O_{13}$ is shown for (a) the low temperature structure and for (b) the newly solved high temperature phase.

A total of 253 unique atoms are present in the structure (two oxygen atoms are located on a special position). Refinement of the atomic positions and isotropic thermal displacement parameters initially led to high R-factors (R/R_w 27/40 %). Refinement of the atomic positions and isotropic thermal displacement parameters (U_{iso}s) was carried out in stages, starting with the heavy elements and finally progressing to the oxygen atoms. A 3 parameter optimal weighting scheme was applied. Final R/R_w were 5.15/9.65 %, indicating a high quality refinement. Repeating the refinement with a minimum $I/\sigma(I)$ ratio of 2 gave R/R_w were 5.64/10.02 %. The refinement details are summarised in Table 5.13.

Table 5.13 Summary of the (unrestrained) refinement data for the datasets recorded at 573 K and 673 K on the Hothead for $(MoO)_2P_4O_{13}$.

	573 K data	653 K data
Crystal System	triclinic	triclinic
Space Group	$P\bar{1}$	$P\bar{1}$
a /Å	17.947(3)	18.001(17)
b /Å	19.864(3)	19.980(30)
c /Å	21.899(3)	22.000(30)
α /°	72.42(3)	72.19(5)
β /°	78.17(4)	78.24(6)
γ /°	68.32(4)	68.42(4)
V /Å^3	6877.2(19)	6877(16)
Z	24	24
Calculated Density /gcm^{-3}	3.220	3.179
μ /mm^{-1}	2.836	2.800
Number of unique reflections	25,767	26,002
Criterion for Observed reflections	7,680 > 2σ	4834 > 3σ
Number of refined parameters	1011	1011
Observations:Parameters ratio	7.6	4.8
R /%	5.64	4.60
R_w /%	10.02	11.73
Goodness of Fit	1.121	0.9939

Due to the large number of atoms within the asymmetric unit of this material, it is again impractical to tabulate all the values of bond lengths and bond angles within the asymmetric unit. These data are presented graphically in the form of histograms in Figures 5.33 to 5.35, with individual values in the spreadsheets contained in the E-Appendix.

The connectivity and expected bond length distributions have been discussed in Section 5.4 for the room temperature structure. Due to the identical structural connectivity in the high temperature phase to that of the low/room temperature structure, the same bond length distributions are expected for this phase. The following histograms show the spread of Mo-O (Figure 5.33) and P-O (Figure 5.34) bond lengths and P-O-P (Figure 5.35) bond angles from the high temperature structure refinement. Temperature factors for all of the atoms are given in Figure 5.36. These have a much larger spread compared to those in Figure 5.13. Average bond lengths for each type of bond are given in Table 5.14 alongside those calculated for the 120 K low temperature structure.

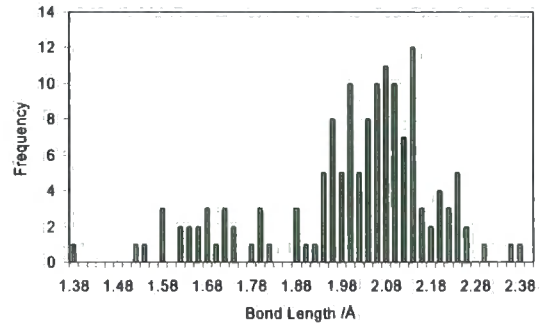

Figure 5.33 The bond length data for all 144 Mo-O bond lengths within the high temperature structure.

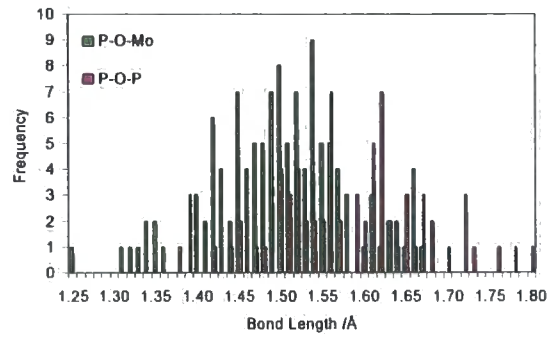

Figure 5.34 Histogram showing the distribution of the 192 P-O bond lengths within the structure dependent on type. The green columns show the data for the Mo-O-P bridges, and the purple columns indicate the P-O-P bridges.

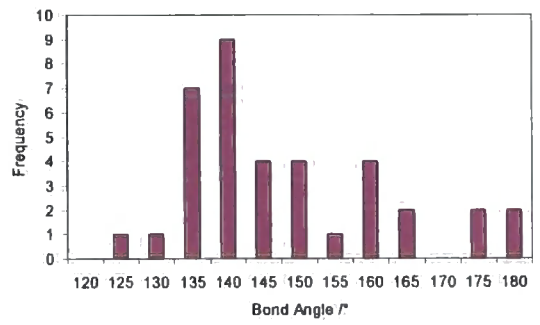

Figure 5.35 The bond angle data for all 36 P-O-P bond angles within the structure.

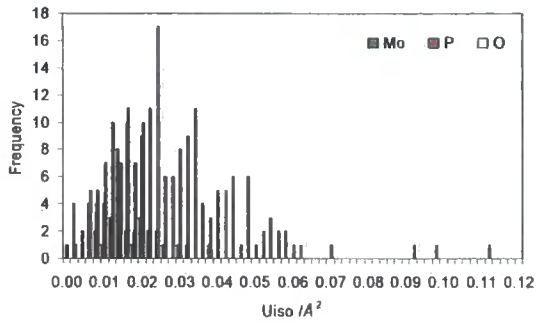

Figure 5.36 A histogram of temperature factors for the structure refinement at 573 K. The spread is very large due to the increased temperature of this data collection when compared to standard single crystal methods at *e.g.* 120 K. One O U_{iso} at 0.1627 $Å^2$ has been omitted from the graph. The atom is oxygen number 212, an atom on a special position. This is discussed further in the text.

Table 5.14 Mean bond length and e.s.d.s for the bond lengths in the refinements at 120 K and 573 K.

120 K		573 K	
Bond Length	Value (e.s.d.) /Å	Bond Length	Value (e.s.d.) /Å
Mo-O (short)	1.653(5)	Mo-O (short)	1.654(100)
Mo-O (medium)	2.025(25)	Mo-O (medium)	2.041(94)
Mo-O (long)	2.167(22)	Mo-O (long)	2.171(89)
P-O(-Mo)	1.500(13)	P-O(-Mo)	1.499(83)
P-O(-P)	1.583(14)	P-O(-P)	1.582(91)

The mean bond lengths for each of the bond types at 573 K equal those at 120 K within a low standard uncertainty. Comparing Figures 5.33 to 5.35 with Figures 5.7 to 5.10, it is clear that the tight distributions around the mean in the 120 K structure solution are no longer present in the high temperature model. This is due to the reduction in intensities recorded on increasing temperature and a lower observation:parameters ratio. The weak reflections in the data are most likely to be affected by this, resulting in larger s.u.s for refining parameters and thus larger spreads (and larger e.s.d.s) in the distributions calculated for each bond type.

5.6.2.3 Improving the structural model using weighted restraints

By comparison with the data collections and refinements summarised in Table 5.5, this data collection contained far fewer reflections above the $I/2\sigma$ ratio used for structural refinement. Restraints were applied to the bond lengths within the structure. The mean bond lengths and standard deviations calculated for each type of bond length distribution in both the 120 K and free refinement at 573 K are given in Table 5.14. Each P-O type (bridging and terminal) and Mo-O type (short, medium and long) were individually assigned an ideal bond length equal to the refinement mean and also a standard deviation from that calculated from the spread of values in the refined model at 120 K.

These restraints were added as additional observations to the refinement described in Section 5.6.2.2. Several cycles of least squares were performed refining a total of 1008 parameters to give final R-factors R/R_w of 6.15/10.73 %. The following tables and figures compare the free/unrestrained model of Section 5.6.2.2 with the restrained model. Table 5.15 gives the calculated means and standard deviations for each bond type in the two refinements. Figures 5.37 to 5.39 compare the distributions of the bond lengths and angles in the restrained refinement graphically.

Table 5.15 Mean bond length and standard uncertainties for the bond lengths in the free refinement at 573 K and the restrained refinement at 573 K.

573 K free refinement		573 K restrained refinement	
Bond Length	Value (e.s.d.) /Å	Bond Length	Value (e.s.d.) /Å
Mo-O (short)	1.654(100)	Mo-O (short)	1.652(9)
Mo-O (medium)	2.041(94)	Mo-O (medium)	2.035(36)
Mo-O (long)	2.171(89)	Mo-O (long)	2.165(24)
P-O(-Mo)	1.499(83)	P-O(-Mo)	1.502(14)
P-O(-P)	1.582(91)	P-O(-P)	1.580(16)

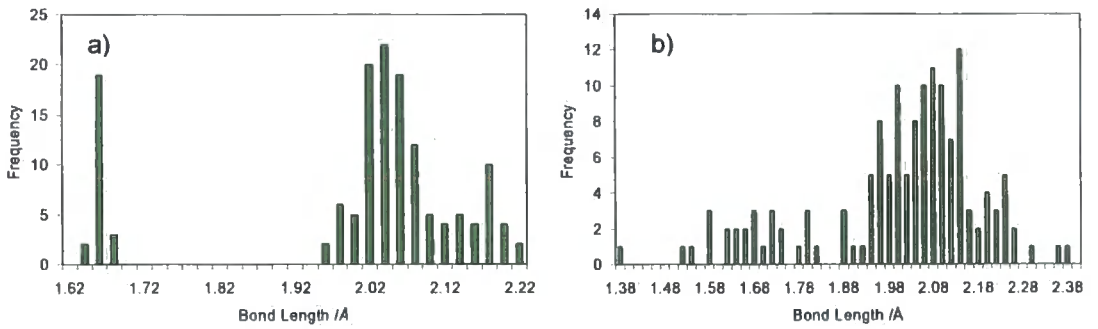

Figure 5.37 Bond length histograms for all 144 Mo-O bond lengths in the a) restrained refinement compared to b) the unrestrained refinement.

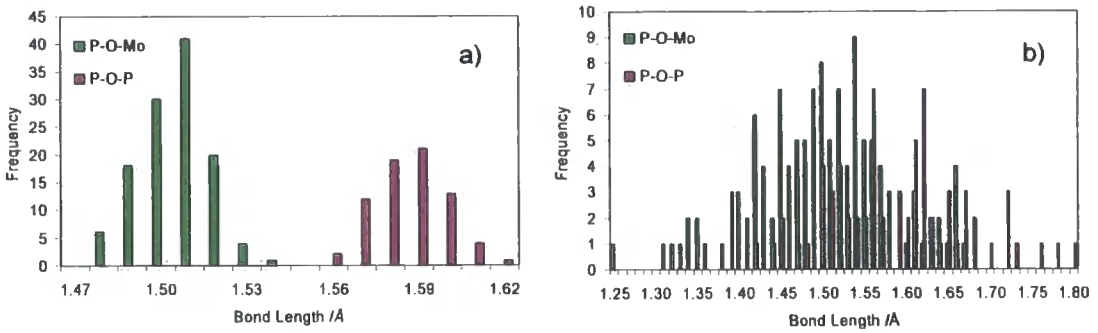

Figure 5.38 Histograms showing the distribution of the 192 P-O bond lengths in the a) restrained refinement compared to b) the unrestrained refinement. The green columns show the data for the Mo-O-P bridges, and the purple columns indicated the P-O-P bridges.

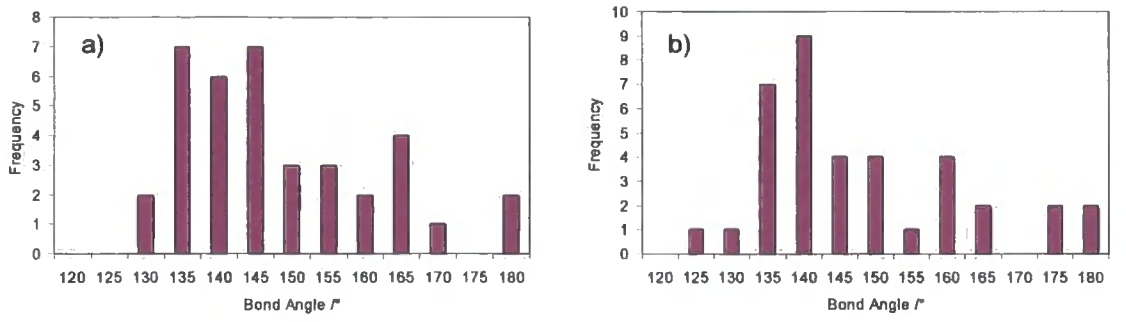

Figure 5.39 Histograms showing the 37 P-O-P bond angles in a) the restrained refinement compared to b) the unrestrained refinement.

All the bond lengths in Figures 5.37 to 5.38 are found to lie within 3σ of the calculated mean for the distribution. The values of the mean, calculated for each bond type, are identical to those from both the 120 K dataset and the free refinement at 573 K (within a standard uncertainty). Application of the restraints has shown that the bond lengths cannot be accurately determined from the data recorded at 573 K. The small increase in R/R_w was expected, and does not give cause for concern. The *cif* from this refinement and the individual values for bond lengths and angles are given in the E-Appendix.

5.6.2.4 Examination of O atoms on special positions

The information about the bond angles within the high temperature phase is contained in Figure 5.35. Within this structure two of the oxygen atoms are located on an inversion centre, namely O206 and O212. As a consequence of this, these bridging oxygens are forced by symmetry to have an average P-O-P bond angle of 180 °; this is energetically unfavourable. These two sites were further examined to investigate whether the oxygens were really on the special position or were in fact on a split position to remove the 180 ° bond angle constraint. The isotropic displacement parameters for each P_2O_7 group are given in Figure 5.40.

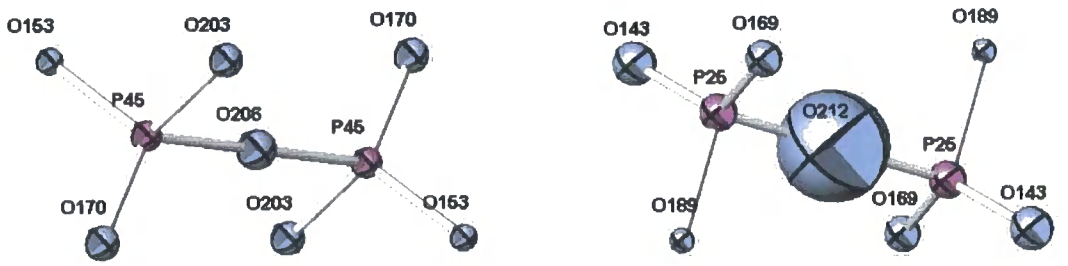

Figure 5.40 Ortep diagrams[29] showing P_2O_7 groups of interest. Symmetry equivalent atoms are plotted for ease of viewing. The isotropic displacement parameters for each of the atoms are drawn with 50 % probability.

It is clear from Figure 5.40 that O212 has a very large thermal displacement parameter. This oxygen was also excluded from the histogram plot of isotropic thermal displacement parameters in Figure 5.36

due to its large magnitude compared to those of other atoms. To investigate the question of site splitting F_{obs} maps were drawn through the O position; Figure 5.41 was drawn using the Platon software.[30]

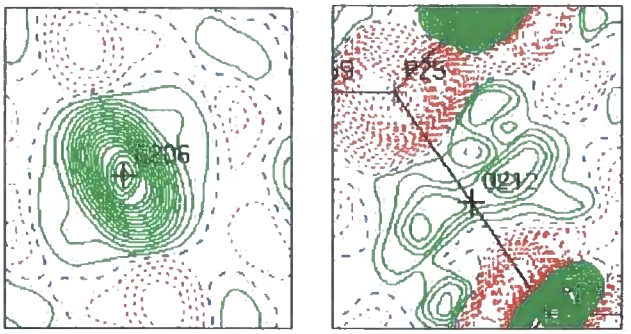

Figure 5.41 F_{obs} map through the two oxygen atoms on an inversion centre. Contours are drawn on increasing intensity from red to blue to green in Platon. O206 has contours in eÅ^{-3} -1.00 to 2.80 in 0.05 steps. O212 has contours in eÅ^{-3} from -0.40 to 1.80 in 0.10 steps.

These electron density maps seem to imply that O206 lies on the special position, whereas O212 is on a split site. Electron density slices of the structure around the O153-O206-O153□ and O143-O212-O143□planes were also drawn using the Slant Fourier method in Crystals,[9] with diagrams drawn in the Marching Cubes program,[31] Figure 5.42.

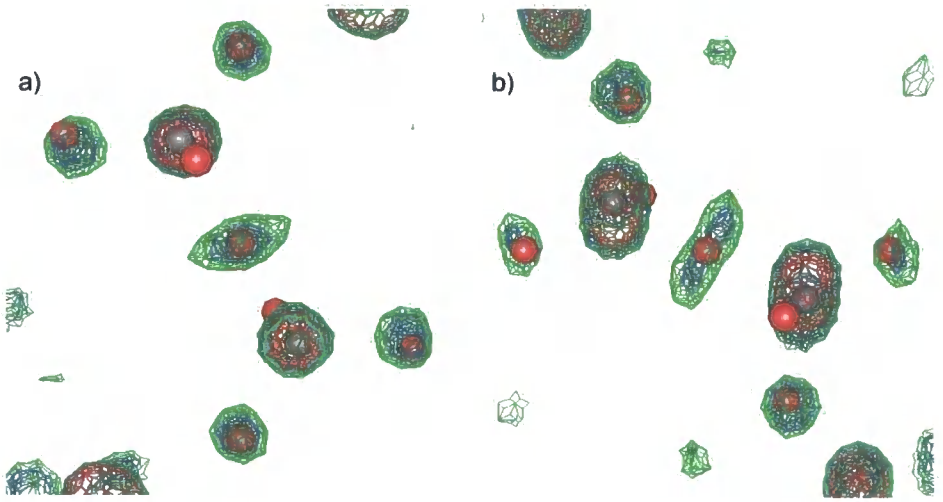

Figure 5.42 F_{obs} maps drawn through a) O153-O206-O153□and b) O143-O212-O143□using the Marching Cubes program.

These pictures provide further evidence for the splitting of O212□s atomic position. For final cycles of refinement, O212 was moved off the special position, and its occupancy changed to 0.5. After several cycles of refinement using 1011 parameters, final R-factors of 6.13/10.70 % were obtained. The *cif* from this refinement and the individual values for bond lengths and angles are given in the E-Appendix.

5.6.2.5 High temperature structure at 653 K

A second high temperature dataset was recorded at 653 K (380dat, 20s/frame) for comparison with that recorded at 573 K. Both of these high temperature datasets were indexed to the same unit cell. The *cif* from Section 5.6.2.4 was read into crystals and the scale, positions and isotropic thermal displacement parameters were refined. Final R/R_w using the unrestrained model were 4.60/11.73 %; the restrained model gave R/R_w 4.95/12.81 %. A summary of the refinement data for the unrestrained model is given in Table 5.13. The distributions of bond lengths were very good; spreadsheets and *cif*s containing these data are included in the E-Appendix.

5.6.2.6 Relationship of the high temperature cell with the subcell model

The high temperature single crystal structure determination has shown that the high temperature structure is not that of the known subcell model, as had been previously suspected. In order to better understand the relationship between the unit cells and the different structures the material adopts at varying temperatures, the geometrical relationship between the subcell model and the high temperature structure was determined. The method was as follows.

For the high temperature dataset, it was possible to index the reflections to both the high temperature cell, and also □ by increasing the I/σ cut-off to 150 □ to the subcell. Reflections that were predicted in both cells could then be used to obtain the geometrical information required. The different *hkl* indices that were assigned to a given reflection from both unit cells described the diffraction arising from equivalent planes in the two cells. Three pairs of indices were used to calculate a transformation matrix between the subcell and the high temperature cell, as given in the following equations.

$$C = A \cdot B \tag{5.11}$$

$$\begin{bmatrix} 3 & 8 & 3 \\ 3 & 6 & \bar{3} \\ \bar{2} & \bar{7} & \bar{1} \end{bmatrix} = \begin{bmatrix} & A & \end{bmatrix} \cdot \begin{bmatrix} \bar{1} & \bar{3} & \bar{2} \\ 1 & 2 & \bar{1} \\ 2 & 6 & 1 \end{bmatrix} \tag{5.12}$$

Matrices B and C contain the *hkl* values indexed to the same reflection using both the high temperature structural model and the subcell model. Matrix A is a 3x3 transformation matrix that relates the two cells. Matrix A was calculated as follows.

$$B^{-1} = \frac{(adjB)^T}{\det B} = \begin{bmatrix} -8/3 & 3 & -7/3 \\ 1 & \bar{1} & 1 \\ -2/3 & 0 & -1/3 \end{bmatrix} \tag{5.13}$$

$$A = \begin{bmatrix} 3 & 8 & 3 \\ 3 & 6 & \bar{3} \\ \bar{2} & \bar{7} & \bar{1} \end{bmatrix} \cdot \begin{bmatrix} -8/3 & 3 & -7/3 \\ 1 & \bar{1} & 1 \\ -2/3 & 0 & -1/3 \end{bmatrix} = \begin{bmatrix} \bar{2} & 1 & 0 \\ 0 & 3 & 0 \\ \bar{1} & 1 & \bar{2} \end{bmatrix} \tag{5.14}$$

As this matrix represents the transformation between the subcell model and the high temperature structure, the determinant of this matrix should equal the ratio of the volumes of the two cells, *i.e.* it should have a value of +12; this is the case. Hence, taking the unit cell vectors *a*, *b* and *c*:

$$\begin{bmatrix} \bar{2} & 1 & 0 \\ 0 & 3 & 0 \\ \bar{1} & 1 & \bar{2} \end{bmatrix} \cdot \begin{bmatrix} a \\ b \\ c \end{bmatrix} = \begin{bmatrix} b-2a \\ 3b \\ b-a-2c \end{bmatrix} = \begin{bmatrix} a_{HT} \\ b_{HT} \\ c_{HT} \end{bmatrix} \quad (5.15)$$

Due to the 3-dimensional nature of this transformation, it is not easy to depict this in 2D graphical form. To give an indication of the relationship between the cells, Figure 5.43 was produced using the internet resource ISODISPLACE.[32]

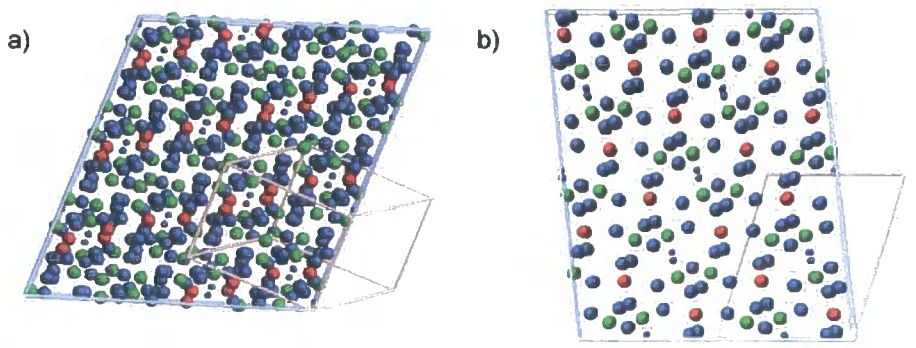

Figure 5.43 The high temperature structural model is shown in the large blue-edged unit cell. The size and orientation of the subcell is indicated by the pink-edged unit cell. Views are a) along the high temperature [100], and b) down the [010] of both cells.

5.7 Confirmation using TOF neutron experiments

Following successful solution and refinement of the high temperature structure of $(MoO)_2P_4O_{13}$, data were collected at HRPD, ISIS to further test the structural model against high resolution neutron powder data. Data were recorded on a sample of $(MoO)_2P_4O_{13}$ (SEL312) in a 15 mm cylindrical V can filled to a depth of 30 mm. Long data collections were recorded at both room temperature and above the phase transition of the material, as given in Tables 5.17 and 5.19, for later structural characterisation. A series of rapid measurements from 303 to 653 K were also recorded to investigate the thermal expansion of the material.

Since data were collected with a 200 ms window only data from the back scattering bank were used for refinements. Data were processed as outlined in Section 2.3.7. For all refinements in this section data were binned to $\Delta d/d=0.003$.

5.7.1 Variable temperature neutron study of $(MoO)_2P_4O_{13}$

Data were recorded on warming from 303 to 653 K, with data collection parameters summarised in Table 5.16. On warming the backscattering bank developed a fault and stopped recording data above 493 K. This wasn't discovered until the material had already been heated up to 543 K. The detector bank was reset and the material cooled to 493 K and data collection continued.

Table 5.16 Data collection parameters for variable temperature data recorded at HRPD, ISIS, HRP39712.xye to HRP39752.xye.

Data Collection Parameters	Values
TOF range /μs	10-210
Sample Environment	Furnace
Temperature /K	VT+10K
Data recorded /μAh	4

A total of 15 parameters were refined for each dataset. These included 6 background coefficients, 4 lattice parameters, scale, absorption correction, an isotropic displacement parameter and 2 parameters to describe the sample peakshape. The refined lattice parameters are given in Figure 5.44. The phase transition temperature is 533 K.

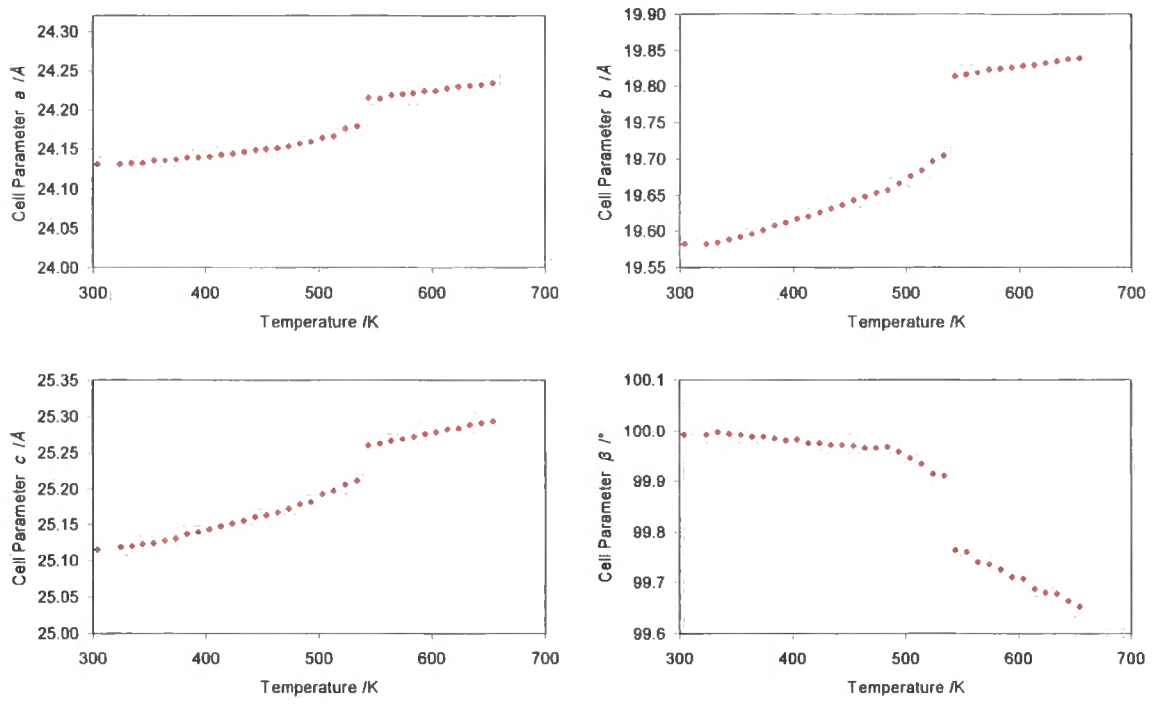

Figure 5.44 These four graphs show the changes in unit cell parameters with increasing temperature from the variable temperature HRPD data. The same % change scale was used for each graph.

The graphs in Figure 5.44 show the changes in the cell parameters of $(MoO)_2P_4O_{13}$ over the temperature range 303 □653 K. The *y* scale axes on the graphs for the *a*, *b* and *c* cell parameters have been scaled to show the relative differences between them. Percentage changes for the cell parameters *a*, *b* and *c* over the whole temperature range are 0.42 %, 1.31 % and 0.70 % respectively. The *a*, *b* and *c* parameters are all found to vary smoothly with temperature, as seen previously in Figure 5.27. There is a discontinuity in the refined parameters at 493 K due to the interruption in the VT data collection. The phase transition at 533 K is evident in the cell parameters; however, the cell

parameters above this temperature do not show any evidence for a second phase transition, as suggested by both the powder lab and single crystal synchrotron data. It was concluded from these high precision neutron data that only one phase transition is present in the material, a conclusion that is supported by the two high temperature single crystal solutions outlined in Section 5.6.

5.7.2 Analysis of the room temperature data

A Rietveld refinement using the known room temperature model of $(MoO)_2P_4O_{13}$ was performed to allow comparison of the data quality with the high temperature model and data. The data collection parameters are given in Table 5.17.

Table 5.17 Data collection parameters for room temperature data recorded at HRPD, ISIS, HRP39963.xye.

Data Collection Parameters	Values
TOF range /μs	10-210
Sample Environment	Candlestick
Temperature /K	300
Data recorded /μA	14

Coordinates were taken from the single crystal data collection 025dat, Section 5.6.2.1. 41 parameters were refined. These included 18 background coefficients, 4 lattice parameters, scale, absorption correction, 3 peakshape parameters, 3 isotropic displacement parameters □one for each atom type □ and 2 parameters to describe the sample peakshape. 9 parameters were used to apply a 4th order spherical harmonic function to describe the *hkl* dependence of the peakshape (one scaling parameter and 8 coefficient terms). The final R_{wp} for this refinement was 5.743 %. The calculated and experimental patterns are in Figure 5.45; further details are given in Table 5.18. The model gives a very good fit to the data, even over the smaller time of flight range highlighted in the inset to the figure. The large discrepancy at ~195 ms is probably a normalisation error at the edge of the TOF window.

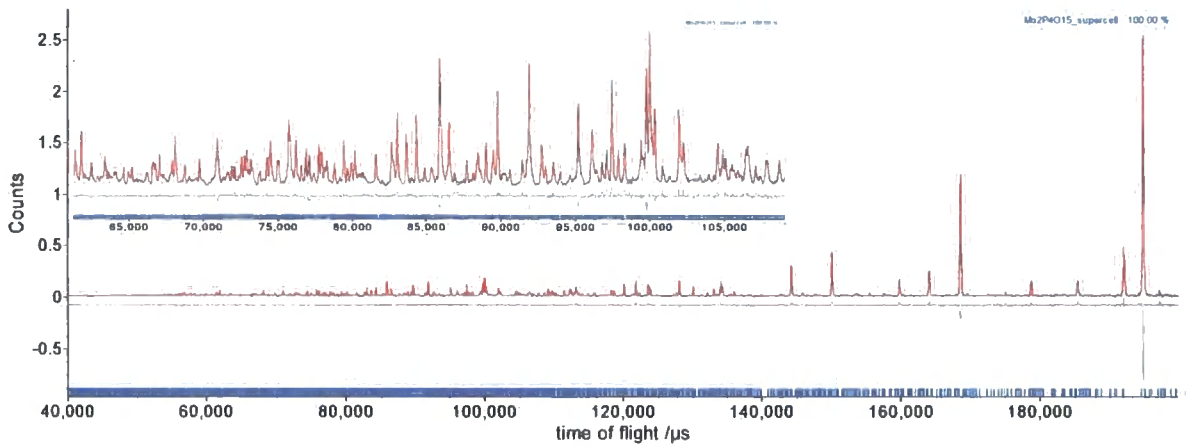

Figure 5.45 Rietveld refinement of $(MoO)_2P_4O_{13}$ superstructure against room temperature HRPD data using a fixed coordinate model, hrp39963_bs.xye, R_{wp} 5.743 %. Inset: the range 60000 to 110000 μs. The figure shows the experimental data in blue, the calculated pattern in red and the difference plot in grey.

Table 5.18 Selected refined values, crystallographic and data collection parameters for hrp39963_bs.

a /Å	24.1243(12)	Space Group	*Pn*
b /Å	19.5752(10)	No. of refined parameters	41
c /Å	25.1092(13)	R_{wp} /%	5.743
β /°	99.9956(75)	R_{Bragg} /%	11.26
Volume /Å^3	11677.52(100)	GOF	1.02

5.7.3 Analysis of the high temperature data using the high temperature single crystal model

An identical refinement was carried out against data recorded at 653 K using the high temperature structural model of $(MoO)_2P_4O_{13}$. The data collection parameters are given in Table 5.19.

Table 5.19 Data collection parameters for high temperature data recorded at HRPD, ISIS, HRP39753.xye.

Data Collection Parameters	Values
TOF range /μs	10-210
Sample Environment	Furnace
Temperature /K	653
Data recorded /μAh	66.2

Coordinates were taken from the 653 K single crystal data collection 380dat; refinement of this model was detailed in Section 5.6.2.5 above. 37 parameters were refined. These included 12 background coefficients, 6 lattice parameters, scale, absorption correction, 3 peakshape parameters, 3 isotropic displacement parameters □ one for each atom type □ and 2 parameters to describe the sample peakshape. 9 parameters were used to apply a 4th order spherical harmonic function to describe the *hkl* dependence of the peakshape (one scaling parameter and 8 coefficient terms). The final R_{wp} for this refinement was 5.018 %. Further details are given in Table 5.20; the calculated and experimental patterns are given in Figure 5.46.

Table 5.20 Selected refined values and crystallographic parameters for hrp39953_bs.

a /Å	17.9283(7)	Space Group	$P\bar{1}$
b /Å	19.8409(7)	No. of refined parameters	37
c /Å	21.8672(8)	R_{wp} /%	5.018
α /°	72.3748(15)	R_{Bragg} /%	12.70
β /°	78.2471(8)	GOF	1.943
γ /°	68.3290(16)	Volume /Å^3	6852.16(45)

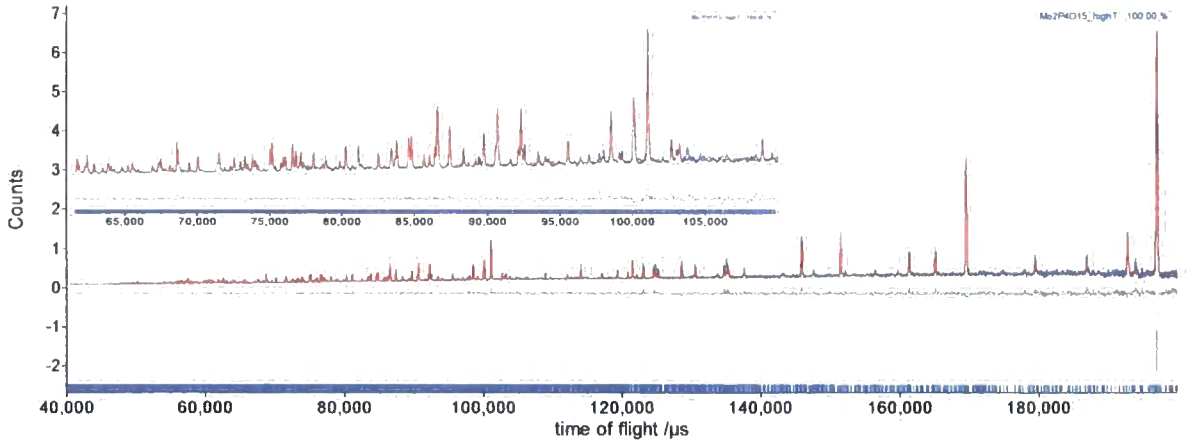

Figure 5.46 Rietveld refinement of the high temperature phase of $(MoO)_2P_4O_{13}$ using HRPD data recorded at 653 K using a fixed coordinate model, hrp39753_bs.xye, R_{wp} 5.018 %. Inset: the range 60000 to 110000 μs. The figure shows the experimental data in blue, the calculated pattern in red and the difference plot in grey.

The agreement between the calculated pattern and the experimental pattern for the high temperature single crystal model (with fixed coordinates) appears good but there are some clear peaks that are not being fitted by this model, notably at 98000 and 103000 μs in time of flight that were not present in the room temperature refinement, Figure 5.45. The latter peak can be rationalised as a V reflection from the sample can on the furnace. Refining the atomic coordinates did not improve the fit to other peaks. The appearance of the extra peaks in the pattern required further investigation.

5.7.4 Analysis of the data recorded in the furnace compared to data from the candlestick

In order to compare the low and high temperature models and also the data recorded on the candlestick and in the furnace, the models used in Sections 5.7.3 and 5.7.4 were also refined against the quick variable temperature data described in Section 5.7.1. The information about the datasets used is given in Table 5.21; the Rietveld fits are given in Figure 5.47.

Table 5.21 Selected refined values and crystallographic parameters for room temperature data recorded on the candlestick (hrp39963_bs) and in the furnace (hrp39910_bs).

	Hrp39963_bs.xye	Hrp39910_bs.xye	Hrp39952_bs.xye	Hrp39953_bs.xye
R_{wp} /%	5.743	5.018	9.913	5.253
Sample Environment	Candlestick	Furnace	Furnace	Furnace
Temperature /K	ambient	303	653	653
Data recorded /μAh	14	8	4	66.2

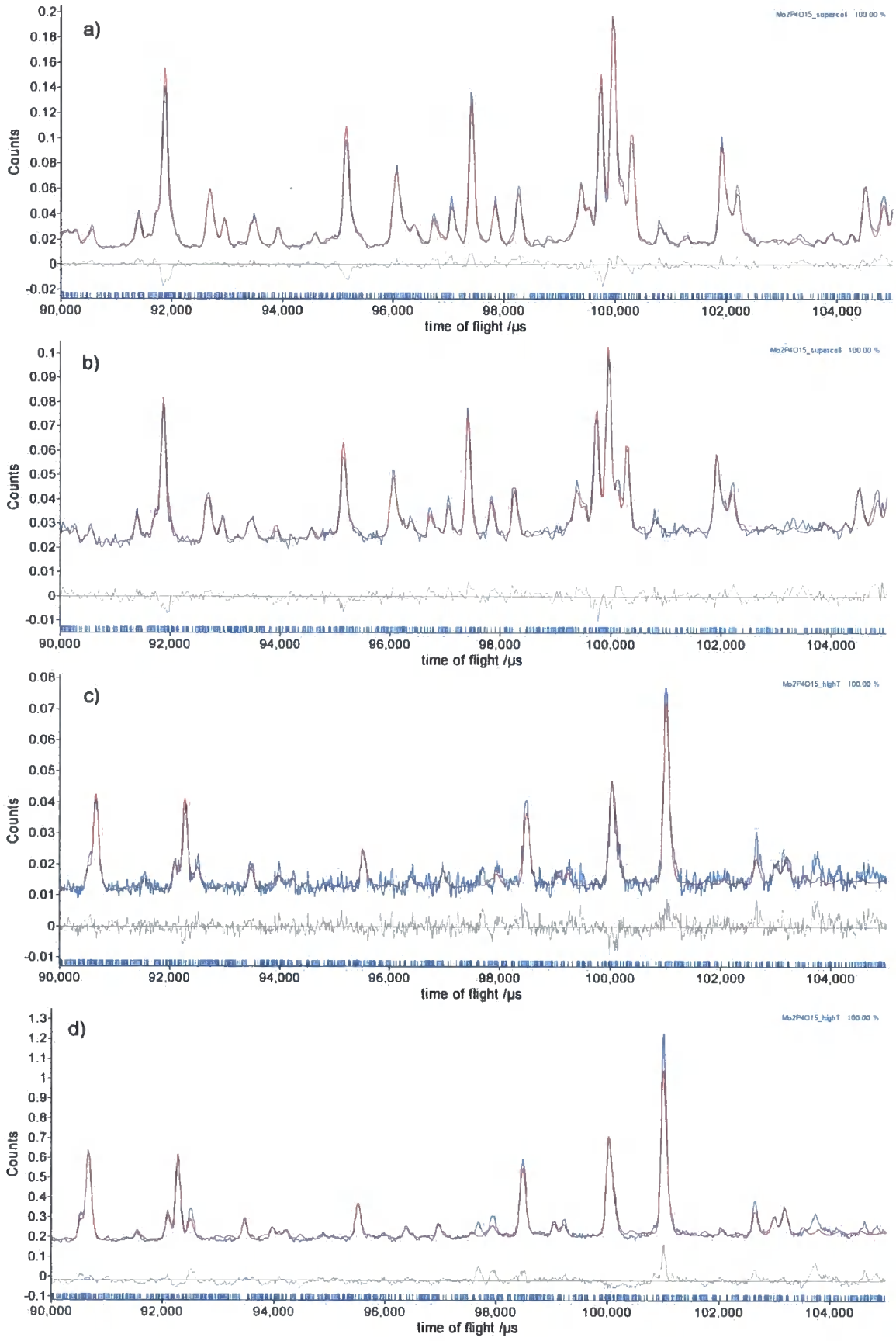

Figure 5.47 Rietveld fits to data a) HRP39963_bs, b) HRP39710_bs, c) HRP39752_bs and d) HRP39753_bs. The figure shows experimental data in blue, the calculated pattern in red and the difference plot in grey.

The first point to note from Figure 5.47 is the significant difference in the scans recorded at room temperature (a and b) and at high temperature (c and d). This highlights the differences between the low and high temperature structures.

Data recorded at room temperature on the candlestick, Figure 5.47a), can be compared with the data recorded on exactly the same sample in the furnace, Figure 5.47. Both Rietveld fits show that some of the most intense peaks shown have small amounts of ill-fitting intensity; however, there are discrepancies above the background level in the room temperature furnace data that are not present in the candlestick data. For example at 91000, 94000, 98000, 100500 and 103500 μA, there are peaks that are not accounted for by the model. These peaks are also present in the scans recorded in the furnace at high temperature, Figure 5.47c) and Figure 5.47d); the peaks are shifted to the right due to thermal expansion. The peak at 103800 μA arises due to the V sample can. These extra peaks have also been noted in other samples that were recorded in the furnace during the same beam time allocation at HRPD.

From these investigations it is concluded that the high temperature model for $(MoO)_2P_4O_{13}$ has been successfully solved, and that discrepancies between the model and the neutron data are due to extra diffraction arising due to scatter from components of the furnace at HRPD, and not due to any inadequacies of the model itself.

5.8 Discussion of the phase transition in $(MoO)_2P_4O_{13}$

5.8.1 Relationship between the two phases of $(MoO)_2P_4O_{13}$

Details have been given within this chapter of the relationship between both the high and the low temperature phases of $(MoO)_2P_4O_{13}$ and the originally reported subcell model. This model has been shown to be an inaccurate description of the structure even at high temperatures. In order to better understand the relationship between the unit cells and the different structures the material adopts at varying temperatures, the geometrical relationship between the two unit cells was calculated. The method was as follows.

As outlined in Sections 5.1 and 5.6.2.6, the transformation matrices that convert the subcell model to both the low and high temperature structures have been determined. From these it is possible to calculate the transformation matrix between the low and high temperature phases.

The transformation matrix for the subcell-high temperature structure is given in Equation 5.14. To reduce the number of calculations, the set of *hkl* reflections from the subcell that had been used in Equation 5.12 to calculate this matrix were used to obtain a set of equivalent *hkl* reflections in the low temperature supercell. This then gave us a new set of equations to solve that yielded the transformation matrix, T, for the supercell to high temperature phase transformation, Equation 5.16.

$$\begin{bmatrix} \bar{1} & 1 & \bar{3} \\ 3 & 0 & 6 \\ 5 & 9 & 15 \end{bmatrix} = \begin{bmatrix} & T & \end{bmatrix} \cdot \begin{bmatrix} \bar{2} & 1 & 0 \\ 0 & 3 & 0 \\ \bar{1} & 1 & \bar{2} \end{bmatrix} \qquad (5.16)$$

Solving this equation for T gave:

$$\begin{bmatrix} \\ T \\ \\ \end{bmatrix} = \begin{bmatrix} -1.25 & 7/12 & -0.5 \\ 0 & 1 & 0 \\ 1 & 0 & \bar{1} \end{bmatrix} \tag{5.17}$$

This transformation matrix has a determinant of 1.75. This is the volume ratio between the unit cells of the two phases. As shown in Equation 5.18, the transformation is not a straightforward one in all dimensions, due in part to the transition being between monoclinic and triclinic systems.

$$\begin{bmatrix} -1.25 & 7/12 & -0.5 \\ 0 & 1 & 0 \\ 1 & 0 & \bar{1} \end{bmatrix} \cdot \begin{bmatrix} a_{HT} \\ b_{HT} \\ c_{HT} \end{bmatrix} = \begin{bmatrix} 7/12\,b - 1.25a - 0.5c \\ b \\ a - c \end{bmatrix} = \begin{bmatrix} a_{LT} \\ b_{LT} \\ c_{LT} \end{bmatrix} \tag{5.18}$$

5.8.2 Classification of the type of phase transition

By inspection of the graph of $(MoO)_2P_4O_{13}$ cell volume *versus* temperature in Figure 5.24, the reversible phase transition present in the material was classified as first order. It was also described as being displacive in nature, since the structural connectivity is retained on passing through the transition temperature. Structure solution of the high temperature phase has provided further evidence in agreement with this classification.

To consider the space groups involved within the transition itself, the group-subgroup relationships are illustrated in Figure 5.48. Referring to the arrows within the figure, a continuous □ second-order transition □ can occur between two space groups that are spatially above or below each other. The removal or addition of a symmetry element that occurs between the two groups can occur without needing to change the symmetry completely. However, a transition that occurs between two space groups that are related to each other horizontally in the figure has a discontinuous □ first-order □ nature. This is the case for the space groups *Pn* and $P\bar{1}$; they are both maximal non-isomorphic subgroups of $P2_1/n$, and thus cannot undergo a transition of continuous nature but are forced to transform between one another in a discontinuous nature.

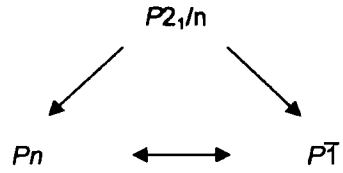

Figure 5.48 Diagram to illustrate the group-subgroup relationships for the transitions of $(MoO)_2P_4O_{13}$. A first order transition is illustrated by a horizontal double-arrow; a second order transition is illustrated by a single-headed diagonal arrow.

5.8.3 Chemical characterisation of the phase transition

At any given temperature, the structure adopted by a material has the lowest free energy by arranging the atoms in their most stable conformation, based on both enthalpic and entropic contributions. At

high temperatures the large entropic term contributes significantly to the free energy; at high temperatures the system is able to dynamically disorder to remove the unfavourable population of the P-O σ^* orbitals. The entropic effects determine the topology formed as the material is synthesised. On cooling the balance between the enthalpy and entropy terms within the free energy changes; the dynamic disorder within the system reduces until the disorder is frozen into the material as static disorder. The system becomes frustrated due to the need to maintain a balance between the locked-in topology of the material and the local bonding requirements for each MoO_6 and P_4O_{13} group. This leads to the formation of complex structures.

In the subcell model one P-O-P bond angle is 180 ° and the other two are 140 °. These three bond angles are contained within one P_4O_{13} group; the □central□ P-O-P bond is linear, the other two □peripheral□ P-O-P bonds are not. The true high temperature structure in $P\bar{1}$ has 35 bent P-O-P linkages; the remaining two P-O-Ps are both on an inversion centre, one of these bonds is a 180 ° angle; the other is on a split site that changes the angle from being 180 to 137(4) °. In the low temperature *Pn* structure all 63 P-O-P bond angles are bent away from 180 °, ranging from 126.2(3)-173.6(3) °. These bond angle ranges and distributions are given in Table 5.22.

Table 5.22 Comparison of the P-O-P bonding angles within the low temperature and high temperature structures, and the hypothetical subcell model.

P-O-P bond /°	*Pn* /120 K	Subcell /293 K	$P\bar{1}$ /573 K
Number	63	3	37
Range	126.2(3)-173.6(3)	138.8(6)-180	125.4(15)-180
Average - all	142.3(96)	152.53	145.7(134)
- central	149.9(93)	180	155.8(144)
-peripheral	138.4(72)	138.8(6)	140.3(92)

The disorder present in the high temperature $P\bar{1}$ structure is a result of frustration at high temperature. The P-O-P bonds on the inversion centres are constrained to be 180 °; however, the dynamic disorder present over the stability range of the structure can remove the unfavourable situation. The split site at O212 alters the 180 ° bond angle to be a more favourable 137(4) °.

At lower temperatures this dynamic disorder is reduced due to decreasing temperature, and thus a reduced entropic contribution. To retain a low free energy the enthalpic contributions must increase. The material is forced to reduce the number of linear P-O-P bonds within the model while maintaining the structural topology. This causes a vast increase in complexity.

5.9 Conclusions

These studies have investigated the structures of $(MoO)_2P_4O_{13}$ over the temperature range 16 □ 753 K. High temperature powder diffraction confirmed the presence of a phase transition seen in DSC. The low temperature structure has lattice parameters *a* 24.1134(6) Å, *b* 19.5324(5) Å, *c* 25.0854(6) Å and β 100.015(1) ° at 120 K. The asymmetric unit contains 441 atoms; this is a highly complex

material when compared to its simple formula. The material consists of Mo centred octahedra and P centred tetrahedra; five of the vertices of an MoO_6 are shared with P_4O_{13} units. This arrangement within the structure results in there being both P-O-P and Mo-O-P linkages. $(MoO)_2P_4O_{13}$ retains this structure at room temperature.

The structure of the high temperature phase has been solved. The new phase has a triclinic unit cell in space group $P\bar{1}$, with lattice parameters *a* 17.947(3) *Å*, *b* 19.864(3) *Å*, *c* 21.899(3) *Å*, α 72.421(3) °, β 78.174(4) ° and γ 68.315(4) ° at 573 K. The asymmetric unit contains 253 atoms. This material has the same structural connectivity as found in the low temperature phase; the phase transition has been confirmed to be 1st order in nature.

The material has the same topology over the whole of the studied temperature range. The local coordination requirements compete with the 3D requirements of the system, resulting in the remarkable structural complexity.

Neutron powder diffraction has been used to confirm the single crystal structures as an accurate description of the bulk material. X-ray data recorded on a capillary sample has been well described using the single crystal structure. Flat-plate reflection geometry scans have been found to suffer from preferred orientation; spherical harmonics have been used to model these effects.

5.10 References

1. I. Schulz, *Z. Anorg. Allg. Chem.*, 1955, **281**, 99-112.
2. P. Kierkegaard, *Ark. Kemi*, 1962, **19**, 51-74.
3. L. K. Minacheva, A. S. Antsyshkina, A. V. Lavrov, V. G. Sakharova, V. P. N. and and M. A. Porai-Koshits, *Rus. J. Inorg. Chem.*, 1979, **24**, 51-53.
4. G. Costentin, A. Leclaire, M. -M. Borel, A. Grandin and B. Raveau, *Z. Kristallogr.*, 1992, **201**, 53-58.
5. S. E. Lister, I. R. Evans, J. A. K. Howard, A. Coelho and J. S. O. Evans, *Chem. Commun.*, 2004, **22**, 2540-2541.
6. S. E. Lister, *Negative Thermal Expansion Materials, 4th Year Project Report*, University of Durham, 2004.
7. Eric Dowty, *Cryscon Version 0.91*, Shape Software, TN, USA, 2002.
8. A. A. Coelho, *TOPAS Academic: General Profile and Structure Analysis Software for Powder Diffraction Data*, Bruker AXS, Karlsruhe, 2004.
9. D. J. Watkin, J. R. Carruthers and P. W. Betteridge, *CRYSTALS User Guide*, Chemical Crystallography Laboratory, University of Oxford, England, 1985.
10. L. Lezama, J. M. Rojo, J. L. Pizarro, M. I. Arriortua and T. Rojo, *Solid State Ionics*, 1993, **63-65**, 657.
11. Powder Diffraction File, *International Centre for Diffraction Data*, Pennsylvania, 1998.
12. D. Watkin, *Acta Crystallogr., Sect. A*, 1994, **50**, 411-437.
13. A. F. Wells, *Structural Inorganic Chemistry (Fifth Edition)*, Clarendon Press, Oxford, 1984.
14. M. O'Keeffe, B. Domenges and G. V. Gibbs, *J. Phys. Chem.*, 1985, **89**, 2304-2309.

15. P. J. Heaney, C. T. Prewitt and G. V. Gibbs, *Silica: Physical Behavior, Geochemistry and Materials Applications*, Mineralogical Society of America, Michigan, 1994.
16. D-K. Seo and M-H. Whangbo, *J. Solid State Chem.*, 1997, **129**, 160-163.
17. J. S. O. Evans, J. C. Hanson and A. W. Sleight, *Acta Crystallogr., Sect. B.*, 1998, **54**, 705-713.
18. S. Allen, *Thermoresponsive Behaviour of AM_2O_8 Materials, Ph. D. Thesis*, University of Durham, 2003.
19. J. S. O. Evans, *Multitopas, Fortran 77 routine*, Durham, 1999.
20. K. Wang and R. R. Reeber, *Phil. Mag. A*, 2000, **80**, 1629-1643.
21. Y. Okada and Y. Tokumaru, *J. Appl. Phys.*, 1984, **56**, 314-320.
22. K. G. Lyon, G. L. Salinger, C. A. Swenson and G. K. White, *J. Appl. Phys.*, 1977, **48**, 865-868.
23. J. P. Cline, *Standard Reference Material 640c - Silicon Powder Line Position and Line Shape Standard for Powder Diffraction*, Gaithersburg, Maryland, USA, 2000.
24. G. W. Stinton, *Structural Studies into AM_2O_7 Framework Materials and Parametric Rietveld Refinement*, University of Durham, 2006.
25. D. Taylor, *Br. Ceram. Trans. J.*, 1984, **83**, 92-98.
26. Bruker AXS, *Apex II v2.1.4: Software for Controlling Bruker Diffractometers*, Karlsruhe, 2007.
27. A. Altomare, M. C. Burla, M. Camalli, G. Cascarano, C. Giacovazzo, A. Guagliardi and G. Polidori, *J. Appl. Cryst.*, 1994, **27**, 435-436.
28. G. Oszlányi and A. Sütő, *Acta Crystallogr., Sect. A*, 2004, **60**, 134-141.
29. C. K. Johnson, *Ortep: A fortran-thermal ellipsoid plot program for crystal structure illustrations*, ORNL-3794, Tennessee, USA, 1965.
30. A. L. Spek, *Platon - A multipurpose crystallographic tool*, Utrecht University, Utrecht, 2003.
31. M. Husak, *Marching Cubes ELD: 3D ELD Map plot for Crystals*, Prague, 2000.
32. B. J. Campbell, H. T. Stokes, D. E. Tanner and D. M. Hatch, *J. Appl. Cryst.*, 2006, **39**, 607-614.

6. Synthesis of MoP_2O_7

6.1 Introduction

The AM_2O_7 family of materials have been widely studied since their first report in the literature.[1] Several of them have been found to display NTE at high temperature. In many of the materials the ~8 Å cubic structure has been found to be a simplified high temperature model and materials go through one or more phase transitions on cooling due to the frustration caused between long-range topology and short-range bonding constraints. These properties have been studied and found to be dependent on the cations/anions in the structures, Section 1.4.2. In this chapter alternative synthetic routes to MoP_2O_7 are investigated.

The pyrophosphate MoP_2O_7 was originally suggested as being isostructural with high temperature ZrP_2O_7 .[2] The structure was later solved by Leclaire *et al.* using single crystal methods at 294 K.[3] However, this work used only 55 reflections and proved to have high thermal parameters for the bridging oxygen. A later investigation using synchrotron X-radiation showed the presence of an orthorhombic supercell,[4] but this structure has not been published in detail to my knowledge.

In order to probe the superstructure, good quality single crystals were sought. Repetition of the literature syntheses did not yield crystals of good enough quality; this led to a search for alternative methods of synthesis. Il'ink *et al.* have shown that the Mo^{VI} compound $MoO_2(PO_3)_2$ ("MoP_2O_8") can be reduced under H_2 according to the following scheme:[5]

$$Mo^{VI}O_2(PO_3)_2 \rightarrow \text{"}Mo^{V}P_2O_{7.5}\text{"} \rightarrow Mo^{IV}P_2O_7 \rightarrow Mo^{III}P \qquad (6.1)$$

However, their description of the "$MoP_2O_{7.5}$" compound is that of an amorphous substance with an intensive dark-purple colour. As the compound $(MoO)_2P_4O_{13}$ (Chapter 5) is a green crystalline substance, it is unclear what has been observed in this experiment, or whether a second form of this compound has been discovered.

This led to attempts to synthesise MoP_2O_7 by reduction of the phases $MoO_2(PO_3)_2$ and $(MoO)_2P_4O_{13}$. In parallel with these investigations the reduction of $(MoO_2)_2P_2O_7$ was also undertaken to search for possible intermediate phases.

The structure of $MoO_2(PO_3)_2$ was described by Kierkegaard[6] in an orthorhombic unit cell, *Pbcm*, as follows. PO_4 tetrahedra are joined together by shared vertices, forming PO_3-chains parallel to the *c* axis, Figure 6.1. Molybdenum atoms sit between these chains, forming face-sharing octahedral units; each MoO_6 shares four vertices with four different PO_4 tetrahedra (in 3 different chains). The final two oxygen atoms are only bonded to Mo atoms. Layers are formed within the material parallel to the *bc* plane; layers are held together by van der Waals forces.

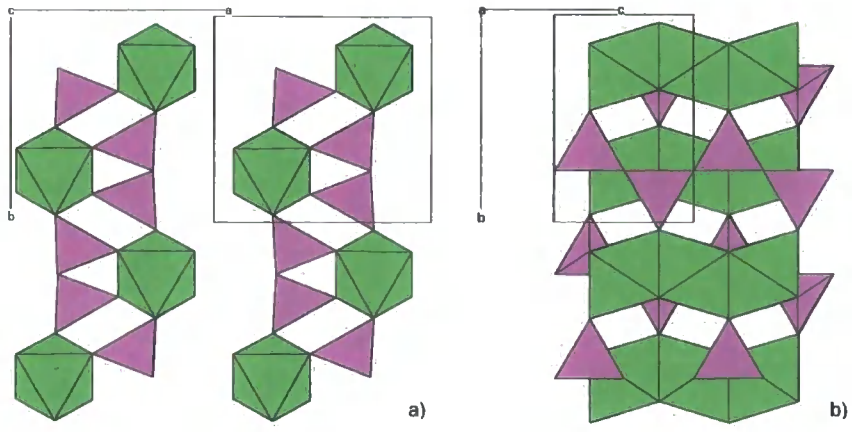

Figure 6.1 The structure of $MoO_2(PO_3)_2$. a) The layers perpendicular to the *a* axis. b) The PO_3 chains and face-sharing octahedra.

6.2 Synthesis and Rietveld analysis of $MoO_2(PO_3)_2$

A sample of $MoO_2(PO_3)_2$ was prepared to investigate its ability to act as a precursor phase to MoP_2O_7. The synthesis followed the preparation described by Kierkegaard,[6] outlined in Equation 6.2.

$$MoO_3 + P_2O_5 \rightarrow MoO_2(PO_3)_2 \qquad (6.2)$$

0.7500 g MoO_3 (5.2 mmol, Alfa, 99.95 %) was added to 3.2696 g P_2O_5 (23.0 mmol, Fisher Chemicals), and the two reactants ground together in an agate pestle and mortar for five minutes. The resulting powder was transferred to a tall alumina crucible and heated as follows:

5 K/min → 773 K, held for 7 days, then cooled *in-situ* to 298 K

This formed a light blue-white solid that was removed from the crucible using copious washings with demineralised water. The sample was then dried at 353 K for an hour and scanned (d5_06325), SEL153. The synthesis yielded 1.1963 g $MoO_2(PO_3)_2$, an 80.2 % yield (PDF 01-074-1389).[7] A broad peak in the diffraction pattern (Figure 6.2) suggested the presence of an additional amorphous phase.

Rietveld refinement was undertaken to assess phase purity, Figure 6.2. 46 parameters were refined in this analysis, including 15 coefficients of a Chebychev polynomial to model the background, a sample height parameter, 1 parameter to model axial divergence, 3 lattice parameters of the $MoO_2(PO_3)_2$ phase, 10 atomic coordinates, 3 isotropic displacement parameters – 1 for each atom type, 4 parameters used to define the TCHZ peak shape and a scale parameter. In addition the amorphous material was modelled using two PV peaks each parameterised using a refining position, intensity, fwhm and Lorentzian/Gaussian ratio. The final R_{wp} was 11.59 %. Selected refinement details are given in Table 6.1. The input file for this refinement is included in the E-appendix.

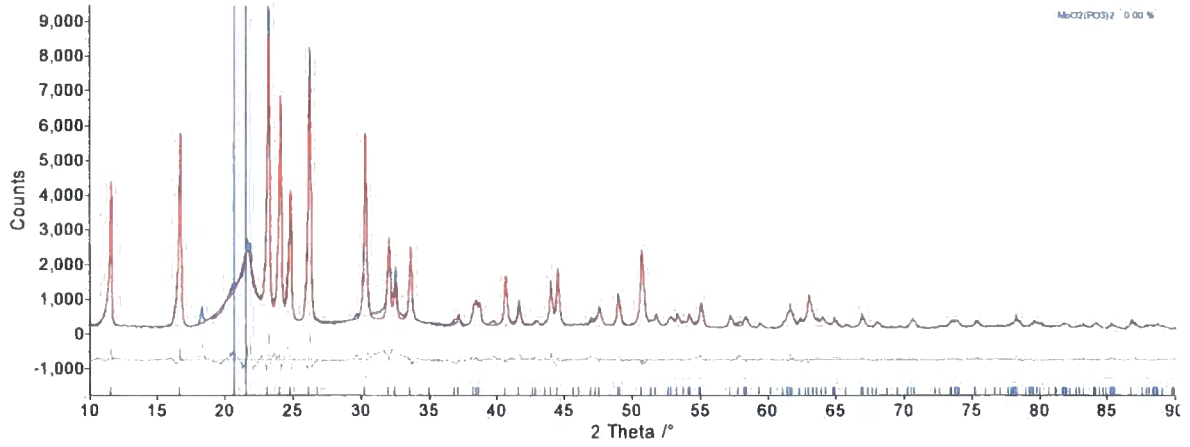

Figure 6.2 Rietveld analysis of SEL153, $MoO_2(PO_3)_2$, in d5_06325, R_{wp} 11.59 %. The two vertical blue lines indicate the positions of the two PV peaks modelling the amorphous intensity present. The figure shows the experimental data in blue, the calculated pattern in red and the difference plot in grey. Tick marks (in blue) show the predicted positions of the peaks.

Table 6.1 Selected refined values, crystallographic and data collection parameters for d5_06325.

Space Group	*Pbcm*	2θ range /°	5-90
a /Å	7.6925(3)	2θ step size /°	0.02
b /Å	7.4184(3)	Time per step /s	12
c /Å	4.8855(2)	R_{wp} /%	11.59
Volume /Å^3	278.80(2)	R_{Bragg} /%	3.51
Refining parameters	48	GOF	2.69

It is clear from Figure 6.2 that this material is not phase pure. However, further attempts to synthesise a pure-phase material failed. Samples of $MoO_2(PO_3)_2$ of this quality were used for further experiments.

6.3 Reduction chemistry of $MoO_2(PO_3)_2$

VT XRD experiments were carried out on $MoO_2(PO_3)_2$ in an H_2/Ar atmosphere. A sample of $MoO_2(PO_3)_2$ (SEL260) was prepared for the *in-situ* reaction as outlined in Section 2.3.2.1. The diffractometer was programmed to heat the sample from 303 K up to 1003 K, recording a thirty minute scan at constant temperature every 10 K, in an H_2/Ar atmosphere, d8_03483.

6.3.1 Visual inspection of data

The scans from this initial experiment are shown in Figure 6.3. This figure shows that in a reducing environment the crystalline phases present are as follows:

$$MoO_2(PO_3)_2 \rightarrow MoP_2O_7 \rightarrow MoP \qquad (6.3)$$

However, in the time/temperature interval immediately before the formation of the pyrophosphate MoP_2O_7, several scans have no Bragg peaks are present, indicating the decomposition of the first phase into the pyrophosphate *via* a purely amorphous material. Also of interest is the lack of peaks arising due to the known $(MoO)_2P_4O_{13}$ phase implying that it ($MoP_2O_{7.5}$) is not an intermediate between "MoP_2O_8" and MoP_2O_7. The reduction of $(MoO)_2P_4O_{13}$ is detailed in Section 6.4.

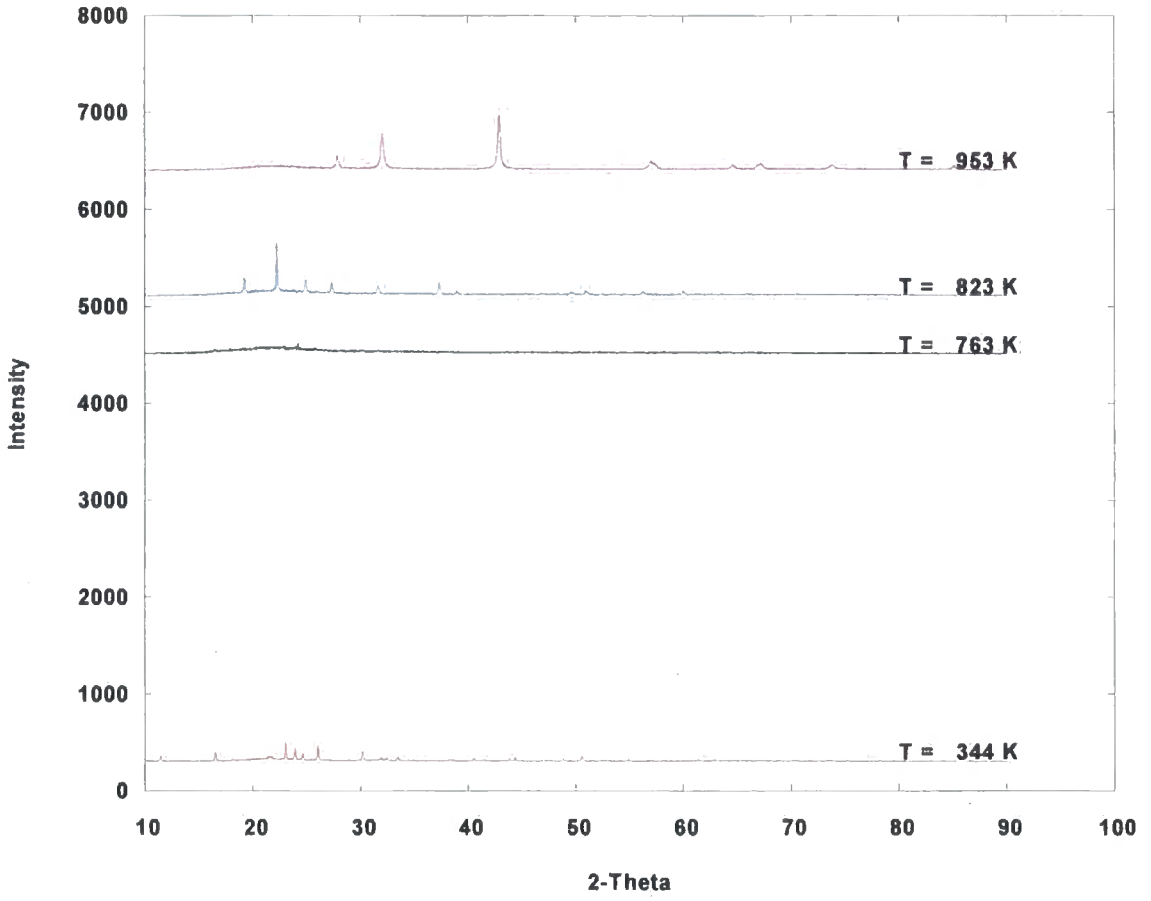

Figure 6.3 VTXRD data recorded over the range 303 – 1003 K in 10 K intervals, d8_03483. The initial phase $MoO_2(PO_3)_2$ (*e.g.* the red scan at 344 K) can be seen to reduce to MoP_2O_7 (*e.g.* the blue scan 823 K) *via* an amorphous intermediate (*e.g.* the black scan at 763 K). The purple scan (953 K) shows formation of molybdenum phosphide (MoP). The scans have been offset along *y* for clarity.

6.3.2 Data analysis

Rietveld analysis of the data was performed to gain information about the phases present during the experiment, most notably the phase percentages of the two phosphates. A three phase refinement was performed with an additional pseudo-Voigt peak used to model the background intensity. 34 parameters were used to model these phases. Each of the crystalline phases was modelled using a TCHZ peak shape that had been refined from d8 data recorded on a highly crystalline sample of CeO_2; excess broadening in each phase was modelled using an individually refining Lorentzian crystallite size terms.

The 34 parameters were 11 global parameters (9 background parameters, a sample height correction and 1 parameter to describe axial divergence), 3 parameters to model the position, intensity and fwhm of a peak used to describe the amorphous content of the phase mixture, 8 parameters to model the $MoO_2(PO_3)_2$ structure (3 cell parameters, 3 isotropic displacement parameters, a scale parameter and a crystallite size parameter), 6 parameters to model the MoP_2O_7 structure (1 cell parameter, 3 isotropic displacement parameters, a scale parameter and a crystallite size parameter) and 6 parameters were used to model the MoP structure (2 cell parameters, 2 isotropic atomic displacement parameters, a scale parameter and a crystallite size parameter). The Rietveld refinement from each of the highlighted ranges in Figure 6.3 is given in Figure 6.4.

Figure 6.5 shows both the refined phase percentages (a) and molar ratios (b) of each phase throughout the experiment. The relative molar quantities are calculated from scale*Z*M*V to allow absolute comparison between the different phases.[p] On consideration of the phase percentages alone, the experiment appears to proceed directly from $MoO_2(PO_3)_2$ to MoP_2O_7 to MoP. However, from the visual inspection and the Rietveld refinements in Figure 6.4 this is known to not be the case. Relative molar quantities, however, show that between the disappearance of the first phase and crystallization of the second phase there is no crystalline material present. This is supported by the increase in background intensity present in the reaction, quantified in Figure 6.7. No further investigation into this amorphous phase has been undertaken.

$$Mo^{VI}O_2(PO_3)_2 \rightarrow \text{amorphous material} \rightarrow Mo^{IV}P_2O_7 \rightarrow Mo^{III}P \qquad (6.4)$$

[p] Z: Number of formula units per unit cell, M: molar mass, V: Volume.

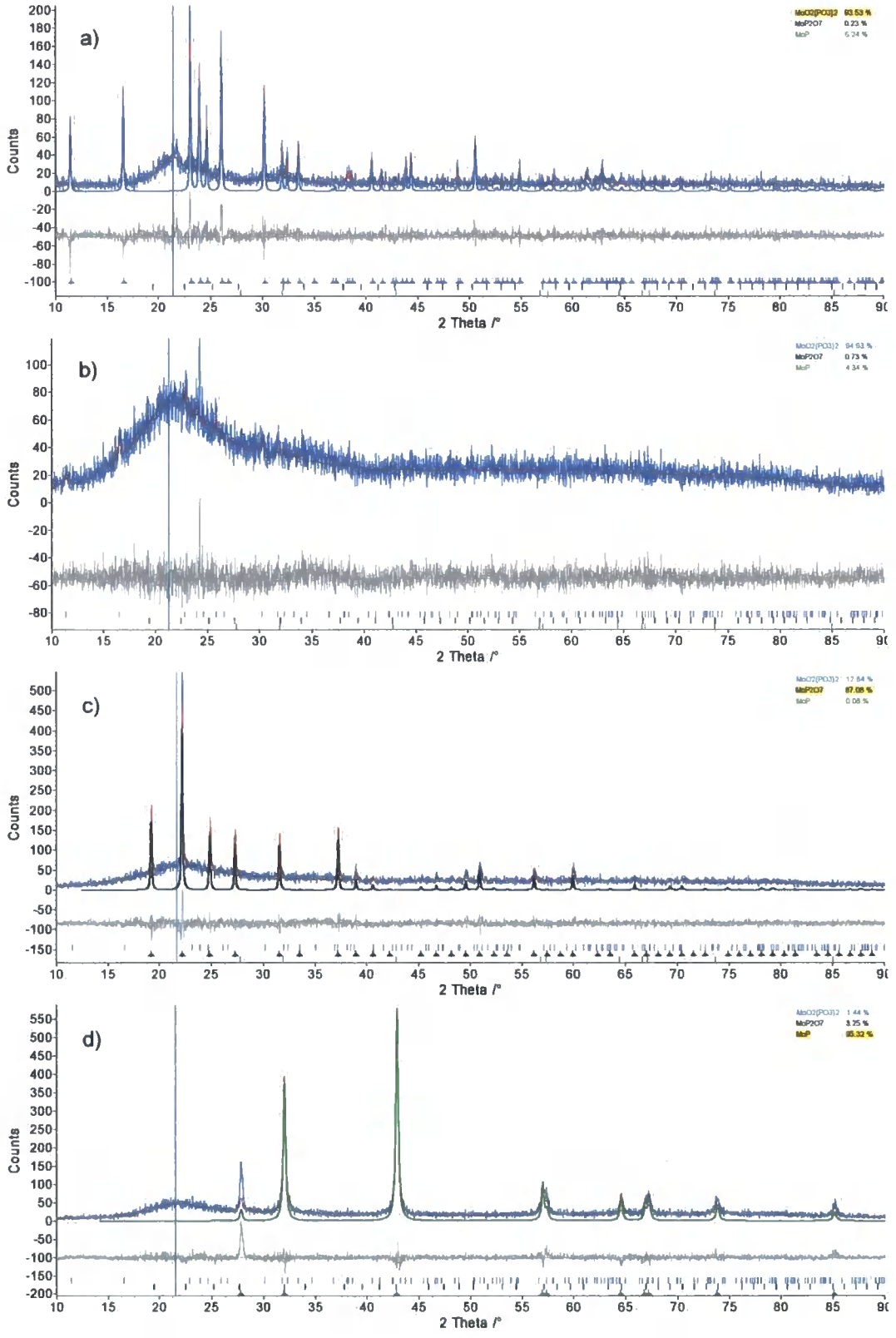

Figure 6.4 A Rietveld refinement for each of the main regions of interest, the main phase present is highlighted where possible. a) $MoO_2(PO_3)_2$ in range 3, R_{wp} 30.21 %. b) Amorphous intermediate, range 46, R_{wp} 19.55 %. c) MoP_2O_7 in range 52, R_{wp} 20.15 %. d) MoP in range 65, R_{wp} 22.13 %. The figure shows the experimental data in blue, the calculated patterns in red and the difference plot in grey.

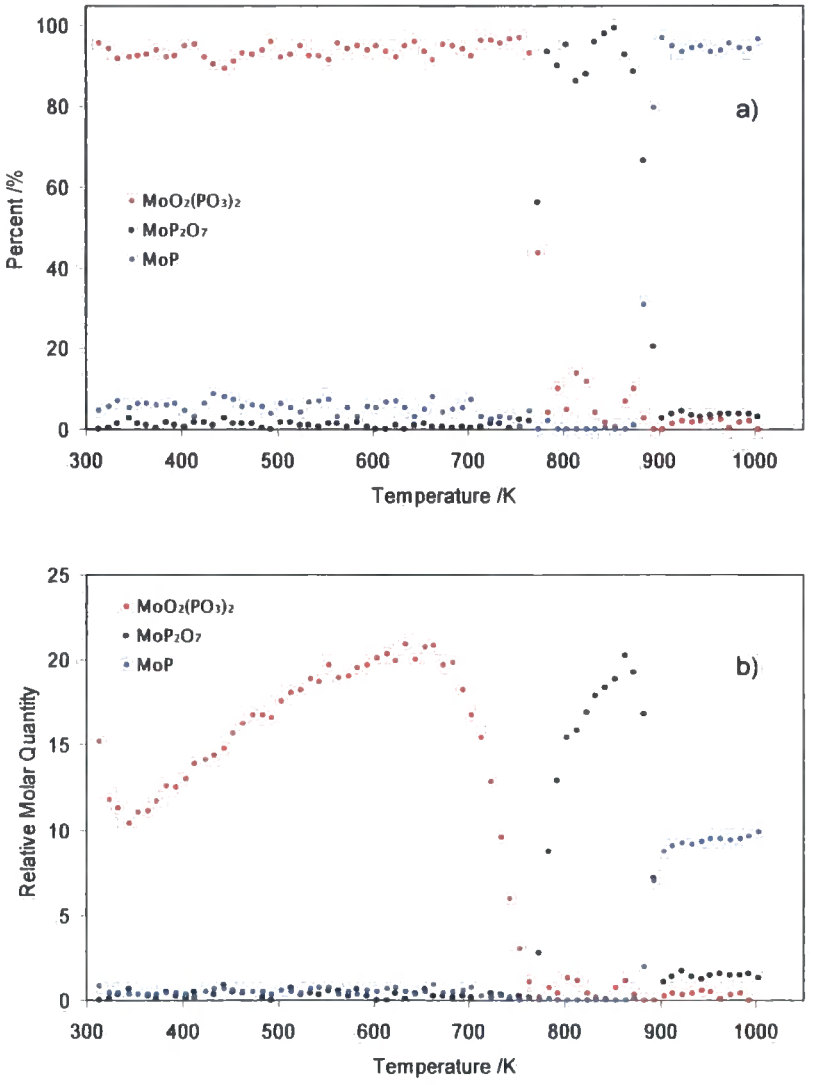

Figure 6.5 Graphs plotting the progress of the reaction in terms of the phase percentages from Rietveld analysis (a) and the molar ratios (b).

Figure 6.6 gives the refined values of the lattice parameters and cell volumes of $MoO_2(PO_3)_2$ in the Rietveld refinements. These show an approximately linear variation in each parameter in the temperature range where each of the phases is present. Outside this range the parameters oscillate between the minimum and maximum values as set in the refinement.

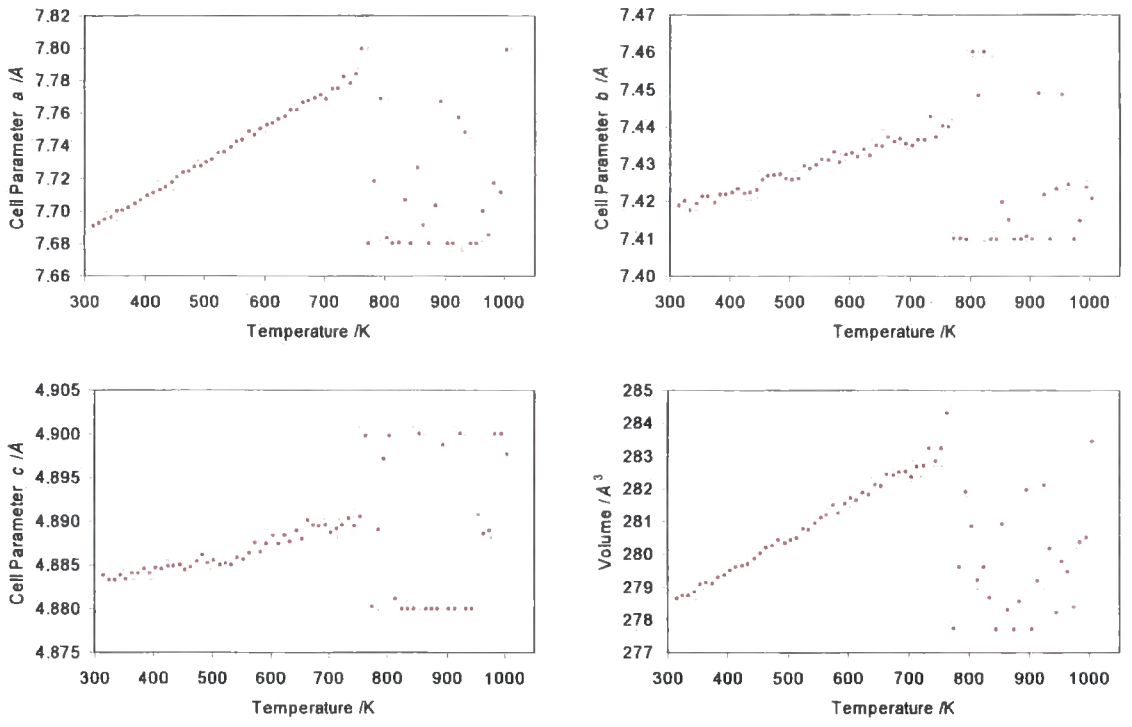

Figure 6.6 Graphs showing the refined lattice parameters and volume for the $MoO_2(PO_3)_2$ phase.

The refined values for the position, intensity and fwhm of the peak used to model the background intensity are given in Figure 6.7. From these graphs it is clear that the intensity increases significantly over the range 750 – 900 K; this is indicative of the formation of an amorphous intermediate within this temperature range. Full results are given in the E-Appendix.

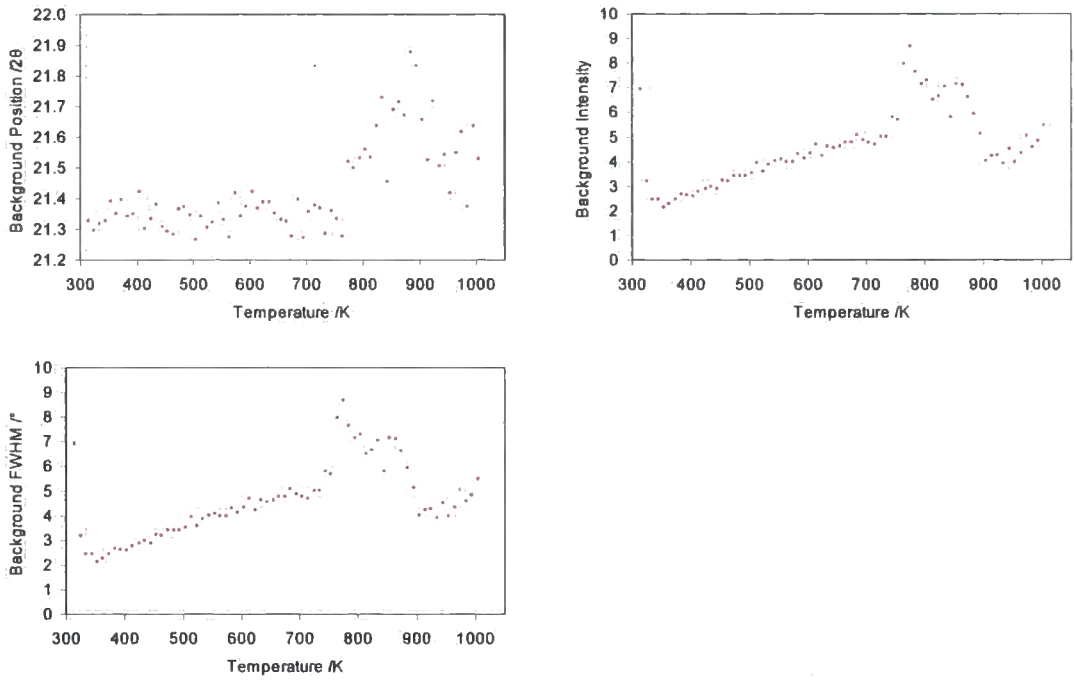

Figure 6.7 Graphs showing the position, intensity and fwhm for the pseudo-Voigt peak used to describe the background hump of amorphous intensity.

6.4 Reduction chemistry of $(MoO)_2P_4O_{13}$

Following the discovery that the material $MoO_2(PO_3)_2$ reduces to MoP_2O_7 *via* an amorphous phase, VT XRD experiments were also carried out on $(MoO)_2P_4O_{13}$ in an H_2/Ar atmosphere. The aim of these experiments was to discover whether it was possible to reduce this compound to form the pyrophosphate, MoP_2O_7.

6.4.1 Reduction experiment on increasing temperature

A sample of $(MoO)_2P_4O_{13}$ (SEL033) was prepared as outlined in Section 6.3, and the diffractometer programmed to heat the sample from 303 K up to 953 K, recording a twenty minute scan at constant temperature every 10 K in an H_2/Ar atmosphere, d8_03085. These scans are shown in Figure 6.8.

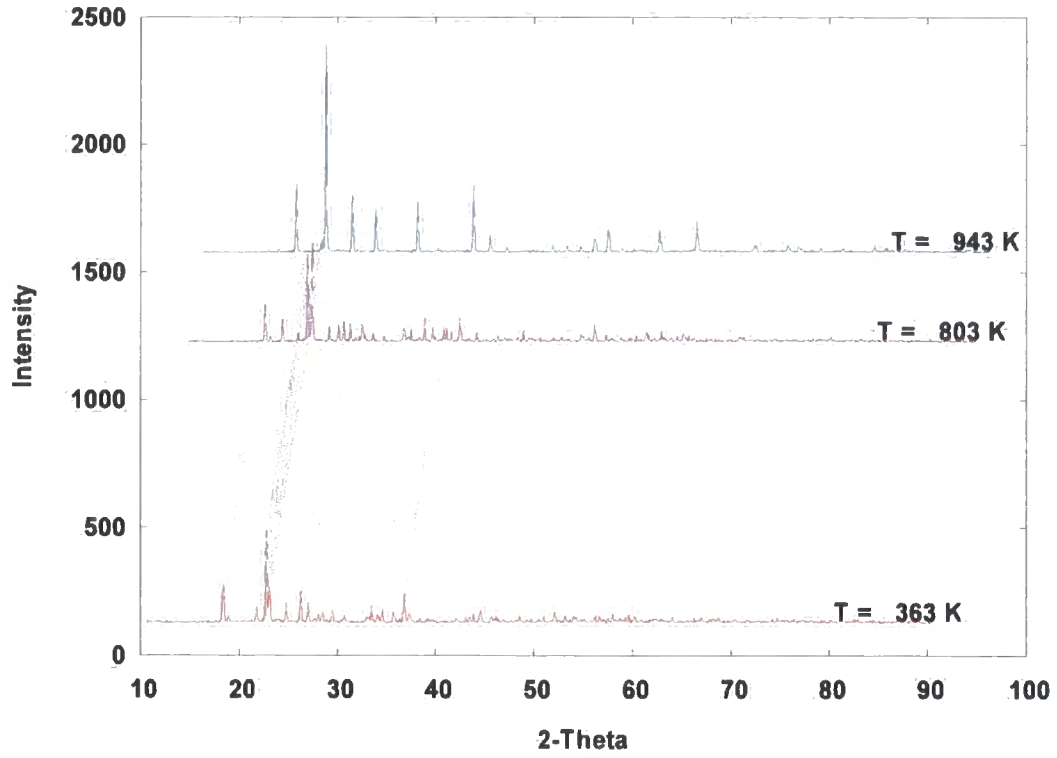

Figure 6.8 VTXRD data recorded over the range 303 – 953 K in 10 K intervals, d8_03085. The scans have been offset in *x* and *y* for clarity. $(MoO)_2P_4O_{13}$ (red scan at 363 K) can be seen to reduce to MoP_2O_7 (blue scan 943 K). The purple scan (803 K) is shown to indicate the temperature at which these two phases exist in a 50:50 mixture.

The scans show that $(MoO)_2P_4O_{13}$ can be reduced to give the pyrophosphate MoP_2O_7. Rietveld analysis of these data was performed using *multitopas* to gain information about the phases present during the experiment. Two Rietveld refinements are given in Figure 6.9. These show a good fit of the structural models to the diffraction data.

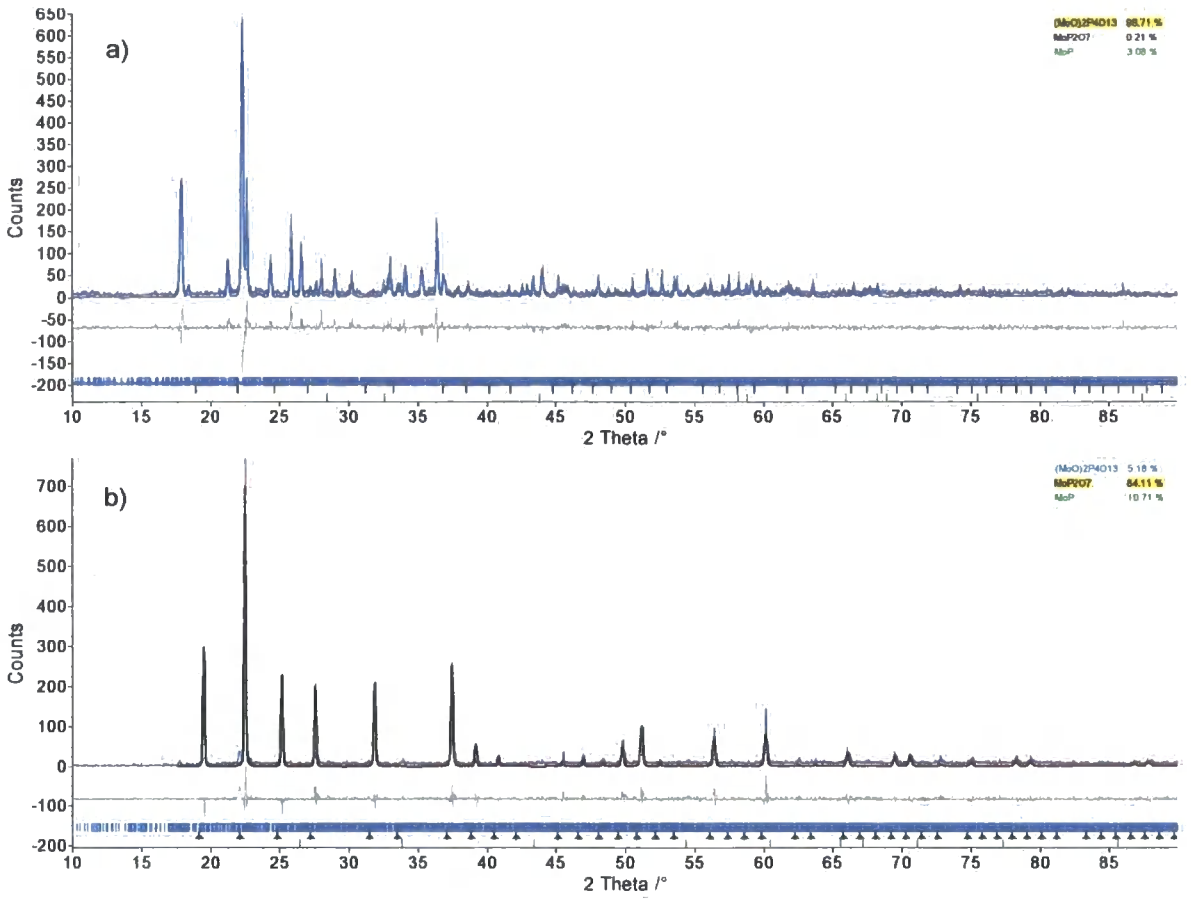

Figure 6.9 A Rietveld refinement for each of the main regions of interest; the main phase present in each is highlighted. a) $(MoO)_2P_4O_{13}$ in range 06, R_{wp} 28.10 %. b) MoP_2O_7 in range 64, R_{wp} 33.07 %. The figure shows the experimental data in blue, the calculated pattern in red and the difference plot in grey.

The powder diffraction patterns in Figure 6.8 show that there is direct conversion from $(MoO)_2P_4O_{13}$ to MoP_2O_7, *i.e.* that the process does not go *via* an amorphous intermediate. Figure 6.10 show the phase percentages cross when α=0.5, *i.e.* when there is 50 % $(MoO)_2P_4O_{13}$ present, there is also 50 % MoP_2O_7.

$$(Mo^{V}O)_2P_4O_{13} \rightarrow Mo^{IV}P_2O_7 \qquad (6.5)$$

These data show that no MoP was formed during this experiment. This is unexpected from the work of Il'ink *et al.*,[5] and may be due to differences in H_2 pressure in the system. The input file and spreadsheet containing the refined values are included in the E-Appendix.

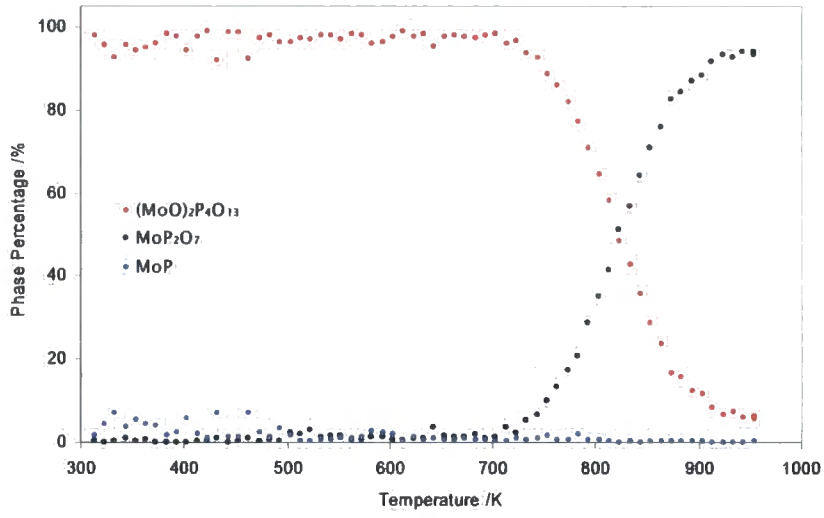

Figure 6.10 Data showing the phase fractions of $(MoO)_2P_4O_{13}$, MoP_2O_7 and MoP during reduction experiment d8_03085. These clearly show the direct conversion of $(MoO)_2P_4O_{13}$ into MoP_2O_7. Slight fluctuations in the percentages are due to low signal/noise levels recorded in the 20 minute scans.

6.4.2 Reduction experiment at constant temperature

Following this experiment it was decided to run continuous scans at a set temperature to follow the formation of the pyrophosphate phase. It was decided to use the crossover temperature to monitor the reaction, as at this point there is no formation of MoP and it is also well below the decomposition temperature of $(MoO)_2P_4O_{13}$. 81 twenty minute scans were recorded at 826 K, from 10 to 90 ° 2θ with step size 0.017 ° 2θ, d8_03157, on sample SEL033. These scans are shown in Figure 6.11.

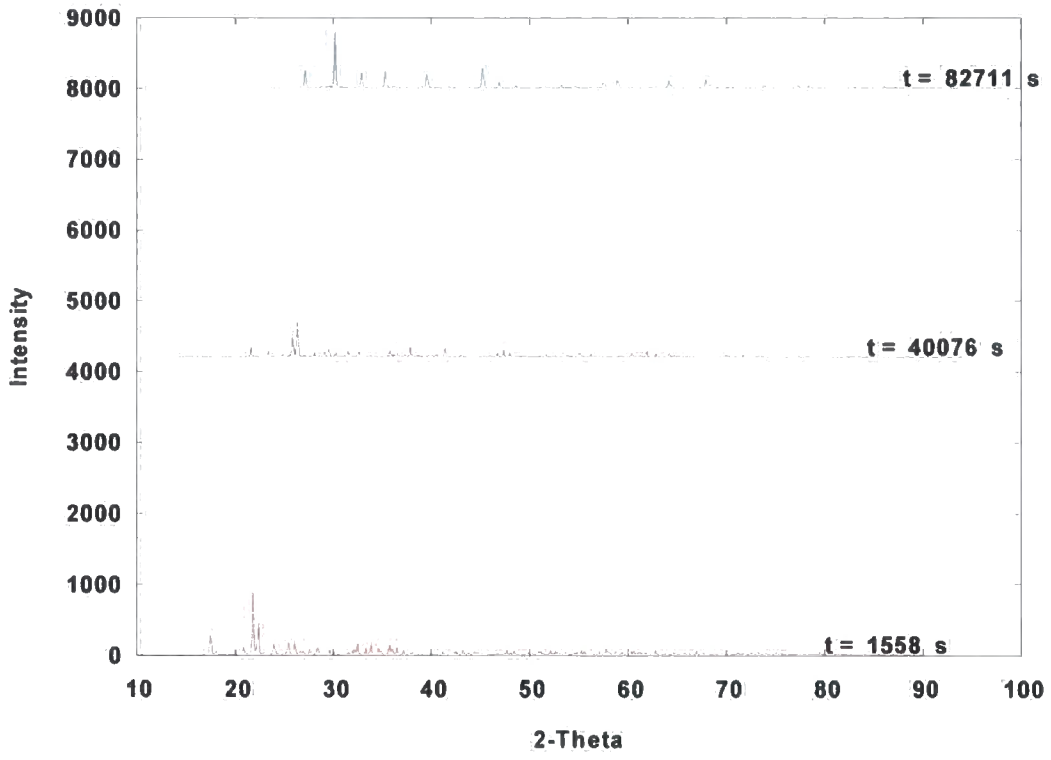

Figure 6.11 VTXRD data recorded as continuous 20 minute scans at 553 K, d8_03157. The scans have been offset in *x* and *y* for clarity. $(MoO)_2P_4O_{13}$ (red scan at t = 1558 s) reduces to MoP_2O_7 (blue scan at t = 82711 s). The purple scan (t = 10076 s) is shown to indicate the temperature at which these two phases exist in a 50:50 mixture.

These data were analysed using multiphase Rietveld refinement. 39 parameters were refined: 14 global parameters (12 background, a sample height and 1 parameter to model axial divergence), 14 parameters to model the $(MoO)_2P_4O_{13}$ phase (4 lattice parameters, 3 isotropic thermal displacement parameters, 6 parameters to model the PV peak shape and a scale parameter) and 11 parameters to model MoP_2O_7 (2 lattice parameters, 3 isotropic thermal displacement parameters, one scale parameter and 6 PV peak shape coefficients). The first scan in this experiment is shown in Figure 6.12. The intensity mismatches are due to the preferred orientation described in Section 5.3.

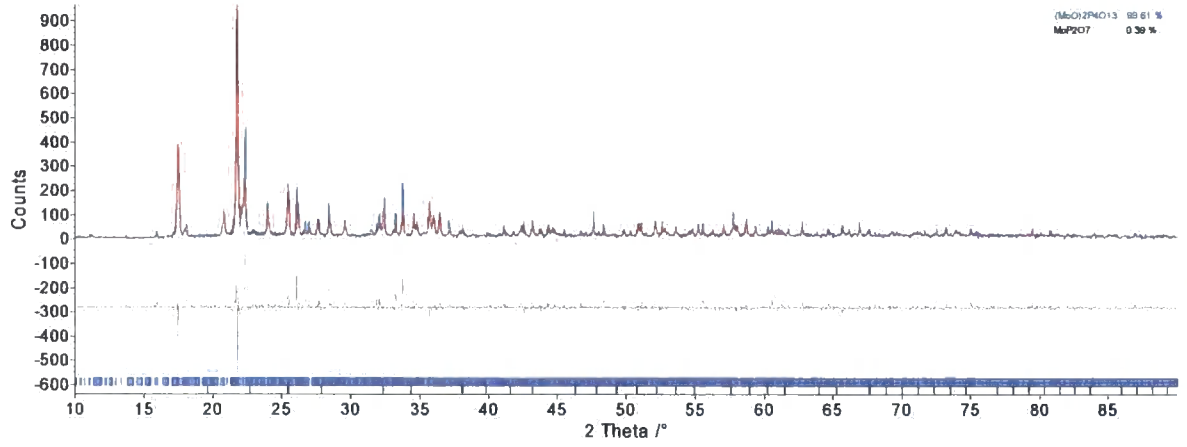

Figure 6.12 The first scan in d8_03157, R_{wp} 28.564. The figure shows the experimental data in blue, the calculated pattern in red and the difference plot in grey.

The changing phase composition for this experiment is given in Figure 6.13, and shows that the formation of the product phase largely occurs in the timeframe 30,000 – 60,000 s. The conversion is again seen to be a direct crystalline to crystalline reduction from $(MoO)_2P_4O_{13}$ to MoP_2O_7.

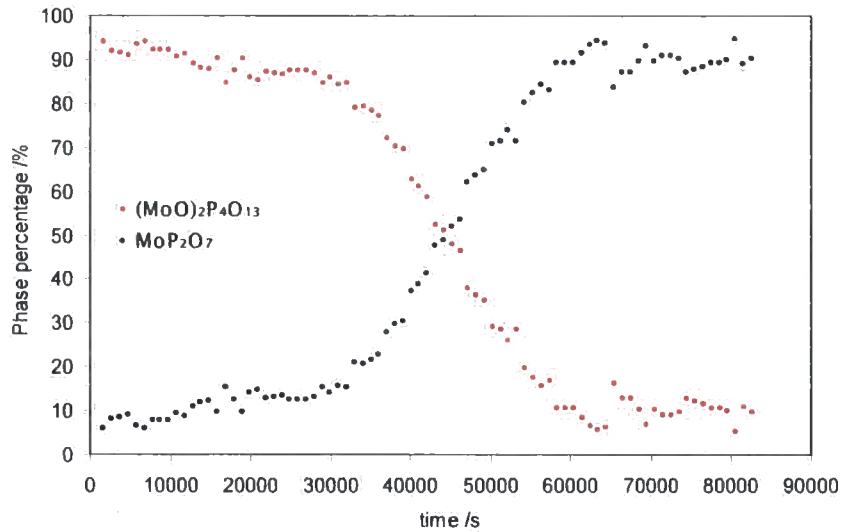

Figure 6.13 Graph of the phase percentages refined for the reduction of $(MoO)_2P_4O_{13}$ at a constant temperature of 826 K.

6.5 Reduction chemistry of $(MoO_2)_2P_2O_7$

VT XRD experiments were also carried out on $(MoO_2)_2P_2O_7$ in an H_2/Ar atmosphere. The sample preparation was identical to that described in Section 6.3; a sample of SEL251 was heated from 313 to 1073 K in 10 K steps, recording a 30 minute scan at each temperature, d8_03481. These diffraction patterns are shown in Figure 6.14, followed by a qualitative discussion of the reaction scheme.

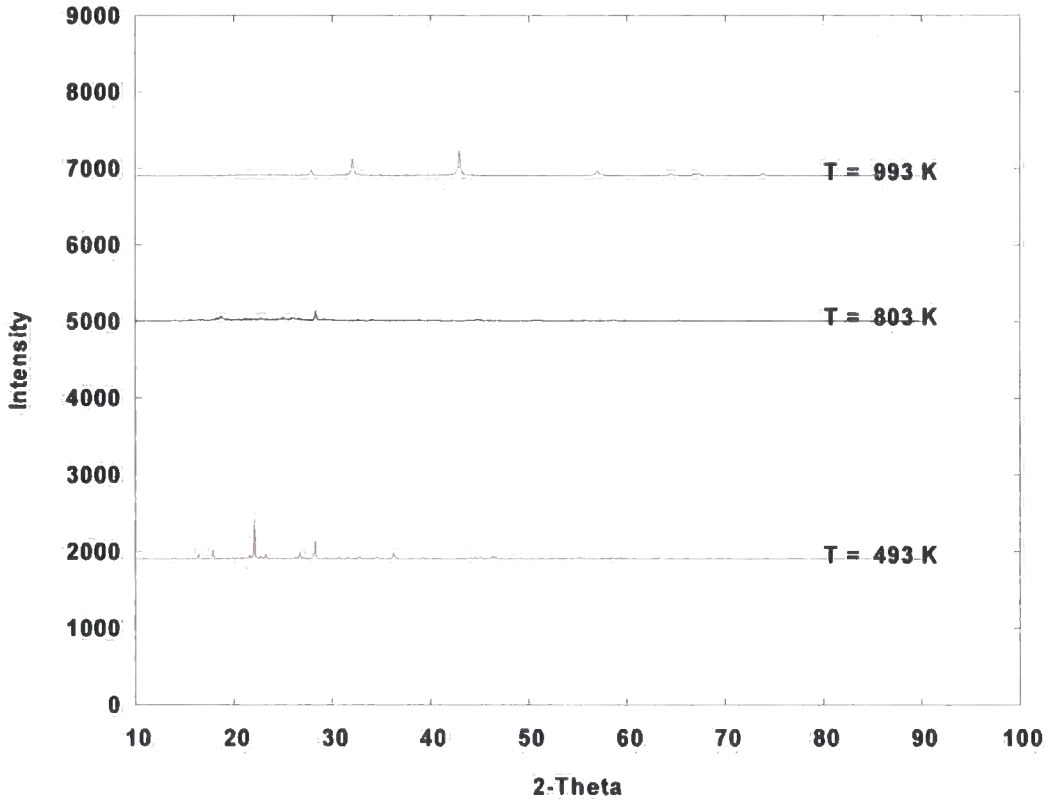

Figure 6.14 VTXRD data recorded over the range 303 – 1073 K in 10 K intervals, d8_03481. The scans have been offset in *y* for clarity. $(MoO_2)_2P_2O_7$ (*e.g.* red scan at 493 K) reduces to give MoP_2O_7 (*e.g.* blue scan 993 K) via a poorly crystalline phase (*e.g.* black scan 993 K).

The initial phase, $(MoO_2)_2P_2O_7$, decomposes above 703 K to give an unknown very poorly crystalline phase. Above 903 K this phase transforms to give MoP as the only crystalline phase. The overall scheme of this reaction is therefore:

$$(Mo^{VI}O_2)_2P_2O_7 \rightarrow \text{amorphous material} \rightarrow Mo^{III}P \qquad (6.6)$$

6.6 Conclusion

The pyrophosphate MoP_2O_7 can be synthesised by reduction of either the Mo(VI) phase $MoO_2(PO_3)_2$ or the Mo(V) containing $(MoO)_2P_4O_{13}$. These reactions are summarised in the following equations:

$$Mo^{VI}O_2(PO_3)_2 \rightarrow \text{amorphous material} \rightarrow Mo^{IV}P_2O_7 \rightarrow Mo^{III}P \qquad (6.4)$$

$$(Mo^{V}O)_2P_4O_{13} \rightarrow Mo^{IV}P_2O_7 \qquad (6.5)$$

Both of these starting precursors contain a Mo:P ratio identical to that in the pyrophosphate phase. It is interesting to note that the reduction to MoP_2O_7 that is summarised in Equation 6.4 proceeds *via* an amorphous (presumably Mo(V)) "phase", whereas the phase can also be formed from reduction of a crystalline Mo^V material, Equation 6.5. The latter reduction has been shown to take place using both a heat/ramp and a continuous heat synthesis. Neither of these techniques has yet been carried out *ex-situ* but are possible routes to produce single crystals for future study.

Reduction of the $(MoO_2)_2P_2O_7$ phase (Mo:P 1:1) does not yield the any intermediate materials, but leads to formation of a poorly crystalline/amorphous material before finally forming $Mo^{III}P$.

6.7 References

1. G. R. Levi and G. Peyronel, *Z. Kristallogr.*, 1935, **92**, 190-209.
2. N. Kinomura, M. Hirose, N. Kumada and F. Muto, *Mat. Res. Bull.*, 1985, **20**, 379-382.
3. A. Leclaire, M. M. Borel, A. Grandin and B. Raveau, *Eur. J. Solid State Inorg. Chem.*, 1988, **25**, 323-328.
4. R. C. Haushalter and L. A. Mundi, *Chem. Mater.*, 1992, **4**, 31-48.
5. V. K. Il'in, A. V. Lavrov, A. V. R. and and I. V. Tananaev, *Zh. Neorg. Khim.*, 1977, **22**, 2738-2741.
6. P. Kierkegaard, *Ark. Kemi*, 1962, **18**, 521-532.
7. Powder Diffraction File, *International Centre for Diffraction Data*, Pennsylvania, 1998.

7. New Route for Synthesis of Cubic $ZrMo_2O_8$

7.1 Introduction

The cubic AM_2O_8 family of materials has attracted interest as components of composite materials due to their thermal expansion properties. The cubic γ- phase of $ZrMo_2O_8$ is particularly interesting as it shows isotropic and linear NTE over the temperature range 11-573 K.[1] It was initially believed to exhibit no phase transitions over this temperature range, though later investigation using neutron diffraction suggested a static oxygen disorder to dynamic oxygen disorder phase transition to be present at 200 K.[2] Thermal expansion coefficients were calculated to be α_l = -6.9*10^{-6} K^{-1} (2-200 K) and α_l = -5.0*10^{-6} K^{-1} (250-502 K). Although the magnitude of negative thermal expansion of γ-$ZrMo_2O_8$ is slightly lower than that encountered in *e.g.* ZrW_2O_8, the phase has several advantages for use. In particular no α-β phase transition as found for ZrW_2O_8 at 450 K is observed and no pressure induced phase transitions occur up to 0.7 GPa.

Whilst cubic ZrW_2O_8 can be prepared directly from its constituent oxides at high temperature, the cubic, γ- phase of $ZrMo_2O_8$ has been reported as being metastable at all temperatures. It has only been prepared to date by careful dehydration of a precursor phase, $ZrMo_2O_7(OH)_2.2H_2O$,[1,3] which has since been shown to proceed *via* an orthorhombic Low-Temperature (LT) form.[4] This synthesis is noted to require very careful preparation of the precursor material and the dehydration requires a specific heating regime to a narrow temperature regime, making this preparation method an unlikely route for industrial production.

There are several other known polymorphs of $ZrMo_2O_8$, many of which show phase transitions as a function of temperature and pressure. These phases are summarised in Figure 7.1. The two thermodynamically stable forms at ambient pressures are the β- monoclinic[5] and α- trigonal[6] forms, which are stable at low and high temperatures respectively. Both materials can be prepared using conventional solid state syntheses. A β- to α-form phase transition occurs at 960 K;[5] the reverse α-β transition can only be carried out by heating the α- form at 873 K for a prolonged time.[7]

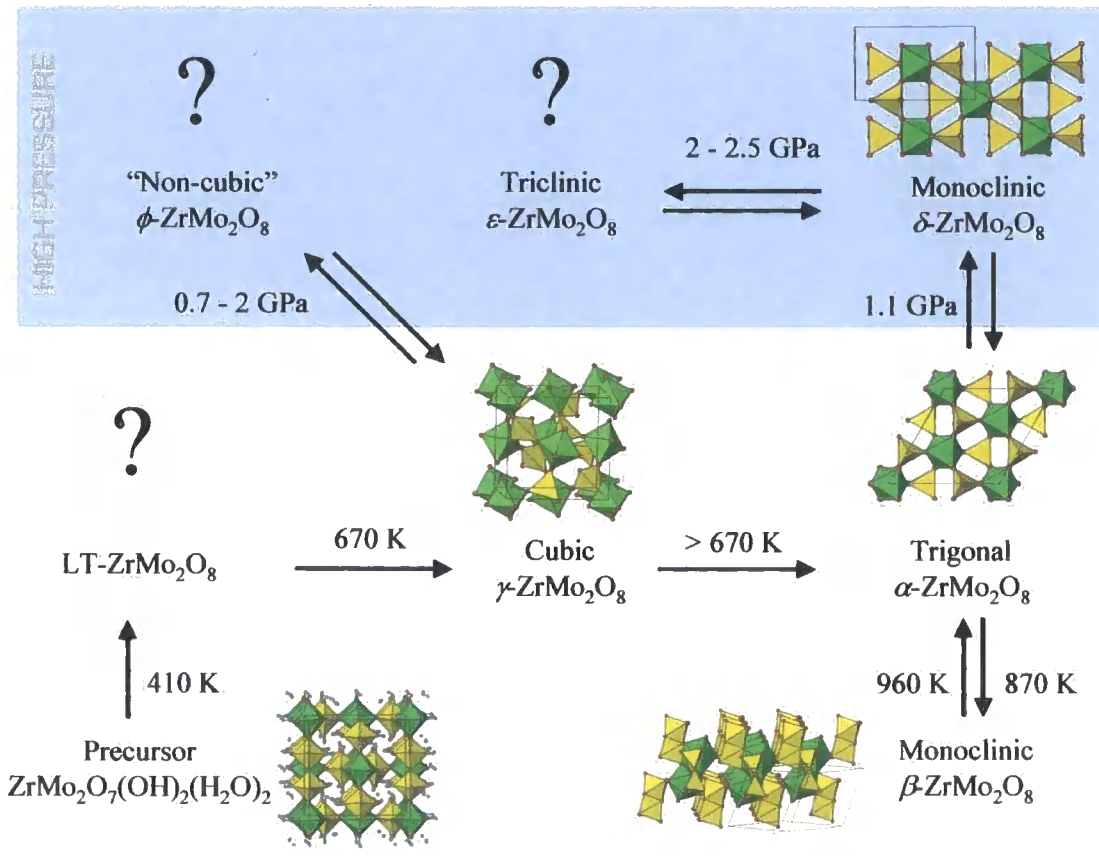

Figure 7.1 Known $ZrMo_2O_8$ and related phases under conditions of varying temperature or pressure. Figure reproduced with kind permission of Simon Allen.[8]

On heating at 663 K the cubic γ- phase will transform to the trigonal α- form;[9] this means that this transition is kinetically controlled as it does not transform to the thermodynamically more stable β-phase at that temperature. The α- form of the material undergoes a reversible phase transition at 1.1 GPa to a δ- form; on increasing the pressure to 2.0 GPa an ε- phase is stable.[10] Amorphous phases with composition $ZrMo_2O_8$ can be obtained by compression of the cubic phase.[11,12] Preparation of these various materials is also complicated by the loss of MoO_3 at high temperature. $ZrMo_2O_8$ has been shown, for example, to lose MoO_3 at temperatures above 1125 K.[13]

The thermodynamics of the $ZrMo_2O_8$ system have been probed, most comprehensively by Varga *et al.*.[14] They conclude that only formation of the monoclinic form from the binary oxides is enthalpically stable at 298 K; the other phases are therefore entropically favoured or metastable. Enthalpies of formation (ΔH_f) are: monoclinic -5.1±3.5 $kJmol^{-1}$, trigonal +32.2±4.5 $kJmol^{-1}$, cubic +45.2±5.3 $kJmol^{-1}$, amorphous +98.9±5.0 $kJmol^{-1}$. Entropies of formation for the cubic and trigonal phases are reported to be 48.5 $Jmol^{-1}K^{-1}$ (298 K) and ≥ 33.1 $Jmol^{-1}K^{-1}$ (973 K) respectively.

Syntheses of $ZrMo_2O_8$ in this laboratory by Dr. Lars Peters using the constituent oxides were carried out using extremely rapid heating to high temperatures for very short time periods followed by rapid quenching. These methods led us to believe that it might be possible to synthesise the metastable cubic phase alongside the trigonal form under carefully controlled conditions. However, the reaction proceeds on a timescale (seconds or less at high temperature) that is difficult to probe using

laboratory methods. For this reason experiments were performed on ID11 at the ESRF to investigate the high temperature synthesis. This chapter outlines the experiments performed to determine optimum synthetic conditions for the cubic NTE material.

7.2 Experiments and calibration

The high intensity available at the synchrotron lends itself to fast time-resolved experiments. The use of ID11 is described in Section 2.3.6. 2D powder diffraction patterns were converted to 1D .xye files using the program Fit2D.[15]

Calibration of the instrument wavelength and detector to sample distance was initially carried out using a Si standard. A small quantity of Si (NIST 640c standard reference material, *a* 5.4311946(92) Å[16]) was loaded into a Pt capillary and aligned on ID11. The Rietveld refinement used the silicon cell parameter to gain an accurate value of the synchrotron wavelength. This refined to λ 0.19909(2) Å; the room temperature Pt lattice parameter refined to *a* 3.9238(3) Å (62.3 keV). This value is in good agreement with literature values.[17] Data in subsequent experiments were normalised to *a*(Pt) = 3.9238 Å. This was to allow for small variations in the sample to detector distance.

Temperature calibration of the mirror furnace used was carried out by Prof. John S. O. Evans as follows. Experimental cell parameters for both Al_2O_3 and Pt were obtained by heating Al_2O_3 in a Pt capillary with different furnace powers over the range to be employed. Values of Pt cell parameters from the literature thermal expansion data were normalised to a room temperature cell of 3.9238 Å. Their temperature dependence was expressed using a polynomial function which could be rearranged to obtain the experimental temperature directly from the Rietveld refinement. These equations are shown in the following Topas lines taken from the input files included in the E-Appendix.

```
a   lpa  3.92375`          `Pt cell parameter
prm !polya  1.16004e-08
prm !polyb  1.90605e-05
prm !polyc  3.91704e+00
prm !te_pt_k = (-polyb+(polyb^2-4*polya*(polyc-lpa))^0.5)/(2*polya);:  297.99265`
```

Figure 7.2 shows the refined temperatures from Pt cell parameters obtained on increasing the furnace power from 0 to 80 % of its maximum 15 V capacity in 160 steps, and repeating in reverse on cooling. The discrepancy between the warming and cooling data in Figure 7.2 is due to the furnace retaining heat on cooling from its maximum 1500 K. These temperatures were used to give an approximate idea of the different percentage power settings required when planning the experiments. Accurate temperatures for each individual experiment have been calculated from Rietveld refinements of Pt cells obtained during those experiments and are quoted in the appropriate section.

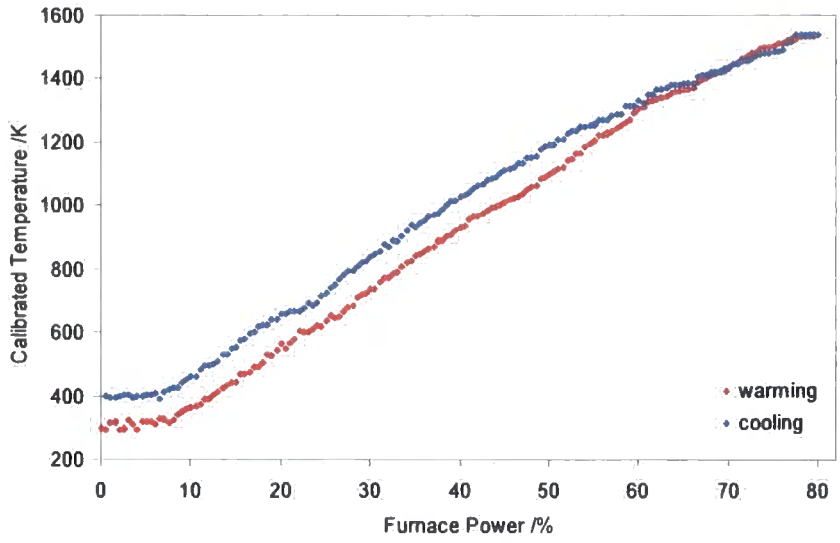

Figure 7.2 Extraction of the real sample temperatures from the furnace power settings.

7.3 Synthetic experiments

This section describes the experiments undertaken to synthesise cubic $ZrMo_2O_8$. A typical experiment was carried out as follows. Each capillary was aligned on ID11 and centred such that it could enter the furnace without obstruction. The capillary's position relative to the synchrotron beam was then optimised by movement of the goniometer stage and/or the main table motors. A diffraction pattern was recorded on the capillary at ambient temperature to enable data calibration. The capillary was then removed from the furnace while the furnace was preheated to a set percentage power, *e.g.* 70 %, and left to equilibrate. The capillary was then moved into the furnace and very rapid diffraction patterns recorded for a set period of time, *e.g.* 0.25 s diffraction patterns over a period of 2 minutes, totalling 480 patterns. The motorised drives typically inserted/removed the capillary in ~ 1 second. Cooling of the sample was undertaken in one of two ways. Either the capillary was removed from the furnace – quench cooling – or the capillary was cooled *in-situ*. Diffraction patterns were recorded either on cooling within the furnace or after the sample had been quenched.

Due to the vast amount of data recorded, the diffraction patterns will be displayed as surface plots drawn in Powder3D.[18] Figure 7.3 shows the patterns that will arise for each of the key phases within these experiments. These powder diffraction patterns were isolated from experimental data presented later in this chapter. Only three key experiments from around 40 performed are presented.

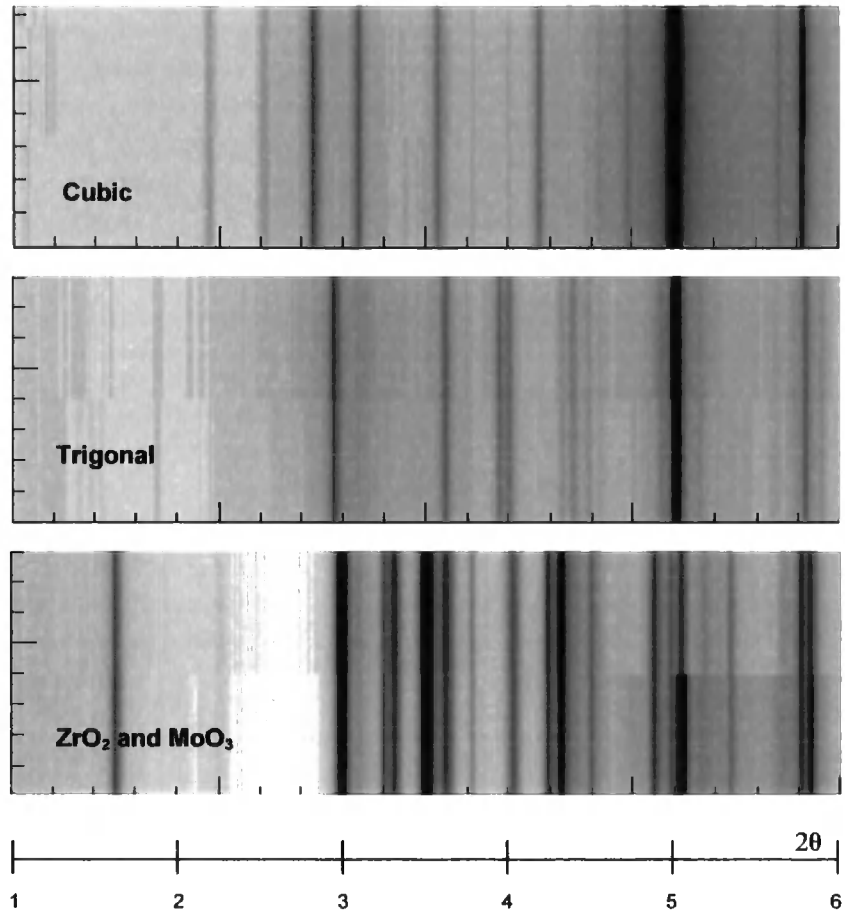

Figure 7.3 Reflection positions for cubic and trigonal $ZrMo_2O_8$ and the constituent oxides, ZrO_2 and MoO_3, over the 2θ range 1-6 °. The data are presented in the form of dummy Debye-Scherrer films. The strong reflection present in each of these "films" at ~5 ° arises from the Pt capillary.

7.3.1 Synthesis of cubic $ZrMo_2O_8$

A stoichiometric ratio of ZrO_2:MoO_3 was loaded into a Pt capillary and aligned on ID11. The furnace was preheated to 70 % of its maximum power; which should correspond to an actual temperature of 1435 K from Figure 7.2. The sample was moved into the hot furnace and diffraction patterns were recorded every 0.25 s for 2 minutes at temperature (480 patterns) and then the furnace was turned off to cool the sample *in-situ*, recording a further 240 0.25 s scans. These are all shown in Figure 7.4; a zoomed region showing the first 48 patterns is given in Figure 7.5 (ZrMo2_0015).

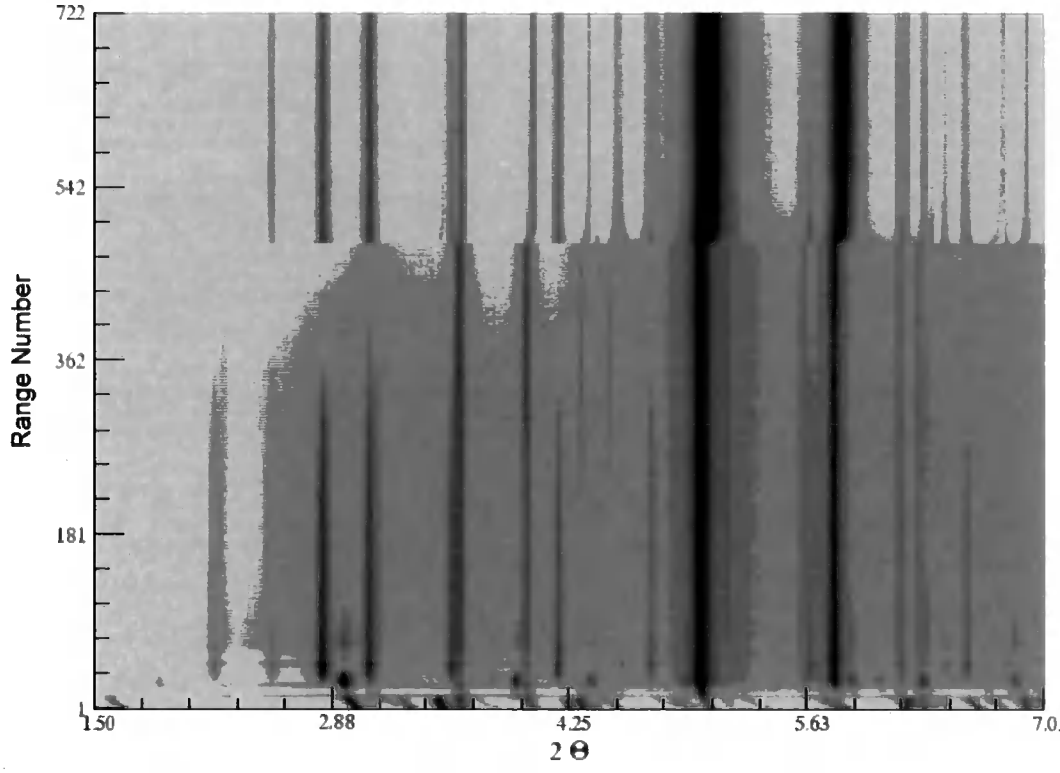

Figure 7.4 720 diffraction patterns recorded in 6 minutes in experiment ZrMo2_0015.

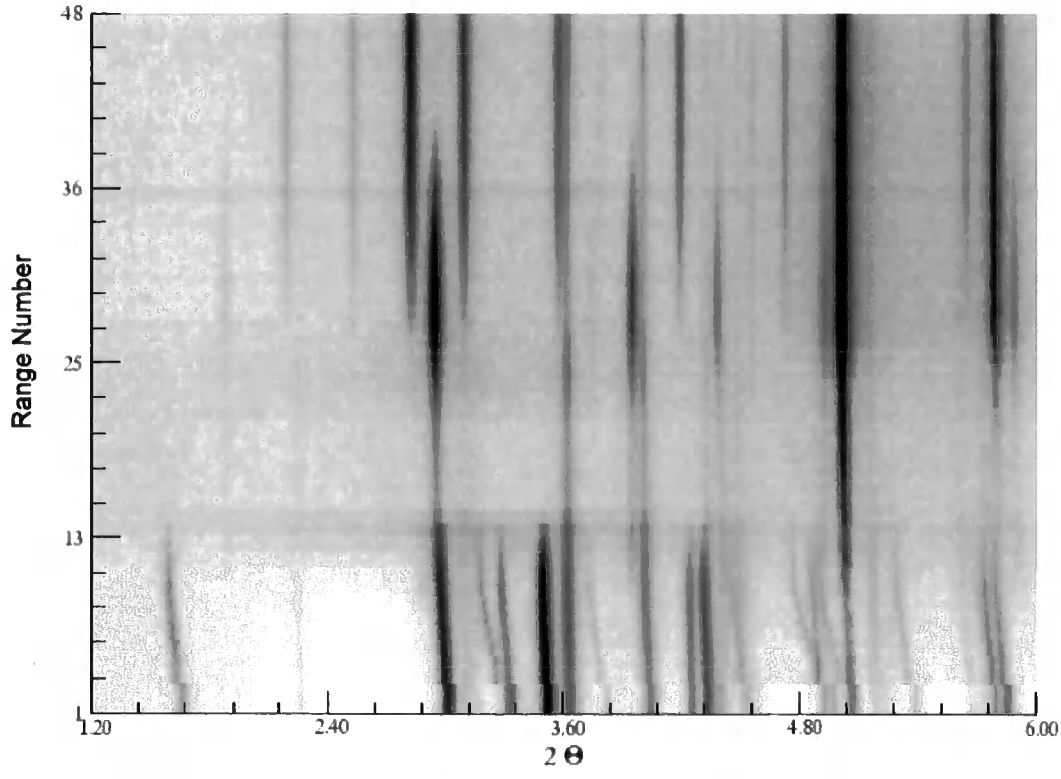

Figure 7.5 A zoomed region of the first 48 ranges (12 seconds) over the 2θ range 1.2-6 °. The cubic phase begins to appear after 6.6 s at 1358 K; the trigonal phase has disappeared after 10.9 s/1378 K.

Visual inspection of these data shows the early formation of the trigonal phase, *e.g.* range 25, from its constituent oxides (ZrO_2 and MoO_3). This phase rapidly disappears as it is transformed to the cubic phase, alongside a small quantity of ZrO_2 (ranges 40-400).

To extract more information from these diffraction patterns, multiphase Rietveld analysis was undertaken. Each of the phases, ZrO_2, MoO_3, Pt and both the trigonal and cubic forms of $ZrMo_2O_8$ were described within an input file to be refined against each of the datasets. A total of 45 parameters were refined. These included 18 background parameters, a zero error, 1 overall isotropic displacement parameter and 4 parameters to model a TCHZ peakshape. The following parameters for each phase were refined: ZrO_2, 4 lattice parameters and a scale term; MoO_3, 3 lattice parameters, a scale term and one parameter to define a March-Dollase preferred orientation correction along the [001] direction; trigonal $ZrMo_2O_8$, 2 lattice parameters and a scale term; cubic $ZrMo_2O_8$, one lattice parameter and a scale term. The Pt capillary was described using one lattice parameter, a scale term, an isotropic displacement parameter and three parameters to describe an 8^{th} order spherical harmonic function to model varying texture in this phase. The first scan was recorded at ambient temperature; the wavelength was calibrated using a Pt cell parameter of 3.9238 *Å* (as refined from the Si calibration). The Rietveld fits for a diffraction pattern in each of the regions of interest during the experiment is given in Figure 7.6.

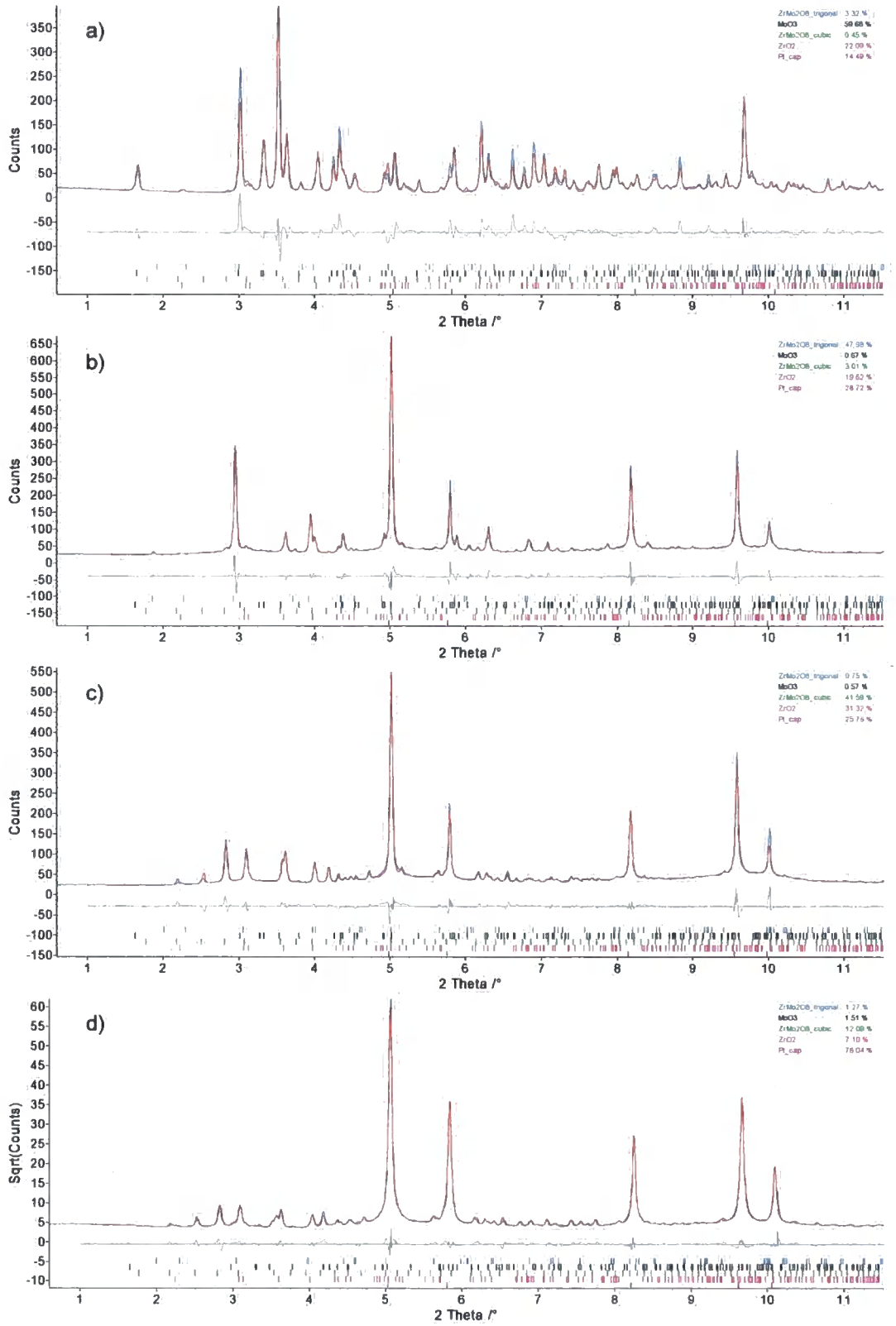

Figure 7.6 A Rietveld refinement for each of the main regions of interest. a) The constituent oxides in range 0000, R_{wp} 14.40 %. b) Trigonal $ZrMo_2O_8$ in range 0025, R_{wp} 6.634 %. c) Cubic $ZrMo_2O_8$ in range 0200, R_{wp} 6.607 %. d) The final phases isolated at ambient temperature, range 0722, R_{wp} 8.757 %. The figure shows the experimental data in blue, the calculated pattern in red and the difference plot in grey. Tick marks (in blue) show the predicted positions of the peaks.

Whilst the Rietveld fit in the first range is not perfect, the major discrepancies are caused by preferred orientation in the MoO_3 material (this could be seen on the images) and was modelled using a March-Dollase correction along the [001] direction. Further correction would have been possible with a spherical harmonic function, but as this would affect the quantitative results of these refinements this was not performed. The other 3 Rietveld fits depicted in Figure 7.6 show good agreement between the calculated model and the observed data. The temperatures for each of these diffraction data were extracted from the refined value of the Pt cubic cell parameter using the calibration equations outlined above, Figure 7.7.

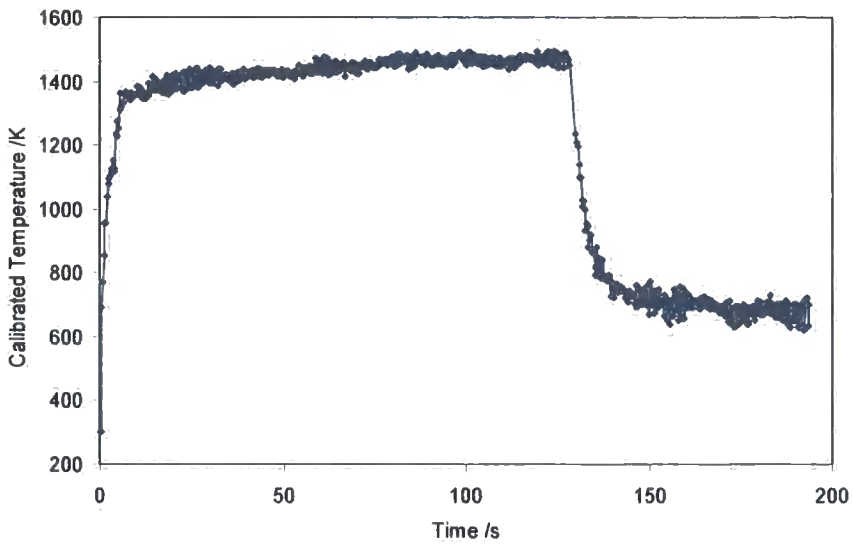

Figure 7.7 Temperatures extracted from the Pt cell parameter using a calculated calibration curve.

This figure shows that the sample capillary was rapidly heated above 1300 K – within 7 s. The temperature rose slightly to a maximum value of 1490 K, before quench cooling *in-situ*. The phase composition present in each of the diffraction scans recorded is displayed graphically in Figure 7.8. Data are plotted as scale*Z*M*V to allow absolute comparison between different phases.[q] Use of this quantity rather than phase percentages prevents both misleading conclusions if the amount of diffracting materials change and artificial percentage changes due to changing texture effects in the Pt capillary.

[q] Z: Number of formula units per unit cell, M: molar mass, V: Volume

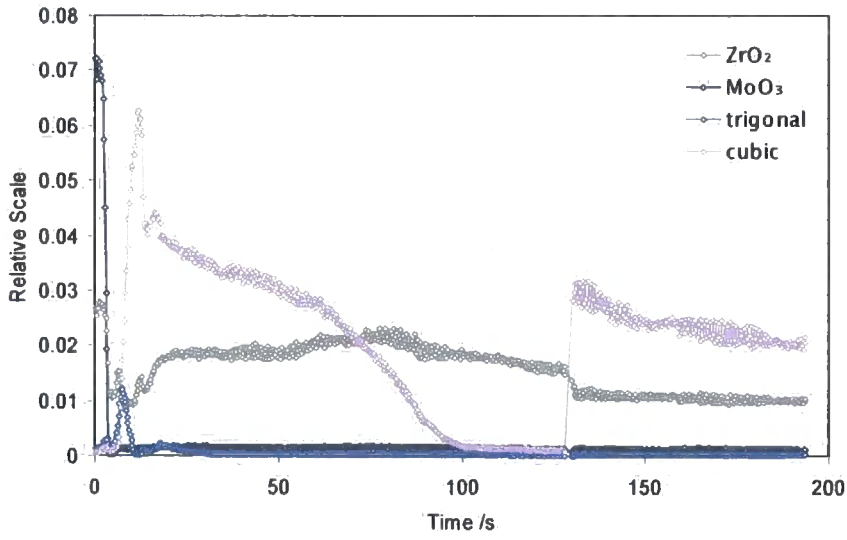

Figure 7.8 The changing phase composition during the experiment ZrMo2_0015.

These results confirm the earlier conclusion from visual inspection. On rapid warming of the sample in the furnace, the first step in the synthesis is the rapid formation of trigonal $ZrMo_2O_8$ from its constituent oxides. On further heating the cubic phase of the material forms. From consideration of Figure 7.7, as the sample temperature rises slightly during the experiment the cubic phase decomposes to give zirconia (and presumably amorphous or molten MoO_3) before the cubic phase is formed again on rapid cooling *in-situ*. This presumably represents its maximum temperature of stability. The input file and spreadsheet containing the refined parameters are included in the E-Appendix.

7.3.2 Isolation of cubic $ZrMo_2O_8$ at ambient temperature

Following the successful synthesis of γ-$ZrMo_2O_8$, a second synthesis was planned to attempt isolation of this phase back at ambient temperature, ZrMo2_0016, based on experiment ZrMo2_0015. A stoichiometric ratio of ZrO_2:2MoO_3 was loaded into a Pt capillary and aligned on ID11. The furnace was preheated to 70 % of its maximum power, corresponding to an expected temperature of 1435 K. The sample was moved into the hot furnace and diffraction patterns were recorded every 0.25 s for 30 seconds at temperature (120 patterns). The capillary was then removed from the furnace which was simultaneously set to cool back to room temperature. After two minutes 8 scans were recorded on the capillary. These were at around 600 K as the furnace was still cooling. These diffraction patterns are shown in Figure 7.9.

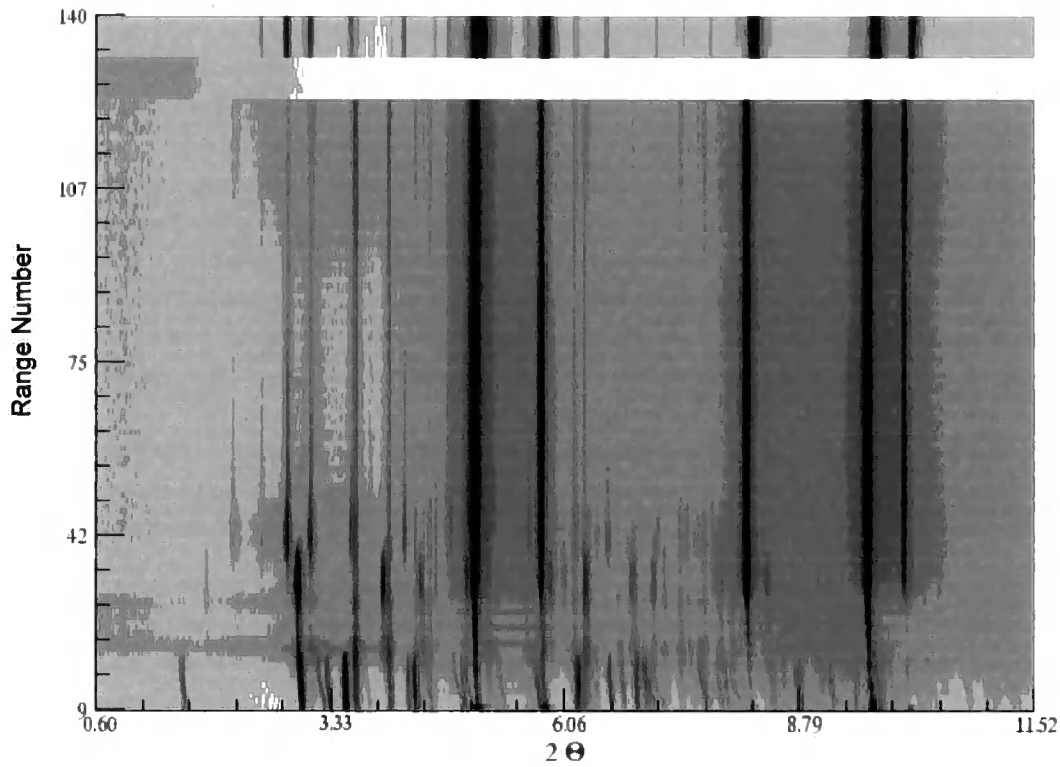

Figure 7.9 Powder diffraction patterns recorded in ZrMo2_0016. The white patterns containing no data were recorded while the capillary was entering the beam. The cubic phase begins to appear after 6.9 s at 1321 K; the trigonal phase has disappeared after 9.3 s/1418 K.

From these data it can be seen that cubic $ZrMo_2O_8$ can be formed without any of the trigonal phase present, and then isolated back to room temperature. This experiment is evidence of a high temperature synthesis being a much quicker route to the formation of this phase, compared with the low temperature precursor route which was the only previously known synthesis of this material.

Multiphase Rietveld analysis was also performed on these data, using the same 45 parameters as described in Section 7.3.1. In all figures to follow, only datapoints from powder diffraction patterns recorded when the capillary was present in the beam have been included. Ranges where the capillary was moving in and out of the furnace (4-7, 124-131) have been excluded as the refined values in these ranges are not true representations of the synthesis at that time. The wavelength was again refined in the first room temperature scan with a fixed Pt lattice parameter of 3.9238 Å. The calibrated temperatures for this experiment are shown plotted against time and range number in Figures 7.10a) and 7.10b) respectively. These graphs highlight the ability to reach high temperatures rapidly using this experimental setup. Figure 7.11 plots the course of the reaction.

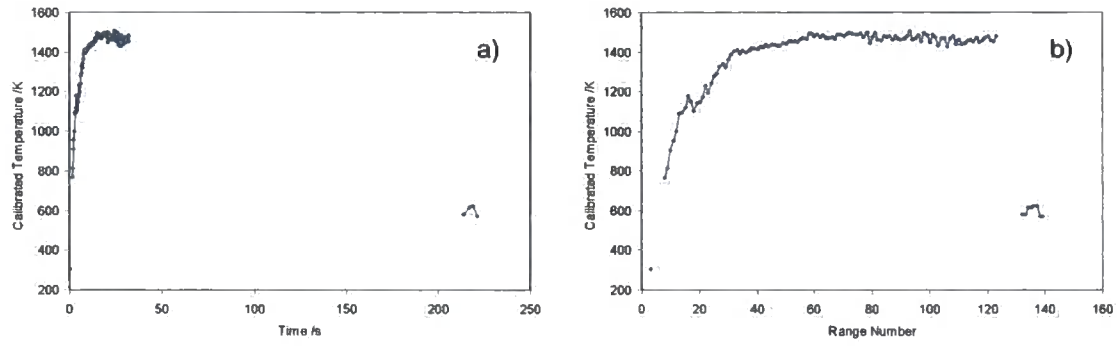

Figure 7.10 Calibrated temperatures extracted from the Rietveld refinement of ZrMo2_0016 as a) a function of time and b) as a function of range number.

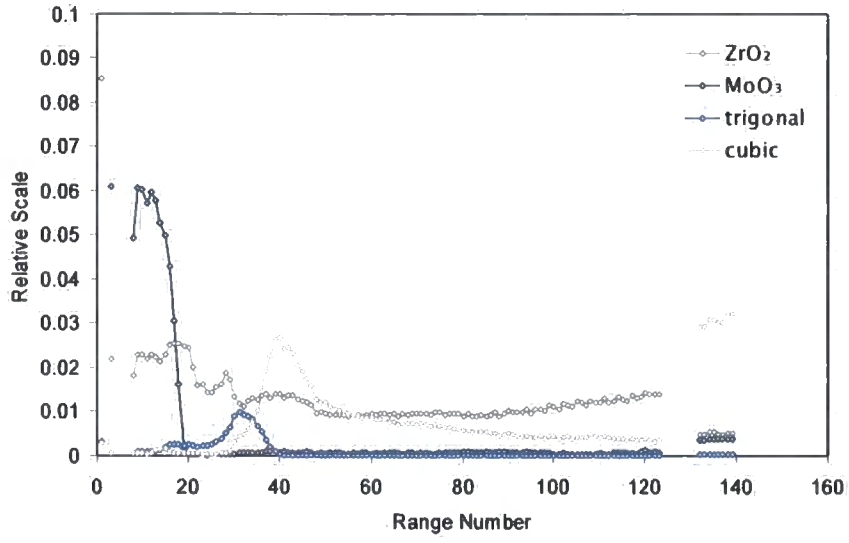

Figure 7.11 The changing phase composition during the experiment ZrMo2_0016; the experimental time for the first 120 runs is 30 seconds

It can be seen once again that the constituent oxides react together first to form the trigonal phase. Soon after this as the capillary is reaching its target temperature, the cubic polymorph becomes the main crystalline phase. On rapidly cooling back to room temperature the cubic phase can be isolated; a small quantity of both of the constituent oxides is also present. The Rietveld fit of this final range is given in Figure 7.12. The input file and spreadsheet containing the refined parameters are included in the E-Appendix.

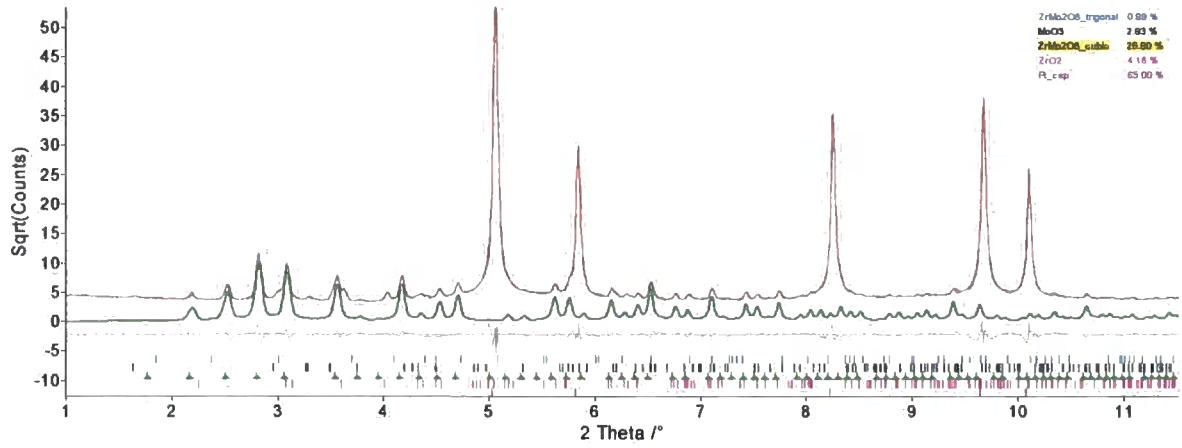

Figure 7.12 The Rietveld refinement of the final range (0139) in ZrMo2_0016. Cubic $ZrMo_2O_8$ (highlighted in green) is present alongside its constituent oxides, R_{wp} 8.78 %. The figure shows the experimental data in blue, the calculated pattern in red and the difference plot in grey. Tick marks show the predicted positions of the peaks.

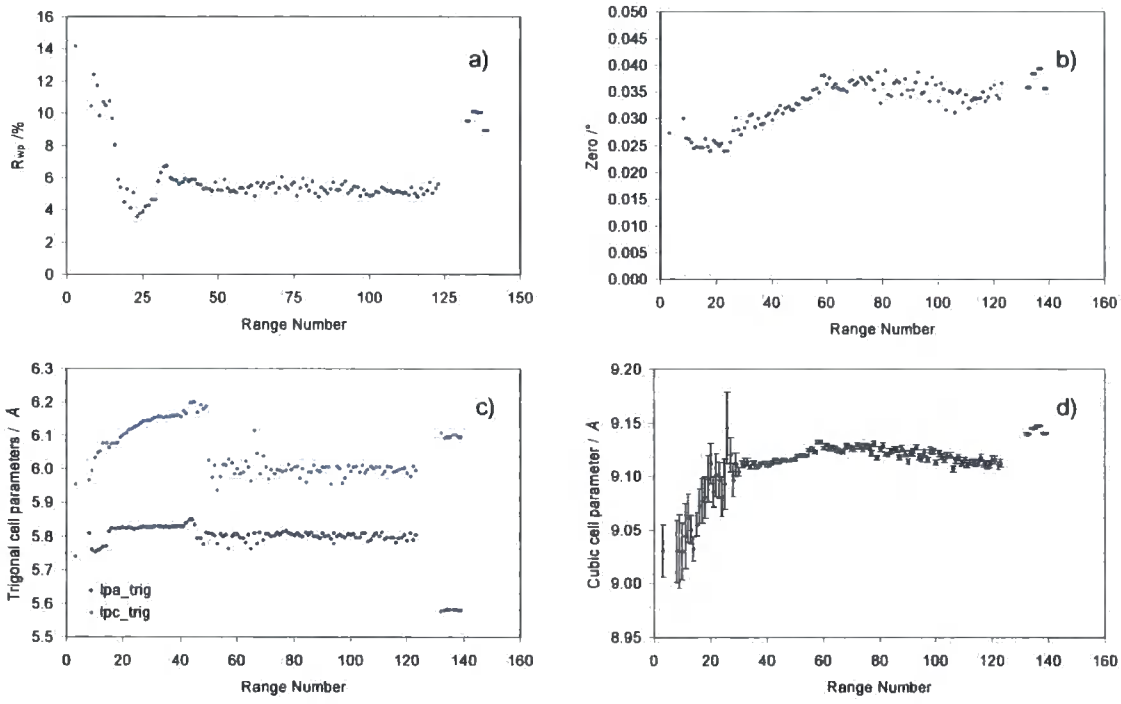

Figure 7.13 Other refined parameters from the Rietveld analysis. a) R_{wp}, b) zero error, c) trigonal cell parameters, d) cubic cell parameters. For the latter two graphs the cell parameters vary significantly in the ranges where the phases are not present. This is highlighted in the displayed s.u.s in d). The NTE of the cubic phase is shown by the increase in cell parameter on cooling back to 600 K.

7.3.3 Thermal stability of cubic $ZrMo_2O_8$

The capillary used in experiment ZrMo2_0016 (Section 7.3.2) was also used to follow the thermal decomposition of metastable cubic $ZrMo_2O_8$. The capillary was heated *in-situ* by increasing the voltage on the furnace from 1 to 80 % of its maximum power, recording scans every 1 %. This was

repeated in reverse on cooling. A total of 159 0.5 s scans were recorded, with 1s equilibration time at each power setting. The scans obtained are shown in Figure 7.14.

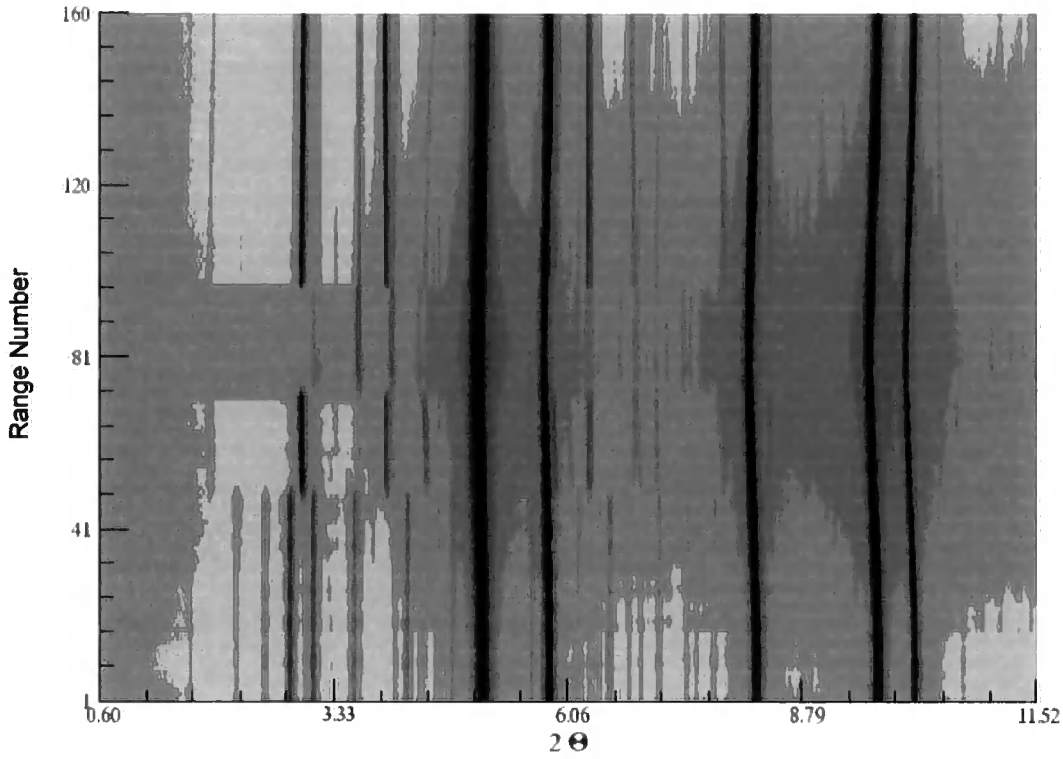

Figure 7.14 The powder diffraction patterns recorded in ZrMo2_0017.

This figure shows the cubic phase exists on continual warming up to 1150 K (range 48). At this temperature the material transforms to the trigonal polymorph, alongside some ZrO_2. Further heating above 1440 K decomposes the trigonal form into its constituent oxides, namely ZrO_2 as a crystalline component and MoO_3 presumably as an amorphous/molten phase.[r] On cooling to 1440 K the trigonal phase reforms implying that the MoO_3 between 1440 and 1540 K must be amorphous/molten. Calibrated temperatures for these diffraction patterns are shown in Figure 7.15. Full Rietveld analysis has not been undertaken on these data.

[r] T_{melt} MoO_3 is 1068 K and TGA data show significant mass loss from ~ 1050 K.[13]

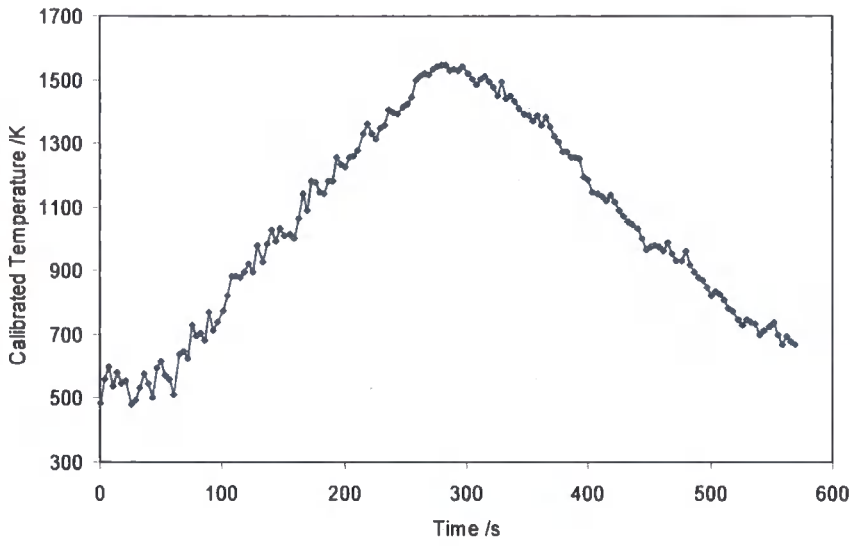

Figure 7.15 Temperature calibration of the diffraction patterns in ZrMo2_0017 from the Pt cell parameter.

This experiment provides further information about the stability of each of the cubic and trigonal phases. The cubic phase remains kinetically stable up to 1150 K when it transforms to the trigonal phase and does not reform on cooling, thus this is an irreversible transition. The trigonal form is thermodynamically stable below 1440 K with respect to its constituent oxides. It is interesting to note that despite the temperatures of ranges 61 to 66 (T = 1330-1356 K) being comparable to that at which cubic $ZrMo_2O_8$ formed from trigonal $ZrMo_2O_8$ in previous experiments (it formed at ~1358 K in experiment 15 and at ~1321 K in experiment 16), none of the cubic phase forms. The transformation from trigonal to cubic $ZrMo_2O_8$ is clearly very dependent on thermal history or perhaps only occurs in the presence of molten MoO_3. None of the monoclinic form is seen on cooling as the transition requires prolonged heating at 873 K.

7.3.4 Synthesis of phase-pure cubic $ZrMo_2O_8$

Following the successful isolation of cubic-$ZrMo_2O_8$ alongside a small amount of ZrO_2 and investigations into its thermal stability, it was decided to attempt the synthesis of a phase-pure material by increasing the Zr:Mo ratio, experiment ZrMo3_0021. A molar ratio of ZrO_2:3MoO_3 was loaded into a Pt capillary and aligned on ID11. The furnace was preheated to 70 % its maximum voltage. After two minutes equilibration time the sample was moved into the hot furnace and diffraction patterns were recorded every 0.25 s for 30 seconds at temperature (480 patterns). A further 20 0.25s scans were recorded over the following ten minutes (with a wait time of 29.75 s in-between), before cooling the sample *in-situ* as the furnace was turned off. After two minutes one final scan was recorded on the capillary. These scans are shown in Figure 7.16.

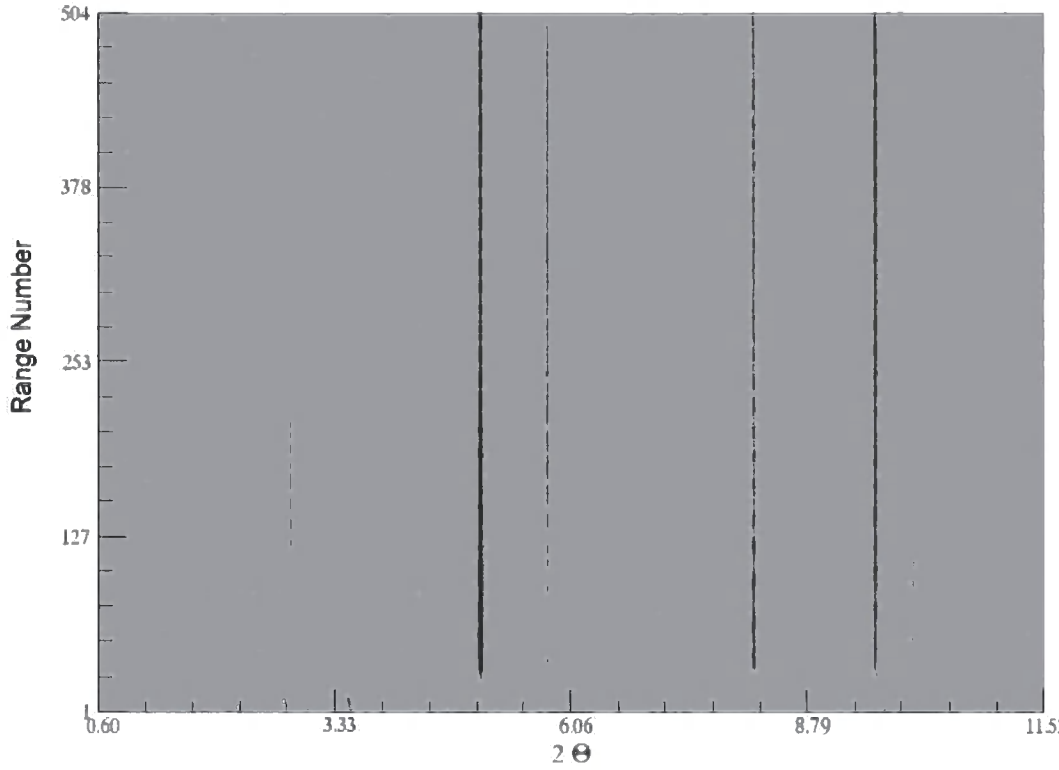

Figure 7.16 The powder diffraction patterns recorded in ZrMo3_0021. The synthesis of pure-phase cubic $ZrMo_2O_8$ is achieved. Note that the *y* scale is not linear in time.

It can be seen from this figure, *c.f.* Figure 7.3, that the cubic phase is the only product in scans 50-490. Multiphase Rietveld analysis was performed on these data, using the same 45 parameters as described in Section 7.3.1. As the range number in this experiment is not linearly related to elapsed time, calibrated temperatures are shown plotted against both range number and time in Figure 7.17. Figure 7.18 plots the course of the reaction as a function of both range number and elapsed time.

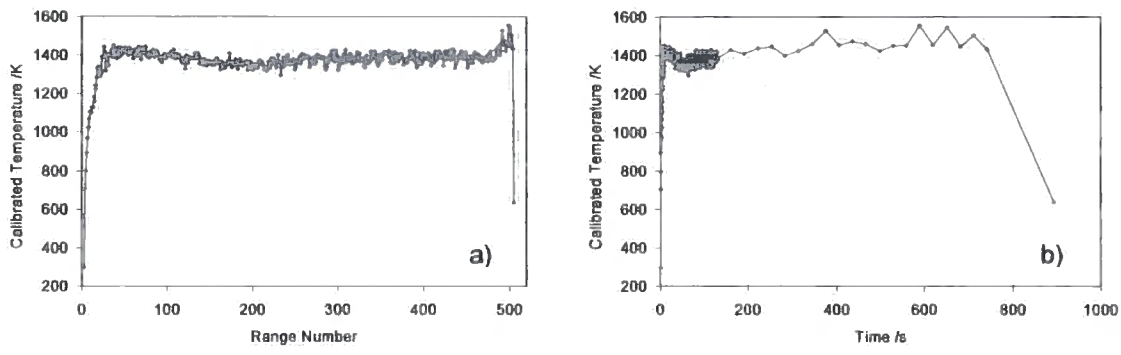

Figure 7.17 Calibrated temperatures extracted from the Rietveld refinement of ZrMo3_0021 plotted as a function of a) range number and b) time.

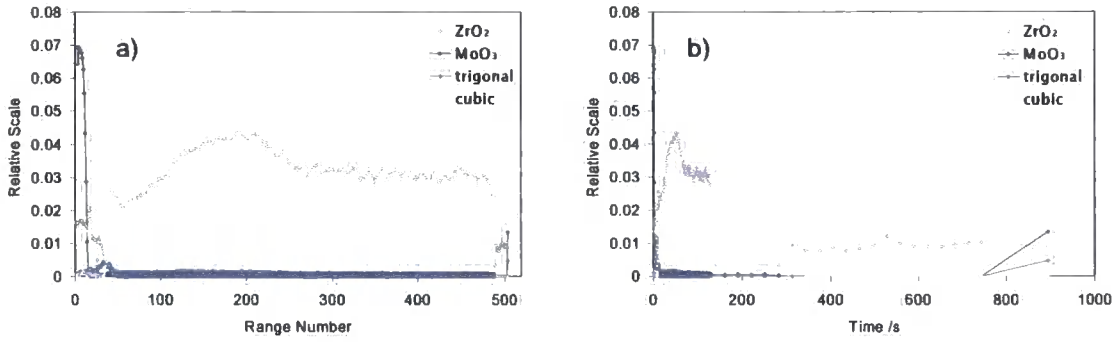

Figure 7.18 The changing phase composition during experiment ZrMo3_0021 plotted as a) a function of range number and b) a function of time.

It is clear from Figure 7.18a) that the cubic material is the only crystalline product of the reaction between ranges 50 and 490. It can be seen in Figure 7.17a that the sample temperature slowly increases beyond this point in the experiment. As a function of time at this higher temperature cubic $ZrMo_2O_8$ eventually decomposes to form ZrO_2 and molten/amorphous MoO_3. On cooling back to low temperature the trigonal phase then forms.

The rise and fall of the relative scale of cubic $ZrMo_2O_8$ in Figure 7.18 is also of interest. It is clear by comparison with Figure 7.17 that at the peak of the relative scale graphs, the temperature is low relative to the rest of the experiment (range 200, T=1325 K), whereas, during the troughs of the relative scale the temperature is relatively high (ranges 271-480, T_{range}=1325-1427 K). When the temperature exceeds 1435 K the amount of cubic material falls significantly. Precise temperature control is therefore critical for maximising yield. The input file and spreadsheet containing the refined parameters are included in the E-Appendix.

7.4 Conclusion

The use of rapid data collections at high temperatures has enabled the quantification of the new and extremely rapid high temperature route to metastable cubic $ZrMo_2O_8$. Multiphase Rietveld analyses have led to quantitative information being gained from these *in-situ* experiments. The cubic phase can be synthesised from its constituent oxides above 1350 K. Rapid quenching after a short reaction time must be employed to isolate the phase back to ambient temperature, otherwise the phase will transform to the trigonal form on cooling. Slow warming of the cubic phase leads to an irreversible cubic-trigonal phase transformation. The trigonal phase is found to be thermodynamically stable up to 1440 K, above which temperature the phase decomposes. Cooling of this mixture below 1440 K yields the trigonal phase again.

Pure-phase cubic $ZrMo_2O_8$ could be synthesised using an increased ZrO_2:MoO_3 ratio of 1:3. This new high temperature synthetic route to cubic $ZrMo_2O_8$ greatly increases the possibility that this material will become industrially significant as a component in composite materials of the future.

7.5 References

1. C. Lind, A. P. Wilkinson, Z. Hu, S. Short and J. D. Jorgensen, *Chem. Mater.*, 1998, **10**, 2335-2337.
2. S. Allen and J. S. O. Evans, *Phys. Rev. B*, 2003, **68**, 1341011-1341013.
3. C. Lind, A. P. Wilkinson, C. J. Rawn and E. A. Payzant, *J. Mater. Chem.*, 2001, **11**, 3354-3359.
4. S. Allen, N. R. Warmingham, R. K. B. Gover and J. S. O. Evans, *Chem. Mater.*, 2003, **15**, 3406-3410.
5. R. F. Klevtsova, L. A. Glinskaya, E. S. Zolotova and P. B. Klevtsov, *Dokl. Akad. Nauk SSSR*, 1989, **335**, 91-95.
6. M. Auray, M. Quarton and P. Tarte, *Acta Crystallogr., Sect. C*, 1986, **42**, 257-259.
7. M. Auray, M. Quarton and P. Tarte, *Powder Diffr.*, 1987, **2**, 36-38.
8. S. Allen, *Thermoresponsive Behaviour of AM_2O_8 Materials, Ph. D. Thesis*, University of Durham, 2003.
9. C. Lind, A. P. Wilkinson, C. J. Rawn and E. A. Payzant, *J. Mater. Chem.*, 2002, **12**, 990-994.
10. S. Carlson and A. M. Krogh Andersen, *Phys. Rev. B*, 2000, **61**, 11209-11212.
11. A. Grzechnik and W. A. Crichton, *Solid State Sci.*, 2002, **4**, 1137-1141.
12. T. Varga, A. P. Wilkinson, C. Lind, W. A. Bassett and C-S. Zha, *Solid State Commun.*, 2005, **135**, 739-744.
13. M. S. Samant, S. R. Dharwadkar, A B. Phadnis and P. N. Namboodiri, *Mater. Chem. Phys.*, 1993, **35**, 120-125.
14. T. Varga, C. Lind, A. P. Wilkinson, H. Xu, C. E. Lesher and A. Navrotsky, *Chem. Mater.*, 2007, **19**, 468-476.
15. A. Hammersley, *Fit2D*, ESRF, Grenoble, France, 1998.
16. J. P. Cline, *Standard Reference Material 640c - Silicon Powder Line Position and Line Shape Standard for Powder Diffraction*, Gaithersburg, Maryland, USA, 2000.
17. B. Manoun, S. K. Saxena, H-P. Liermann and M. W. Barsoum, *J. Am. Ceram. Soc.*, 2005, **88**, 3489-3491.
18. B. Hinrichsen, R. E. Dinnebier and M. Jansen, *Powder 3D, v1.1*, Stuttgart, 2004.

8. Index to the E-Appendix

A hyperlinked version of this file is saved on the E-Appendix, E-Appendix.xls.

Section	Description	Filetype	Filename
3.2	Synthesis and Rietveld analysis	input	Chapter3\32_Synthesis\d9_02374_SEL234.inp
3.3	In-situ studies of the dehydration		
3.3.3	Whole Pattern Fitting at 793 K	input	Chapter3\33_Dehydration\d8_03342_11.inp
		spreadsheet	Chapter3\33_Dehydration\d8_03342_data_analysis.xls
	Range 1	input	Chapter3\33_Dehydration\d8_03342_09_001.inp
	Range 25	input	Chapter3\33_Dehydration\d8_03342_09_025.inp
	Range 46	input	Chapter3\33_Dehydration\d8_03342_09_046.inp
	Range 249	input	Chapter3\33_Dehydration\d8_03342_09_249.inp
	Pawley fit MoOH.H2O.PO3OH	input	Chapter3\33_Dehydration\d8_03342_pawley_01.inp
	Pawley fit MoO3	input	Chapter3\33_Dehydration\d8_03342_pawley_02.inp
	Pawley fit (MoO2)2P2O7	input	Chapter3\33_Dehydration\d8_03342_pawley_03.inp
	Whole pattern fitting at 773 K	input	Chapter3\33_Dehydration\d8_03337_04.inp
		spreadsheet	Chapter3\33_Dehydration\d8_03337_data_analysis.xls
	Pawley fit MoOH.H2O.PO3OH	input	Chapter3\33_Dehydration\d8_03337_pawley_01.inp
	Pawley fit MoO3	input	Chapter3\33_Dehydration\d8_03337_pawley_02.inp
	Pawley fit (MoO2)2P2O7	input	Chapter3\33_Dehydration\d8_03337_pawley_03.inp
3.4	Structure determination of UNK1		
3.4.2	Pawley fit of indexed cell	input	Chapter3\34_UNK1\d6_00480_pawley_01.inp
	Structure solution of UNK1	input	Chapter3\34_UNK1\d6_00480_riet_06.inp
		cif	Chapter3\34_UNK1\mMoOPO4.cif
3.4.3	Approximated model 1	cif	Chapter3\34_UNK1\UNK1_1_Pm.res
	Approximated model 2	cif	Chapter3\34_UNK1\UNK1_2_Pm.res
3.5	Structure determination of UNK2		
3.5.2	Pawley fit of indexed cell in P222	input	Chapter3\35_UNK2\d9_02380_pawley_p222.inp
3.5.3	Pawley fit of indexed cell in C2221	input	Chapter3\35_UNK2\d9_02380_pawley_c2221.inp
3.5.5	Structure solution of UNK2	input	Chapter3\35_UNK2\hrpd_id31_c2221_01sel.inp
		cif	Chapter3\35_UNK2\C2221_str_01.cif
3.6	Rietveld analysis of the dehydration		

	Rietveld fit - all phases	input	Chapter3\33_Dehydration\d8_03342_14_orig.inp
		spreadsheet	Chapter3\33_Dehydration\d8_03342_12.xls
	Range 1	input	Chapter3\33_Dehydration\d8_03342_14_001.inp
	Range 25	input	Chapter3\33_Dehydration\d8_03342_14_025.inp
	Range 46	input	Chapter3\33_Dehydration\d8_03342_14_046.inp
	Range 249	input	Chapter3\33_Dehydration\d8_03342_14_249.inp
3.8	Rietveld analysis of (MoO2)2P2O7	input	Chapter3\38_Isolation\d9_02843_SEL315.inp
4.2	Variable Temperature Studies		
4.2.1	PheniX VT - cooling	input	Chapter4\42_VT\421_PheniX\d9_02442_01.inp
		output	Chapter4\42_VT\421_PheniX\d9_02442_01.res
		spreadsheet	Chapter4\42_VT\421_PheniX\phase_changes.xls
	PheniX VT - warming	input	Chapter4\42_VT\421_PheniX\d9_02443_01.inp
		output	Chapter4\42_VT\421_PheniX\d9_02443_01.res
		spreadsheet	Chapter4\42_VT\421_PheniX\phase_changes.xls
4.2.2	HTK VT - all	input	Chapter4\42_VT\422_HTK\d8_03413_01_orig.inp
		output	Chapter4\42_VT\422_HTK\d8_03413_01.res
		spreadsheet	Chapter4\42_VT\421_PheniX\phase_changes.xls
4.2.3	ID31 VT	input	Chapter4\42_VT\423_ID31\seed.inp
		output	Chapter4\42_VT\423_ID31\ch2627_sel315_ramping_01.res
		spreadsheet	Chapter4\42_VT\423_ID31\ch2627_sel315_ramping_01.xls
4.3	High Temperature Structure		
4.3.1	High T synchrotron refinements	input	Chapter4\43_HighT_str\ch2627_sel315_423K_long_riet_03.inp
4.3.2	High T neutron refinements	input	Chapter4\43_HighT_str\MoOPO058_riet_02.inp
4.3.3	Combined High T refinements	input	Chapter4\43_HighT_str\highT_ID31_NIST_04.inp
		cif	Chapter4\43_HighT_str\highT_ID31_NIST_04.cif
4.3.4	High T model with Low T data	input	Chapter4\43_HighT_str\lowT_ID31_NIST_04.inp
4.4	Low Temperature Superstructure		
4.4.2	Supercell Model	input	Chapter4\44_superstr\453_EDPs\d8_03559_pawley_electrondiff_P2sup.inp
	Subcell Model	input	Chapter4\44_superstr\453_EDPs\d8_03559_pawley_electrondiff_Pnmasub.inp

4.4.4	P21/c model	input	Chapter4\44_superstr\455_str_soln\P21c_Jul08_07.inp
		spreadsheet	Chapter4\44_superstr\455_str_soln\P21c_Jul08_07.xls
4.4.5	Pbar1 model	input	Chapter4\44_superstr\455_str_soln\Pbar1_Jul08_07.inp
		spreadsheet	Chapter4\44_superstr\455_str_soln\Pbar1_Jul08_07.xls
5.3	Rietveld refinement		
5.3.1	Flat plate Rietveld	input file	Chapter5\53_synthesis\d8_03014_120K.inp
5.3.2	Capillary sample	input file	Chapter5\53_synthesis\d6_00082.raw
			Chapter5\53_synthesis\d6_00082_riet_01.inp
5.4	RT single crystal	cif	Chapter5\54_RT_single_crystal\293_m3.cif
		spreadsheet	Chapter5\54_RT_single_crystal\Room_Temperature.xls
5.5	VT studies		
5.5.1	LowT PheniX	input	Chapter5\55_insitu_VT\phenix\seed.inp
		spreadsheet	Chapter5\55_insitu_VT\phase_change_data.xls
5.5.2	HighT HTK	input	Chapter5\55_insitu_VT\htk\seed_orig.inp
		spreadsheet	Chapter5\55_insitu_VT\phase_change_data.xls
5.6	HighT single crystal		
5.6.1	Daresbury cell data	spreadsheet	Chapter5\56_Hothead\DL_data.xls
5.6.2.1	Room Temperature Data	cif	Chapter5\56_Hothead\025dat_02.cif
		spreadsheet	Chapter5\56_Hothead\Room_temperature.xls
5.5.2.2	Charge Flipping	input file	Chapter5\56_Hothead\cf_400mop1.inp
		coordinates	Chapter5\56_Hothead\400mop1_xtal_01.inp
		cif	Chapter5\56_Hothead\400mop1_cf.cif
	Unrestrained refinement	cif	Chapter5\56_Hothead\300dat_09.cif
		spreadsheet	Chapter5\56_Hothead\Unrestrained_refinement.xls
5.5.2.3	Restrained refinement	cif	Chapter5\56_Hothead\300dat_12.cif
		spreadsheet	Chapter5\56_Hothead\Restrained_refinement.xls
5.5.2.4	Split Sites	cif	Chapter5\56_Hothead\300dat_13.cif
		spreadsheet	Chapter5\56_Hothead\Restrained_refinement_split_Site.xls

5.5.2.5	653K data - unrestrained	cif	Chapter5\56_Hothead\380dat_01.cif
	653K data - restrained	cif	Chapter5\56_Hothead\380dat_02.cif
	653K data - all	spreadsheet	Chapter5\56_Hothead\380_unrestrained_restrained.xls
5.7	TOF neutron data		
5.7.1	VT TOF refinements	input	Chapter5\57_HRPD_data\seed_orig_supercell_model.inp
		spreadsheet	Chapter5\57_HRPD_data\mo2p4o15_hrpd_vt.xls
5.7.2	candlestick at HRPD	input file	Chapter5\57_HRPD_data\300Khothead_hrp39963_candlestick_01.inp
5.7.3	furnace (380 °C) at HRPD	input file	Chapter5\57_HRPD_data\653Khothead_hrp39753_bs_02.inp
5.7.4	furnace (RT) at HRPD	input file	Chapter5\57_HRPD_data\300Khothead_hrp39710_bs_01.inp
	furnace (380 °C) at HRPD	input file	Chapter5\57_HRPD_data\653Khothead_hrp39752_bs_01.inp
6.2	Rietveld of MoO2(PO3)2	input	Chapter6\d5_06325.inp
6.3	VTXRD on MoO2(PO3)2	input	Chapter6\d8_03483_06.inp
		spreadsheet	Chapter6\d8_03483.xls
6.4	VTXRD on (MoO)2P4O13		
6.4.1	Ramping experiment	input	Chapter6\d8_03085.inp
		spreadsheet	Chapter6\d8_03085.xls
6.4.2	Constant T experiment	input	Chapter6\d8_03157.inp
		spreadsheet	Chapter6\d8_03157.xls
7.2	Calibration using NIST Si	input file	Chapter7\si_calib_01.inp
	Pt temperature calibration	input file	Chapter7\pt_calibration_04.inp
		spreadsheet	Chapter7\Pt_calibration.xls
7.3.1	Synthesis of ZrMo2O8	input	Chapter7\zrmo2_0015_03.inp
		spreadsheet	Chapter7\zrmo2_0015_results.xls
7.3.2	Isolation of ZrMo2O8	input	Chapter7\zrmo2_0016_04.inp
		spreadsheet	Chapter7\zrmo2_0016_results.xls
7.3.4	Phase pure ZrMo2O8	input	Chapter7\zrmo3_0021_03.inp
		spreadsheet	Chapter7\zrmo3_0021_results.xls